Investigations of Statistical Properties of Galactic Foreground Components and the CMB

A thesis

submitted for the degree of

Doctor of Philosophy

in

The Department of Physics,

Pondicherry University,

Puducherry - 605 014, India

by

Fazlu Rahman P P

Indian Institute of Astrophysics,

Bangalore - 560 034, India

August 2023

Investigations of Statistical Properties of Galactic Foreground Components and the CMB

Fazlu Rahman P P
Indian Institute of Astrophysics

Indian Institute of Astrophysics
Bangalore - 560 034, India

Title of the thesis	:	**Investigations of Statistical Properties of Galactic Foreground Components and the CMB**
Name of the author	:	**Fazlu Rahman P P**
Address	:	Indian Institute of Astrophysics II Block, Koramangala Bangalore - 560 034, India
Email	:	fazlu.rahman@iiap.res.in
Name of the supervisor	:	**Prof. Pravabati Chingangbam**
Address	:	Indian Institute of Astrophysics II Block, Koramangala Bangalore - 560 034, India
Email	:	prava@iiap.res.in

Declaration of Authorship

I hereby declare that the matter contained in this thesis is the result of the investigations carried out by me at the Indian Institute of Astrophysics, Bangalore, under the supervision of Prof. Pravabati Chingangbam. This work has not been submitted for the award of any other degree, diploma, associateship, fellowship, etc. of any other university or institute.

Fazlu Rahman P P
PhD Student,
Indian Institute of Astrophysics,
Bangalore – 560034, India

Date: 12 January, 2024

Certificate

This is to certify that the thesis entitled **'Investigations of Statistical Properties of Galactic Foreground Components and the CMB'** submitted to the Pondicherry University by Mr. Fazlu Rahman P P for the award of the degree of Doctor of Philosophy, is based on the results of the investigations carried out by her under my supervision and guidance, at the Indian Institute of Astrophysics. This thesis has not been submitted for the award of any other degree, diploma, associateship, fellowship, etc. of any other university or institute.

Prof. Pravabati Chingangbam
Thesis Supervisor,
Indian Institute of Astrophysics,
Bangalore – 560034, India

Date: 12 January, 2024

List of Publications

Refereed Publications

1. **F. Rahman**, P. Chingangbam and T. Ghosh 2021, *The nature of non-Gaussianity and statistical isotropy of the 408 MHz Haslam synchrotron map*, Journal of Cosmology and Astroparticle Physics (JCAP) **07** (2021) 026 [arXiv:2104.00419 [astro-ph.CO]]

   Chapter 5

2. **F. Rahman**, P. Chingangbam and T. Ghosh, *Statistical properties of Galactic Synchrotron temperature and polarization maps — a multi-frequency comparison*, Journal of Cosmology and Astroparticle Physics (JCAP) **01** (2024) 036 [arXiv:2212.06076 [astro-ph.CO]]

   Chapter 6

Papers under Revision

1. P. Chingangbam and **F. Rahman**, *Minkowski Functionals for composite smooth random fields*, undergoing revision in Physical Review D [arXiv:2311.12571 [astro-ph.CO]]

   Chapter 4

In Preparation

1. **F. Rahman**, P. Chingangbam, T. Ghosh and C. Park, *Morphological statistics of thermal dust emission*, in preparation

   Chapter 7

2. P. Chingangbam, K. P. Yogendran, S. Appleby, **F. Rahman** and C. Park, *Total absolute curvature for random fields in two dimensions*, in preparation

   Chapter 8

Presentations

1. Poster presentation on *Multi-frequency Statistics of Galactic Synchrotron Emission*, in the Frontiers in Cosmology conference held at Raman Research Institute, Bengaluru, Feb 2023.

2. Oral presentation on *Morphological Statistics of Galactic Synchrotron Emission* in the Galactic Science and CMB Foreground Science conference held at Tenerife, Spain, December 2022 (Hybrid mode)

3. Oral presentation on *Multi-frequency Statistics of Galactic Synchrotron Emission* in the Cosmoglobe Workshop, University of Oslo, May 2022 (Online)

4. Contributed talk on *Multi-Frequency Statistics of Galactic Synchrotron Emission*, in ASI 2022, held at IIT Roorkee, March 2022.

5. Contributed Talk on *The Nature of Non-Gaussianity and Statistical Isotropy of the 408 MHz Haslam Synchrotron Map* in the Workshop & School on 21-cm Cosmology & Reionization, April 2021 (Online)

6. Poster presentation on *Gaussianity and Statistical Isotropy of Galactic Synchrotron at 408 MHz* in the B-mode from Space workshop at Max-Planck-Institut für Astrophysik, Munich, Germany, Dec 2019.

7. Poster presentation on *Gaussianity and Statistical Isotropy of Galactic Synchrotron at 408 MHz*, in XIII Tonale Winter School on Cosmology, Passo del Tonale, Italy, Dec 2019

8. Contributed Talk on *Gaussianity and Statistical Isotropy of Galactic Synchrotron at 408 MHz* in the Young Astronomers Meet 2019 held at Kodaikanal Solar Observatory, Kodaikanal, Tamil Nadu, Sept 2019

9. Contributed Talk on *Gaussianity and Statistical Isotropy of Galactic Synchrotron at 408 MHz* in the Workshop on Geometrical and Topological Methods for Cosmological Data Analysis, at NISER Bhubaneswar, July 2019

10. Poster presentation on *Gaussianity and Statistical Isotropy for Galactic Foregrounds Using Planck* in the Asia Pacific Winter School and Workshop on Gravitation and Cosmology, YITP, Kyoto University, Japan, Feb 2019.

Acknowledgements

I express my immense gratitude to my supervisor, Prof. Pravabati Chingangbam, for her invaluable guidance, unwavering encouragement, and consistent involvement throughout my doctoral journey. Her insightful perspectives, subject expertise, and vast knowledge have been instrumental in shaping my research during my Ph.D. Working with her has been a pleasure and privilege, and I am truly thankful to her for believing in me and pushing me beyond my limits.

I want to thank my long-term collaborator, Dr. Tuhin Ghosh, for our enriching and productive discussions. He has an amazing personality, and I have learnt a lot from him. I sincerely thank my collaborators, Prof. Changbom Park and Dr. Stephen Appleby. I acknowledge the support and kind hospitality of Prof. Park during my visit to the Korea Institute for Advanced Study (KIAS), Seoul. I extend my heartfelt thanks to my collaborators, Prof. Hans Kristian Eriksen and Prof. Ingunn Wehus, for their insightful comments about my work and for hosting me at the Institute of Theoretical Astrophysics (ITA), University of Oslo. I thank Dr. Duncan Watts and other members of the Oslo CMB group for teaching me the CMB data analysis techniques.

My heartfelt appreciation goes to my group mates Vidhya, Joby, Akanksha, Priya and Masroor for their valuable contributions to our academic discussions and their timely support. I enjoyed collaborating with all of them a lot.

I sincerely thank the esteemed members of my doctoral committee: Dr. Suraj Kumar Sinha, Prof. Mousumi Das, and former committee member Dr. S.V.M Satyanarayana (late). I am indebted to the Indian Institute of Astrophysics (IIA) for providing an exceptional academic environment and the necessary research facilities during my tenure. Special thanks to the Board of Graduate Studies (BGS) at IIA, particularly Sankara and Vijayalakshmi, for their kind support with

the administrative work. I am also grateful to the staff at Pondicherry University for their timely assistance.

I extend my gratitude to my life partner and best friend, Ladeeda, whose love and care I cherish the most. I consider myself truly fortunate to have her in my life. My heartfelt appreciation goes out to my friends and fellow students at IIA and Bhaskara, who contributed to making my PhD journey memorable. I want to give special thanks to my friends Deepthi and Sonith, who have been with me through all the highs and lows. I thank all my loving batch mates, Anirban, Indrani, Sioree and Swastik. We had a lot of fun together. My dear friend Ashraf, who has always stood beside me as my closest companion and best buddy, I want to extend my heartfelt thanks to you.

I express my profound gratitude to my family members and teachers for their continuous support and encouragement during my academic journey. Lastly, with the utmost appreciation, I would like to recognize the boundless love and steadfast support of my parents, whose sacrifices have been indispensable in my path. Words can never fully convey the depth of my gratitude for all they have undertaken. I owe special thanks to my brothers and sisters for their love and support.

With immense appreciation, I extend my thanks to all those who have contributed to my academic and personal development.

Data sets and Software Usage

Most of the research work presented in this thesis was carried out utilizing the computational resources at the Indian Institute of Astrophysics (IIA), particularly the Nova High Performance Computing (HPC) cluster (https://www.iiap.res.in/?q=facilities/computing/nova). I extend my heartfelt gratitude to the computer support team at IIA for their unwavering assistance and support at every step of the way.

The works were conducted using the archival data primarily taken from the Legacy Archive for Microwave Background Data Analysis (LAMBDA) website (https://lambda.gsfc.nasa.gov/). The data from the Planck mission was obtained from the Planck Legacy Archive (PLA)(https://pla.esac.esa.int/. To generate the theoretical CMB power spectrum, the Code for Anisotropies in the Microwave Background (CAMB) package (https://camb.readthedocs.io/) was used. CAMB employs numerical techniques to solve the Boltzmann equations. The BeyondPlanck data products used in the analysis were taken from the BeyondPlanck website (https://beyondplanck.science/).

The work made use of various software packages. To handle CMB and foreground data on the sphere, Healpix f90 and healpy packages were used (Górski et al. 2005; Zonca et al. 2019). We used Polspice (Szapudi et al. 2001; Chon et al. 2004) and Namaster (Alonso et al. 2019) software packages as the angular power spectrum estimators, which take care of the effects due to incomplete sky region. Other major python packages used in the work are: (i) Numpy (van der Walt et al. 2011) (ii) Scipy (Virtanen et al. 2020) (iii) Matplotlib (Hunter 2007).

To all the beautiful humans who believed in me, pushed me beyond my limits, and instilled in me the power of perseverance.

Abstract

Accurate component separation of full-sky maps in the radio and microwave frequencies, such as the cosmic microwave background (CMB), relies on a thorough understanding of the statistical properties of the Galactic foreground emissions. These Galactic emissions include Galactic synchrotron, free-free, Anomalous Microwave Emission (AME), thermal dust emissions, etc. This thesis aims to characterize these foreground components with the goal of improving the component separation methods in experiments looking for cosmological signals. For this, we utilize a set of geometric and topological tools such as Minkowski functionals (MFs) and Minkowski tensors (MTs), along with conventional tools like power spectrum, skewness, kurtosis, etc. We begin our analysis by studying the MFs for composite random fields, which are the sum of two fields. Using analytic expressions for MFs, we examine and quantify how the presence of a secondary field, such as noise or any residual contamination, affects the morphology of the field of interest, say the CMB field. We find that the secondary field can alter the amplitude and nature of non-Gaussianity of the signal field, depending on the signal-to-noise ratio (SNR) and the relative size of structures of the two fields. Next, we focus on the statistical properties, namely non-Gaussianity and statistical isotropy (SI), of the all-sky Haslam 408 MHz temperature map, which is widely used as a proxy for synchrotron emission. Our goal is to investigate how the non-Gaussian properties vary at different spatial regions as well as angular scales of the Haslam map. We find that the overall level of the non-Gaussian deviations does decrease as more high-emission regions are masked and as we go down to smaller scales, in agreement with the results obtained in earlier works. Our results show that the leading sources of non-Gaussianity are the kurtosis terms, with skewness terms being subdominant at all angular scales. We test the SI of the Haslam map and find that it becomes increasingly more isotropic towards smaller scales. Next, we examine the Galactic emission maps at high-frequency bands provided by WMAP and Planck CMB experiments. Here,

our goals are two-fold. First, we determine the variation of morphological properties of the total foreground with observing frequency and compare them with simulations. This study elucidates how the morphology varies with frequency due to the relative dominance of different foreground components at different frequencies. This is an example of a composite field composed of different foreground signals. Secondly, we use various component-separated synchrotron temperature and polarization maps to determine the nature of non-Gaussianity and SI of synchrotron fluctuations towards smaller scales. We find that all maps exhibit kurtosis-type non-Gaussianity, in agreement with the Haslam map. This result can be an important input for modelling small-scale synchrotron fluctuations for component separation pipelines. From a comparison of the different component-separated maps, we find that these synchrotron maps show morphological differences of varying statistical significance. Our analysis suggests a combination of residual AME and/or free-free emissions and point sources as contributing to these differences and underscores the need for further improvement of the pipelines. As a next step, we study the statistical properties of other major Galactic emissions, namely free-free, AME and thermal dust. In this work, we investigate whether the observed kurtosis nature of non-Gaussianity in synchrotron maps is a generic feature of foreground emissions or any random field with positively skewed probability distribution. Our study using different toy models of random fields reveals that the nature of non-Gaussianity is dependent on the underlying distribution of the field and is not a generic feature. We find that, at small scales, the non-Gaussianity of all the foreground fields is of kurtosis origin, with different levels of non-Gaussianity for different fields. These findings provide valuable insights into preparing realistic non-Gaussian models of foreground components. In the last part of the thesis, we introduce a new morphological tool known as total absolute curvature (K), which can complement MFs in extracting the properties of different random fields, including foreground fields. Our results open up new avenues in the statistical modelling of foreground components, thereby enhancing the efficiency of foreground removal techniques for CMB and other cosmological experiments.

Contents

List of Figures

List of Tables

Chapter 1

Introduction

In the past several decades, the understanding of the universe has made rapid progress. This is due to advancements in observational cosmology along with theoretical developments. These developments have led to the formulation of the Λ-CDM model or the standard model of the universe. The Λ-CDM stands for Lambda-Cold Dark Matter model. This model is described by six basic parameters, with the spatial curvature being zero (flat universe). More complicated extensions have more than six parameters. According to the Λ-CDM model, the universe is composed of three primary constituents: dark energy, dark matter and ordinary matter. These comprise roughly 70%, 26% and 4% of the total energy density of the universe, respectively (Hinshaw et al. 2013a). Radiation (photons and neutrinos) in the universe constitutes a small portion of this energy budget, about 0.001%. The Λ-CDM model tells that the dark matter in the universe is non-relativistic and cold, and the cosmological constant (Λ) is the most plausible candidate for dark energy. The universe began as a hot and dense system in its early history. This phase is usually termed as the hot big bang phase. It has been expanding since then, and at present, the rate of expansion is accelerating (Riess et al. 1998; Perlmutter et al. 1999). The major evidence in support of the Λ-CDM

model has been provided by observations of the cosmic microwave background (CMB) (Planck Collaboration et al. 2020a). Further evidence has been provided by the observations of large-scale structures such as galaxies, galaxy clusters and quasars (Alam et al. 2021).

The general theory of relativity provides the framework for theoretically understanding the universe. The Cosmological Principle (CP), which states that the universe is homogeneous and isotropic on sufficiently large scales, reduces the number of dynamical degrees of freedom (DOF) of the metric to just one. This DOF is just the expansion factor of the 3-dimensional space*. CP is indeed supported by observations of the spatial distribution of galaxies and clusters (Yadav et al. 2010; Andrade et al. 2022). Towards smaller scales, the universe exhibits inhomogeneities in the form of a complex web of structures – groups and clusters of galaxies, voids, filaments, walls, etc. This is also seen in the CMB in the form of tiny anisotropies (Smoot et al. 1992). To theoretically study the universe at these length scales, we express the metric as a spatially constant background term and a spatially fluctuating term. The distribution of matter and radiation can be similarly decomposed (Harrison 1967; Bardeen 1980). The equations for the background and perturbed part are given by Einstein's equation and the energy-momentum conservation equations.

Λ-CDM model, by itself, does not explain the origin of fluctuations that we see in the distribution of matter and radiation. This explanation is provided by invoking a phase of accelerated expansion in the very early universe, which is usually driven by a scalar field (inflaton field) (Starobinskii 1979; Guth 1981; Linde 1982; Mukhanov & Chibisov 1981; Guth & Pi 1982). This period is referred to as 'inflation'. The quantum fluctuations of the inflaton field explains the origin of density fluctuations in the universe. These tiny perturbations then got enhanced under

*There is another degree of freedom, the curvature of the universe, which, based on observations, can be regarded as zero.

gravity and became seeds for the growth of structures such as galaxies and clusters. These perturbations are also responsible for the anisotropies observed in the CMB sky (Mukhanov 1992; Dodelson 2021).

The CMB radiation holds fundamental significance in our understanding of the origin and evolution of the universe. Predicted in 1948 (Gamow 1948; Alpher & Herman 1948) and discovered in 1965 (Penzias & Wilson 1965), it provides strong evidence for Λ-CDM model. In the early universe, the photons, electrons and other charged particles were in constant interactions in the primordial plasma through Thomson scattering. As the universe expanded and cooled, neutral atoms began to form combining electrons and protons, thereby ceasing these interactions. As a result, the photons started free-streaming, and the universe became transparent to light. The CMB is this relic radiation from the big bang. At this point, the universe was approximately 380,000 years old. The surface from which the CMB was emitted is known as the last scattering surface (LSS). In other words, the CMB provides a snapshot of the LSS, bringing us information on the physical conditions pertaining to the early universe.

CMB is thermal radiation. It is the most perfect black body radiation ever measured. As discussed earlier, it has a mean temperature of $T_0 = 2.725\,\mathrm{K}$, with an rms fluctuation of $10^{-5}\,\mathrm{K}$. According to inflationary theory, CMB anisotropies are Gaussian distributed. Consequently, these anisotropies are well studied using the angular power spectrum, through which we constrain the cosmological parameters associated with the Λ-CDM model. CMB is linearly polarized. Quadrupole anisotropy at LSS via the Thomson scattering of photons and ions leads to the polarization of CMB signals. In CMB polarization analysis, Stokes parameters Q and U are expressed in terms of two scalar quantities E- and B-modes. Scalar density fluctuations are responsible for the E-mode signals. Primordial tensor perturbations produce B-modes and, thus, B mode signals are the signatures of primordial gravitational waves.

Advancements in CMB science have been realized through a series of observations employing ground-based, space-based, and balloon-borne telescopes (Penzias & Wilson 1965; Mather et al. 1990; Bennett et al. 2013; Thornton et al. 2016; Planck Collaboration et al. 2020a; Balkenhol et al. 2023). Efforts are ongoing to uncover the subtle features within the CMB anisotropies. One major area of investigation is CMB polarization, specifically the detection of primordial B-mode signals. CMB B-modes provide strong observational support for the theory of inflation and measure the energy scale of inflation. Other major CMB characteristics being explored include the search for primordial non-Gaussianity and distortions in the black-body spectra, small-scale features such as CMB lensing, etc., which all can shed light on the physical processes that happened at different evolutionary epochs of the universe (Abazajian et al. 2019; Chang et al. 2022; Allys et al. 2023).

Foreground emissions, mainly the signals from our Galaxy, pose a severe challenge for detecting tiny features in the CMB. CMB B-mode measurement is complicated because of the highly polarized Galactic synchrotron and thermal dust emission, which dominates at all the frequency bands and the sky regions (Remazeilles et al. 2016). Foreground signals are highly non-Gaussian and, therefore, bias the measurement of primordial non-Gaussianity (Hill 2018). This necessitates the process of component separation in the CMB data analysis, removing unwanted Galactic emissions and isolating the signal of interest (Delabrouille & Cardoso 2009). Many of these separation techniques are based on the idea of *'know your enemy'*, involving a thorough characterization of foreground emissions to subtract them effectively. As a result, an in-depth understanding of the properties of Galactic signals is crucial to obtaining an unbiased estimate of subtle CMB features. This thesis is developed with the objective of enhancing our understanding of Galactic foregrounds, particularly focusing on their statistical and morphological characteristics.

In section 1.1, we discuss the background cosmology and dynamical evolution

of the universe. A detailed description of perturbations in the context of CMB anisotropies is included in the next chapter. In section 1.2, we elaborate further on the challenges posed by foreground signals for CMB observation. Section 1.3 describes the statistics we use to characterize different foreground emissions. Section 1.4 provides a summary of the main objectives of the thesis. This chapter concludes by providing an overview of the thesis structure in section 1.5.

1.1 Background cosmology

One of the major milestones in our understanding of the cosmos is Hubble's discovery of the expanding universe. Through his observations of distant galaxies in the 1920s, Hubble found that galaxies are moving away from one another, indicating an overall expansion of the universe (Hubble 1929). This also meant that, extrapolating backwards in time, all the galaxies were close together. This led to the concept of the hot big bang, where the universe began as an extremely hot and dense system approximately 13.8 billion years ago.

The groundbreaking discovery of Hubble gave us the Hubble-Lemaître law, which established the direct relationship between the distance to a galaxy and its recessional velocity as

$$v = H_0 d, \tag{1.1}$$

where H_0 is called the Hubble constant. Using Cepheid variables, Hubble completed his observations and estimated H_0 as 500 km/s/Mpc.

Assuming CP, we can write the FLRW metric (Friedmann 1924; Lemaître 1931; Robertson 1935; Walker 1937) with the line element (ds) as,

$$ds^2 = -c^2dt^2 + a^2(t)\Big[\frac{dr^2}{1-kr^2} + r^2d\theta^2 + r^2\sin^2\theta\, d\phi^2\Big]. \tag{1.2}$$

The scale factor $a(t)$ describes the expansion of the space for any time t. k is the curvature parameter that represents the geometry of the universe. The value of k is either 0, +1 or −1. If $k = 0$, the universe has a flat geometry (Euclidean). $k = +1$ corresponds to positive curvature while $k = -1$ indicates negative curvature.

r, θ and ϕ are called the comoving coordinates, which are the spatial coordinates when there is no expansion. In a comoving coordinate system, objects remain static and do not experience expansion. The spatial distance between two objects in this coordinate system is called comoving distance (d_c), which remains fixed with respect to the expansion. However, the actual distance between the two objects, called the proper distance (d_p), varies with time because of the expansion of the underlying space between them. In other words, the recession of galaxies from one another in an expanding universe is not due to their intrinsic motion through space. Instead, galaxies remain fixed in their coordinates while the space between them expands.

Comoving distance and the proper distance are related as,

$$d_p(t) = a(t)d_c. \tag{1.3}$$

Normalising the present-day value of scale factor ($a(t_0)$) as unity, $a(t)$ for any time t tells us how small the universe was then with respect to today. Also, at the big bang, the scale factor is zero. The rate of change of proper distance is given as

$$v(t) \equiv \dot{a}d_c = \frac{\dot{a}(t)}{a(t)}d_p(t) \equiv H(t)d_p(t). \tag{1.4}$$

Here, the dot denotes the derivative with respect to time and $H(t)$ is the Hubble parameter. In this way, we recover the Hubble's relation between the velocity of the receding galaxies and their distance, with $H(t)$ given as,

$$H(t) = \frac{\dot{a}(t)}{a(t)}. \tag{1.5}$$

$H(t)$ determines the rate of expansion of the universe at a given time and is again a function of time. Today, Hubble parameter value (H_0 as seen in Hubble's law) is found to be around 70 km/s/Mpc, with slight variations of a few per cent depending on the cosmological measurements and data sets utilized (Planck Collaboration et al. 2020d; Riess et al. 2022).

For $k = 0$[†], FLRW metric given in eq. (1.2) becomes,

$$ds^2 = -c^2dt^2 + a^2(t)\left(dr^2 + r^2d\theta^2 + r^2\sin^2\theta\, d\phi^2\right). \tag{1.6}$$

The light from a galaxy located at r distance from the Earth (assuming the Earth to be the origin) follows a null geodesic ($ds^2 = 0$) i.e.,

$$c^2dt^2 = a^2(t)\left(dr^2 + r^2d\theta^2 + r^2\sin^2\theta\, d\phi^2\right). \tag{1.7}$$

Light travels radially towards us ($d\theta = 0$, $d\phi = 0$), and hence, the comoving radial distance to the galaxy,

$$r = \int \frac{cdt}{a(t)}, \tag{1.8}$$

and, the proper distance is,

$$d_p = a(t)\int \frac{cdt}{a(t)}. \tag{1.9}$$

As light travels through expanding space, its wavelength gets stretched. So, when we receive light from a galaxy, it will be redshifted proportional to the amount of expansion it has undergone since it was emitted. The farther the source, the greater the expansion and the larger the redshift. This cosmological redshift (z) is expressed in terms of the scale factor as,

$$\frac{\lambda_o}{\lambda_e} = \frac{a(t_o)}{a(t_e)} = \frac{1+z_e}{1+z_0}, \tag{1.10}$$

[†]Observations have shown that the universe has a flat geometry (de Bernardis et al. 2000; Lange et al. 2001). In the forthcoming discussions, we consider k to be equal to 0, unless stated otherwise.

where the subscript e and o correspond to emission and observation, respectively. The scale factor today, which is also the scale factor during observation, is set to unity. Also, the redshift in the present-day universe is taken as zero. Therefore, light emitted when the universe was $1/a$ times the current size undergoes a redshift z given by,

$$1 + z = \frac{1}{a(t)}. \tag{1.11}$$

Thus, redshift indicates how small the universe was compared to the current size. For instance, the redshift when the CMB started free-streaming is 1100, implying that during recombination, the universe was 1100 times smaller than today.

Einstein equation of the general theory of relativity explains the dynamics of the universe.

$$\mathcal{R}_{\mu\nu} - \frac{1}{2}\mathcal{R}g_{\mu\nu} = \frac{8\pi G}{c^4}\mathcal{T}_{\mu\nu}, \tag{1.12}$$

where $\mathcal{R}_{\mu\nu}$ is the Ricci tensor and $\mathcal{R}$ is its contracted version, called Ricci scalar. They are the measure of the curvature of the space-time. $\mathcal{R}_{\mu\nu}$ is obtained using the second derivatives of metric tensor $g_{\mu\nu}$. $\mathcal{T}_{\mu\nu}$ represents the energy-momentum tensor, which is the measure of the energy and momentum contained in the space-time. Assuming CP, it is possible to consider the matter in the universe as a homogeneous perfect fluid. For such a fluid, $\mathcal{T}_{\mu\nu}$ can be written as,

$$\mathcal{T}_{\mu\nu} = (\rho + p)u_\mu u_\nu - pg_{\mu\nu}, \tag{1.13}$$

Here, ρ and p are the energy density and pressure of the fluid, respectively. u_ν is the four-velocity of the fluid.

Using the above expression for $\mathcal{T}_{\mu\nu}$ and the FLRW metric applied in the Einstein equation, we get the Friedmann equations that govern the dynamics of the

background universe.

$$\left(\frac{\dot{a}}{a}\right)^2 + \frac{k}{a^2} = \frac{8\pi G\rho}{3} \tag{1.14}$$

$$\frac{\ddot{a}}{a} = -\frac{4\pi G\rho}{3}(\rho + \frac{3p}{c^2}). \tag{1.15}$$

Here, ρ is the total energy density of the universe, which is the sum of the energy densities of different constituents, $\rho = \sum_i \rho_i$, namely matter, radiation and dark energy. Matter encompasses baryonic matter (the combined term for all visible matter in the universe) and dark matter, while radiation comprises photons and relativistic neutrinos. Each of these components is characterized by the equation of state (EoS; ω), which is the ratio of the pressure (p) of the component to its energy density (ρc^2). Matter in the universe is pressure-less ($\omega = 0$), while the radiation follows $\omega = 1/3$. The most acceptable model for dark energy is the cosmological constant (Λ), having $\omega = -1$.

The second Friedmann equation provides information about the nature of the expansion, indicating whether it is accelerating or decelerating. The second derivative of the scale factor, $\ddot{a}$, is negative for matter ($p = 0$) and radiation ($p = \rho c^2/3$), implying that these components result in an expansion that slows down with time. For dark energy, the pressure is negative ($p = -\rho c^2$ for the cosmological constant model). As a result, $\ddot{a}$ is always positive, explaining the observed accelerated expansion of the current universe.

We can redefine the energy density of each of these components with respect to the total energy density as dimensionless density parameters,

$$\Omega_i \equiv \frac{\rho_i}{\rho_c} = \frac{8\pi G\rho_i}{3H^2}, \tag{1.16}$$

where $\rho_c = 3H^2/8\pi G$ is the total energy density for flat geometry, also called the critical density. Today, the critical density has a value of approximately

$10^{-26}\,\mathrm{kg/m^3}$.

Using the continuity equation, we can study the evolution of the energy density for different components. It is obtained from the Bianchi identity, which says that the covariant derivative of the energy-momentum tensor is zero ($\nabla_\mu T_{\mu\nu} = 0$). Continuity equation is given as,

$$\dot{\rho} + 3H(\rho + \frac{p}{c^2}) = 0. \tag{1.17}$$

The energy density of each component varies with scale factor as $\rho \propto a^{-3(1+\omega)}$, where ω is the equation of state. For matter, $\rho_m \propto a^{-3}$, while for radiation, $\rho_r \propto a^{-4}$. For cosmological constant with $\omega = -1$, ρ_Λ remains unchanged with time. Today, the energy composition is predominantly governed by dark energy ($\Omega_\Lambda \sim 0.7$). Using the above relationships for the evolution of energy densities, we can infer that there are epochs in which different components, namely matter and radiation, assume dominance in the universe. This allows us to categorize cosmic history into distinct epochs: radiation-dominated (RD), matter-dominated (MD), and dark energy-dominated (ΛD).

In the beginning, the dominant component in the universe was radiation[‡]. In this epoch, the scale factor varied with time as $a(t) \propto t^{1/2}$, and the Hubble parameter $H(t) = 1/2t$. This epoch remained until 47,000 years after the big bang, followed by matter-epoch, where the universe was filled with matter, with $a(t) \propto t^{2/3}$. During this time, $H(t) = 2/3t$. In both these epochs, the expansion of the universe was decelerating. After the matter-dominated era, the dark energy-dominated era started with accelerated expansion. In this phase, $a(t)$ follows an exponential evolution with time, $a(t) \propto e^{H_0 t}$, and the Hubble parameter remains constant. A schematic plot of ρ versus a for different constituents is shown in figure 1.1.

[‡]Note that the inflationary epoch was even before this. For the sake of the continuity of discussion, we postpone the discussion on inflation to a later section.

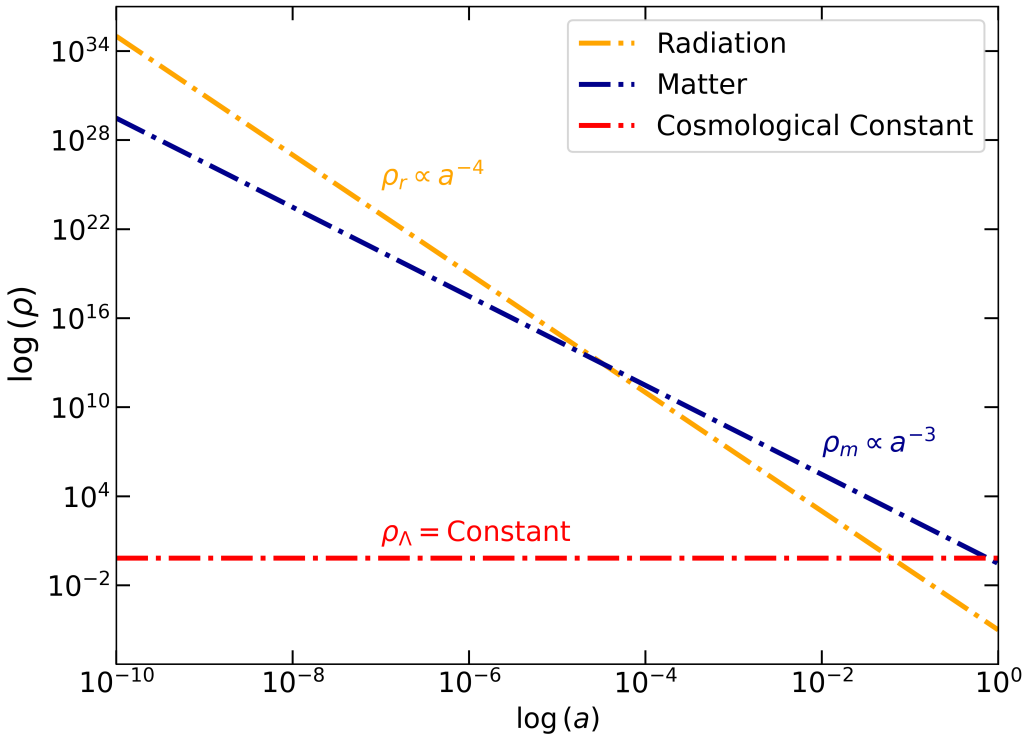

FIGURE 1.1: Energy density (ρ) versus scale factor (a) for different constituents in the universe.

Friedmann equation (eq. (1.15)) governs the evolution of the Hubble parameter and hence, the rate of expansion at different epochs. Using the relation between the energy density of different constituents with scale factor and the density parameters, we can express the Hubble parameter in terms of scale factor as,

$$H^2(a) = H_0^2 \left[\Omega_{m,0} a^{-3} + \Omega_{r,0} a^{-4} + \Omega_{\Lambda,0}\right] . \tag{1.18}$$

The subscript 0 in $\Omega_{i,0}$ represents the present value of the corresponding density parameter. Using $a(t) = 1/(1+z)$, we can express the Hubble parameter as a function of the observable quantity z,

$$H^2(z) = H_0^2 \left[\Omega_{m,0}(1+z)^3 + \Omega_{r,0}(1+z)^4 + \Omega_{\Lambda,0}\right] . \tag{1.19}$$

Parameter	**Name**	**Value**
Ω_m	matter density	0.3158
Ω_Λ	cosmological constant density	0.6842
Ω_b	baryonic matter density	0.0498
Ω_c	dark matter density	0.2675
Ω_r	radiation density	7.9×10^{-5}
$H_0\,[\mathrm{km\,s^{-1}\,Mpc^{-1}}]$	Hubble parameter	67.32

TABLE 1.1: The present-day density parameters ($\Omega_{i,0}$) and Hubble parameter (H_0) estimated using the latest Planck CMB temperature and polarization measurements (Planck Collaboration et al. 2020d).

Rearranging $H(t) = \dot{a}(t)/a(t)$, we can calculate the time at any epoch since the big bang as

$$t = \int_0^a \frac{da'}{a' H(a')}. \tag{1.20}$$

Substituting for $H(a)$ from eq. (1.18) and taking $a = 1$ for the present time, the age of the universe today is,

$$t_0 = \frac{1}{H_0} \int_0^1 \frac{da/a}{\left[\Omega_{m,0} a^{-3} + \Omega_{r,0} a^{-4} + \Omega_{\Lambda,0}\right]^{1/2}}. \tag{1.21}$$

From the above expression, it is clear that the age of the universe is dependent on various cosmological parameters in the present-day universe. According to the latest estimates of cosmological parameters from Planck CMB data, the age of the universe is approximately 13.79 billion years (Planck Collaboration et al. 2020d). Density parameters and the Hubble parameter obtained from Planck measurements are given in table (1.1).

The temperature and the energy density of radiation are related by $\rho_r \propto T^4$, following Stefan's law. Additionally, we have seen that the energy density falls with scale factor as $\rho_r \propto a^{-4}$. Combining both these, we get

$$T \propto 1/a. \tag{1.22}$$

As the universe expands, the scale factor increases and the temperature of the universe falls down. During the early days, the size of the universe was smaller, and the temperature and the density were very high, giving rise to the hot big bang phase. The present-day average temperature of the universe is $T_0 = 2.725\,\mathrm{K}$ (Fixsen 2009), the average CMB temperature.

Now, let us summarize the key physical processes that took place in the early universe in chronological order. These processes, which are strongly influenced by the ambient temperature at each epoch, played a crucial role in shaping the universe as we observe it today.

- **Inflation** — This is the phase when the universe underwent an exceptionally rapid exponential expansion for about 10^{-36} s. Inflation must have happened $10^{-33} - 10^{-32}$ s after the big bang. During inflation, the volume of the universe increased by a factor of approximately 10^{78}. In the basic models, inflation is driven by the inflaton field, with an energy scale of about $10^{15} - 10^{16}$ GeV. While the exact cause of this expansion is still an active research topic, the concept of inflation is crucial in explaining several key features of the observed universe. These features include the uniformity observed in the CMB (horizon problem), the flat geometry of the universe (flatness problem), the absence of magnetic monopoles etc. More importantly, the inflationary phase in the early universe played a significant role in generating the primordial density fluctuations, which resulted in the formation of structures such as stars and galaxies in the present universe.

- **Reheating** — Reheating is the period after inflation when the inflaton field decays to ordinary standard model particles such as radiation, baryons and leptons. The oscillations of the scalar field play a crucial role in particle production and reheating. As inflation concludes, the field undergoes oscillations near the minimum of its effective potential, generating elementary particles.

These particles subsequently interact and eventually reach thermal equilibrium, giving rise to the concept of the temperature of the universe (Kofman et al. 1997). The temperature at this phase is referred to as the reheating temperature. Our understanding of this epoch in the universe is limited. Theoretical works indicate that reheating is associated with a parametric resonance instability.

- **Baryogenesis** — This is the process that led to the baryon asymmetry in the universe, ie. the excess of matter (baryons) over anti-matter (anti baryons). According to the standard model, there must be an equal amount of baryons and anti-baryons in the universe, which is contrary to what we see today; the universe has a non-zero baryon number. The most preferred view is that the universe began with the perfect symmetry of matter and anti-matter, which is later broken due to the physical process that happened during baryogenesis. Several theories within the realm of particle physics, such as the Sakharov conditions, propose scenarios where processes during the early universe involving violations of baryon number conservation and CP-symmetry led to the generation of more baryons than antibaryons (Sakharov 1967).

- **Nucleosynthesis** — Big bang nucleosynthesis (BBN) is the process through which light atomic nuclei are formed in the early stages of the universe when the temperature was approximately 10^9 K (Alpher & Herman 1949). In this phase, which was approximately 200 seconds after big bang, protons and neutrons in the primordial hot and dense plasma combined to form nuclei of the light elements such as deuterium, helium and trace amounts of lithium. The abundance of these light elements was strongly influenced by the balance between the rate at which the universe expands and the rate of nuclear reactions. As the universe expanded and cooled, the reactions gradually ceased.

The predictions of primordial nucleosynthesis are in excellent agreement with abundance measurements of light elements in the universe (Fields et al. 2020). This further supports the validity of the hot big bang theory and provides valuable insights into the conditions and processes that prevailed during the first few minutes after the big bang.

- **Recombination and Photon Decoupling** — As the universe continued to expand and cool down to approximately 3,000 K, the conditions became favourable for recombination to occur. Recombination involves the formation of neutral hydrogen atoms as free electrons combined with protons. At the same time, due to the expanding universe, the universe further cooled down, and the energy of the photons decreased to a point where they were no longer able to ionize the atoms or interact with them. This process is called decoupling, which led to the release of CMB radiation. This happened when universe was about 3×10^5 years old ($z \sim 1100$). Until then, photons were interacting with the electrons and protons in the primordial plasma via Thomson scattering, and therefore, the universe was opaque. At the LSS, photons started travelling freely, largely unimpeded, until they reached us as the CMB. As a result, the universe became transparent to light.

- **Dark ages, formation of luminous objects and reionization** — After the decoupling, the universe entered a period known as the "dark ages", filled with neutral hydrogen and without significant light sources. Over time, the density fluctuations started to clump under gravity, forming the first luminous objects, stars and galaxies and marking the end of the dark ages. These luminous sources started to form when the universe had an age of about 1 billion years ($z \sim 20$). The energetic radiation from these sources led to the reionization of the neutral hydrogen in the intergalactic medium, transforming it from a neutral to an ionized state. This phase is known as the Epoch of Reionization (EoR). Our knowledge about this epoch is limited. Understanding the dark ages, the formation of the first luminous objects,

and the process of reionization is an important future goal in cosmology. 21 cm radiation emitted by the neutral hydrogen is a key observable in studying the epochs of the dark ages and the reionization process.

- **Structure Formation** — The formation of cosmic structures, such as stars, galaxies and clusters, from the initial density fluctuations in the universe is termed as structure formation. As the universe evolves, the initial inhomogeneities in the universe grow under gravity to become more denser. Yet, until decoupling, baryonic matter was in constant interaction with photons, which prevented the gravitational clustering of ordinary matter. Dark matter, on the other hand, does not interact with photons, and thus, dark matter density fluctuations could grow denser even before CMB release. As the universe decoupled, baryonic matter started collapsing under gravity and started falling into the potential well of dark matter. Over time, gas within these gravitational wells cools, condenses, and collapses, leading to the formation of galaxies and galaxy clusters, as we see today (Peebles 1980).

- **Dark Energy Dominated Era** — In the later phase of the universe, dark energy takes centre stage, driving the expansion of the universe accelerating. This phase, which commenced around 5 to 6 billion years ago ($z \sim 2$) and continues until today, marks a significant shift in cosmic dynamics. It influences the formation and distribution of cosmic structures, including galaxy clusters and superclusters. This epoch is similar to the inflationary epoch, where the scale factor grows exponentially. Due to the rapid expansion, gravitational potential wells in the universe evolve quickly, inducing additional anisotropies in the CMB. Ongoing research seeks to understand the nature of dark energy and its profound implications, shedding light on the dynamics of the universe at late times.

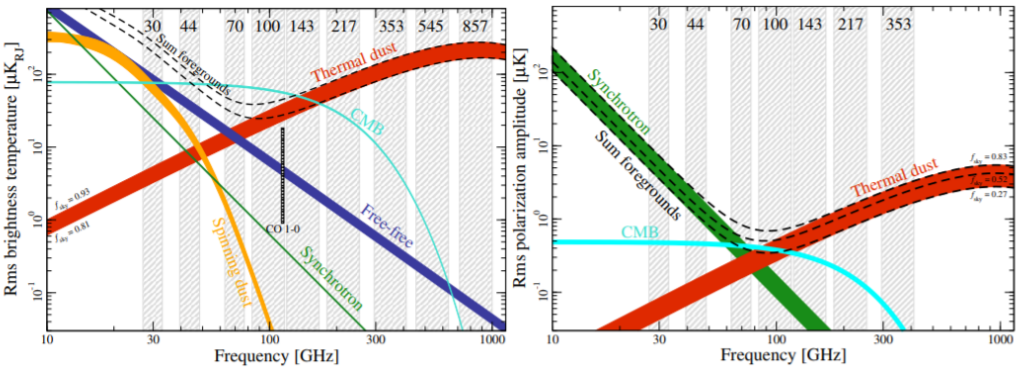

FIGURE 1.2: The rms amplitude of CMB and various Galactic emissions in temperature (left) and polarization (right) (Planck Collaboration et al. 2020a).

1.2 Foreground challenges for CMB observations

As noted earlier, the presence of foreground signals creates substantial hurdles when trying to detect the tiny features within the CMB. These microwave emissions originate from various sources, such as our atmosphere, the solar system, the Milky Way galaxy, and other galaxies, and contaminate the primordial signal. Out of these sources, diffused emission from our Galaxy proves to be the most problematic. Major Galactic foregrounds include Galactic synchrotron emission, free-free radiation (thermal bremsstrahlung), dust emission, Anomalous Microwave Emission (AME), etc. Additionally, there are molecular line emissions such as carbon monoxide (CO) emissions.

Galactic emissions can be broadly classified based on their polarization properties and how they bias the CMB polarization studies. In intensity, all these five foreground components contribute. Free-free, AME and molecular lines are not known to be polarized and, thus, do not cause major challenges for CMB polarization studies. On the other hand, Galactic synchrotron and thermal dust emission, due to their association with the Galactic magnetic field (GMF), are highly polarized. As a result, these two signals cause significant difficulties in detecting CMB B-modes (Dunkley et al. 2009; Ade et al. 2015; Planck Collaboration et al. 2020f).

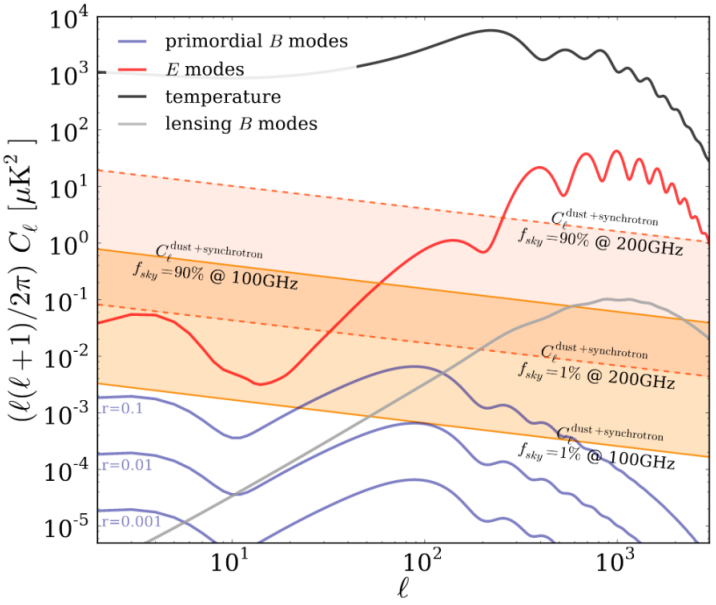

FIGURE 1.3: Angular power spectra (C_ℓ) of primordial B-modes for different tensor-to-scalar ratio (r), along with the power spectra of Galactic foregrounds (dust+synchrotron). C_ℓ for temperature, E-modes and lensing B-modes are also shown for comparison. The figure is taken from Dunkley et al. (2009).

Figure 1.2 shows the rms amplitude of CMB and various Galactic components in temperature (left panel) and polarization (right panel) in the frequency range where Planck observed. The plots illustrate how different components exhibit distinct frequency spectra, which are shaped by the astrophysics of their emissions. Although there are numerous foregrounds in temperature, there is a frequency window ($60 - 140$ GHz) where the CMB signal surpasses the cumulative impact of all foreground emissions. This simplifies the task of creating CMB temperature maps from raw data. However, for polarization studies, the case is more complex. Although there are only two foreground components, there exists no frequency range where primordial signals are dominant over the sum of foregrounds. The

situation is even worse for the primordial B-mode signal. The angular power spectrum (C_ℓ) of primordial B-modes for different tensor-to-scalar ratio (r)[§] together with the C_ℓ of the sum of Galactic foregrounds (synchrotron + dust) is shown in Figure 1.3. We see that the primordial signals have amplitudes much lower than the Galactic signals, complicating the attempts for B-mode detection. In fact, the false B-mode detection by the BICEP collaboration in 2014 was because of the improper handling of polarized thermal dust emission (BICEP2 Collaboration et al. 2014; Ade et al. 2015).

Accurate modelling of foreground emissions and improving the performance of component separation methods are major ways forward. Several efforts have been undertaken in this direction (Leach et al. 2008; Planck Collaboration et al. 2014, 2020f). Since each foreground component exhibits unique frequency characteristics, a standard practice in separation methods involves fitting an effective parametric signal model to a set of multi-frequency observations. The Commander algorithm, which was widely used in Planck analysis, is an example of such a technique (Eriksen et al. 2004b, 2008). Increasing the frequency coverage of the experiment and including external data sets as foreground templates are other possible pathways to address the foreground challenge. For example, the all-sky Haslam 408 MHz map (henceforth, Haslam map) is widely used as a synchrotron template (Haslam et al. 1981, 1982). Planck had a wide frequency coverage so as to include the bands where thermal dust emission dominates. H-α templates are used as a proxy for free-free in WMAP and Planck analysis (Finkbeiner 2003).

Synchrotron emission, due to the interaction of relativistic electrons with the GMF, has a power-law frequency spectrum, $I_{\rm sync} \propto \nu^{\beta_{\rm sync}}$. Here, $\beta_{\rm sync}$ is the spectral index (Rybicki & Lightman 1985). Modelling the parameter $\beta_{\rm sync}$ becomes intricate as it shows variations across the sky (Miville-Deschênes et al. 2008; Fuskeland

[§]The tensor-to-scalar ratio (r) quantifies the relative strength of B-modes (tensor perturbations) in comparison to E-modes (scalar perturbations). Detailed discussions on angular power spectrum and tensor-to-scalar ratio are included in chapter 2.

et al. 2021) and exhibits spectral steepening, in both temperature and polarization (Kogut 2012; Dickinson et al. 2019). WMAP 23 GHz map is a good proxy for synchrotron polarization but is limited by low sensitivity at high Galactic latitudes where the CMB analysis is carried out. At very low frequencies ($< 5\,\mathrm{GHz}$), synchrotron polarization is strongly influenced by depolarization effects like Faraday rotation, demanding all-sky synchrotron templates in the range $5 - 50\,\mathrm{GHz}$. SPASS, CBASS and QUIJOTE surveys are being set up with this objective (Carretti et al. 2019; Harper et al. 2022; Rubino-Martin et al. 2023).

Thermal dust emission is due to the heating of interstellar dust grains by the starlight and is polarized due to their preferential alignment with the GMF (Draine 2011). Dust emission is modelled as a modified black-body, $I_{\mathrm{dust}} \propto \nu^{\mathrm{dust}} B_\nu(T_{\mathrm{dust}})$, where B_ν is the Planck function. β_{dust} and T_{dust} are the spectral index and temperature of the dust grains, respectively. Dust parameters also vary across the sky as well as along the line of sight. More than one dust cloud can be present in a single sky direction, with varying dust parameters and magnetic field orientations (Planck Collaboration et al. 2017). In polarization studies, this can result in the cancellation/suppression of the signal as well as the rotation of the polarization angle with frequency. This effect is known as frequency decorrelation, meaning dust emission in different frequencies is no longer correlated. As a result, knowing the dust emission at one frequency will not help us predict the emission at other frequencies. Frequency decorrelation has been reported in Planck data (Pelgrims et al. 2021) and is a serious challenge for component separation.

In the pursuit of improving the separation techniques, it is crucial to extract all sorts of information about foregrounds. Numerous efforts are underway to investigate and harness the statistical features of Galactic emissions. Planck analysed the intensity and polarization characteristics of various foregrounds, examining their correlations with each other and with the GMF (Planck Collaboration et al. 2016b,d). Angular power spectrum (C_ℓ) of polarized synchrotron and thermal dust

maps are well studied. It was found that the ratio of the B-mode power spectrum amplitude to that of E-mode power spectrum is 0.5 for thermal dust and 0.22 for synchrotron (Planck Collaboration et al. 2020c; Martire et al. 2022). Planck also measured the non-zero correlation between temperature and B-mode polarization[¶] (C_ℓ^{TB}) for thermal dust. Given the non-Gaussian nature of foreground components, higher-order correlations of these emissions are studied, such as bispectrum (Jung et al. 2018; Rana et al. 2018; Coulton & Spergel 2019), skewness-kurtosis (Ben-David et al. 2015; von Hausegger et al. 2019), scattering transforms (Allys et al. 2019; Regaldo-Saint Blancard et al. 2020, 2021), Minkowski functionals (Rana et al. 2018; Hervias-Caimapo & Huffenberger 2022; Martire et al. 2023) etc.

1.3 Morphological statistics

Various tools and techniques have been developed to study the statistics of random fields in astrophysics and cosmology. For Gaussian random fields such as CMB, the two-point correlation function or its Fourier counterpart, the power spectrum, encapsulates all the statistical information. Consequently, the angular power spectrum (C_ℓ) is widely used to describe the statistical properties of the CMB field. Mild non-Gaussianity within CMB can be captured by computing the three-point and four-point functions (or the Fourier equivalents, bispectrum and trispectrum, respectively). In the case of CMB, higher-order non-Gaussian terms vanish as a result of perturbation theory. Chapter 3 contains a detailed discussion on CMB non-Gaussianity.

As mentioned in the previous section, interstellar radiation fields and Galactic foreground components are also characterized using these conventional statistical tools. However, the interactions those govern the Galactic emissions are generally

[¶]This is a parity odd signal and is measured as zero for CMB.

non-linear, and we do not expect that the interaction may be expressed as a small perturbation term added to an interaction-free physical system. As a result, foreground emissions are expected to be highly non-Gaussian, and there is a strong need to employ methods that capture information beyond the two-point function. The standard non-Gaussianity estimators such as bispectrum, skewness, kurtosis and other N-point functions, when used alone, also fail to fully capture these properties due to a lack of a priori knowledge of the true nature of these foreground fields.

Morphological statistics such as scalar Minkowski functionals (MFs) (Minkowski 1903; Schneider 2013; Tomita 1986) are computed in real space and contain information of all the N-point correlation functions. This makes them particularly advantageous in searches for non-Gaussianity in situations where the non-Gaussian properties are a priori unknown and/or when the field is highly non-Gaussian. Hence, MFs are found to be highly effective in characterizing Galactic emissions. MFs are based on excursion set formalism. It probes the geometry and topology of connected regions and holes for the excursion sets of the random field (Schmalzing & Buchert 1997; Matsubara 2003). Betti numbers are related topological quantities, which count the number of connected regions and holes (Chingangbam et al. 2012; Park et al. 2013). In $2d$, there are three scalar MFs: area-fraction, contour length and genus. These MFs being scalar, are not sensitive to the directional information. Minkowski tensors (MTs) are the tensor generalizations of MFs (Schröder-Turk et al. 2010; Chingangbam et al. 2017b). Specifically, the contour Minkowski Tensor (CMT) is the tensor generalization of contour length and contains the shape information and measures the anisotropy and alignment of structures (Ganesan & Chingangbam 2017; Chingangbam et al. 2017b). Other morphological and topological tools are shapefinders (Sahni et al. 1998), skeleton (Novikov et al. 2006), extrema counts (Pogosyan et al. 2011), persistent homology (van de Weygaert et al. 2013; Pranav 2021). All these quantities are extensively used to study cosmological (Bardeen et al. 1986; Mecke et al. 1994;

Bharadwaj et al. 2000; Matsubara 2003; Hikage & Matsubara 2012; Kapahtia et al. 2018; Goyal et al. 2020; Munshi et al. 2013)[‖] and astrophysical (Henderson et al. 2017; Makarenko et al. 2018) fields.

1.4 Goals of the thesis

The main goal of this thesis is to investigate the statistical properties of various Galactic foreground components using morphological and topological tools, extending well beyond the usual power spectrum analysis. The outcome of these investigations will deepen our understanding of Galactic foreground emissions, which will enable us to improve the component separation in CMB experiments. We have examined different foreground maps, including Galactic synchrotron, AME, free-free and thermal dust, using a range of tools starting from one-point probability distribution function (PDF), angular power spectrum, skewness-kurtosis, scalar Minkowski functionals and Minkowski tensors. It should be noted that the scope of the findings from our foreground analysis is not limited to CMB studies. They are also relevant for addressing foreground challenges in other cosmological endeavours, such as Epoch of Reionization (EoR) 21 cm experiments and Line Intensity Mapping (LIM) experiments.

Listed below are the key questions addressed within this thesis.

- We begin our analysis by studying the morphology of composite random fields, focusing on how the Minkowski functionals and other statistical properties of a composite field can be related to those of its individual constituent fields. In real-world situations, observed data is a sum of true signal and noise

[‖] This list is incomplete and we recommend Matsubara & Kuriki (2020) for a more comprehensive compilation.

or may contain other residual components. Galactic foregrounds are also a sum of different emissions. By examining how the behaviour of a primary field is affected by the presence of a secondary field, we can assess the potential bias it might introduce in the final conclusions we obtain. This work sets the stage for the discussions in the subsequent works.

- We study the nature of non-Gaussianity of the Haslam map using scalar MFs. We then analyse the statistical isotropy (SI) of the map using Minkowski tensors. Here, we study these features of the Haslam map at different sky regions and angular scales. In synchrotron modelling, the fluctuations are approximated as Gaussian distributed and statistically isotropic at small angular scales. The main aim of this work is to verify the validity of this approximation. We also use generalized skewness and kurtosis parameters to explore the exact nature of non-Gaussianity.

- Motivated by our analysis with the Haslam map, we next study the morphological properties of synchrotron temperature and polarization maps provided by different experiments. We use the data sets from Planck, WMAP, BeyondPlanck and Stockert-Villa, along with the simulated foreground maps from PySM simulations. Here, the main objective is to examine whether the properties of synchrotron radiation are frequency-dependent and to compare the non-Gaussian and SI nature of these observed synchrotron maps with previous results of the Haslam map.

- We study the non-Gaussian features of foreground components such as free-free, AME and thermal dust emission. Our particular emphasis lies in delving deeper into the kurtosis nature evident from our synchrotron findings. For this, we also examine the properties of some toy models — random fields with positively skewed probability distributions. The primary question that is being addressed in this work is whether the kurtosis nature is a universal feature and its potential application in the small-scale modelling of different Galactic components.

- We present a new morphological quantity, known as total absolute curvature (K), to study the geometry of the excursion sets of random fields. This tool carries independent information and complements MFs in studying the non-Gaussianity of CMB and foreground fields.

1.5 Thesis plan

The thesis is organised as follows.

- Chapter 2 contains a detailed discussion on cosmological perturbation theory in the context of CMB and the physics of Galactic emissions. Additionally, we provide a brief overview of the historical background and present state of CMB experiments.

- Chapter 3 reviews the smooth random fields and the statistical tools used to characterize them. It also includes definitions of morphological tools, MFs and MTs and further explains the mathematical principles behind them. The chapter discusses how these quantities can be applied to characterize various random fields and outlines the numerical methods used in computing them.

- In chapter 4, we present our work on the morphology of composite fields, providing an analytical estimate of how the scalar MFs of a field are affected by the presence of noise or residual components.

- Chapter 5 investigates the non-Gaussianity and statistical isotropy of the Haslam map using scalar MFs and MTs.

- In chapter 6, we extend the formalism developed on studying the morphology of Haslam map to different synchrotron maps provided by WMAP and Planck.

- In chapter 7, we estimate the amplitude of non-Gaussianity and its nature for different foreground components given by Planck. Our main objective of this work is to examine if the kurtosis non-Gaussianity is a universal feature of foreground fields or random fields in general at small angular scales.

- In chapter 8, we introduce total absolute curvature (K) and discuss its potential application in studying different random fields in the universe.

- In chapter 9, we summarize our research work and discuss future directions.

Chapter 2

Physics of the CMB and Galactic Foregrounds

In this chapter, we present a concise overview of the basic physics of CMB and various Galactic emissions, which are crucial topics for this thesis. Section 2.1 discusses cosmological perturbation theory and inflationary physics in the context of CMB. This section also contains a summary of the current experimental efforts aimed at detecting the primordial features in CMB signals, which serve as the long-term goals of the research work carried out in the thesis. Section 2.2 gives an outline of different Galactic foregrounds, such as Galactic synchrotron, free-free, AME and thermal dust emissions. Lastly, in section 2.3, we describe the different methods used in CMB experiments to separate these foreground emissions and recover clean CMB maps.

2.1 Cosmology using CMB

2.1.1 Primordial perturbations and initial conditions

The background cosmology we have discussed so far is built upon the assumption of the Cosmological Principle. The tiny fluctuations in the background density that existed in the early universe got enhanced under gravity and led to the inhomogeneous universe we observe today. CMB anisotropies are also associated with the density fluctuations in the early universe. As discussed earlier, we can write the density as a background term that only depends on time and a spatially varying fluctuation term. Mathematically, this can be expressed as $\rho(\mathbf{x}, t) = \bar{\rho}(t) + \delta\rho(\mathbf{x}, t)$. Similarly, the metric can be decomposed into a spatially constant term and a perturbed term.

The hot big bang model doesn't explain how the density fluctuations originated in the primordial universe. The theory of inflation offers a valuable solution to this issue. Quantum fluctuations of the inflaton field are responsible for the generation of density fluctuations in the early universe. Under gravity, these tiny fluctuations were enhanced, and later, the gravitational collapse of the overdense regions gave rise to the formation of the inhomogeneous universe we see today. The anisotropies observed in the CMB sky are also a result of these inhomogeneities. In this subsection, we will provide an overview of the generation and evolution of density and metric perturbations in the expanding universe.

Cosmological perturbations in the universe are studied using the linearized Einstein equations. The linear theory is generally effective in explaining the majority of observed fluctuations, except when these fluctuations grow and become nonlinear during the late-time epochs. Under linear approximation, the metric $g_{\mu\nu}$

is

$$g_{\mu\nu}(\mathbf{x}, t) = \bar{g}_{\mu\nu}(t) + h_{\mu\nu}(\mathbf{x}, t), \tag{2.1}$$

where $\bar{g}_{\mu\nu}$ is the background FLRW metric defined in eq. (1.6). By making use of the gauge freedom, we can write the line element of the perturbed space-time,

$$ds^2 = -(1 + 2\Psi(\mathbf{x}, t))dt^2 + a^2(t)\left[(1 - 2\Phi(\mathbf{x}, t))\gamma_{\mu\nu} + 2h_{\mu\nu}\right] dx^\mu dx^\nu. \tag{2.2}$$

Ψ and Φ are the Bardeen potentials (Bardeen 1980), which correspond to the Newtonian potential and the perturbations in the spatial curvature, respectively. This line element is defined in the conformal Newtonian gauge. Any metric perturbations can be broken down into three components: scalar, vector, and tensor. Scalar perturbations are given by Bardeen potentials. According to the inflationary theory, any vector perturbations, if they exist at all, will rapidly die out as the universe expands. Hence, they are not considered here. $h_{\mu\nu}$ is the trace-less and transverse tensor component of the perturbation, which gives rise to the primordial gravitational waves from inflation. At the linear order, the Einstein equations for scalar, vector, and tensor modes evolve independently. As a result, this helicity decomposition proves to be highly valuable in studying the individual evolution of each mode.

Through Einstein equation, the metric perturbation is related to the perturbations in the energy-momentum tensor of each component as,

$$T_{\mu\nu}(\mathbf{x}, t) = \bar{T}_{\mu\nu}(t) + \delta T_{\mu\nu}(\mathbf{x}, t). \tag{2.3}$$

decomposing $T_{\mu\nu}$ into a background component, which depends only on time and a spatially varying perturbed term. In other words, the distribution function of different constituents is perturbed in the early universe, and we need the Boltzmann equation to study the evolution of these components. Boltzmann equation takes care of the various interactions between photons, electrons, neutrinos, protons and

dark matter in the primordial plasma and solves how the distribution evolves with the expanding universe. For the distribution function f of any species in the phase space, the Boltzmann equation is

$$\frac{df(\mathrm{x}, \mathrm{p}, t)}{dt} = C[f]. \tag{2.4}$$

All the possible interactions are included in the term $C[f]$.

Together with Einstein equation, the Boltzmann equation governs the growth of the perturbations in the universe. By solving these coupled equations, we obtain the transfer function, which tells us how the amplitude of perturbations at one epoch is related to that of a later epoch. In this way, we can understand how the initial density fluctuations grew under gravity and evolved to form the observed distribution of matter at large angular scales, temperature anisotropies in the CMB, etc.

The initial conditions for the perturbations were set by inflation. This phase of rapid accelerated expansion was first proposed by Alan Guth in 1980 to solve two major issues in the hot big bang model: horizon problem and flatness problem (Guth 1981). The horizon problem arises from the fact that the regions in the universe, which are expected to be causally disconnected due to the finite age of the universe, exhibit remarkable similarity in temperature. In other words, the CMB temperature is highly uniform across the sky, but the horizon size* of the universe at LSS is approximately 1° angular size in the sky today. The flatness problem is related to the observation that the present-day geometry of the universe is flat. Since $k = 0$ is an ideal scenario, even a tiny deviation to the flat case in the early universe would have been amplified as it expanded, resulting in a non-zero curvature for the universe today.

*Horizon size is the maximum distance light could travel since the big bang and represents the largest causally connected region.

Inflationary cosmology resolves the horizon problem by positing that the regions that seem disconnected today were, in fact, in causal contact before the inflationary epoch. In this way, they got ample time to reach thermal equilibrium before being pushed beyond each other's horizon. Similarly, the exponential expansion during the inflationary epoch smoothed out any tiny departure from flat geometry in the early universe, leaving us with the observed near-perfect flatness on cosmological scales today.

According to the simplest inflationary models, inflation was driven by the inflaton field (ϕ). Similar to dark energy, this scalar field has to have negative pressure. However, in this case, we cannot have accelerated expansion forever; inflation has to stop. Therefore, we need a mechanism where the inflation terminates after a certain point and the inflaton field decays to hot matter constituents through the process called reheating. The slow-roll model provides a simple and effective way to achieve this. With the background FLRW metric, the dynamics of the scalar field are given by the Klein-Gordon equation,

$$\ddot{\phi} + 3H\dot{\phi} + \frac{dV(\phi)}{d\phi} = 0, \tag{2.5}$$

where $V(\phi)$ is the potential of the inflaton field. $3H\dot{\phi}$ represents the Hubble expansion, which acts like a friction term here.

For the field ϕ, the energy density and pressure are

$$\rho_\phi = \frac{1}{2}\dot{\phi}^2 + V(\phi) \qquad p_\phi = \frac{1}{2}\dot{\phi}^2 - V(\phi). \tag{2.6}$$

Friedmann equation for the inflaton field is

$$H^2 \equiv \frac{8\pi G}{3}\rho_\phi = \frac{8\pi G}{3}\left[\frac{1}{2}\dot{\phi}^2 + V(\phi)\right]. \tag{2.7}$$

Klein-Gordon equation and the Friedmann equation are coupled, and together, they determine the dynamics of the inflaton field.

The first condition for the slow-roll model is that the potential energy of the field is large compared to the kinetic energy:

$$\frac{\dot{\phi}^2}{2V(\phi)} \ll 1. \tag{2.8}$$

This condition ensures the pressure to be negative ($p \approx -\rho$) and, thus, accelerated expansion. This is equivalent to saying that the first slow-roll parameter $\epsilon \ll 1$, where

$$\epsilon = -\frac{\dot{H}}{H^2} = \frac{\frac{3}{2}\dot{\phi}^2}{\frac{1}{2}\dot{\phi}^2 + V(\phi)} \ll 1. \tag{2.9}$$

For the inflaton potential to slow-roll and thus the inflation to sustain for a longer period of time, the inflaton field has to evolve slowly compared to the expansion of the universe. This is the second condition for the slow-roll model,

$$\eta \equiv \left| \frac{\ddot{\phi}}{H\dot{\phi}} \right| \ll 1. \tag{2.10}$$

η is the second slow-roll parameter. When η is small, the Hubble friction term in eq. (2.5) dominates, retaining inflation for an extended period. During this time, the energy density of the inflaton field evolves very slowly. Eventually, the field approaches the minimum of the potential, the slow roll conditions are violated, and the energy density of inflaton begins to fall. At this point, the inflation stops, and the energy stored in the inflaton field gets converted to matter and radiation, marking the transition to the hot big bang era. Figure 2.1 depicts the slowly rolling inflaton field falling into the potential well.

The quantum fluctuations in the inflaton field are primarily responsible for the density fluctuations in the early universe. These fluctuations at the microscopic level are arising from the quantum mechanical uncertainty principle for the vacuum

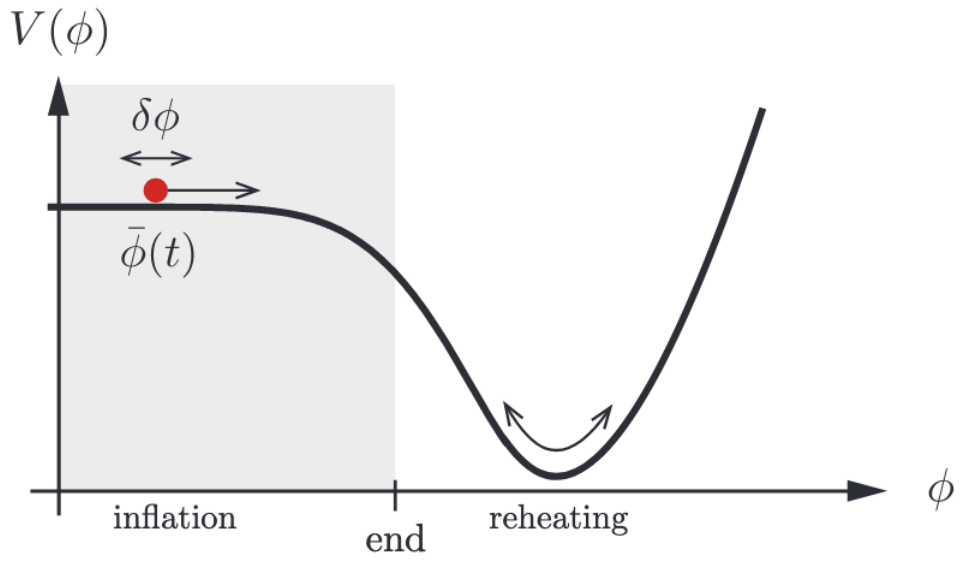

FIGURE 2.1: The slowly rolling inflaton field ϕ down it's potential $V(\phi)$. This figure is adapted from David Baumann's lecture notes.

state. Cosmological observations, from CMB and large-scale structure, tell us that these fluctuations are nearly scale-invariant, Gaussian distributed and adiabatic. The exponential expansion during inflation stretched out these perturbations to cosmic scales and when the inflationary period came to an end, these primordial fluctuations served as the initial seeds for the formation of cosmic structures.

The link between the inflation and post-inflationary universe is given by the primordial curvature perturbations $\mathcal{R}$. In Newtonian gauge, $\mathcal{R}$ is defined in terms of Bardeen potentials as,

$$\mathcal{R} \propto [\Psi + H^{-1}\Phi]. \tag{2.11}$$

$\mathcal{R}$ is a gauge invariant quantity. One of the key predictions of inflation is that $\mathcal{R}$ is a Gaussian random field and, hence, can be described using the power spectrum, with Fourier modes $\vec{k}$,

$$\langle \mathcal{R}(\vec{k})\mathcal{R}(\vec{k}')^* \rangle = (2\pi)^3 \delta(\vec{k} - \vec{k}')P(k), \tag{2.12}$$

where $P(k) = (2\pi^2/k^3)P_{\mathcal{R}}(k)$. $P_{\mathcal{R}}(k)$ is the curvature power spectrum, which can be parametrized as,

$$P_{\mathcal{R}}(k) = A_{\mathcal{R}}\Big(\frac{k}{k_*}\Big)^{n_s-1}. \tag{2.13}$$

$A_{\mathcal{R}}$ and n_s are the amplitude and the spectral index of the curvature power spectrum, respectively. k_* is the pivot scale, which can be chosen arbitrarily. Many of the inflationary models predict that the primordial fluctuations are nearly scale-invariant, implying that the n_s is close to 1. Observations, such as those from Planck, have estimated the value of the spectral index n_s to be 0.964 (Planck Collaboration et al. 2020d).

In addition to scalar perturbations, inflation also gives rise to tensor fluctuations in the fabric of space-time. These tensor fluctuations manifest as gravitational waves, which carry valuable information about the underlying physics driving the inflationary process. Scalar perturbations led to the formation of structures. On the other hand, tensor perturbations and the associated primordial gravitational waves offer a unique window into the study of inflation and its associated mechanisms. The imprint of these gravitational waves can be observed through the distinct polarization patterns in CMB called the CMB B-modes. A primary objective of current and upcoming CMB experiments is to detect this primordial signature. A detailed discussion on CMB polarization and tensor B-modes is included in the next subsection.

The two-point correlations of tensor fluctuations ($h(\vec{k})$) can be related to the tensor power spectrum $P_h(k)$ as,

$$\langle h^\dagger(\vec{k})h(\vec{k'})^*\rangle = (2\pi)^3\delta(\vec{k}-\vec{k'})P_h(k). \tag{2.14}$$

$P_h(k)$ also follows a power law of the form:

$$P_h(k) = A_T\Big(\frac{k}{k_*}\Big)^{n_T}, \tag{2.15}$$

with A_T and n_T are, respectively, the amplitude and spectral index for the tensor modes. In observations, the tensor modes are constrained by estimating the tensor-to-scalar ratio (r), defined as,

$$r = \frac{A_T}{A_{\mathcal{R}}}. \tag{2.16}$$

The estimation of the r from CMB B-mode observations enables us to derive the energy scale of inflation. A joint analysis of Planck and BICEP CMB experiments yields $r < 0.032$ (Tristram et al. 2022).

For an extensive review of the various inflationary models, we recommend Martin et al. (2014); Vazquez Gonzalez et al. (2020).

2.1.2 CMB and early universe physics

As discussed earlier, around 380,000 years after the big bang, recombination and decoupling happened, enabling photons to free stream from the last scattering surface. These photons now form CMB radiation, offering a valuable glimpse into the early universe and the physics of the processes that took place in the primordial plasma.

CMB radiation was predicted by George Gamow, Ralph Alpher, and Robert Herman in the late 1940s (Gamow 1948; Alpher & Herman 1948). They proposed that if the universe originated from a hot and dense phase, then faint black body radiation left over from that period should still be detectable today. The actual discovery of the CMB came in 1964 with the accidental detection by Arno Penzias and Robert Wilson at Bell Labs in New Jersey (Penzias & Wilson 1965). They discovered an unknown background signal emanating from all directions in their radio antennae, which was later identified as CMB radiation. The discovery of CMB provided strong support for the big bang theory, for which the Nobel Prize

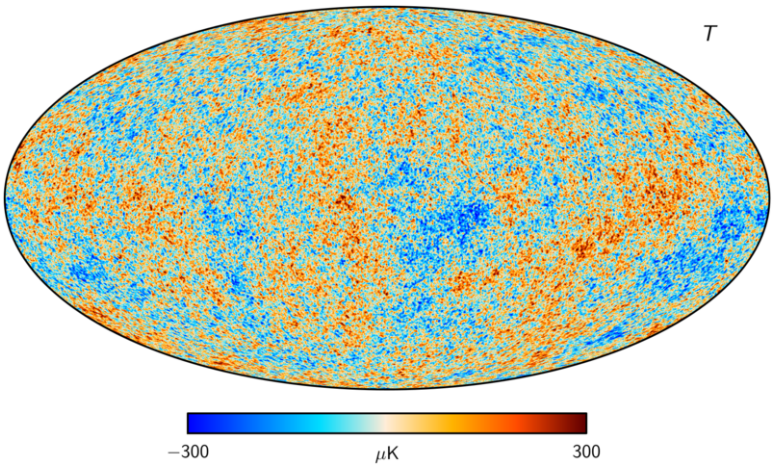

FIGURE 2.2: All-sky CMB temperature map ($\Delta T/T_0$) seen by Planck (Planck Collaboration et al. 2020a).

in Physics was awarded to Penzias and Wilson in 1978. Although their measurement was at a specific frequency, later studies confirmed the black body nature of the radiation (Mather et al. 1990).

CMB is not an isotropic radiation. CMB anisotropies arising from the density perturbations in the early universe serve as a snapshot of the overdensities and underdensities existing in the universe when the CMB photons started free-streaming. As a result, these temperature fluctuations have given us a detailed picture of the evolution of primordial fluctuations, the rich physics during and before recombination, etc.

CMB temperature fluctuations are expressed as,

$$\Theta(\hat{n}) = \frac{\Delta T(\hat{n})}{T_0} = \frac{T(\hat{n}) - T_0}{T_0}, \tag{2.17}$$

where T_0 is the background temperature and $\hat{n}$ is the sky direction. The typical value of fluctuations is of the order 10^{-5}. Figure 2.2 shows the all-sky map of temperature fluctuations as measured by the Planck satellite (Planck Collaboration et al. 2020a).

On the sphere, $\Theta(\hat{n})$ can be decomposed into spherical harmonics,

$$\Theta(\hat{n}) = \sum_{\ell=2}^{\infty} \sum_{m=-\ell}^{\ell} a_{\ell m} Y_{\ell m}(\hat{n}). \tag{2.18}$$

$\ell = 1$ (dipole) is excluded here as the dipole is dominated by the contribution arising from the motion of the Earth with respect to the CMB rest frame, which is accurately subtracted in the CMB data analysis[†].

Owing to the primordial density fluctuations being Gaussian distributed, CMB temperature fluctuations are also expected to be Gaussian random fields. Thus, the statistics of CMB fluctuations can be fully described using the two-point correlation functions (C(θ)) and its Fourier equivalent, angular power spectrum (C_ℓ).

$$C(\theta) \equiv \langle \Theta(\hat{n}) \Theta(\hat{n'}) \rangle, \tag{2.19}$$

where $\cos(\theta) \equiv \hat{n}.\hat{n}'$. Similarly for the multipole moments $a_{\ell m}$,

$$\langle a_{\ell m} a^*_{\ell' m'} \rangle = C_\ell \delta_{\ell \ell'} \delta_{m m'}. \tag{2.20}$$

C_ℓ is the angular power spectrum. Kronecker deltas in the above equation stems from the underlying assumption of homogeneity and isotropy.

Given the $a_{\ell m}$s of an observed temperature field $\Theta(\hat{n})$, we can write an estimator for C_ℓ as,

$$\hat{C}_\ell = \frac{1}{2\ell + 1} \sum_m |a_{\ell m}|^2, \tag{2.21}$$

such that $\langle \hat{C}_\ell \rangle = C_\ell$. The error associated with this estimator is then,

$$\frac{\Delta C_\ell}{C_\ell} \equiv \frac{\sqrt{\langle (C_\ell - \hat{C}_\ell)^2 \rangle}}{C_\ell} = \sqrt{\frac{2}{2\ell + 1}}. \tag{2.22}$$

[†]Our solar system is moving relative to the CMB frame. As a result, there exists a non-zero dipole moment of magnitude 3.36 mK in the observed data (Kogut et al. 1993). This dipole component is accurately measured and subtracted during CMB analysis.

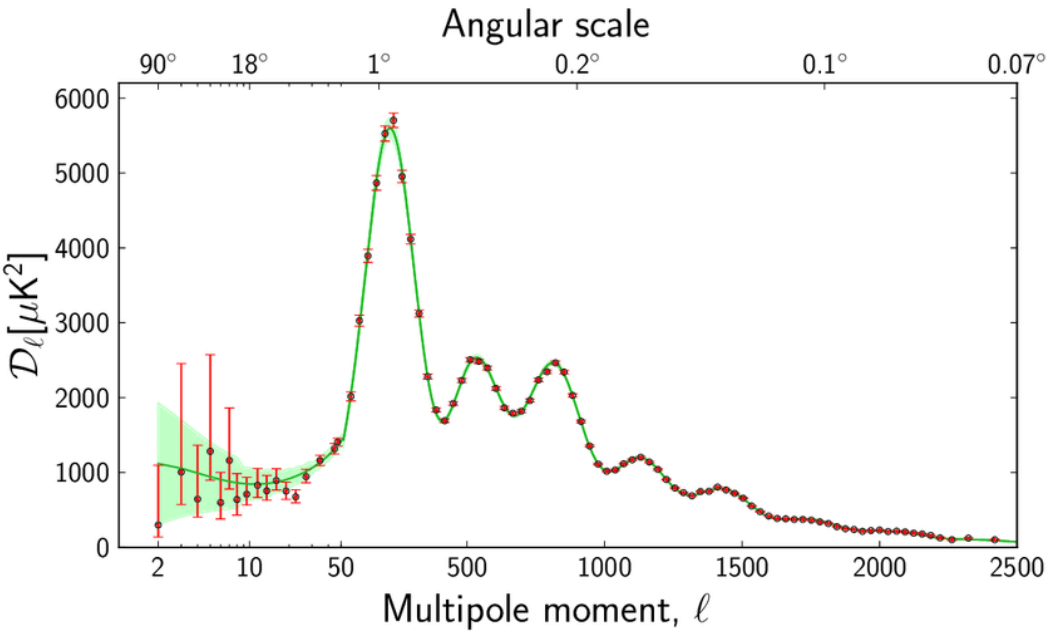

FIGURE 2.3: The observed CMB temperature angular power spectrum ($D_\ell = \ell(\ell+1)C_\ell/2\pi$) as observed by Planck, along with the associated error bars and the best fit Λ-CDM theoretical predictions (Planck Collaboration et al. 2014). The red dots indicate the data, while the green line denotes the theoretical values. The error bars are large for the lower ℓ values due to cosmic variance. This figure is adapted from Durrer (2015).

This error is called cosmic variance, which dominates at the lower values of ℓ (large angular scales). It arises due to the fact that we have only one observable universe to measure, limiting our ability to completely capture the statistical nature of the fluctuations. The observed CMB angular power spectrum from the Planck is shown in figure 2.3, along with the error bars and the best fit theoretical Λ-CDM model.

To explore the primordial physics contained in the CMB, it is important to understand how the observed angular power spectrum of the CMB (C_ℓ) is related to the power spectrum of the initial curvature perturbations ($P_\mathcal{R}(k)$). This relation is given as

$$C_\ell \equiv \int \mathrm{d}\ln k\, \Theta_\ell^2(k) P_\mathcal{R}(k). \tag{2.23}$$

Here, $\Theta_\ell(k)$ denotes the transfer function, which encapsulates the evolution of

primordial perturbations, the decoupling of photons at the last scattering surface (LSS), and the projection of inhomogeneities in the photon distribution functions onto the observable sky. Consequently, this process involves two essential steps: first, establishing a connection between the observed features in the sky and the fluctuations at the LSS, and then, relating these fluctuations to the initial curvature perturbations.

The temperature fluctuations observed today along the line of sight are related to the physical processes happening at the LSS as

$$\frac{\delta T}{T_0}(\hat{n}) = \left(\frac{1}{4}\delta_\gamma + \Psi\right)_* - (\hat{\mathbf{n}}.\mathbf{v}_b)_* + \int_{\eta_*}^{\eta_0} \mathrm{d}\eta\,(\Phi' + \Psi'). \tag{2.24}$$

$*$ denotes the time corresponding to the last scattering surface. Note that the integration is with respect to conformal time defined as $\mathrm{d}\eta = dt/a(t)$ and $'$ denotes the derivative with respect to time.

In the above expression, there are three contributors to the temperature fluctuations seen today:

- SW – The first term in the bracket is called the Sachs-Wolfe term. This includes the intrinsic temperature fluctuations at the LSS, along with the temperature perturbations induced due to the gravitational redshift of the photons, denoted as Ψ_*.
- Doppler – Doppler fluctuations arise from the variations in the bulk velocity of electrons at the LSS. When the photons scatter off these electrons, they get additional temperature fluctuations due to the Doppler effect.
- ISW – This term corresponds to the Integrated Sachs-Wolfe (ISW) effect,

accounting for the additional gravitational redshift the CMB photon encounters while travelling through evolving gravitational potentials after recombination. When a photon enters a potential well, it gains energy. However, if the potential changes with time before the photon leaves the well, it won't lose all the energy it got while entering, resulting in a net gain of the energy. This late-time effect contributes to the anisotropies in the CMB and is more prominent in the dark-energy-dominated era.

The detailed evaluation of the transfer function ($\Theta_\ell(k)$) is beyond the scope here. For a comprehensive discussion, we recommend Baumann (2022).

The large angular scales (multipole $\ell < 100$) CMB fluctuations were coming from the modes that were outside the horizon during the recombination. As a result, these fluctuations directly probe the inflationary perturbations. In this regime, the fluctuations are dominated by the Sachs-Wolfe term,

$$\frac{\delta T}{T}(\hat{n}) \sim \left(\frac{1}{4}\delta_\gamma + \Psi\right)_* = \frac{1}{3}\Psi_* = \frac{1}{5}\mathcal{R}. \tag{2.25}$$

This is evaluated assuming adiabatic initial conditions. The transfer function for the large-scale Sachs-Wolfe limit is,

$$\Theta_\ell^{\rm SW}(k) = \frac{1}{5} j_\ell(k\chi_*), \tag{2.26}$$

where j_ℓ are the spherical Bessel function and χ_* corresponds to each spatial point on the last scattering surface. The power spectrum (eq. (2.23)) now becomes,

$$C_\ell^{\rm SW} \equiv \int \mathrm{d}\ln k\, P_\mathcal{R}(k) j_\ell(k\chi_*), \tag{2.27}$$

and substituting $P_\mathcal{R}(k) = A_\mathcal{R}(k/k_*)^{ns-1}$, we finally get,

$$\frac{\ell(\ell+1)}{2\pi} C_\ell^{\rm SW} \equiv \text{constant}. \tag{2.28}$$

This implies that the scale-invariance in the primordial curvature power spectrum can be directly translated to the constancy of the CMB angular power spectrum at large angular scales. The flat region observed for low multipoles in figure 2.3 corresponds to the Sachs-Wolfe regime. These modes are totally unaffected by the interactions in the primordial plasma and provide a direct probe of inflationary physics.

Further small scales, the anisotropies in the CMB sky are determined by the dynamics of the photon-baryon system in the primordial plasma. These interactions give rise to acoustic oscillations or pressure waves, i.e. the regions of higher density experienced greater gravitational attraction, causing compression and enhancing the pressure waves. Conversely, regions of lower density experienced rarefaction. These sound waves, also called Baryon Acoustic Oscillations (BAO), at the decoupling left distinct imprints on the CMB power spectrum as acoustic peaks. In this regime, the transfer function is obtained by numerically solving the Boltzmann equation, incorporating various physical processes such as photon diffusion and damping, Compton scattering, acoustic oscillations, etc.

The position and heights of acoustic peaks provide valuable information about the fundamental properties of the universe. The position of the first peak is directly related to the geometry of the universe (flat, positively curved or negatively curved). The observed position of the first peak ($\ell \sim 200$, as shown in figure 2.3) is consistent with flat geometry. Baryon, dark matter and dark energy densities can influence the height of the first peak. The relative heights of different peaks, specifically the first and the third, give information about the baryon density. Beyond the peaks, the power spectrum exhibits a damping tail (known as Silk damping), where the amplitude of fluctuations gradually falls with higher multipole moments. The damping tail carries information about the diffusion of photons, as well as the sound horizon and free-streaming of baryons and dark matter. Analysing the damping tail tells us the total matter density and the properties of neutrinos.

CMB is linearly polarized. Thomson scattering of electrons and ions with photons at the LSS creates distinct polarization patterns in the presence of quadrupole anisotropies (Coulson et al. 1994; Hu & White 1997). However, due to the tight coupling of electrons and photons in the pre-recombination plasma, the generated quadrupole is small, resulting in a relatively low polarization fraction for the CMB, approximately 10%.

Linear polarization of CMB is expressed using Q and U Stokes parameters. These parameters are components of polarization matrix $\mathcal{P}$, given as,

$$\mathcal{P} = \begin{pmatrix} Q & U \\ U & -Q \end{pmatrix}. \tag{2.29}$$

The quantity $\mathcal{P}$ exhibits spinor-like properties (spin-2), implying that Q and U are coordinate-dependent quantities (Seljak & Zaldarriaga 1997). The transformation of Q and U under rotation with angle θ is

$$\begin{pmatrix} Q' \\ U' \end{pmatrix} = \begin{pmatrix} \cos 2\theta & \sin 2\theta \\ -\sin 2\theta & \cos 2\theta \end{pmatrix} \begin{pmatrix} Q \\ U \end{pmatrix}, \tag{2.30}$$

or the linear combination of Q and U transform as,

$$(Q \pm iU)'(\hat{n}) = e^{\mp 2i\theta}(Q \pm iU)(\hat{n}). \tag{2.31}$$

On the sphere, we can express these quantities with spin-2 spherical harmonics as the basis,

$$(Q \pm iU)(\hat{n}) = \sum_{\ell m} {}_{\pm 2}a_{\ell m}\, {}_{\pm 2}Y_{\ell m}(\hat{n}). \tag{2.32}$$

To avoid the ambiguity associated while dealing with coordinate-dependent quantities, we define two scalar quantities — polarization E and B modes (Kamionkowski et al. 1997; Zaldarriaga 2001). These modes are, respectively, the gradient and curl components of linear polarization. Using the spin-2 multipole moments, we

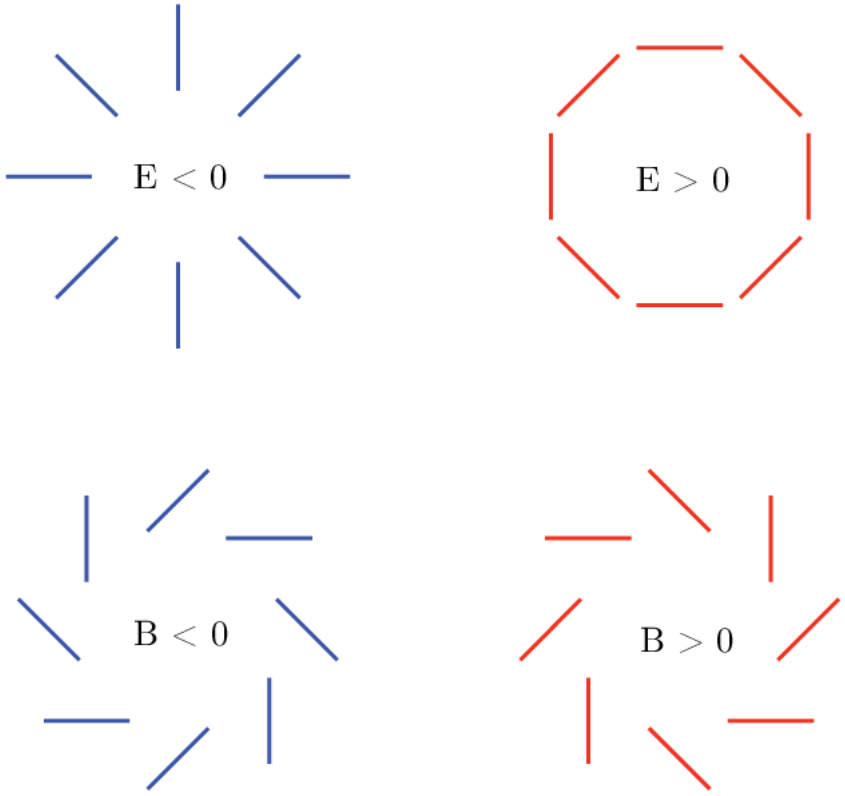

FIGURE 2.4: Polarization patterns for E and B modes. The figure is taken from Baumann et al. (2009).

get

$$a^E_{\ell m} = -[{}_{+2}a_{\ell m} + {}_{-2}\,a_{\ell m}]/2, \qquad a^B_{\ell m} = i[{}_{+2}a_{\ell m} - {}_{-2}\,a_{\ell m}]/2, \tag{2.33}$$

Using these $a_{\ell m}$s, we can obtain the E and B mode maps[‡] as

$$E(\hat{n}) = \sum_{\ell m} a^E_{\ell m} Y_{\ell m}, \qquad B(\hat{n}) = \sum_{\ell m} a^B_{\ell m} Y_{\ell m}. \tag{2.34}$$

This decomposition of the polarization matrix into scalar components is similar to the decomposition of a vector into the gradient of a scalar and the curl of a vector (Helmholtz's theorem). Under parity transformation ($\hat{n} \to -\hat{n}$), B-mode component flips the sign, while the E-mode component, like temperature, remains invariant. Figure 2.4 shows the polarization patterns for E and B modes.

[‡]This should not be confused with electric (**E**) and magnetic (**B**) fields in electrodynamics. However, the similarity with them is that the **E** and the E-mode fields are curl-free, while the **B** and the B-mode fields are divergence-free.

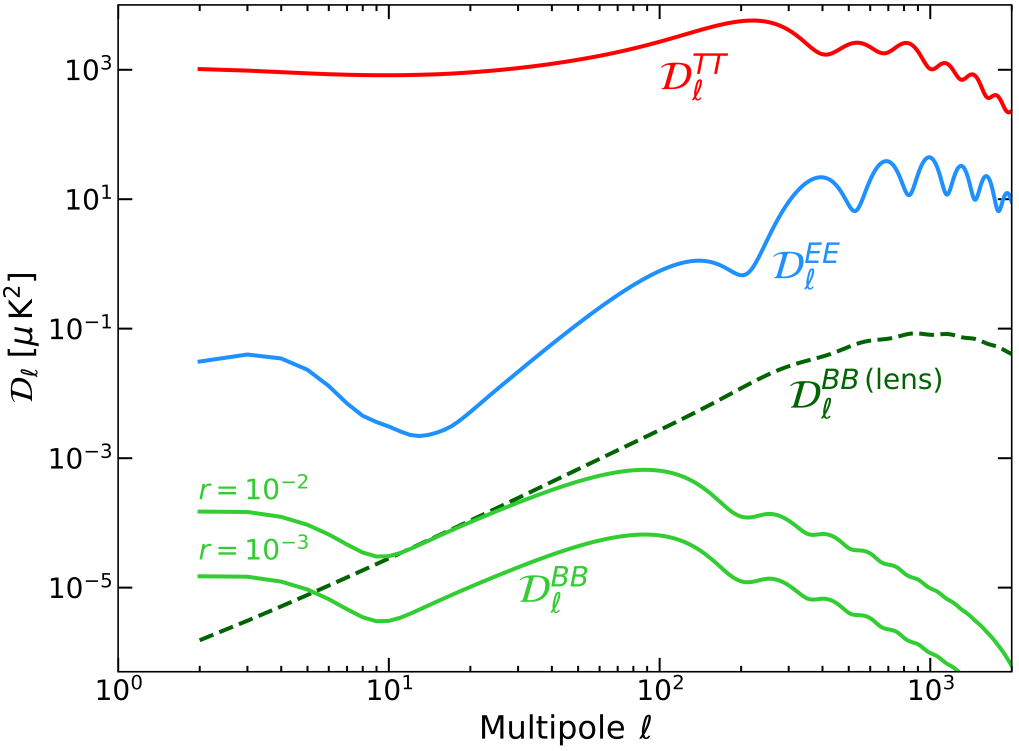

FIGURE 2.5: CMB TT, EE and BB power spectra ($\mathcal{D}_\ell = \ell(\ell+1)C_\ell/2\pi$) for the best-fit cosmological parameters from Planck (Planck Collaboration et al. 2020a) and two different values of r. The lensing BB power spectrum (dashed line) is also shown for comparison.

For temperature and polarization fields $[T, E, B]$, we can define the auto and cross angular power spectra,

$$\begin{aligned}
\langle a^T_{\ell m} a^{*T}_{\ell' m'} \rangle &= C_\ell^{TT} \delta_{\ell\ell'} \delta_{mm'}, & \langle a^T_{\ell m} a^{*E}_{\ell' m'} \rangle &= C_\ell^{TE} \delta_{\ell\ell'} \delta_{mm'}, \\
\langle a^E_{\ell m} a^{*E}_{\ell' m'} \rangle &= C_\ell^{EE} \delta_{\ell\ell'} \delta_{mm'}, & \langle a^T_{\ell m} a^{*B}_{\ell' m'} \rangle &= C_\ell^{TB} \delta_{\ell\ell'} \delta_{mm'}, \\
\langle a^B_{\ell m} a^{*B}_{\ell' m'} \rangle &= C_\ell^{BB} \delta_{\ell\ell'} \delta_{mm'}, & \langle a^E_{\ell m} a^{*B}_{\ell' m'} \rangle &= C_\ell^{EB} \delta_{\ell\ell'} \delta_{mm'}.
\end{aligned} \tag{2.35}$$

Due to the odd parity of the B-mode and even parity for $[T, E]$ modes, C_ℓ^{TB} and C_ℓ^{EB} are expected to be zero. Figure 2.5 shows the theoretical spectra for temperature and polarization maps.

Primordial density fluctuations are the underlying source of these polarization

patterns. Like the temperature fluctuations, the scalar density perturbations are responsible for the E-mode polarization. This is due to the rotational symmetry in the scalar plane-wave perturbations. The quadrupole anisotropy arising from the velocity gradient in the photon-baryon fluid generates E-mode polarization patterns. As a result, the acoustic oscillations of E-mode spectrum are out of phase with those of temperature.

Tensor fluctuations during inflation produce non-zero E and B modes. In other words, B-mode signals are created only via tensor perturbations or primordial gravitational waves. Hence, the detection of CMB B-modes serves as a distinct signature for the presence of metric perturbations in the early universe. In CMB experiments, the detection of B-mode is quantified by r, which represents the relative amplitude of tensor fluctuations compared to scalar perturbations during the inflationary period. The value of r can be directly related to the slow-roll parameters ϵ and η and thus, provides the energy scale of inflation,

$$E_{\rm inf} \equiv (3H^2 M_{Pl}^2)^{1/4} \simeq \left(\frac{r}{0.01}\right)^{1/4} \times 10^{16}\,{\rm GeV}, \tag{2.36}$$

where M_{Pl} is the Planck mass. Thus, the detection of primordial tensor modes in the CMB provides definite proof of inflation. More importantly, tensor fluctuation amplitude is very sensitive to different high-energy mechanisms that drove inflation. As a result, the measurement of r provides crucial constraints on the physics of inflation and the nature of quantum gravity.

Figure 2.5 shows the B-mode power spectrum for two different r values. It should be noted that via gravitational lensing of CMB photons, scalar fluctuations also produce B-mode polarization. As the CMB photons travel through large-scale structures such as galaxies and clusters, gravitational lensing rotates the E-mode signals resulting in the generation of B-mode polarization. These B-modes from

lensing are less dominant at degree angular scales where primordial B-modes dominate. Observational efforts are still ongoing to measure the primordial B-mode signal and the estimation of the r. The joint measurement from the Planck and BICEP experiments sets an upper limit for r at $r < 0.032$ (Tristram et al. 2022).

There are other sources that affect the CMB anisotropies on its path towards us after recombination, creating secondary anisotropies. Reionization of the neutral hydrogen by the photons from the first luminous sources in the universe generates free electrons that interact with the CMB radiation. This happened around $z \sim 10$ and resulted in the suppression of temperature fluctuations and the enhancement of polarization E-modes (Wise 2019). The contribution of the ISW effect was already discussed; the additional anisotropies generated when the CMB photon travels through a gravitational potential that evolves with time. This effect is dominant when the universe gets dark energy dominated, around $z \sim 2$ and has been detected by Boughn & Crittenden (2005). When the CMB photons travel through the matter distribution such as galaxies and galaxy clusters, they experience gravitational lensing (Lewis & Challinor 2006). This lensing effect leads to small-scale anisotropies in the CMB temperature and polarization patterns, providing insights into the distribution of matter in the universe. Inverse Compton scattering of the fast-moving electrons in the intergalactic medium (IGM) with the CMB photons distorts the CMB black body spectrum to higher frequencies and creates additional temperature fluctuations (Sunyaev & Zeldovich 1970). This phenomenon is called the Sunyayev-Zeldovich effect and is useful for exploring the distribution of galaxy clusters and the physics of IGM.

2.1.3 Status of CMB experiments

Since the first detection of CMB by Penzias & Wilson (1965) at the Bell laboratory, there have been several efforts to extract the wealth of information microwave

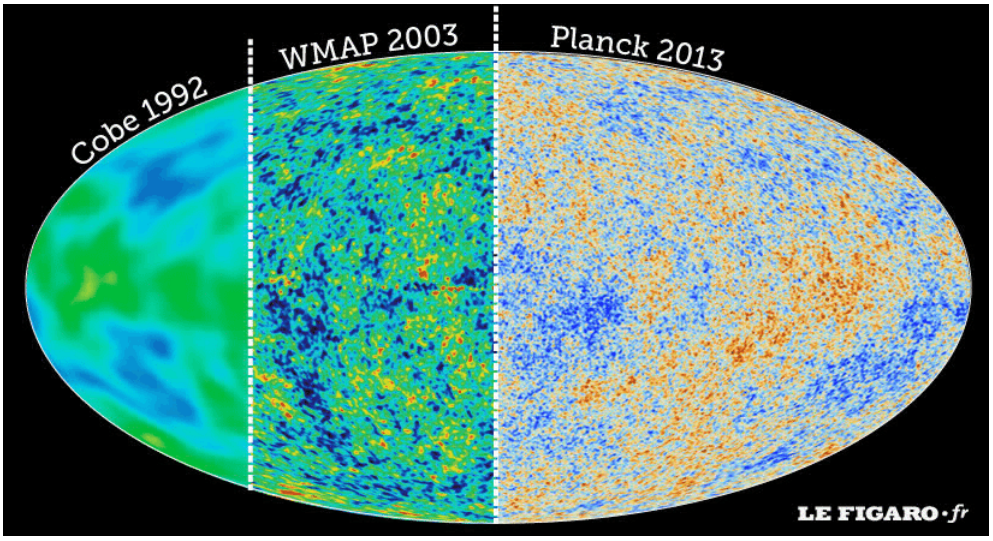

FIGURE 2.6: A comparative illustration showing the angular resolutions of CMB space telescopes: COBE, WMAP, and Planck. This figure is taken from Vazquez Gonzalez et al. (2020).

background encodes about the early universe, including the verification of the true black body nature of the radiation and finding the anisotropies in the CMB sky.

The far infrared absolute spectrometer (FIRAS) instrument onboard the cosmic background explorer (COBE) satellite, made the first accurate estimate of the CMB black-body spectrum (Mather et al. 1990). FIRAS measured the CMB temperature with remarkable precision as (Fixsen 2009),

$$T_0 = 2.72548 \pm 0.00057\text{K}. \tag{2.37}$$

The temperature anisotropies in CMB were discovered by the COBE Differential Microwave Radiometer (DMR) on an angular scale of 7° (Smoot et al. 1992). For these two major milestones in CMB science, George Smoot and John Mather, the lead scientists of these two experiments, were awarded the Physics Nobel Prize in 2006.

Inspired by these results, many balloon and ground-based experiments explored

the anisotropies in the CMB to further small angular scales and the acoustic peaks in the CMB power spectrum. The first peak in the power spectrum was first measured by BOOMERanG (Mauskopf et al. 2000) and MAXIMA-1 (Hanany et al. 2000) experiments, demonstrating that the geometry of our universe is flat, rather than curved. DASI telescope, located at the South Pole, detected the second and third peaks and subsequently measured the CMB E-mode polarization signal for the first time (Kovac et al. 2002). POLARBEAR experiment directly observed the CMB B-mode polarization signal resulting from the gravitational lensing of the E-mode polarization (Polarbear Collaboration et al. 2014).

After COBE, two space telescopes dedicated to CMB science were the WMAP and Planck. WMAP stands for Wilkinson Microwave Anisotropy Probe. It had five frequency bands ($23 - 94$ GHz). Launched in 2001, it observed the sky for the next nine years. The telescope made very precise CMB temperature and polarization maps with arcminute resolution and measured the power spectrum till the multipole range of $\ell = 1000$. This marked the beginning of precision cosmology, establishing a solid foundation for the six-parameter Λ-CDM model, the so-called standard model for big bang cosmology (Hinshaw et al. 2013a).

Following this, the Planck mission by the European Space Agency (ESA) carried out a detailed investigation of the CMB anisotropies, looking further at small angular scales than WMAP. An illustration in figure 2.6 presents a comparison of the angular resolutions of the three CMB space telescopes: COBE, WMAP, and Planck. The wide frequency coverage of Planck, spanning from 30 GHz to 857 GHz, provided a significant advantage in mitigating the contamination from the foreground emissions. With its highly sensitive bolometer and radiometer detectors, Planck attained exceptional precision in measuring polarization signals. Planck results show improved agreement with the WMAP findings of cosmological parameters, with smaller error bars (Planck Collaboration et al. 2020a). The temperature and polarization power spectra as measured by Planck, are shown in

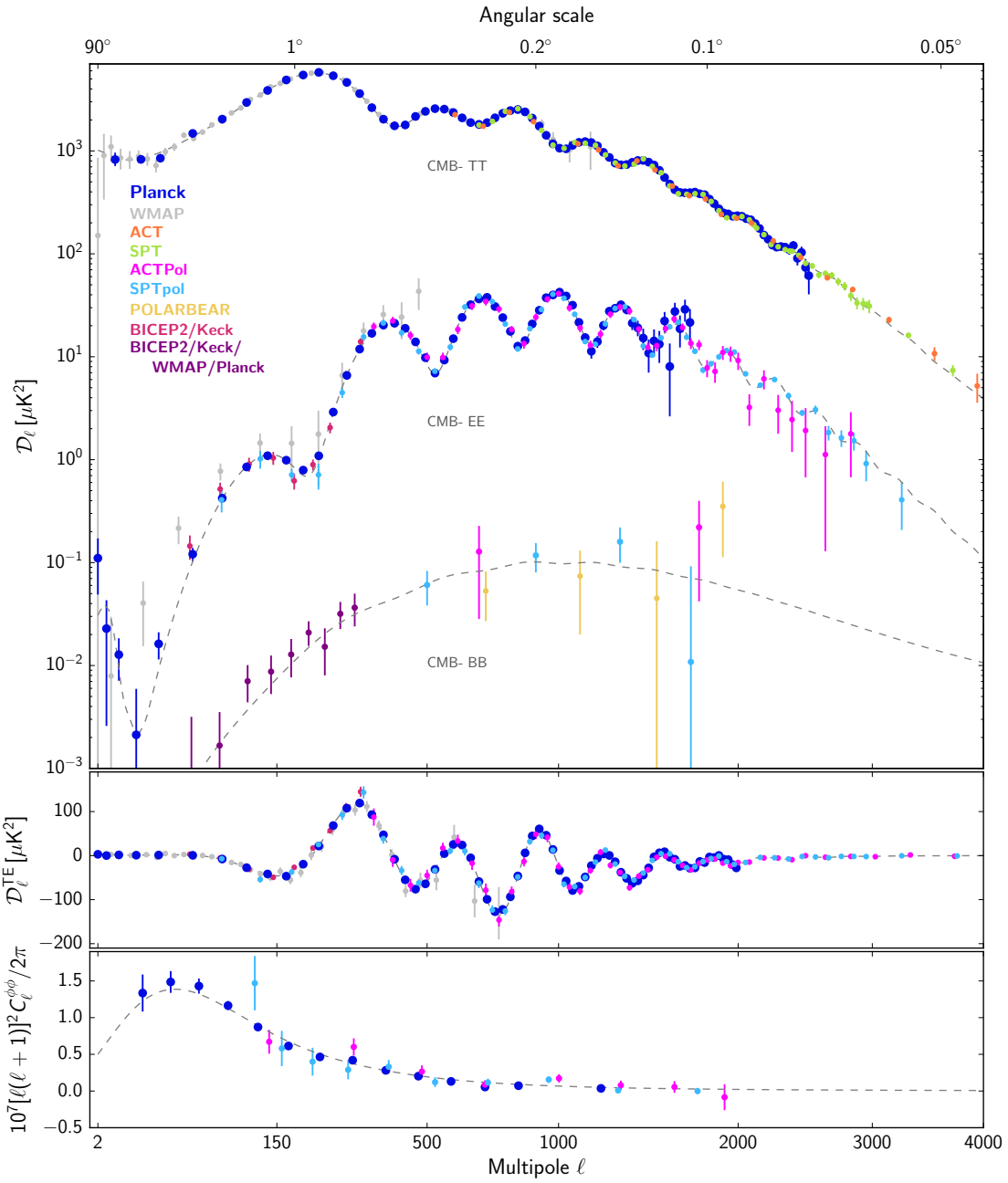

FIGURE 2.7: The CMB angular power spectrum obtained using different experiments (Planck Collaboration et al. 2020a). The last row shows the power spectrum for the CMB lensing potential $\mathcal{D}_\ell^{\phi\phi}$.

figure 2.7, together with the results from other CMB experiments.

There are several ongoing ground-based experiments dedicated to measuring the CMB anisotropies. BICEP telescope in the South Pole is the first targeted experiment to detect primordial B-modes (Keating et al. 2003). In 2014, BICEP2

Collaboration et al. (2014) claimed the first detection of primordial B-mode polarization with $r = 0.2^{+0.07}_{-0.05}$. Further analysis, using data from Planck, demonstrated that the excess r value measured by BICEP2 was a result of contamination from Galactic dust emissions (Ade et al. 2015). Ongoing efforts to detect B-mode signals continue at the south pole site through missions such as the updated BICEP3/Keck, POLARBEAR, CLASS, etc. (Chang et al. 2022).

Other important ground-based experiments are the Atacama Cosmology Telescope (ACT) located in the Atacama desert, Chile and the South Pole Telescope (SPT) situated in Antartica (Thornton et al. 2016; Balkenhol et al. 2023). These telescopes are designed to measure the CMB anisotropies at the scale of arcminutes. They are able to study the small-scale features in the CMB, such as the Sunyaev-Zeldovich effect and gravitational lensing. In this way, these experiments provides further insights into the physics of galaxy clusters and the evolution of the universe at smaller angular scales. By conducting cross-correlation studies with the galaxy surveys and other observations in the nearby universe, these telescopes have yielded improved estimates on the dark energy equation of state, Hubble parameter, properties of dark matter, the sum of neutrino masses etc. (Qu et al. 2023; Kitayama et al. 2023).

The upcoming LiteBIRD satellite, a joint project of the Japanese Space Agency (JAXA) and National Aeronautics and Space Administration (NASA), is aimed at measuring the primordial B-mode signal from inflation, with $\delta r < 0.001$ (Matsumura et al. 2014; Allys et al. 2023). There are ongoing efforts to increase the sensitivity of ground-based telescopes including the South Pole Observatory and the Simons Observatory (Ade et al. 2019). Another promising future endeavour, CMB-S4 encompasses a wide range of scientific objectives within four key themes: exploring primordial gravitational waves and inflation, unravelling the mysteries of the dark universe, mapping the distribution of matter in the cosmos, and observing the time-variable millimetre-wave sky. Classified as a "Stage 4" CMB

experiment, it is planned to have 500,000 detectors and an order of magnitude higher sensitivity than all previous generation detectors (Abazajian et al. 2019).

To ensure effective component separation, it is crucial to have dedicated missions specifically focused on studying foreground emissions. Increasing the spectral coverage at GHz frequencies, where synchrotron, free-free and AME dominate, can mitigate the complications associated with low-frequency foregrounds. QUIJOTE experiment is one such mission, observing the sky at the frequency bands $10 - 40$ GHz and providing us with high-sensitive temperature and polarization all-sky maps at degree-angular scales (Rubino-Martin et al. 2023). At 5 GHz, the C-Band All Sky Survey (CBASS) is designed for preparing an all-sky map that can characterize the low-frequency foreground components (Harper et al. 2022). At 2.3 GHz, the S-band Polarization All-Sky Survey (S-PASS) prepared the first map of polarized radio emission in the southern sky using the Parkes radio telescope (Carretti et al. 2019).

2.2 Diffuse foreground contamination

In this section, we will provide an overview of the physics underlying different Galactic foreground emissions. Also, we will describe the parametric models considered for the foreground signals that go inside the component separation pipelines in the CMB experiments. For an in-depth review of foregrounds, see Dickinson (2016).

2.2.1 Galactic synchrotron

Relativistic electrons interacting with magnetic fields in the Galaxy emit synchrotron radiation. Cosmic rays (CR), which include relativistic electrons, arrive at our Galaxy from all directions. Their interaction with the magnetic field in the Galaxy results in synchrotron emission roughly in the frequency range of 20 MHz to 100 GHz. The intensity of the synchrotron emission is related to the strength of the magnetic field and the number density of CR electrons, both of which vary with respect to direction. As a consequence, the intensity of Galactic synchrotron emission shows variations across the sky.

Let the energy distribution of relativistic electrons be given by the power law form

$$N_e(E)\mathrm{d}E \propto E^{-p}\mathrm{d}E, \tag{2.38}$$

where p is the index which in this case depends on the CR composition. Let $I_{\mathrm{sync}}(\hat{n}, \nu)$ denote the intensity of synchrotron emission in sky direction $\hat{n}$, at frequency ν. Let $B_\perp$ be the magnitude of the magnetic field perpendicular to the line-of-sight radial coordinate r. Then $I_{\mathrm{sync}}(\hat{n}, \nu)$ can be related to $B_\perp$ as

$$I_{\mathrm{sync}}(\hat{n}, \nu) \propto \nu^{\beta_s} \int \delta r B_\perp^{-\beta_s+1}(\hat{n}). \tag{2.39}$$

The spectral index (β_s), which is related to p as $\beta_s = -(p-1)/2$, shows variations in the sky given the difference in the strength of Galactic magnetic field and the CR distribution along the line-of-sight (Westfold 1959; Rybicki & Lightman 1985). The spectrum also exhibits steepening at higher frequency bands due to the radiative losses and the ageing effects of CR electrons, and the presence of multiple components (Kogut 2012; Orlando & Strong 2013).

Radio telescopes used in sky surveys do not measure I_{sync} directly. Rather, what

is measured is the brightness temperature $T_{\rm sync}$ which is related to $I_{\rm sync}$ as $T_{\rm sync} = I_{\rm sync}/\nu^2$. Sky surveys to obtain $T_{\rm sync}(\hat{n}, \nu)$ have been conducted at a number of radio frequencies. Of these, the Haslam map is widely used in the CMB component separation pipelines. Remazeilles et al. (2015) has reprocessed the original version of the Haslam map. Figure 2.8 (top panel) shows this cleaned version of the Haslam map. In this frequency range and in terms of brightness temperature, spectral index (β_s) is -2.7 ± 0.12 (Platania et al. 2003). This low-frequency radio map is free from other interstellar radiation fields, such as the free-free and spinning dust emissions, which makes it an ideal synchrotron intensity map for parametric component separation techniques.

Due to their interaction with the Galactic magnetic field, synchrotron emission is highly polarized, with theoretical estimates showing about 70% polarization efficiency (Rybicki & Lightman 1985). However, at frequencies below approximately 5 GHz, mainly near the Galactic plane, depolarization effects such as Faraday rotation become dominant, leading to a decrease of the polarization fraction to approximately 20% (Carretti et al. 2019). Figure 2.8 (bottom panel) shows the synchrotron polarization amplitude map given by Planck (Planck Collaboration et al. 2020c).

Several studies in the literature focus on large-scale spatial fluctuations of synchrotron emission. The spatial variation of the spectral index, which is important to understand the morphology of synchrotron emission at frequencies relevant for CMB experiments, is studied in Miville-Deschênes et al. (2008); Fuskeland et al. (2021). Polarization properties of the filamentary structures in the synchrotron map are studied using Haslam map and WMAP low-frequency channels (Vidal et al. 2015). The spatial correlations are studied using the power spectrum for both intensity and polarization maps (Baccigalupi et al. 2001; Burigana et al. 2006; La Porta et al. 2008; Planck Collaboration et al. 2020c; Martire et al. 2022). Many of these works have used the frequency dependence of the power spectrum

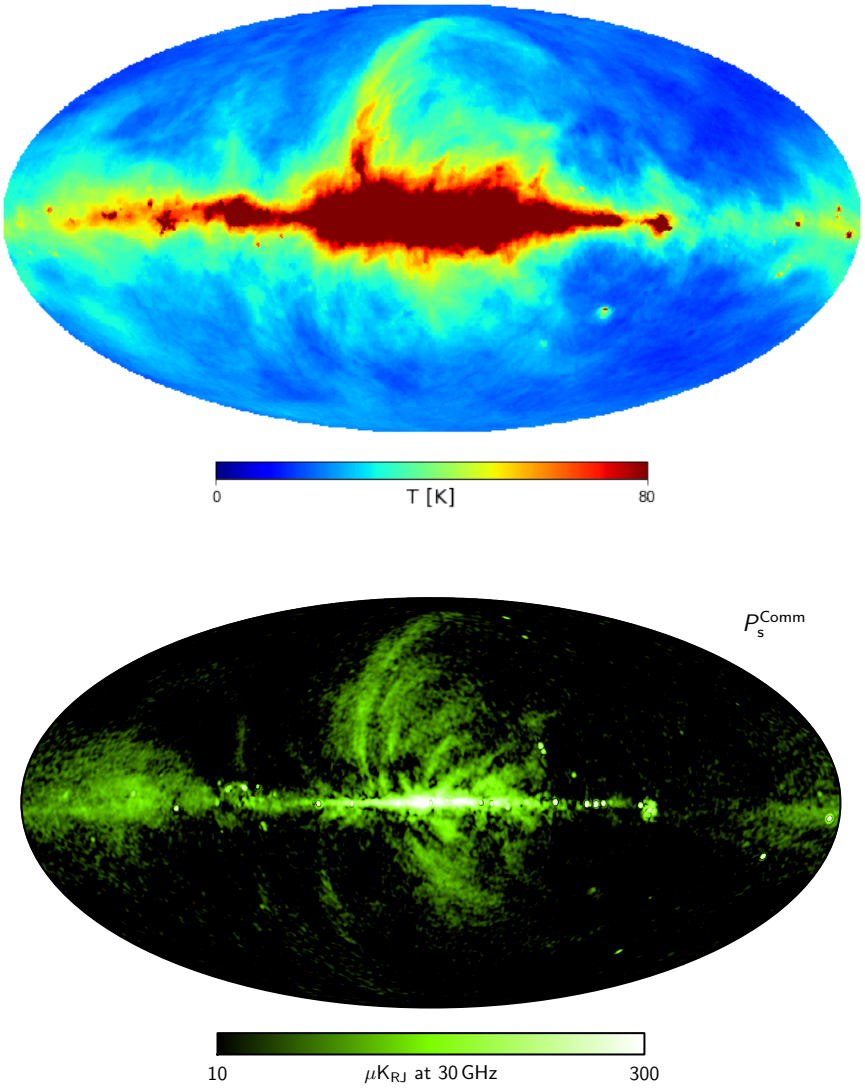

FIGURE 2.8: *Top:* All-sky Haslam 408 MHz synchrotron map reprocessed by Remazeilles et al. (2015). *Bottom:* Synchrotron polarization amplitude as measured by Planck (Planck Collaboration et al. 2020c).

($C_\ell \propto \nu^{2\beta_s}$) to estimate the synchrotron spectral index and also calculated the correlations between synchrotron and thermal dust emissions (La Porta et al. 2008; Martire et al. 2022; Planck Collaboration et al. 2020f; Krachmalnicoff et al. 2018). The angular features carry a wealth of information regarding the properties of the interstellar medium and the structure of the Galactic magnetic field (Mertsch & Sarkar 2013). Cho & Lazarian (2010) analysed how the angular spectrum of synchrotron emission is related to the MHD turbulence in the interstellar medium.

Lazarian & Pogosyan (2012) carried out extensive theoretical calculations to explain the observed correlations of synchrotron fluctuations in terms of the CR electron spectra and the axisymmetric nature of the magnetic turbulence. Non-Gaussianity and other higher-order statistical features of synchrotron temperature and polarization maps are studied in Ben-David et al. (2015); Rana et al. (2018); von Hausegger et al. (2019); Rahman et al. (2021); Martire et al. (2023).

2.2.2 Free-free emission

Due to the scattering and deceleration of free electrons by ions and other charged particles in the ionized regions of the interstellar medium, free-free emission is produced. This radiation is also known as *thermal bremsstrahlung*. The H-α line emission serves as a valuable tracer of free-free radiation since both originate from the HII regions of the ISM. The spectrum of free-free radiation is well understood. In the optically thin regime, which is typically above a few GHz, the spectral index remains consistent at $\beta_f = -2.1$, with minimal dependence on electron temperature. As the frequency increases towards 100 GHz, the spectrum undergoes a slight steepening, still maintaining a spectral index of $\beta_f = -2.13$. The similarity of the free-free spectrum with that of synchrotron and AME poses challenges in component separation. However, H-α templates are helpful tools for effectively distinguishing and separating free-free signals in CMB experiments (Dickinson et al. 2003).

The free-free emissivity is given as,

$$j_{\mathrm{ff},\nu} = \frac{8}{3}\left(\frac{2\pi}{3}\right)^{1/2} g_{\mathrm{ff},i}(\nu, T_e)\frac{e^6}{m_e^2 c^3}\left(\frac{m_e}{kT_e}\right)^{1/2} e^{-h\nu/kT_e} n_e Z_i^2 n_i, \tag{2.40}$$

where $g_{\mathrm{ff},i}(\nu, T)$ is the Gaunt factor for free-free transitions that takes care of the quantum mechanical effects and T_e is the electron temperature (Draine 2011).

Due to the inherent randomness and isotropic nature of Thomson scattering, it is expected that the polarization of the free-free emission is close to zero. Using WMAP maps, Macellari et al. (2011) showed that the degree of polarization of free-free emission is less than 3% (with 95% confidence level). In this way, free-free emission is unlikely a significant foreground for CMB polarization studies.

2.2.3 Thermal dust emission

Interstellar dust grains get heated up by absorbing starlight and emit radiation in microwave and infrared wavelengths. The grains are made up of silicates, graphites and Polycyclic Aromatic Hydrocarbons (PAHs), and exhibit a typical temperature of 20 K (refer Draine (2003) for a detailed review).

The observed spectrum of thermal dust emission is modelled as a modified blackbody (MBB, also known as greybody) and is given as,

$$I_\nu = \nu^{\beta_d} B_\nu(T_d), \tag{2.41}$$

where ν^{β_d} represents the spectral dependence on the dust emissivity and B_ν is the Planck function. The dust spectral index β_d is approximately 1.6. However, this is a simplified model, assuming a single component of the dust grain. In reality, dust composition is more complex, with multiple dust clouds exhibiting varying properties across the sky as well as along the line of sight. More sophisticated models have been developed to address this by adopting MBB spectral laws with multiple components (Meisner & Finkbeiner 2015; Hensley & Bull 2018). Moment expansion techniques are also implemented to better remove dust foregrounds (Chluba et al. 2017; Remazeilles et al. 2021).

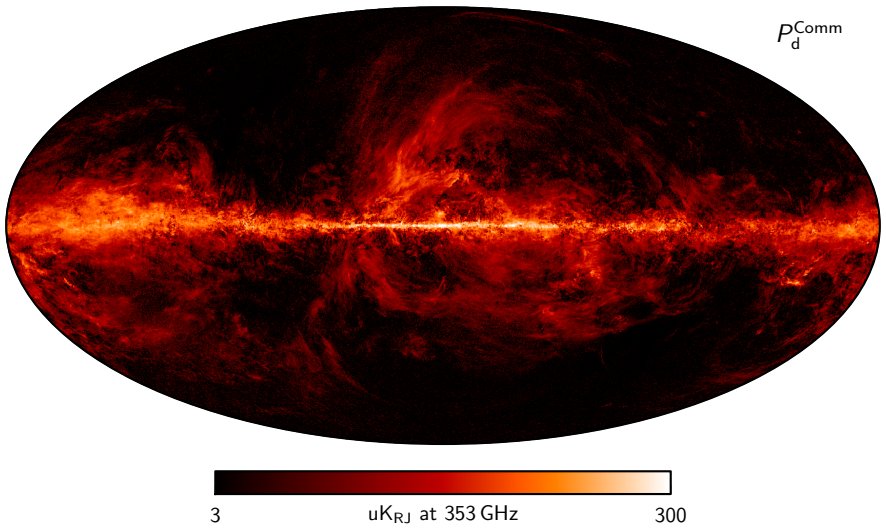

FIGURE 2.9: Thermal dust polarization amplitude provided by Planck (Planck Collaboration et al. 2020c).

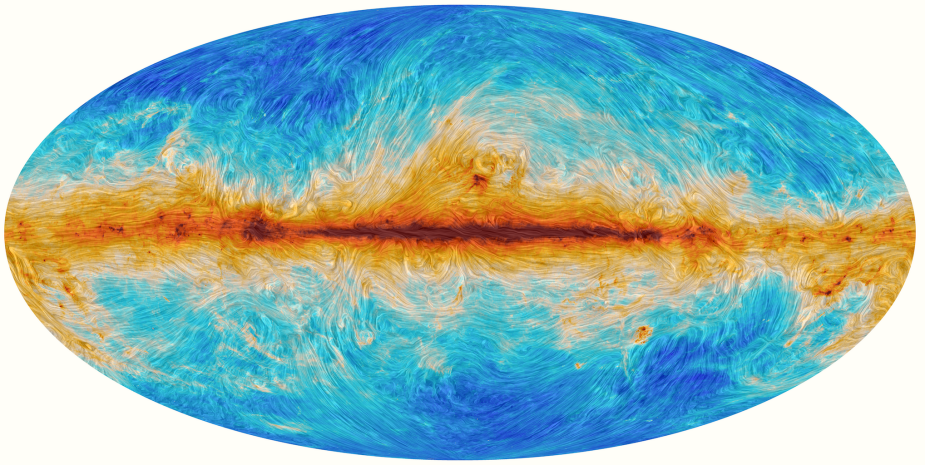

FIGURE 2.10: Galactic magnetic field lines traced by the polarized dust emission from Planck (Planck Collaboration et al. 2016a).

Dust grains with aspherical shapes exhibit differential absorption of starlight, resulting in the emission of radiation predominantly along the long axis. The short axis of these grains aligns efficiently with the Galactic magnetic field and gives rise to a net polarization. The polarization fraction of thermal dust emission is estimated to be significantly high, reaching values up to 20% at high Galactic latitudes (Planck Collaboration et al. 2020c). Figure 2.9 shows the all-sky map of thermal dust polarization amplitude (top panel) from Planck, along with the magnetic field lines (bottom panel) traced by it.

The statistical properties of dust emission are well studied at the power spectrum level. Planck has measured the power spectrum of polarization E- and B- modes of dust, finding that the amplitude of E-mode is twice that of B-mode. Also, Planck has detected a non-zero TB power spectrum, shedding light on the parity-violating physics involved in the mechanism of emission (Planck Collaboration et al. 2020f). Coulton & Spergel (2019); Jung et al. (2018) calculated the angular bispectrum of Planck thermal dust maps to estimate the level of non-Gaussianity and how it can bias the detection of primordial non-Gaussianity in the CMB. Skewness and kurtosis of polarized dust maps were studied by von Hausegger et al. (2019). Higher-order correlations were studied using wavelet transforms and wavelet phase harmonics (Regaldo-Saint Blancard et al. 2020, 2023). Machine learning methods were also implemented to characterize further the properties of thermal dust emission (Aylor et al. 2020; Krachmalnicoff & Puglisi 2021; Thorne et al. 2021).

2.2.4 Anomalous microwave emission

The Anomalous Microwave Emission (AME) is a Galactic emission that peaks in the microwave frequencies between $10 - 60$ GHz and has strong correlations with thermal dust emission (Dickinson et al. 2018). It was detected recently by Kogut et al. (1996); Leitch et al. (1997). The origin of this emission is still a topic of research, with the most plausible explanation that the rapidly spinning ultra-small dust grains with non-zero dipole moment emit electric dipole radiation at microwave ranges. These dust grains rotate at GHz frequencies, and hence, the emission is also called spinning dust emission (Draine & Lazarian 1998a,b). Another mechanism proposed to explain AME is magnetic dipole radiation, which is caused by the thermal fluctuations of the magnetization of interstellar dust grains (Draine & Lazarian 1999). In this case, the emission is called magnetic dust emission.

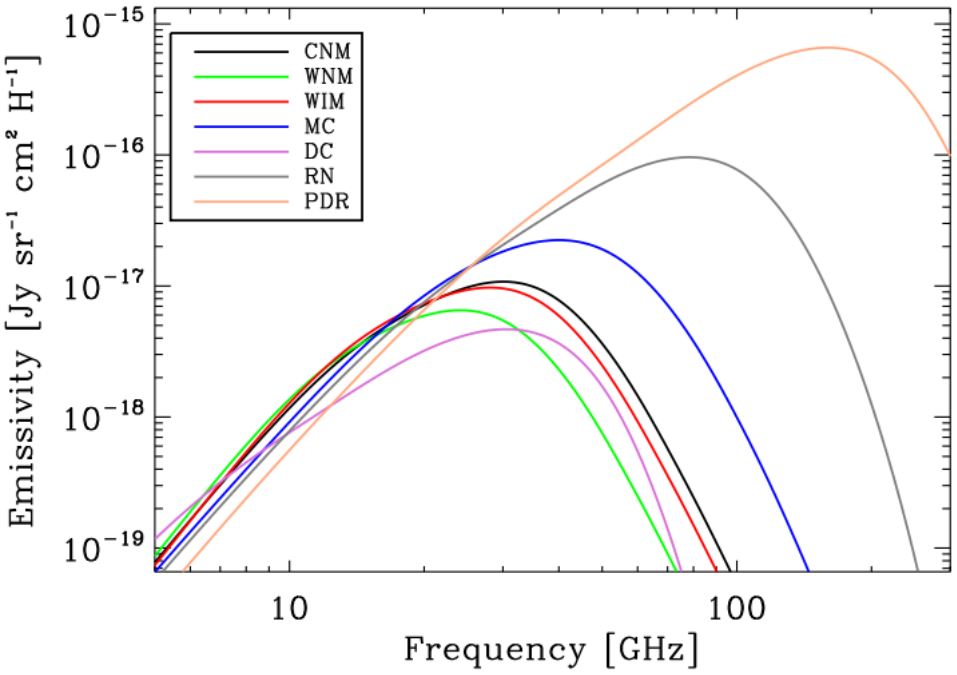

FIGURE 2.11: Emissivity of spinning dust as a function of frequency across different phases of the interstellar medium, generated using the `SpDust2` code. We see that the emissivity strength, as well as the peak frequency, vary for different interstellar environments, with higher values in dense molecular clouds and photo-dissociation regions (PDR). The plot is taken from Dickinson et al. (2018).

There are several studies focused on determining the spectra of spinning dust emission by considering the size distribution of the grains, their electric dipole moments, rotation rates etc. (Draine & Lazarian 1998b; Ali-Haimoud et al. 2009; Silsbee et al. 2011). Figure 2.11 shows the variation of spinning dust emissivity with frequency for different phases of the interstellar medium, prepared using the widely used `SPDust2`[§] code. The plot is adapted from Dickinson et al. (2018). The Planck 2015 analysis assumes two spinning dust components with different peak frequencies to obtain a better parametric fit for the observed data. Here, the peak frequency of one of the components varies spatially. By fitting the observed data with the models based on the `SpDust2` code, Planck results provide the full-sky maps for AME (Planck Collaboration et al. 2016b).

[§] `http://cosmo.nyu.edu/yacine/spdust/spdust.html`

The polarization of the spinning dust emission is expected to be small, for the lack of sufficient alignment of the grains with the ambient magnetic field. Draine & Hensley (2016) has shown that the alignment of the dust grains is impacted by the quantum suppression of dissipation, which results in a negligible degree of polarization. On the other hand, if the AME is dominated by magnetic dust emission, the polarization fraction is expected to be significantly higher, up to 30% (Draine & Lazarian 1999; Draine & Hensley 2013).

Most of the observational studies of AME support the theoretical predictions of the low-level polarization of spinning dust emissions. QUIJOTE survey, along with Planck and WMAP, estimated upper limits for polarization fraction in the molecular complex W43r as 0.39, 0.52 and 0.22% at frequencies 16.7, 22.7, and 40.6 GHz, respectively (Génova-Santos et al. 2016). In the Perseus region, Planck Collaboration et al. (2016d) found a polarization fraction less than 1.6%. The all-sky analysis using WMAP data sets by Macellari et al. (2011) obtained an upper limit of 5%. It is important to note that neglecting even 1% of AME polarization can lead to a non-negligible bias in the accurate estimation of r for CMB B-mode experiments (Remazeilles et al. 2016). This underscores the necessity of obtaining more stringent limits on AME polarization through low-frequency observations (Harper et al. 2022; Rubino-Martin et al. 2023).

2.3 Component separation techniques

Based on the earlier discussions, it is evident that foreground emissions from our Galaxy, as well as other sources, present significant challenges in capturing subtle features in CMB signals. To address this, component separation techniques are employed in CMB experiments to distinguish and subtract foregrounds so as to obtain clean CMB maps (Tegmark & Efstathiou 1996). The total emission at each

pixel ($\hat{n}$) on the sky at a specific frequency, ν, is given as,

$$y(\nu, \hat{n}) = \sum_c a_c(\nu, \hat{n}) s_c(\hat{n}) + n(\nu, \hat{n}). \tag{2.42}$$

Here, c denotes different astrophysical components, a_c is the spectral response of each component, and s_c is the amplitude of the components. This is called the linear mixture model of component separation. Generalizing this for different frequencies (or different detectors), we can express the given data in the matrix form at each pixel as,

$$Y = AS + N, \tag{2.43}$$

where S is the column matrix containing the amplitudes of all the components, and N is the column matrix for the noise element at each frequency. The matrix A, known as the mixing matrix, comprises the spectral information of distinct sky components. Our main objective is to derive the sky components S, with a special interest in CMB, from the given data Y. The idea of component separation, then, boils down to the inversion of this linear system in order to isolate the sky components S (Delabrouille & Cardoso 2009). In this regard, various methodologies have been developed, broadly classified as blind methods and non-blind methods.

Blind methods are implemented assuming minimum prior information of each foreground component, and require the knowledge of the frequency spectrum of the signal of interest, in this case, the CMB spectrum. This means that the knowledge of the foreground components in the mixing matrix A is not crucial in these methods. Moreover, blind methods consider the statistical differences between CMB and foregrounds, such as CMB is Gaussian while foreground fluctuations are non-Gaussian in general. Conversely, non-blind methods rely on using the spectral features of each foreground component. This implies that these methods necessitate the availability of a fully parametrized mixing matrix containing information on all the foreground components. In the following subsections, we provide an overview of the major parametric, blind, and semi-blind methods used

in the WMAP and Planck CMB experiments. For more details, refer to the works of Bennett et al. (2003); Delabrouille & Cardoso (2009); Planck Collaboration et al. (2020c).

2.3.1 Commander algorithm

`Commander` is a Bayesian parametric component separation method based on Monte Carlo and Gibbs sampling techniques (Eriksen et al. 2004a, 2008). It involves fitting an explicit parametric model, which incorporates cosmological, astrophysical, and instrumental parameters, to the observations by exploring the posterior distribution.

`Commander` framework is one of the important foreground separation algorithms implemented in Planck analysis. Given the data d, our goal is to estimate the CMB power spectrum (C_ℓ), amplitudes (s_c) and the spectral parameters β_c of different foreground components, instrumental parameters etc., which are collectively represented as θ. This is achieved in the standard Bayesian way by maximising the posterior distribution calculated using the Bayes theorem as,

$$P(\theta|d) \propto \mathcal{L}(d|\theta)P(\theta), \tag{2.44}$$

where $P(\theta)$ is the prior assumed on different model parameters.

In Planck, different astrophysical components are modelled as,

$$\begin{aligned} d(\nu,\hat{n}) &= \sum_c a_c(\hat{n},\nu)s_c(\hat{n}) \\ &= s_{\rm CMB}(\hat{n}) + s_{\rm s}(\hat{n})\left(\frac{\nu}{\nu_{0,\rm s}}\right)^{\beta_{\rm s}} + s_{\rm ff}(\hat{n})\left(\frac{\nu}{\nu_{0,\rm ff}}\right)^{-2}\frac{g_{\rm ff}(\nu;T_e)}{g_{\rm ff}(\nu_{0,\rm ff};T_e)} \\ &\quad + s_{\rm ame}(\hat{n})\left(\frac{\nu}{\nu_{0,\rm ame}}\right)^{-2}\frac{s_0^{\rm sd}(\nu)}{s_0^{\rm sd}(\nu_{0,\rm ame})} \\ &\quad + s_{\rm d}(\hat{n})\left(\frac{\nu}{\nu_{0,\rm d}}\right)^{\beta_d+1}\frac{\exp(h\nu_{0,\rm d}/k_BT_d)-1}{\exp(h\nu/k_BT_d)-1}, \end{aligned} \tag{2.45}$$

where $\nu_{0,c}$ denotes the reference frequency of any component c. $s_0^{\rm sd}$ is the spectra obtained using the spinning dust `SpDust2` code. Note that for the sake of readability, the integration over the bandpass and the unit conversions between the flux density, antenna and thermodynamic units are not explicitly shown in this expression[¶]. In addition to the Planck data, external data sets are used as foreground templates for the analysis. For instance, the H-α map provided by Finkbeiner (2003) is used as the free-free template. Similarly, the Haslam map (Remazeilles et al. 2015) is included as the synchrotron template.

In the earlier Planck analysis, `Commander` is applied in the pixel-space, as originally developed in Eriksen et al. (2004a). This version is called `Commander1`. However, this requires all the data sets to be at a common angular resolution. `Commander2` (Seljebotn et al. 2019) models foreground maps at the harmonic space instead of pixel space, enabling a full-resolution analysis of Planck maps. The latest version of the algorithm, `Commander3`, applies the formalism directly on the time-ordered data (TOD) rather than pixel maps (Galloway et al. 2022). `BeyondPlanck` analysis is based on this methodology (BeyondPlanck Collaboration et al. 2020).

[¶]Also, this expression does not include all foreground components, such as CO line emissions, for instance.

2.3.2 Maximum entropy method

Maximum Entropy Method (MEM) is also a pixel-based Bayesian model-fitting technique assuming a spectral model for different Galactic components and using external data sets as priors (Bennett et al. 2003). Here, the model is designed in such a way that the priors play a crucial role in determining the accuracy of the fitting in regions with a low signal-to-noise ratio (SNR).

Similar to `Commander`, at each frequency band and sky pixel, the model temperature is formulated as,

$$\begin{aligned} T_m(\nu,\hat{n}) &= S_{\rm CMB}(\nu,\hat{n})T_{\rm CMB}(\hat{n}) + S_{\rm s}(\nu,\hat{n})T_{\rm s}(\hat{n}) + S_{\rm ff}(\nu,\hat{n})T_{\rm ff}(\hat{n}) \\ &\quad + S_{\rm AME}(\nu,\hat{n})T_{\rm AME}(\hat{n}) + S_{\rm d}(\nu,\hat{n})T_{\rm d}(\hat{n}). \end{aligned} \tag{2.46}$$

The index s,ff and d correspond to synchrotron, free-free and dust emissions, respectively. $S_c(\nu,\hat{n})$ and $T_c(\hat{n})$ represent the frequency spectrum and the spatial amplitude (at the reference frequencies) for each component c. For synchrotron, AME and free-free emissions, the reference frequency is chosen as 23 GHz (corresponding to the WMAP K band), while thermal dust is normalized at 94 GHz (W band frequency). For the synchrotron frequency spectrum, the power law model with a constant spectral index, $\beta = -3.0$, is considered. Similarly, power law frequency spectra with $\beta = -2.15$ and $+1.8$ are assumed for free-free and thermal dust emissions, respectively. For spinning dust, the models of Ali-Haimoud et al. (2009) and Silsbee et al. (2011) are adopted.

These models are fitted with the data by minimizing the functional $H(\hat{n}) = A(\hat{n}) + \lambda(\hat{n})B(\hat{n})$, with $A(\hat{n})$ the standard χ^2 defined as,

$$A(\hat{n}) = \sum_{\nu} \left[T(\nu,\hat{n}) - T_m(\nu,\hat{n})\right]^2 / \sigma^2, \tag{2.47}$$

and $B(\hat{n})$ is given by,

$$B(\hat{n}) = \sum_c T_c(\hat{n}) \ln \left[T_c(\hat{n})/P_c(\hat{n})\right] . \tag{2.48}$$

λ is the regularizing parameter that determines the weighting assigned to either the data or the prior in the fitting procedure. It varies with the sky pixel.

P_c is the prior model for the sky map of each component, given at the same reference frequency as T_c. In WMAP analysis, these prior maps are chosen as follows. The Haslam map scaled to K band using power-law spectrum with β_s is used for synchrotron emission. The prior for free-free emission is the extinction- and scattering-corrected H-α maps (Finkbeiner 2003). For thermal dust, model 8 of Finkbeiner et al. (1999) is used. Temperature-corrected dust map from Schlegel et al. (1998) is used as the prior for spinning dust.

2.3.3 Blind methods

The key advantage of blind component separation methods is that they are model-independent and, therefore, free from biases due to our incomplete knowledge of foreground emissions. This is achieved by assuming statistical independence of the various components of the linear mixture defined in eq. (2.42). Furthermore, the blind approach allows data processing, even when there is a possibility of missing or not identifying certain components.

The following are the major blind methods used for component separation in Planck maps.

- Internal Linear Combination (ILC) — This separation technique is based on the linear combination of multi-frequency maps and identifying the weights

for each map such that the variance is minimum while retaining unit response to the CMB (Bennett et al. 2003; Eriksen et al. 2004b). The idea here is to suppress foregrounds and noise as much as possible. At each frequency channel i, the data y_i is,

$$y_i(\hat{n}) = s(\hat{n}) + f_i(\hat{n}). \tag{2.49}$$

Here $s(\hat{n})$ is the signal of interest, i.e. CMB, which is independent of the frequency. f_i is the collection of all the foregrounds and noise components. The goal is to construct an estimator $\widehat{s}(\hat{n})$ of $s(\hat{n})$,

$$\widehat{s}(\hat{n}) = \sum_i \omega_i(\hat{n}) y_i(\hat{n}) = s(\hat{n}) + \sum_i \omega_i(\hat{n}) f_i(\hat{n}), \tag{2.50}$$

with weights ω_i, such that the signal of interest can be isolated effectively. The simple version of ILC is to identify the weights ω_i such that the variance of the estimator is minimum and $\sum_i \omega_i = 1$. Using this approach, the estimator effectively separates the CMB signal by reducing the impact of foreground components.

Assuming that CMB is statistically independent of residual signals, weights ω_i corresponding to minimum variance is,

$$\omega_i = \frac{\sum_j C_{ij}^{-1}}{\sum_{ij} C_{ij}}, \tag{2.51}$$

where the signal covariance matrix C_{ij} is,

$$C_{ij} = \langle \Delta y_i(\hat{n}) \Delta y_j(\hat{n}) \rangle = \langle (y_i(\hat{n}) - \bar{y})(y_j(\hat{n}) - \bar{y}) \rangle, \tag{2.52}$$

and $\langle .. \rangle$ denotes the average over the entire sky pixels of interest.

While the basic formulation of ILC may produce noisy results, there are improved versions of ILC techniques such as Harmonic ILC (Kim et al. 2008),

Needlet ILC (Basak & Delabrouille 2013), Generalized Needlet ILC (Remazeilles et al. 2011) etc., which were extensively used in WMAP and Planck data analysis.

- SMICA — SMICA stands for Spectral Matching Independent Component Analysis and is employed in the harmonic space. A limited set of templates with flexible power spectra, frequency spectra and correlation among different components represents the foregrounds. Here, the goal is to minimize the mismatch between the model and the auto- and cross-power spectra of frequency channel maps. A set of weights is then generated using the solution obtained to combine the frequency maps in the Fourier space. Using these weights, CMB maps are obtained (Cardoso et al. 2008).

- SEVEM — SEVEM, Spectral Estimation Via Expectation Maximization, is based on internal template fitting and, thus, a semi-blind method. In this method, foreground templates are prepared internally by subtracting two different frequency maps so that the CMB contribution in the template is minimized (Martínez-González et al. 2003). These template maps are then used along with a set of weights to derive CMB from the CMB-dominating frequency channels (Fernández-Cobos et al. 2012). In Planck, four sets of templates are obtained as the difference between the pairs of Planck channels: $(30-44)$, $(44-70)$, $(545-353)$, and $(857-545)$ GHz. They are then used to clean the CMB dominating channels, 143 GHz and 217 GHz. Note that this method can be implemented in both real and wavelet space.

Chapter 3

Statistical Tools for Smooth Random Fields

In this chapter, we summarise the properties of smooth random fields and the mathematical and statistical tools used to characterize them. We begin with the definition of random fields and introduce Gaussian random fields in section 3.1. Moreover, we describe the different properties of GRFs and how they are important in cosmological studies. In section 3.2, we discuss non-Gaussianity and how higher-order N-point functions such as skewness, kurtosis, and bispectrum tell us about the non-Gaussian properties of the cosmological fields. Finally, section 3.3 presents the morphological tools, such as Minkowski functionals (MFs) and Minkowski tensors (MTs), which are extensively used in the development of this thesis. We will explain the mathematics of these tools, the analytical formulation for mildly non-Gaussian cases and the methods used to compute them.

3.1 Gaussian random fields

Let us begin with the definition of a random field. The discussions presented here are based on Adler (2010). A random field is a collection of random variables $f(\mathbf{x})$ defined on a probability space, such that $\mathbf{x} = (x^1, x^2, ..., x^n)$ be the coordinate system for an n dimensional smooth manifold $\mathcal{M}$. A random field is characterized by it's k-point joint probability distribution function (PDF) defined for any k points on $\mathcal{M}$ as,

$$\mathcal{P}(f(\mathbf{x}_1), f(\mathbf{x}_2), ..., f(\mathbf{x}_k)). \tag{3.1}$$

The covariance function ξ_{ij} for the random field $f(\mathbf{x})$ gives the spatial correlation between any two points $\mathbf{x}_i$ and $\mathbf{x}_j$ on $\mathcal{M}$. It is defined as

$$\xi_{ij} = \langle (f(\mathbf{x}_i) - \mu_{\mathbf{x_i}})(f(\mathbf{x}_j) - \mu_{\mathbf{x_j}} \rangle. \tag{3.2}$$

The angular bracket, $\langle .. \rangle$, denotes the ensemble average. $\mu_{\mathbf{x_i}}$ and $\mu_{\mathbf{x_j}}$ represents the mean values of the random variables at $\mathbf{x}_i$ and $\mathbf{x}_j$, respectively. Now, for any $\mathbf{x}$, the variance of the random variable f at $\mathbf{x}$ is given by the auto-covariance,

$$\xi(\mathbf{x}, \mathbf{x}) = \langle f(\mathbf{x})^2 \rangle = \sigma_0^2(\mathbf{x}). \tag{3.3}$$

If the transformation $\mathbf{x} \to \mathbf{x} + \mathbf{a}$ makes the probability distribution $\mathcal{P}(f)$ invariant, then the field f is *homogeneous (stationary)*. This has the following consequences.

1. For every point $\mathbf{x}$ on $\mathcal{M}$, the PDF of random variable is the same.

2. Covariance function satisfies,

$$\xi_{ij} \equiv \xi(\mathbf{x}_i, \mathbf{x}_j) = \xi(\mathbf{x}_i - \mathbf{x}_j). \tag{3.4}$$

3. Auto covariance (or the variance) $\xi(\mathbf{x}, \mathbf{x}) = \xi(0) = \sigma_0^2$ is constant over $\mathcal{M}$. Similarly, the mean $\mu_{\mathbf{x}}$ of $f(\mathbf{x})$ remains constant for any $\mathbf{x}$.

Under rotation, If the covariance function ξ_{ij} remains invariant, then the random field is isotropic, following the condition

$$\xi(\mathbf{x}_i, \mathbf{x}_j) = \xi(|\mathbf{x}_i - \mathbf{x}_j|). \tag{3.5}$$

For a homogeneous isotropic field f, the covariance function between two points depends only on the distance between them.

If the covariance function ξ_{ij} is twice differentiable with the derivatives being finite at any two points $\mathbf{x}_i = \mathbf{x}_j$, then the first derivative of the field exists on the manifold. Similarly, any k-th derivative of the field exists if ξ is $2k$ differentiable. In the case of random fields, which are homogeneous and isotropic, all their higher-order derivatives are also homogeneous and isotropic.

A random field is Gaussian if all of its k-point joint PDFs are multivariate Gaussian distributions,

$$\mathcal{P}(f(\mathbf{x}_1), f(\mathbf{x}_2), ..., f(\mathbf{x}_k)) = \frac{1}{\sqrt{(2\pi)^k \det(\Xi)}} \exp\left(-\frac{1}{2} \sum_{i,j=1}^{k} f_i (\Xi^{-1})_{ij} f_j \right), \tag{3.6}$$

where $f_i \equiv \{f(\mathbf{x}_i)\} = \{f(\mathbf{x}_1), f(\mathbf{x}_2), ..., f(\mathbf{x}_k)\}$ with mean zero. Ξ is the $k \times k$ covariance matrix of f_i, with it's elements given by ξ_{ij}. From the joint PDF, it is evident that the statistics of a Gaussian random field (GRF) are fully characterized by the two-point correlation (covariance) function, ξ_{ij}. For a Gaussian field f, all of its derivative fields are also Gaussian distributed. Further, the field and the derivative fields form a multi-variate Gaussian random field.

In cosmology, Gaussian random fields (GRFs) are used to model the initial conditions of the universe and the distribution of matter on large scales. As discussed previously, inflation predicts that the primordial quantum fluctuations are Gaussian distributed, which then evolved to form the anisotropies in the CMB and the galaxy distributions as we observe today. Therefore, the CMB anisotropies ($\Delta T(\hat{n})$) or the matter fluctuations ($\delta_m(\mathbf{x})$) can be well-modelled as GRFs. By comparing the predicted statistical properties of GRFs with that of the observed data (both CMB and galaxy observations), one can distinguish various theoretical models and obtain important insights into the physical processes that happened in the primordial epochs.

To fully characterize the statistics of random fields, it is essential to compute ensemble averages over multiple realizations of the random process. However, the universe manifests itself as a single realization, which restricts our capacity to completely describe its statistical properties. To circumvent this problem, we utilize the notion of *ergodicity* for homogeneous random fields. This allows us to replace the ensemble average over multiple universes with the spatial average over a single universe (realization). Mathematically, this can be expressed as

$$\int \mathrm{d}f\, \mathcal{P}(..) \Longleftrightarrow \frac{\int_{\mathcal{M}} \mathrm{d}V(..)}{\int_{\mathcal{M}} \mathrm{d}V}, \tag{3.7}$$

$\mathrm{d}V$ is the infinitesimal volume element on the space $\mathcal{M}$. This means that different regions of the universe can be considered as different realizations of the underlying random process. However, ergodicity breaks down when the volume of observation is limited, resulting in statistical fluctuations known as cosmic variance. The effect is prominent while studying the features towards large angular scales. This is because of the finite survey volume of galaxy observations or the finite size of the observable universe for CMB studies.

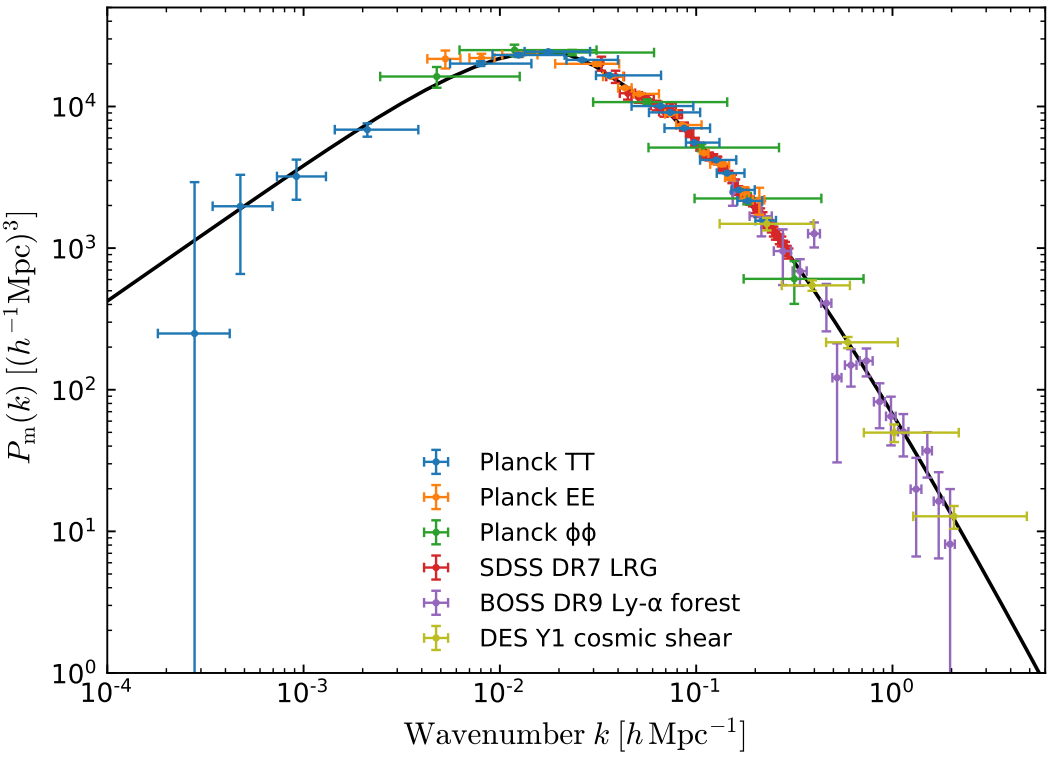

FIGURE 3.1: Matter power spectrum ($P_m(k)$) obtained using Planck and various other cosmological probes (Planck Collaboration et al. 2020a).

As long as the evolution of density perturbations is linear, the initial Gaussian fluctuations remain Gaussian distributed. As a result, the Fourier modes of fluctuations remain uncoupled and evolve independently. It is, therefore, more convenient to represent the Gaussian statistics in terms of the power spectrum, the Fourier transform of the two-point correlation function. For 3D matter distribution $\delta_m(\mathbf{x})$,

$$\begin{aligned}\langle\tilde{\delta_m}(\mathbf{k})\tilde{\delta^*_m}(\mathbf{k}')\rangle &= \int \mathrm{d}^3x\,\mathrm{d}^3x'\,e^{-i\mathbf{k}.\mathbf{x}}e^{-i\mathbf{k}'.\mathbf{x}'}\langle\delta_m(\mathbf{x})\delta_m(\mathbf{x}')\rangle \\ &\equiv (2\pi^3)\delta_{\rm D}(\mathbf{k}-\mathbf{k}')\,P_m(k). \end{aligned} \tag{3.8}$$

$P_m(k)$ represents the matter power spectrum. The delta function, $\delta_{\rm D}$, emerges due to the assumption of homogeneity, implying that each Fourier mode evolves independently. Also, due to isotropy, $P_m(k)$ depends only on the magnitude of the wave vector, $|\mathbf{k}| \equiv k$. $P_m(k)$ obtained using Planck and various other cosmological probes is shown in figure 3.1.

CMB anisotropies (ΔT) are defined on a sphere. As we saw in the previous chapter, ΔT can be decomposed using spherical harmonics as,

$$\Delta T(\hat{n}) = \sum_{\ell,\, m} a_{\ell m} Y_{\ell m}(\hat{n}), \tag{3.9}$$

and similar to eq. (3.8), the covariance of the multipole coefficients can be written in terms of the angular power spectrum (C_ℓ) as,

$$\langle a_{\ell m} a^*_{\ell' m'} \rangle = \delta_{\ell \ell'} \delta_{m m'} C_\ell. \tag{3.10}$$

C_ℓs are independent of m due to the assumption of isotropy.

3.1.1 Estimation of angular power spectrum

For a given field $f(\hat{n})$ defined on a sphere, angular power spectrum C_ℓ can be estimated as,

$$\hat{C}_\ell = \frac{1}{2\ell + 1} \sum_m |a_{\ell m}|^2, \tag{3.11}$$

where $a_{\ell m}$s are computed using the orthogonality property of $Y_{\ell m}$ as,

$$a_{\ell m} = \int \mathrm{d}^2\hat{n}\, f(\hat{n}) Y^*_{\ell m}(\hat{n}). \tag{3.12}$$

In the actual computation of the power spectrum, there are two challenges associated. First, for a map with $N_{\rm pix}$ number of pixels, C_ℓ estimation involves $\mathcal{O}(N^2_{\rm pix})$ operations. For high resolution maps such as from Planck ($N_{\rm pix} \sim 10^7$) or ACT ($N_{\rm pix} \sim 10^{10}$), this becomes computationally quite expensive. Second, in most cases, we do not get the full sky for the analysis due to the unavailability of data or the contamination from other sources, such as Galactic foregrounds at certain

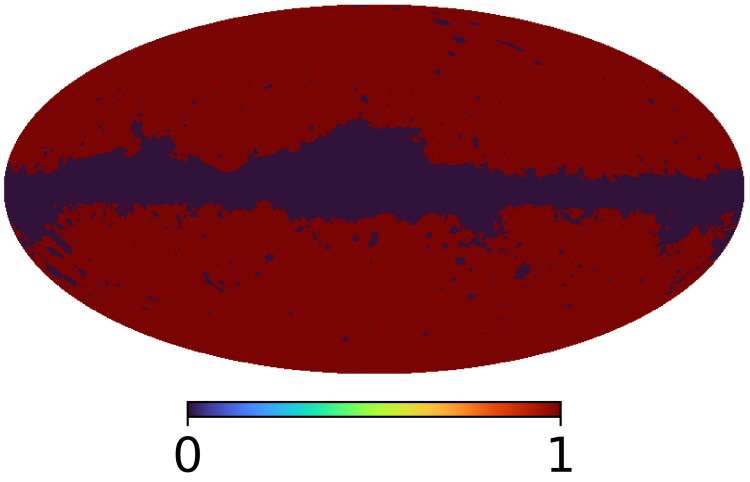

FIGURE 3.2: Planck common mask used for temperature analysis (Image Credit: Planck Legacy Archive (PLA))

pixels. Therefore, we define a mask $M(\hat{n})$ such that,

$$f_m(\hat{n}) = f(\hat{n}) \times M(\hat{n}). \tag{3.13}$$

$M(\hat{n})$ has values zero and one for the masked and the unmasked pixels, respectively. Figure 3.2 shows the common mask used in Planck CMB analysis.

However, this multiplication can alter the $a_{\ell m}$ coefficients and therefore, $\hat{C}_\ell$, inducing coupling of Fourier modes,

$$\tilde{a}_{\ell m} = \int \mathrm{d}\hat{n}\, f(\hat{n}) M(\hat{n}) Y^*_{\ell m}(\hat{n}), \qquad \tilde{C}_\ell = \frac{1}{2\ell+1} \sum_m |\tilde{a}_{\ell m}|^2. \tag{3.14}$$

$\tilde{C}_\ell$ is called pseudo power spectrum. The ensemble average, $\langle \tilde{C}_\ell \rangle$ is related to the full-sky power spectrum average $\langle \hat{C}_\ell \rangle$ as,

$$\langle \tilde{C}_\ell \rangle = \sum_{\ell'} K_{\ell\ell'} \langle \hat{C}_\ell \rangle, \tag{3.15}$$

where $K_{\ell\ell'}$ is the kernel that quantifies the mode-mode coupling associated with the masking. It can be shown that $K_{\ell\ell'}$ depends only on the geometry of the mask (see appendix of Hivon et al. (2002)). Furthermore, in polarization studies,

incomplete sky coverage can result in the leakage of E-mode signals to B-modes. This can lead to a biased estimation of polarization power spectra. Inverting eq. (3.15) by calculating the inverse of the coupling matrix $K_{\ell\ell'}$, the full angular power spectrum can be obtained (Hivon et al. 2002), thereby minimising the bias associated with the cut-sky.

There are several pseudo-C_ℓ algorithms developed for a fast and computationally inexpensive estimation of power spectrum while mitigating the effects of mode coupling due to masking (Szapudi et al. 2001; Chon et al. 2004; Tristram et al. 2005; Alonso et al. 2019). Many of these packages are publicly available* and are used in the analysis pipelines of WMAP, Planck and other CMB experiments.

3.2 Non-Gaussianity and higher-order correlations

As discussed previously, the primordial quantum fluctuations and, as a result, the CMB anisotropies are Gaussian distributed and can be well explained using the two-point correlation functions (equivalently, the power spectrum). However, due to the self-interaction of the inflaton field or coupling with other fields, inflationary models predict the fluctuations to have a tiny deviation from Gaussian behaviour (for a discussion on the non-Gaussianity from different inflationary models, refer to Bartolo et al. (2004)). The detection of primordial non-Gaussianity is another powerful tool to understand the nature of interactions during inflation and, thereby, constrain various inflationary models (Komatsu & Spergel 2001; Maldacena 2003; Meerburg et al. 2019). So far, the CMB and large-scale structure studies have not reported deviations from Gaussianity (Planck Collaboration et al. 2020e; Rezaie et al. 2023). Upcoming galaxy surveys will shed more light on primordial non-Gaussianity (Sartoris et al. 2016).

*See for example, Polspice, Xpol and NaMaster

When a random field deviates from Gaussian statistics, relying solely on two-point correlations and power spectrum becomes inadequate to fully characterize its features. Higher-order correlations and more sophisticated statistical measures are necessary to fully characterize the complex and non-linear features exhibited by non-Gaussian fields. In the case of cosmological fields, the statistics of fluctuations deviate slightly from Gaussianity, what is known as "mildly non-Gaussian" behaviour. In this case, the non-Gaussian deviations can be expanded perturbatively in terms of the linear order Gaussian fluctuations (Salopek & Bond 1990). As a result, the higher order interaction terms become negligible, and thus, the mild-non-Gaussianity can be quantified in terms of three-point (skewness) and four-point (kurtosis) functions or its Fourier transforms, bispectrum and trispectrum, respectively.

The most simple non-Gaussian scenario for the single-field slow-roll inflation is the so-called local-type non-Gaussianity (Maldacena 2003). Here, the Bardeen curvature potential $\Phi(\mathbf{x})$ can be expanded as,

$$\Phi(\mathbf{x}) = \phi_G(\mathbf{x}) + f_{\rm NL}(\phi_G^2(\mathbf{x}) - \langle\phi_G^2(\mathbf{x})\rangle) + g_{\rm NL}\phi_G^3(\mathbf{x}) + ..., \tag{3.16}$$

where $\phi_G(\mathbf{x})$ is the corresponding Gaussian field. $f_{\rm NL}$ and $g_{\rm NL}$ are the non-linearity parameter that characterizes the amplitude of non-Gaussian interactions. For local-type non-Gaussianity, Planck constraints are $f_{\rm NL} = -0.9 \pm 5.1$ and $g_{\rm NL} = (-5.8 \pm 6.5) \times 10^4$, consistent with zero detection of primordial non-Gaussianity (Planck Collaboration et al. 2020e).

As the evolution of density fluctuations becomes non-linear under gravity, the fluctuations start exhibiting non-Gaussian behaviour. This late-time non-Gaussianity arising from the gravitational clustering can be observed in the distribution of dark matter, galaxies and clusters. Unfortunately, this poses a serious challenge in the

observations of large-scale structures to detect primordial non-Gaussianity. Accurate theoretical modelling is required to disentangle the primordial and late-time non-Gaussianities (Tellarini et al. 2016; Uhlemann et al. 2018).

Although CMB is a clean probe of inflationary non-Gaussianity, it is limited by cosmic variance at large angular scales. The secondary anisotropies in CMB, such as gravitational lensing and the Sunyaev-Zeldovich effect, can induce additional non-Gaussianity. These secondary effects can also significantly bias the measurements of primordial non-Gaussianity at small angular scales (Hill 2018; Coulton et al. 2023). Moreover, the Galactic emissions are highly non-Gaussian and accurate component separation is crucial to avoid the leakage of these signals in the CMB non-Gaussianity measurements (Jung et al. 2018). Through the improved sensitivity as well as the careful treatment of secondary effects, upcoming facilities such as Simons Observatory and CMB-S4 are expected to provide better estimates of primordial non-Gaussianity (Ade et al. 2019; Abazajian et al. 2016).

3.2.1 Estimators for Non-Gaussianity

As discussed earlier, the two-point correlation function completely describes the statistics of a Gaussian field. Consequently, all the odd N-point correlations are zero, and the even N-point correlation functions can be expressed in terms of the two-point functions. This is not the case for a non-Gaussian field. Non-Gaussianity introduces higher-order correlations among the field values as well as the derivative fields. Hence, the non-Gaussianity of a given field can be tested by computing higher-order N-point correlation functions of the field and its derivatives.

Given a non-Gaussian field, the skewness parameters (three-point correlators) are the first set of non-zero higher-order N-point functions for a non-Gaussian field. These are the third moments of the underlying joint PDF. For a given field u

with mean zero, its gradient ∇u, and Laplacian $\nabla^2 u$, the skewness parameters are defined as follows,

$$S_0 = \frac{\langle u^3 \rangle_c}{\sigma_0^4}, \quad S_1 = \frac{\langle u^2 \nabla^2 u \rangle_c}{\sigma_0^2 \sigma_1^2}, \quad S_2 = \frac{2\langle |\nabla u|^2 \nabla^2 u \rangle_c}{\sigma_1^4}, \tag{3.17}$$

where $\sigma_0 = \langle u^2 \rangle$ and $\sigma_1 = \langle |\nabla u|^2 \rangle$. The subscript c indicates that these quantities are the connected cumulants. As the field is mean-free, the third-order cumulants are equal to the third-order moments.

Similarly, the four-point functions, also called kurtosis parameters, are given as,

$$\begin{aligned} K_0 &= \frac{\langle u^4 \rangle_c}{\sigma_0^6}, \qquad K_1 = \frac{\langle u^3 \nabla^2 u \rangle_c}{\sigma_0^4 \sigma_1^2}, \\ K_2 &= \frac{2\langle u |\nabla u|^2 \nabla^2 u \rangle_c + \langle |\nabla u|^4 \rangle_c}{\sigma_0^2 \sigma_1^4}, \\ K_3 &= \frac{\langle |\nabla u|^4 \rangle_c}{2\sigma_0^2 \sigma_1^4}. \end{aligned} \tag{3.18}$$

Fourth-order cumulants are given in terms of the moments (Matsubara & Kuriki 2020) as,

$$\langle u^4 \rangle_c = \langle u^4 \rangle - 3\sigma_0^4, \tag{3.19}$$

$$\langle u^3 \nabla^2 u \rangle_c = -3\langle u^2 |\nabla u|^2 \rangle_c = -3(\langle u^2 |\nabla u|^2 \rangle - \sigma_0^2 \sigma_1^2), \tag{3.20}$$

$$\langle u |\nabla u|^2 \nabla^2 u \rangle_c = \langle u |\nabla u|^2 \nabla^2 u \rangle + \sigma_1^4, \tag{3.21}$$

$$\langle |\nabla u|^4 \rangle_c = \langle |\nabla u|^4 \rangle - 2\sigma_1^4. \tag{3.22}$$

One important consequence of non-Gaussianity is the coupling between Fourier modes, which is absent for a Gaussian field. Therefore, it is more convenient to measure the non-Gaussian features of a random field in harmonic space. Angular bispectrum, the Fourier transform of three-point functions, is commonly used in constraining primordial non-Gaussianity of CMB maps. It is defined in terms of

spherical harmonic coefficients as,

$$B_{\ell_1\ell_2\ell_3} \equiv \sum_{m_1 m_2 m_3} \begin{pmatrix} \ell_1 & \ell_1 & \ell_3 \\ m_1 & m_1 & m_3 \end{pmatrix} \langle a_{\ell_1 m_1} a_{\ell_1 m_1} a_{\ell_1 m_1} \rangle, \tag{3.23}$$

where the matrix is the Wigner 3-j symbol (Komatsu & Spergel 2001). $B_{\ell_1\ell_2\ell_3}$ is averaged over m with the assumption of rotational invariance. In the same manner, the Fourier equivalent of the four-point function, trispectrum, is a standard tool used to capture the quadratic features in CMB and other data sets (Hu 2001). Recently, Philcox (2023a,b) has developed pipelines to compute the power, bi- and tri-spectra for scalar and tensor fields defined on a sphere by taking into account various real-life data challenges such as instrumental effects and masking[†].

Morphological statistics such as scalar Minkowski functionals (MFs) (Minkowski 1903; Tomita 1986) are computed in real space and contain information on all orders of N-point functions. This makes them particularly advantageous over Fourier space methods such as the bispectrum and trispectrum in searches for non-Gaussianity in situations where the non-Gaussian properties are a priori unknown and/or when the field is highly non-Gaussian. According to Hadwiger's theorem, any morphological descriptors in d-dimensional space can be represented in terms of $d+1$ MFs (Hadwiger 1959). In $2d$, there are three MFs: area-fraction, contour length and genus, denoted as V_0, V_1 and V_2, respectively.

MFs have been extensively used in CMB cosmology for measuring the primordial non-Gaussianity (Mecke et al. 1994; Schmalzing & Buchert 1997; Novikov et al. 2000; Chingangbam & Park 2009; Chingangbam et al. 2017a; Planck Collaboration et al. 2016c; Buchert et al. 2017). They have also found application in finding residual foreground signals in the cleaned WMAP CMB maps (Chingangbam & Park 2013), and to understand the properties of Galactic synchrotron radiation (Rana et al. 2018). Related topological quantities like Betti numbers were also employed

[†]The implementation is publicly available as PolyBin package.

to understand the morphology of the interstellar turbulence (Makarenko et al. 2018). Scalar MFs can be generalized as tensors, which are called Minkowski tensors (MTs). They carry shape information and can be used to study the alignment of structures (Schröder-Turk et al. 2010; Ganesan & Chingangbam 2017). The rank-2 translation invariant MTs contain the scalar MFs as their traces. They have been developed to study the random fields defined on curved $2d$ manifolds, specifically, spaces of constant curvature such as the sphere (Chingangbam et al. 2017b). Ganesan & Chingangbam (2017); Joby et al. (2019); Kochappan et al. (2021) have used MTs to probe the departure from SI of the CMB. Similarly, they are used to study how weak lensing affects the CMB maps (Goyal et al. 2020; Goyal & Chingangbam 2021), the time evolution of the fields of the EoR (Kapahtia et al. 2018, 2019; Kapahtia et al. 2021), and matter density evolution and redshift space distortion (Appleby et al. 2018b, 2022).

In the next section, a detailed discussion of the mathematics of MFs in terms of their tensor generalization, MTs, is given. We also discuss how the properties of random fields can be extracted by making use of these quantities.

3.3 Morphological tools - Minkowski Functionals

Tensorial Minkowski Functionals (also referred to as Minkowski tensors) are geometrical quantities that encode the morphological properties of structures. They are defined on flat space. For analysing all-sky data, such as the CMB map, we need to analyse it on the sphere. The generalization of MTs to curved space was given in Chingangbam et al. (2017b). We briefly outline the notations and the method described there, analytic expressions and methods for their numerical calculation.

We begin with the definition of tensorial and scalar Minkowski functionals in a unified way. Let us first consider a closed curve, denoted by C, on the unit sphere, $\mathcal{S}^2$. The rank-2 Minkowski tensors (MTs) denoted by $\mathcal{W}_k$, with $k = 0, 1, 2$, are defined to be (Chingangbam et al. 2017b),

$$\mathcal{W}_0 = \frac{B_0}{2}\,\mathbb{I}\int \mathrm{d}a, \quad \mathcal{W}_1 = B_1\int_C \hat{T}\otimes\hat{T}\,\mathrm{d}l, \quad \mathcal{W}_2 = \frac{B_2}{2\pi}\int_C \hat{T}\otimes\hat{T}\,\kappa\,\mathrm{d}l. \tag{3.24}$$

In the above, $\mathbb{I}$ is the 2×2 identity matrix, and $\otimes$ denotes the symmetric tensor product given by $\hat{T}\otimes\hat{T} = \frac{1}{2}\big(\hat{T}_i\hat{T}_j + \hat{T}_j\hat{T}_i\big)$. κ is the geodesic curvature, which is defined as the derivative of the tangent vector at each point on the curve. It explains how much the curve deviates from a geodesic at each point. The coefficients B_k are constants which we leave unspecified here so as to focus on the geometrical meaning of $\mathcal{W}_k$. The traces of $\mathcal{W}_k$ give the three scalar MFs denoted by V_k, as given below,

$$V_0 = B_0\int \mathrm{d}a, \quad V_1 = B_1\int_C \mathrm{d}l, \quad V_2 = \frac{B_2}{2\pi}\int_C \kappa\,\mathrm{d}l. \tag{3.25}$$

V_0 is proportional to the area enclosed by the curve and V_1 to the perimeter of the curve.

According to the Gauss-Bonnet theorem, V_2, the integrated curvature along the boundary, is equal to the topological quantity Euler characteristic (χ), or equivalently the genus[‡] (g, $\chi = 2 - 2g$). However, for curved manifolds, the generalized Gauss-Bonnet theorem expresses χ (or g) in terms of the linear combinations of V_ks and thus, χ is not exactly V_2. Consequently, for a single curve, V_2 equals B_2 if the space is flat, making it a topological quantity. In the case of curved spaces, it is equal to B_2 plus a term that is proportional to V_0. In our analysis, we compute V_2 on the sphere, and therefore, it is not strictly the genus. Nevertheless, for ease of reference, we still use the term genus for V_2 throughout the thesis.

[‡]It differs from the mathematical definition of the genus by one.

In short, the Minkowski tensors combine the information contained in the scalar MFs along with new information on the shape of structures encoded in $\mathcal{W}_1$.

Next, we consider smooth random fields on $\mathcal{S}^2$. We represent the field with the symbol u. The boundaries of a level or excursion set of the field, $u = \nu$, where ν denotes the chosen field level or threshold value, form smooth closed curves. Let Q_ν denote the set of points in the excursion set and ∂Q_ν denote its boundary. The subscript is used to remind us that the excursion set depends on ν. Then, we can generalize the definition of $\mathcal{W}_k$ to the excursion set by the following,

$$\mathcal{W}_0(\nu) = \frac{B_0}{2}\,\mathbb{I}\int_{Q_\nu} \mathrm{d}a, \quad \mathcal{W}_1(\nu) = B_1 \int_{\partial Q_\nu} \hat{T}\otimes\hat{T}\,\mathrm{d}l, \quad \mathcal{W}_2(\nu) = \frac{B_2}{2\pi}\int_{\partial Q_\nu} \hat{T}\otimes\hat{T}\,\kappa\,\mathrm{d}l. \tag{3.26}$$

$\mathcal{W}_1$, the tensorial analogue of the contour length V_1, encodes the information of the existence of any particular alignment for the structures. If the structures in the excursion set do not exhibit any special orientation, then $\mathcal{W}_1$ can be expressed as a constant times the identity matrix. Let $\overline{\mathcal{W}}_1$ denote the sum over the $\mathcal{W}_1$ for all the curves in a given threshold. Let Λ_1 and Λ_2 be its eigenvalues. Then, we can define the parameters α as,

$$\alpha = \frac{\Lambda_1}{\Lambda_2} \qquad\qquad \Lambda_1 < \Lambda_2. \tag{3.27}$$

α gives the measure of the relative alignment or the deviation from SI of the field. $\alpha = 1$ is obtained when $\overline{\mathcal{W}}_1$ is proportional to the identity matrix, and it implies that the field preserves SI, whereas deviation from unity indicates the presence of alignment for the structures.

Effect of translation of field values on MFs and MTs: For any field, translating the field values as $u \to u - a$, where a is some constant, merely translates the field levels, but does not change the geometrical and topological properties of the field. Subtracting the mean value of the field is such an operation.

Effect of scaling of field values on MFs and MTs: A rescaling $u \to u/a$, where $a > 0$ is some constant, also remaps the field levels. However, this transformation does not alter the topology and the geometry of the excursion sets. Consequently, it is a common practice to rescale the field using its standard deviation before calculating the Minkowski functionals.

Before we proceed, a discussion regarding our notation is in order. The scalar and tensorial MFs are usually expressed per unit area in the form of densities when applied to random fields in cosmology. We use the same symbols $\mathcal{W}_k$ and V_k, with $k = 0, 1, 2$, to denote the densities by including the area factor in the coefficients. In the next section, in place of B_k, we will use coefficients A_k, which include the area factors and whose values are commonly used in the literature. Thus, V_0 gives the area fraction of the excursion set, V_1 the total boundary contour length per unit area, and V_2 the genus per unit area at each field threshold. Similarly, $\mathcal{W}_1$ denotes the contour MT per unit area.

3.3.1 Analytical formulation of scalar MFs for mildly non-Gaussian fields

Let u denote a generic Gaussian random field having zero mean and standard deviation σ_0, and let ν now denote threshold values of the normalized field u/σ_0. Then the expectation values of the scalar MFs per unit area, as functions of the threshold ν, are given by Tomita (1986),

$$V_k(\nu) = A_k \, e^{-\nu^2/2} v_k^G(\nu), \tag{3.28}$$

where $k = 0, 1, 2$ and the coefficients A_k are

$$A_k = \frac{1}{(2\pi)^{(k+1)/2}} \frac{\omega_2}{\omega_{2-k}\omega_k} \left(\frac{\sigma_1}{\sqrt{2}\sigma_0}\right)^k. \tag{3.29}$$

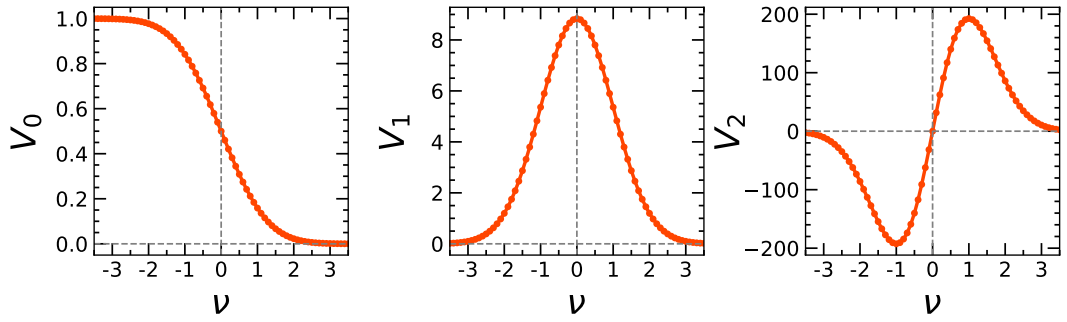

FIGURE 3.3: V_k versus ν for a Gaussian random field, according to eq. (3.28).

$\sigma_1 \equiv \sqrt{\langle |\nabla u|^2 \rangle}$, where ∇u is the gradient of the field. The numerical factors are $\omega_0 = 1,\ \omega_1 = 2,\ \omega_2 = \pi$. The functions v_k^G are

$$v_0^G(\nu) = \sqrt{\frac{\pi}{2}}\, e^{\nu^2/2}\, \mathrm{erfc}\left(\frac{\nu}{\sqrt{2}}\right), \tag{3.30}$$

$$v_1^G = 1, \tag{3.31}$$

$$v_2^G(\nu) = \nu. \tag{3.32}$$

The superscript 'G' stands for Gaussian. Figure 3.3 shows the variation of the three MFs (V_k) as a function of threshold values (ν) for a Gaussian field.

For mildly non-Gaussian fields, again denoted by u, the scalar MFs can be expressed in the same form as eq. (3.28), but with v_k^G replaced by v_k, which can be expanded in powers of the standard deviation σ_0 (Matsubara 2010) as,

$$v_k = v_k^G + v_k^{(1)}\sigma_0 + v_k^{(2)}\sigma_0^2 + \mathcal{O}(\sigma_0^3). \tag{3.33}$$

The first-order non-Gaussian terms are given in terms of three skewness cumulants defined in eq. (3.17) as,

$$v_0^{(1)}(\nu) = \frac{S_0}{6} H_2(\nu), \tag{3.34}$$

$$v_1^{(1)}(\nu) = \frac{S_0}{6} H_3(\nu) - \frac{S_1}{4} H_1(\nu), \tag{3.35}$$

$$v_2^{(1)}(\nu) = \frac{S_0}{6} H_4(\nu) - \frac{S_1}{2} H_2(\nu) - \frac{S_2}{2} H_0(\nu). \tag{3.36}$$

$H_n(\nu)$ are the Hermite polynomials.

The second-order terms are given in terms of four kurtosis cumulants given in eq. (3.18) as,

$$v_0^{(2)}(\nu) = \frac{S_0^2}{72}H_5(\nu) + \frac{K_0}{24}H_3(\nu), \tag{3.37}$$

$$v_1^{(2)}(\nu) = \frac{S_0^2}{72}H_6(\nu) + \frac{K_0 - S_0S_1}{24}H_4(\nu) - \frac{1}{12}\left(K_1 + \frac{3}{8}S_1^2\right)H_2(\nu) - \frac{K_3}{8}, \tag{3.38}$$

$$v_2^{(2)}(\nu) = \frac{S_0^2}{72}H_7(\nu) + \frac{K_0 - 2S_0S_1}{24}H_5(\nu) - \frac{1}{6}\left(K_1 + \frac{1}{2}S_0S_2\right)H_3(\nu) - \frac{1}{2}\left(K_2 + \frac{1}{2}S_1S_2\right)H_1(\nu). \tag{3.39}$$

Alternatively, analytic expressions for MFs for mildly non-Gaussian fields can be obtained using the Gram-Charlier expansion of the joint probability distribution for the field and its derivatives (Gay et al. 2012; Codis et al. 2013).

To measure the non-Gaussian deviation of a given field, we define

$$\Delta V_k = V_k - V_k^G, \tag{3.40}$$

where V_k^G is the MFs corresponding to a Gaussian field. In the case of MFs for a mildly non-Gaussian field, ΔV_k isolates the non-Gaussian perturbative terms as in eq. (3.33). This quantity is often calculated by normalizing with the amplitude of V_k^G.

Next, let us examine the behaviour of MFs for mildly non-Gaussian fields. We consider the local-type $f_{\rm NL}$ and $g_{\rm NL}$ non-Gaussian CMB maps in the Sachs-Wolfe (SW) limit. In this limit, $\Delta T_{\rm SW} = -\Phi/3$ and using eq. (3.16),

$$\frac{\Delta T_{\rm SW}}{T} = \frac{\Delta T_{\rm G}}{T} - 3f_{\rm NL}\left(\frac{\Delta T_{\rm G}}{T}\right) + 9g_{\rm NL}\left(\frac{\Delta T_{\rm G}}{T}\right)^2 + ..., \tag{3.41}$$

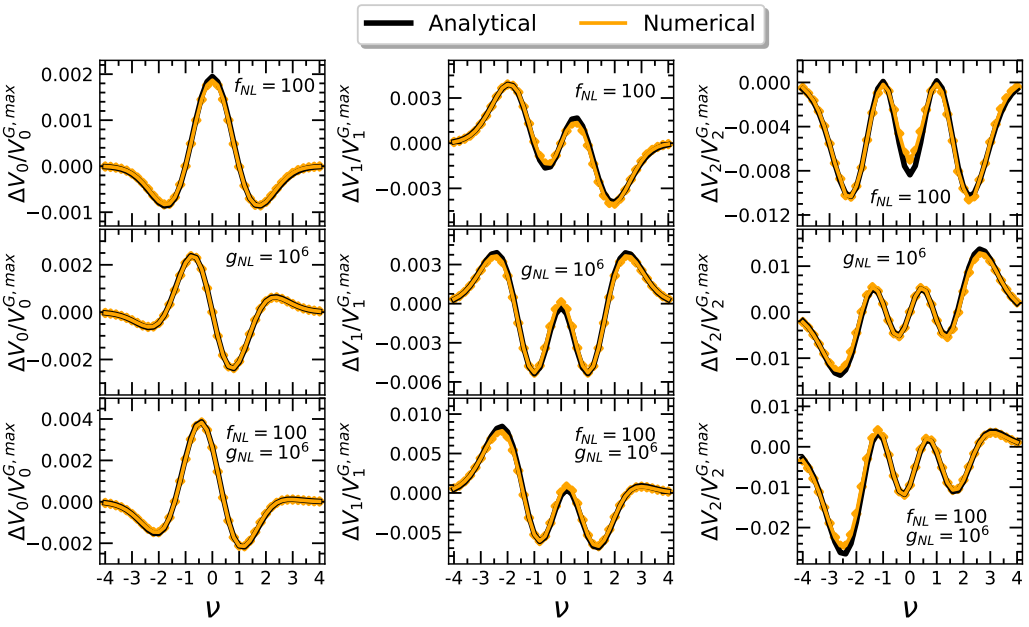

FIGURE 3.4: The normalized non-Gaussian deviations (ΔV_k) for local type primordial non-Gaussianity for the cases $f_{\rm NL} = 100$, $g_{\rm NL} = 0$ (top), $f_{\rm NL} = 0$, $g_{\rm NL} = 10^6$ (middle) and $f_{\rm NL} = 0$, $g_{\rm NL} = 10^6$ (bottom) for the three Minkowski functionals. The black lines are the results obtained using the analytic formulae (eq. (3.33)), and the orange lines are the results from the numerical calculations.

where $\Delta T_{\rm G}/T$ is the Gaussian CMB map obtained using the power spectrum,

$$\frac{\ell(\ell+1)}{2\pi} C_\ell^{\rm SW} = 10^{-10} \tag{3.42}$$

for $\ell < 750$ and zero otherwise. We generate 1000 Gaussian and non-Gaussian maps with `healpix`[§] resolution, $N_{\rm side} = 512$ for three cases: only $f_{\rm NL}$, only $g_{\rm NL}$ and $f_{\rm NL}$ plus $g_{\rm NL}$. We take $f_{\rm NL} = 100$ and $g_{\rm NL} = 10^6$, for which the non-Gaussian terms are of comparable amplitudes.

Scalar MFs are computed numerically for these maps using the method outlined in the next section. Also, we obtain MFs using the analytical formula given in eq. (3.33) in terms of the skewness and kurtosis values of the maps. ΔV_ks (as defined in eq. (3.40)) are then calculated for both analytical and numerical MFs and are shown in figure 3.4. We find good agreement between the numerical

[§] https://healpix.sourceforge.io/

calculations and analytical results. We see that for different non-Gaussian types, MFs follow characteristic shapes. This shows the potential of MFs in distinguishing the nature of non-Gaussianity in different fields.

3.3.2 Computing scalar and tensorial Minkowski functionals

3.3.2.1 Method 1 - using field derivatives

Given the field u, we rescale it to make it mean-free and unit standard deviation. MFs can be computed at each threshold value ν in terms of u and its derivatives. The line integrals in eq. (3.26) can be converted into surface integrals. In terms of the field u, V_0 is given as,

$$\mathrm{V}_0(\nu) = \int_{S^2} \Theta(u-\nu)\,\mathrm{d}a, \tag{3.43}$$

where Θ is the step function. Using $\hat{T}_i = \epsilon_{ij}\frac{u_{;j}}{|\nabla u|}$, where ϵ is the two dimensional anti-symmetric Levi-Civita tensor and $u_{;j}$ the j-th component of the covariant derivative, we get

$$\overline{\mathcal{W}}_1 = \frac{1}{4}\int_{S^2} \delta(u-\nu)\,\frac{1}{|\nabla u|}\,\mathcal{M}\,\mathrm{d}a, \tag{3.44}$$

$$\overline{\mathcal{W}}_2 = \frac{1}{2\pi}\int_{S^2} \delta(u-\nu)\,\frac{\kappa}{|\nabla u|}\,\mathcal{M}\,\mathrm{d}a. \tag{3.45}$$

The expression for κ is

$$\kappa = \frac{2u_{;1}u_{;2}u_{;12} - u_{;1}^2 u_{;22} - u_{;2}^2 u_{;11}}{|\nabla u|^3} \tag{3.46}$$

and $\mathcal{M}$ is,

$$\mathcal{M} = \begin{bmatrix} u_{;2}^2 & -u_{;1}u_{;2} \\ -u_{;1}u_{;2} & u_{;1}^2 \end{bmatrix}$$

For a field in discretized space, the δ-function is taken as $\delta(u-\nu) = 1/\Delta\nu$, if $u \in [\nu - \Delta\nu/2, \nu + \Delta\nu/2]$ and zero otherwise. $\Delta\nu$ is the bin size. Using this method, we compute V_0, $\mathcal{W}_1$ and $\mathcal{W}_2$. From the eigenvalues of $\mathcal{W}_1$, we calculate α. Further, by taking the traces of $\overline{\mathcal{W}}_1$ and $\overline{\mathcal{W}}_2$, we obtain V_1 and V_2. All these quantities are then divided by the total area to get their corresponding densities. The δ function approximation is shown to have inherent numerical error in Lim & Simon (2012). This error will be present in the calculations of $\mathcal{W}_1$ and $\mathcal{W}_2$, and in V_1 and V_2. For comparison, we will compute V_1 and V_2 using the geometric method, which is described in the next section. It was shown in Goyal et al. (2020) that the numerical errors in the two eigenvalues of $\mathcal{W}_1$ are comparable and, hence, get cancelled out when computing α. Therefore, the calculation of α is unbiased.

3.3.2.2 Method 2 - geometric method for scalar MF estimation

The geometric estimation of MFs is carried out by first identifying the structures from the excursion sets at different field thresholds. In the following, we briefly outline the method followed by the `CND_REG2D` (Ducout et al. 2013) code that we have used. For more details, we recommend checking the original papers.

The excursion sets are obtained as a binary field by identifying pixels where the fields have values below or above the chosen threshold ν. The algorithm identifies each structure (connected region or hole) by marking boundary pixels as different from the pixels in the inner part of the structures. The total number of pixels included in each structure will constitute the first MF, area fraction V_0. Next, the genus, V_2, is obtained by computing the vertices of the pixel grid at the boundaries of the structures. It uses the Gauss-Bonnet theorem, which relates the genus to

the integration of the curvature along the boundary. As topological properties are invariant under the continuous transformation of the boundary, summing the vertices with appropriate weights will give the genus of the region. The estimation of the next MF, the contour length, V_1, is a bit more involved. The length of the perimeter of the polygon formed by the boundary gives V_1. Due to the pixelated form, the error in the estimation of the length can be large. In order to control the error, interpolation of field values between adjoining boundary pixels is performed so as to smoothen the pixelated boundary and obtain a sufficiently accurate estimate of the length of the polygon.

Chapter 4

Minkowski Functionals for Composite Smooth Random Fields*

The morphology of smooth random fields encodes a vast amount of valuable information concerning the underlying physical processes that generate these fields. In the context of cosmology, various geometrical and topological statistical quantities have been proposed in the literature to quantify the morphology of cosmological random fields and extract physical information. As discussed in the previous chapter, Minkowski functionals (MFs) are undeniably one of the most used statistical tools that have found wide application to investigate a myriad of physical characteristics in cosmological fields.

In real-world scenarios, any observed data always contains noise apart from the true signal and may be contaminated by other signals. It is important to systematically review and quantify how the presence of secondary fields (including

*The chapter is based on the work which is undergoing revision for publication. The pre-print is available as Chingangbam & Rahman (2023).

noise and other contaminating signals) impacts the morphological and statistical properties of the underlying signal of interest. With this motivation, this chapter extends the formulae derived in Matsubara & Kuriki (2020) to *composite fields*, which are the summation of two different fields.

We obtain the analytic expressions of MFs for composite fields in $2d$ in terms of their constituent fields and apply the formulae to two toy examples of composite fields. The first instance involves adding a Gaussian CMB temperature map with a Gaussian noise map, while in the second case, the field is a combination of a non-Gaussian CMB map and a Gaussian noise map. This analysis is motivated by our previous research focused on understanding the statistical nature of Galactic foreground emissions (Rahman et al. 2021; Rahman et al. 2022), which form the basis for the forthcoming two chapters, and how the cleaned CMB maps are impacted by the contamination from residual foregrounds (Chingangbam & Park 2013).

Chapter organization is as follows. Section 4.1 contains a brief overview of the analytical formulae for ensemble expectations of MFs for mildly non-Gaussian fields for general dimension d. Section 4.2 presents our extension of the formulae to composite fields, expressing the MFs for the composite field in terms of the MFs of constituent fields. As an application of the formulae, we derive the bias introduced by noise on the morphology and non-Gaussianity of CMB temperature maps. This is discussed in section 4.3. In section 4.4, we include a summary of our results and discussion.

4.1 Review of MFs for mildly non-Gaussian field

For a given field f, we define the following spectral parameters,

$$\sigma_0^2 \equiv \langle f^2 \rangle, \quad \sigma_1^2 \equiv \langle |\nabla f|^2 \rangle, \quad \sigma_2^2 = \langle (\nabla^2 f)^2 \rangle, \quad r_c \equiv \sigma_0/\sigma_1. \tag{4.1}$$

We take the mean of the field f as zero so as to simplify the discussion. It is easy to generalize the discussions presented here to fields with non-zero means.

If the field f is non-Gaussian, the higher-order connected cumulants are non-zero. The generalized skewness cumulants are defined (Matsubara & Kuriki 2020) as

$$\begin{aligned} S^{(0)} &= \frac{\langle f^3 \rangle_c}{\sigma_0^4}, \\ S^{(1)} &= \frac{3}{2}\frac{\langle f|\nabla f|^2 \rangle_c}{\sigma_0^2 \sigma_1^2}, \\ S^{(2)} &= \frac{-3d}{2(d-1)}\frac{\langle |\nabla f|^2 \nabla^2 f \rangle_c}{\sigma_1^4}. \end{aligned} \tag{4.2}$$

The generalized kurtosis cumulants are

$$\begin{aligned} K^{(0)} &= \frac{\langle f^4 \rangle_c}{\sigma_0^6}, \\ K^{(1)} &= 2\frac{\langle 2f^2 |\nabla f|^2 \rangle_c}{\sigma_0^4 \sigma_1^2}, \\ K_1^{(2)} &= \frac{-2d}{(d+2)(d-1)}\frac{(d+2)\langle f|\nabla f|^2 \nabla^2 f \rangle_c + \langle |\nabla f|^4 \rangle_c}{\sigma_0^2 \sigma_1^4}, \\ K_2^{(2)} &= \frac{-2d}{(d+2)(d-1)}\frac{(d+2)\langle f|\nabla f|^2 \nabla^2 f \rangle_c + d\langle |\nabla f|^4 \rangle_c}{\sigma_0^2 \sigma_1^4}, \\ K^{(3)} &= \frac{2d^2}{(d-1)(d-2)}\frac{\langle |\nabla f|^2 (\nabla^2 f)^2 \rangle_c - \langle |\nabla f|^2 f_{ij} f_{ij} \rangle_c}{\sigma_1^6}, \end{aligned} \tag{4.3}$$

where d is the dimension of the space. The subscript c on the angle brackets implies that these quantities are connected cumulants[†]. For $d = 1, 2$, $K^{(3)}$ is

[†]These cumulant definitions are for any general d-dimensional manifold. They are slightly different from the skewness-kurtosis definitions given in the previous chapter, which are solely

undetermined, but it does not appear in the analytical expressions for MFs in these dimensions. For a mean-free field, the third-order cumulants are the same as the third-order moments. Further, the fourth-order cumulants are given in terms of the moments (Matsubara & Kuriki 2020) as,

$$\begin{aligned}
\langle f^4\rangle_c &= \langle f^4\rangle - 3\sigma_0^4, \\
\langle f^2|\nabla f|^2\rangle_c &= \langle f^2|\nabla f|^2\rangle - \sigma_0^2\sigma_1^2, \\
\langle f|\nabla f|^2\nabla^2 f\rangle_c &= \langle f|\nabla f|^2\nabla^2 f\rangle + \sigma_1^4, \\
\langle|\nabla f|^4\rangle_c &= \langle|\nabla f|^4\rangle - \frac{d+2}{2}\sigma_1^4, \\
\langle|\nabla f|^2(\nabla^2 f)^2,\rangle_c &= \langle|\nabla f|^2(\nabla^2 f)^2\rangle - \sigma_1^2\sigma_2^2, \\
\langle|\nabla f|^2 f_{ij}f_{ij}\rangle_c &= \langle|\nabla f|^2 f_{ij}f_{ij}\rangle - \sigma_1^2\sigma_2^2.
\end{aligned} \tag{4.4}$$

Here f_{ij} are derivatives with respect to i^{th} and j^{th} coordinates for any manifold $\mathcal{M}$, with $i, j = 1, 2, ..., d$.

As demonstrated by Matsubara (2003, 2010); Matsubara & Kuriki (2020), analytic formulae for the ensemble expectation of MFs per unit volume for mildly non-Gaussian fields in d-dimension can be expressed as perturbative expansions in

for $2d$ and were based on Matsubara (2010). In this chapter, we will use these generalized definitions, while in the upcoming chapters, we will switch back to the previous $2d$ definitions.

powers of σ_0. Keeping up to σ_0^2 order, the expressions are given by

$$\begin{aligned}\bar{V}_k^{(d)}(\nu) \;\simeq\; & A_k e^{-\nu^2/2}\Bigg[H_{k-1}(\nu) \\ & +\left\{\frac{1}{6}S^{(0)}H_{k+2}(\nu)+\frac{k}{3}S^{(1)}H_k(\nu)+\frac{k(k-1)}{6}S^{(2)}H_{k-2}(\nu)\right\}\sigma_0 \\ & +\Bigg\{\frac{1}{72}(S^{(0)})^2H_{k+5}(\nu)+\left(\frac{1}{24}K^{(0)}+\frac{k}{18}S^{(0)}S^{(1)}\right)H_{k+3}(\nu) \\ & +k\left(\frac{1}{8}K^{(1)}+\frac{k-1}{36}S^{(0)}S^{(2)}+\frac{k-2}{18}(S^{(1)})^2\right)H_{k+1}(\nu) \\ & +k\left(\frac{k-2}{16}K_1^{(2)}+\frac{k}{16}K_2^{(2)}+\frac{(k-1)(k-4)}{18}S^{(1)}S^{(2)}\right)H_{k-1}(\nu) \\ & +k(k-1)(k-2)\left(\frac{1}{24}K^{(3)}+\frac{k-7}{72}(S^{(2)})^2\right)H_{k-3}(\nu)\Bigg\}\sigma_0^2+\mathcal{O}(\sigma_0^3)\Bigg],\end{aligned} \tag{4.5}$$

where $k = 0, 1, \ldots, d+1$. $H_k(\nu)$ are the (probabilist) Hermite polynomials, and $H_{-1}(\nu) = \sqrt{\frac{\pi}{2}}e^{\nu^2/2}$. The amplitude A_k is given by

$$A_k = \frac{1}{(2\pi)^{(k+1)/2}}\frac{\omega_d}{\omega_{d-k}\omega_k}\left(\frac{\sigma_1}{\sqrt{d}\sigma_0}\right)^k, \tag{4.6}$$

where the factors ω_n for integer $n \geq 0$ are given by $\omega_n = \pi^{n/2}/\Gamma(n/2+1)$. So, we have $\omega_0 = 1,\ \omega_1 = 2,\ \omega_2 = \pi$, $\omega_3 = 4\pi/3$, and so on.

4.2 MFs for $2d$ composite fields

We now focus on composite fields, which are sums of two fields, on $2d$ manifolds. It is straightforward to extend this formalism to sums of more than two fields. Consider the field f given as $f = u + v$, where u and v are either Gaussian or mildly non-Gaussian smooth random fields. Here, our goal is to convert the

formulae for the MFs of f into MFs of the component fields u and v. This will enable us to better understand the respective contributions of these constituent fields. Afterwards, we can explore specific cases and apply this approach to several intriguing physical examples. For physical applications, we take u to be the *signal* of interest, whereas v is either noise or a contaminating field. We will use a superscript, 'f, u, v', for the quantities $\sigma_0, \sigma_1, r_c, S^{(i)}, K^{(i)}$ to specify the field.

Alongside the spectral parameters and the typical size of structures for u, v, and f (as defined in eq. (4.1)), it is essential to introduce the cross-correlation of u and v, as well as the cross-correlation of their first derivatives, which we denote by,

$$c^{uv} = \frac{\langle uv \rangle}{\sigma_0^u \sigma_0^v}, \quad c_1^{uv} = \frac{\langle \nabla u . \nabla v \rangle}{\sigma_1^u \sigma_1^v}. \tag{4.7}$$

Let us also denote,

$$\epsilon = \frac{\sigma_0^v}{\sigma_0^u}, \quad p = \frac{r_c^u}{r_c^v} = \epsilon^{-1} \frac{\sigma_1^v}{\sigma_1^u}. \tag{4.8}$$

Note that in the expression for ϵ, the numerator contains v, whereas, in the expression for p, the numerator contains u. ϵ compares the size of fluctuations of the field values of u and v, while p compares the size of spatial fluctuations of u and v. When considering u as the desired physical signal and v as a noise field, ϵ can be seen as the inverse of the signal-to-noise ratio between the two fields. As per the definition, the four parameters have the following specified ranges,

$$0 < \epsilon < \infty, \quad 0 < p < \infty, \quad |c^{uv}| \leq 1, \quad |c_1^{uv}| \leq 1, \tag{4.9}$$

The relative significance of the fields u and v in the MFs of their composite field is determined by these four parameters $\epsilon, p, c^{uv}, c_1^{uv}$.

The amplitude A_k, and skewness and kurtosis quantities are expressed in terms of ϵ, p, c^{uv} and c_1^{uv} using the following factors,

$$\left(\sigma_0^f\right)^2 = \left(\sigma_0^u\right)^2 \left(1+\epsilon^2+2\epsilon c^{uv}\right), \tag{4.10}$$

$$\left(\sigma_1^f\right)^2 = \left(\sigma_1^u\right)^2 \left(1+\epsilon^2 p^2+2\epsilon p c_1^{uv}\right). \tag{4.11}$$

Next, we analyse the expressions for the amplitude, skewness and kurtosis terms that go inside the formulae for MFs, one by one.

4.2.1 Amplitude of MFs

Given that the amplitude A_k^f of MFs is proportional to $(r_c^f)^{-k}$, our job is only to express r_c^f in terms of ϵ, p, c^{uv} and c_1^{uv}. When $k=2$, corresponding to V_2, the expression becomes,

$$\left(r_c^f\right)^{-2} = \left(\frac{\sigma_1^f}{\sigma_0^f}\right)^2 = \left(r_c^u\right)^{-2} \left[\frac{1+\epsilon^2 p^2+2\epsilon p c_1^{uv}}{1+\epsilon^2+2\epsilon c^{uv}}\right]. \tag{4.12}$$

Similarly, the expressions for other MFs can be obtained using the corresponding powers of k.

Let us begin our discussions with the special case where u and v are uncorrelated, with $c^{uv}=0$ and $c_1^{uv}=0$. Eq. (4.12) then simplifies as,

$$\left(r_c^f\right)^{-2} = \left(r_c^u\right)^{-2} \left[\frac{1+\epsilon^2 p^2}{1+\epsilon^2}\right]. \tag{4.13}$$

This means that when both $\epsilon \ll 1$ and $p \lesssim \mathcal{O}(1)$, we get $\left(r_c^f\right)^{-2} \simeq \left(r_c^u\right)^{-2}$, which is as expected. This is the limiting case when the standard deviation of the v field is much lower than u, and the typical size of its structures is larger than or roughly the same as that of u.

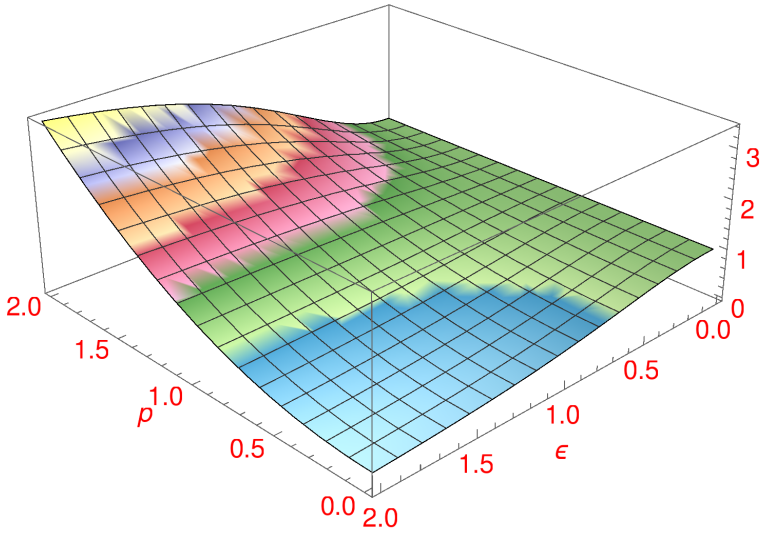

FIGURE 4.1: Plot of the factor $B(\epsilon, p) = (1+\epsilon^2 p^2)/(1+\epsilon^2)$ that relates $\left(r_c^f\right)^{-2}$ and $(r_c^u)^{-2}$ in eq. (4.12). In the green regions, $B(\epsilon, p)$ takes values ~ 1. Blue regions are where it has values less than one, while the other colour bands towards the top left denote regions where the values are larger than one.

For practical scenarios, it is more interesting to investigate intermediate values of ϵ and p in the vicinity of one. For these values, in order to understand how $\left(r_c^f\right)^{-2}$ gets affected relative to $(r_c^u)^{-2}$, it is instructive to visualize the factor $B(\epsilon, p) = (1 + \epsilon^2 p^2)/(1 + \epsilon^2)$ that connects both the quantities in eq. (4.12). Figure 4.1 shows a plot of B as a function of ϵ and p. It is noteworthy to observe the following different cases as per the values of ϵ and p.

1. If $\epsilon = 1$, with p unconstrained, then we have

$$\left(r_c^f\right)^{-2} = \frac{1}{2}\left(\frac{1}{(r_c^u)^2} + \frac{1}{(r_c^v)^2}\right). \tag{4.14}$$

   This is just the average of the amplitudes of the two fields.

2. If $p = 1$, with ϵ unconstrained, then $r_c^f = r_c^u = r_c^v$. In this case, the two fields contain structures of equal sizes. This indicates that if the spatial size of structures in both fields u and v, normalized by their respective standard

deviations, are identical, then the field f will also exhibit structures of the same size, irrespective of the value of ϵ. Consequently, the amplitudes of the MFs will remain the same.

3. If $p < 1$ with ϵ unconstrained, then we get $\left(r_c^f\right)^{-2} < (r_c^u)^{-2}$. In this case, the amplitudes of the MFs of f will be less compared to that of the u field.

   For $\epsilon < 1$, expanding the denominator to ϵ^2 order, we get

$$\left(r_c^f\right)^{-2} \simeq (r_c^u)^{-2}\left[1 - \epsilon^2(1-p^2)\right], \tag{4.15}$$

   while for $\epsilon > 1$ we have

$$\left(r_c^f\right)^{-2} \simeq (r_c^u)^{-2}\left(1/\epsilon^2 + p^2\right). \tag{4.16}$$

4. If $p > 1$ with ϵ unconstrained, then we get $\left(r_c^f\right)^{-2} > (r_c^u)^{-2}$. In this case, the amplitudes of the MFs of f will show a rise in comparison to those of the u field.

   For $\epsilon < 1$ we get

$$\left(r_c^f\right)^{-2} \simeq (r_c^u)^{-2}\left[1 + \epsilon^2 p^2\right], \tag{4.17}$$

   while for $\epsilon > 1$ we get

$$\left(r_c^f\right)^{-2} \simeq (r_c^u)^{-2} p^2 = (r_c^v)^{-2}. \tag{4.18}$$

These cases tell us that the impact of the v field on the amplitudes of the MFs of the composite field will be minimal only when $p \sim 1$, or when $\epsilon \to 0$ and $\epsilon p \to 0$.

For the general case where there exist correlations between u and v fields, the hike or fall of the amplitudes of the MFs of the composite field relative to those of u will be determined by whether the factor $(1 + \epsilon^2 p^2 + 2\epsilon p c_1^{uv})/(1 + e^2 + 2\epsilon c^{uv})$ is

equal to, greater, or less than one. A positive correlation ($c^{uv} > 0$) decreases the amplitude, whereas negative correlations result in raising it. In contrast, when there is a positive correlation in the first derivatives ($c_1^{uv} > 0$), the tendency is for the amplitude to increase, and conversely for the negative correlation.

4.2.2 Generalized skewness and kurtosis

Next, we express the generalized skewness and kurtosis cumulants of the composite field in terms of the cumulants of u and parameters ϵ, p. To simplify the discussions, we assume that u and v are uncorrelated.

Consider u as the mildly non-Gaussian field and v as the Gaussian field. The non-Gaussian deviations of the MFs of f arise from u. We then present the generalized skewness cumulants of f in terms of the corresponding cumulants of u and ϵ, p as,

$$S^{(0)\,f}\sigma_0^f = S^{(0)\,u}\sigma_0^u \frac{1}{(1+\epsilon^2)^{3/2}}, \tag{4.19}$$

$$S^{(1)\,f}\sigma_0^f = S^{(1)\,u}\sigma_0^u \frac{1}{(1+\epsilon^2)^{1/2}(1+\epsilon^2 p^2)}, \tag{4.20}$$

$$S^{(2)\,f}\sigma_0^f = S^{(2)\,u}\sigma_0^u \frac{(1+\epsilon^2)^{1/2}}{(1+\epsilon^2 p^2)^2}. \tag{4.21}$$

Eqs. (4.19) and (4.20) show that the factors that constitute ϵ, p result in *always decreasing* the non-Gaussian contribution from $|S^{(0)}|$ and $|S^{(1)}|$ of u. On the other hand, the non-Gaussian contribution from $|S^{(2)}|$ of u increases for $p < 1$, and decreases if $p > 1$. These relative changes of the terms involving $S^{(0)}$, $S^{(1)}$ and $S^{(2)}$ will alter the shapes of non-Gaussian deviations of the MFs of f when compared with u.

The generalized kurtosis cumulants are more complex because of the extra terms related to the spectral factors. The generalized kurtosis cumulants are,

$$K^{(0)\,f}(\sigma_0^f)^2 = K^{(0)\,u}(\sigma_0^u)^2 \frac{1}{(1+\epsilon^2)^2} - \frac{6\epsilon^2}{(1+\epsilon^2)^3}, \tag{4.22}$$

$$K^{(1)\,f}(\sigma_0^f)^2 = K^{(1)\,u}(\sigma_0^u)^2 \frac{1}{(1+\epsilon^2)\,(1+\epsilon^2 p^2)} - \frac{3\epsilon^2+3\epsilon^2p^2+8\epsilon^4p^2}{(1+\epsilon^2)(1+\epsilon^2p^2)}, \tag{4.23}$$

$$K_2^{(1)\,f}(\sigma_0^f)^2 = K_2^{(1)\,u}(\sigma_0^u)^2 \frac{1}{(1+\epsilon^2p^2)^2} + \frac{\epsilon^2p^2}{(1+\epsilon^2p^2)^2}, \tag{4.24}$$

$$K_2^{(2)\,f}(\sigma_0^f)^2 = K_2^{(2)\,u}(\sigma_0^u)^2 \frac{1}{(1+\epsilon^2p^2)^2} + 2\frac{\epsilon^2p^2}{(1+\epsilon^2p^2)^2}. \tag{4.25}$$

It is straightforward to obtain the formulae for the generalized skewness and kurtosis expressed in terms of the corresponding cumulants for v if u is Gaussian and v is non-Gaussian. In the broader context, when both u and v are mildly non-Gaussian, the resulting generalized skewness and kurtosis cumulants of the composite field f can be presented as the sum of the corresponding ones for the constituent fields u and v. Finally, in the most general case, when the two fields are correlated, the additional terms corresponding to the cross-correlations between the two fields and their first and second derivatives will not be taken as zero. Accordingly, these terms will contribute to the non-Gaussianity of the composite field. The detailed expressions for the general case are not included here.

4.2.3 MFs in terms of skewness and kurtosis

Now, we can write the analytical ensemble expectations for MFs given in eq. (4.5) for $2d$, in terms of skewness and kurtosis. In this way, we can estimate how the

bias in the skewness and kurtosis parameters due to the presence of secondary fields can translate to the bias in the MFs of the composite fields.

The first-order non-Gaussian terms are given in terms of the skewness cumulants, as,

$$v_0^{(1)}(\nu) = \frac{S^{(0)}}{6}H_2(\nu), \tag{4.26}$$

$$v_1^{(1)}(\nu) = \frac{S^{(0)}}{6}H_3(\nu) + \frac{S^{(1)}}{3}H_1(\nu), \tag{4.27}$$

$$v_2^{(1)}(\nu) = \frac{S^{(0)}}{6}H_4(\nu) + \frac{2S^{(1)}}{3}H_2(\nu) + \frac{S^{(2)}}{3}H_0(\nu). \tag{4.28}$$

The second-order non-Gaussian terms are given in terms of kurtosis cumulants,

$$v_0^{(2)}(\nu) = \frac{\left(S^{(0)}\right)^2}{72}H_5(\nu) + \frac{K^{(0)}}{24}H_3(\nu), \tag{4.29}$$

$$\begin{aligned} v_1^{(2)}(\nu) = {} & \frac{\left(S^{(0)}\right)^2}{72}H_6(\nu) + \frac{1}{24}\left(K^{(0)} + \frac{4}{3}S^{(0)}S^{(1)}\right)H_4(\nu) \\ & + \frac{1}{8}\left(K^{(1)} + \frac{4}{9}\left(S^{(1)}\right)^2\right)H_2(\nu) \\ & - \frac{1}{16}\left(K_1^{(2)} - K_2^{(2)}\right)H_0(\nu), \end{aligned} \tag{4.30}$$

$$\begin{aligned} v_2^{(2)}(\nu) = {} & \frac{\left(S^{(0)}\right)^2}{72}H_7(\nu) + \frac{1}{24}\left(K^{(0)} + \frac{8}{3}S^{(0)}S^{(1)}\right)H_5(\nu) \\ & + \frac{1}{4}\left(K^{(1)} + \frac{2}{9}S^{(0)}S^{(2)}\right)H_3(\nu) \\ & + \frac{1}{4}\left(K^{(2)} - \frac{8}{9}S^{(1)}S^{(2)}\right)H_1(\nu). \end{aligned} \tag{4.31}$$

4.3 Practical Applications of Composite Fields

In this section, we apply the aforementioned formalism in the analysis of random fields of physical origin. Again, f is the composite of a signal field u and an additional field v, which we consider to be noise. Our aim is to determine how the

presence of noise gives rise to bias in the amplitude and nature of non-Gaussianity of the signal field. This is done using the analytic formulae for MFs and comparing them with the numerical calculations. Our numerical computation of MFs is based on the method discussed in Schmalzing & Buchert (1997) and outlined in chapter 3.

4.3.1 Sum of two Gaussian fields - CMB and noise

Consider u, a simulated Gaussian CMB map generated from Planck best-fit CMB power spectrum (Planck Collaboration et al. 2020a) using CAMB[‡] (Lewis et al. 2000). The map is at a resolution given by `healpix` parameter $N_{\rm side} = 256$. For the secondary field v, we take the toy example of a Gaussian noise map. v is prepared using `healpix` at the same $N_{\rm side}$ as the CMB map by taking a power spectrum of the form $C_\ell \propto \ell$. We choose this power spectrum following the pattern of noise in CMB experiments, which tends to have more power at higher ℓ values (small scales). We take one map each for CMB and noise.

The top panel of figure 4.2 shows the simulated CMB and noise maps in the top panels, with their composite map shown in the middle panel. In this case, $\epsilon = 0.4$ and $p = 1.35$. As $\epsilon < 1$, it is difficult to distinguish the composite map from the CMB map visually.

In figure 4.2, the bottom panels show the numerically computed V_1 and V_2 as a function of ν for the CMB (red), noise (purple) and their composite (cyan) maps. V_0 is independent of cosmological parameters for Gaussian fields and is not shown here. The black dashed lines, which coincide with the cyan lines, represent plots of the analytical formulae for the MFs, which are obtained using the right-hand side of eq. (4.13) as inputs in the amplitude of the MFs. We observe good agreement between the analytical formulae and the numerically calculated MFs. As discussed

[‡] `https://camb.readthedocs.io/`

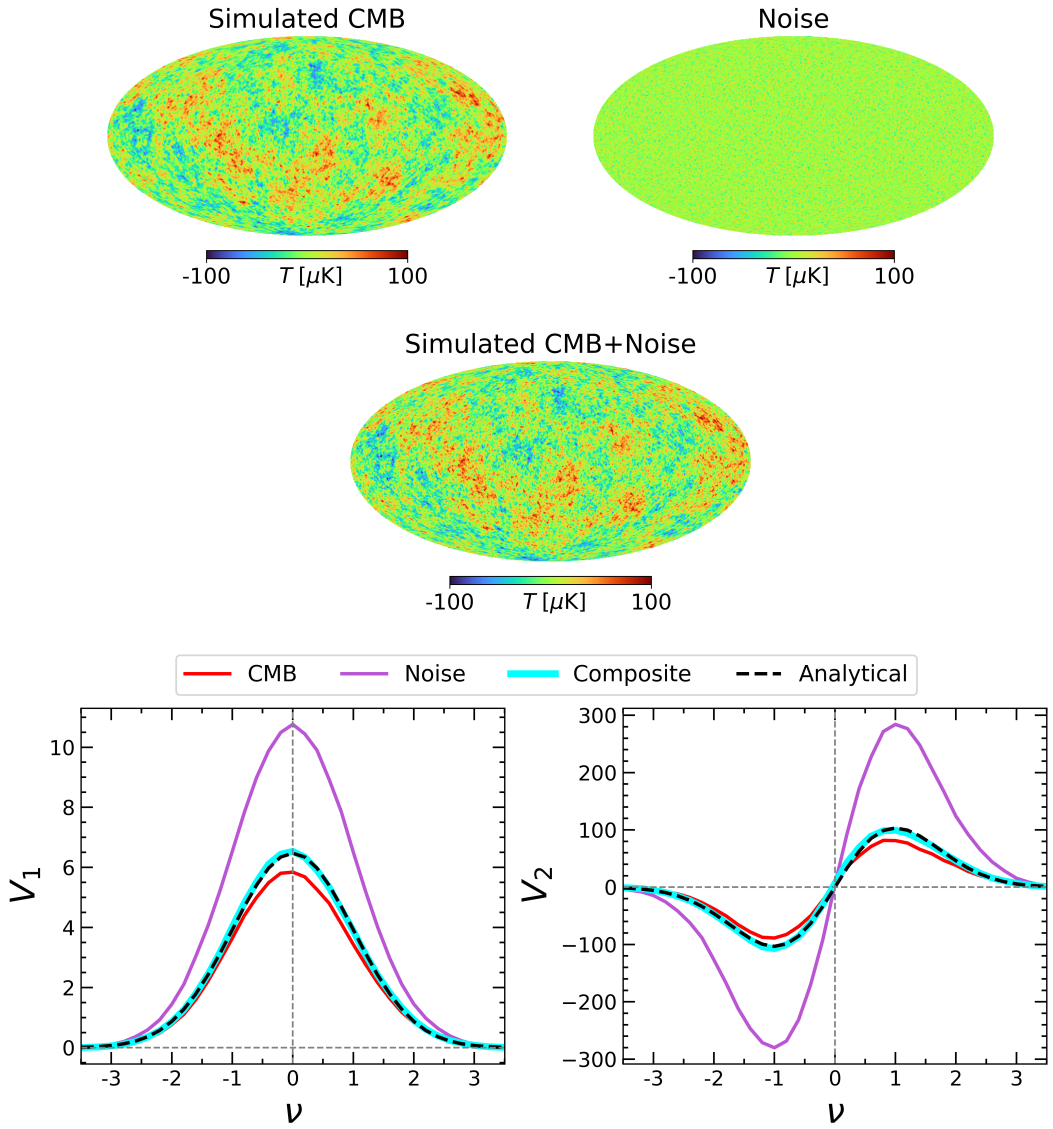

FIGURE 4.2: *Top*: Simulated CMB (left) and noise (right) maps. *Middle*: The composite of CMB and noise maps. *Bottom*: The MFs V_1 (left) and V_2 (right) for CMB (red), noise (purple) and their composite (cyan) maps. The black dashed line, which overlaps the cyan lines, corresponds to the MFs using the analytic formula.

in section 4.2.1, when $p > 1$, the amplitudes of both V_1 and V_2 for the composite fields will be larger than that of the signal u. This is what we see in our results.

We conclude that the presence of noise in the CMB maps leads to a bias in the amplitude of the MFs, which is governed by the values of ϵ and p. For $p > 1$, the bias is positive (resulting in an increase of A_k), while for $p < 1$, the bias is negative

(leading to a decrease of A_k). It's worth noting that while we have illustrated the effect using CMB and noise maps, these findings are relevant and applicable to any composite field in general.

4.3.2 Sum of mildly non-Gaussian CMB and Gaussian noise maps

Next, we analyse a composite field as the sum of non-Gaussian and Gaussian fields. As a signal, a simulated CMB map with local type $f_{\rm NL}$ non-Gaussianity (Maldacena 2003) is considered. Similar to the previous case, we consider the noise map as the secondary map. As before, both maps are at $N_{\rm side} = 256$. For the signal field, we take an unrealistically large value $f_{\rm NL} = 500$ simply to highlight the impact of noise without worrying about statistical fluctuations. Furthermore, the non-Gaussian CMB maps are simulated in the Sachs-Wolf (SW) limit (using eq. (3.41)), simplifying the procedure for creating simulated non-Gaussian maps. We use 1000 non-Gaussian CMB maps to obtain ensemble expectations.

Before computing the MFs of f, it is instructive to discuss its PDF, which can be derived as follows. It was shown in Ganesan et al. (2015) that the PDF of a mildly non-Gaussian zero-mean random variable u of local $f_{\rm NL}$ type is given by the form,

$$\begin{aligned} P_u(x) &= \frac{1}{\sqrt{2\pi(\sigma_0^u)^2}} \exp\left\{-\frac{x^2}{2(\sigma_0^u)^2}\right\} \\ &\quad \times \left[1 + f_{\rm NL}\sigma^u \left\{\frac{x^3}{(\sigma_0^u)^3} - \frac{3x}{\sigma_0^u}\right\}\right], \end{aligned} \tag{4.32}$$

where x denotes values of u in its domain. In terms of $\nu = u/\sigma_0^u$ we get

$$P_u(\nu) = \frac{1}{\sqrt{2\pi(\sigma^u)^2}} e^{-\nu^2/2} \left[1 + f_{\rm NL}\sigma^u \left\{\nu^3 - 3\nu\right\}\right]. \tag{4.33}$$

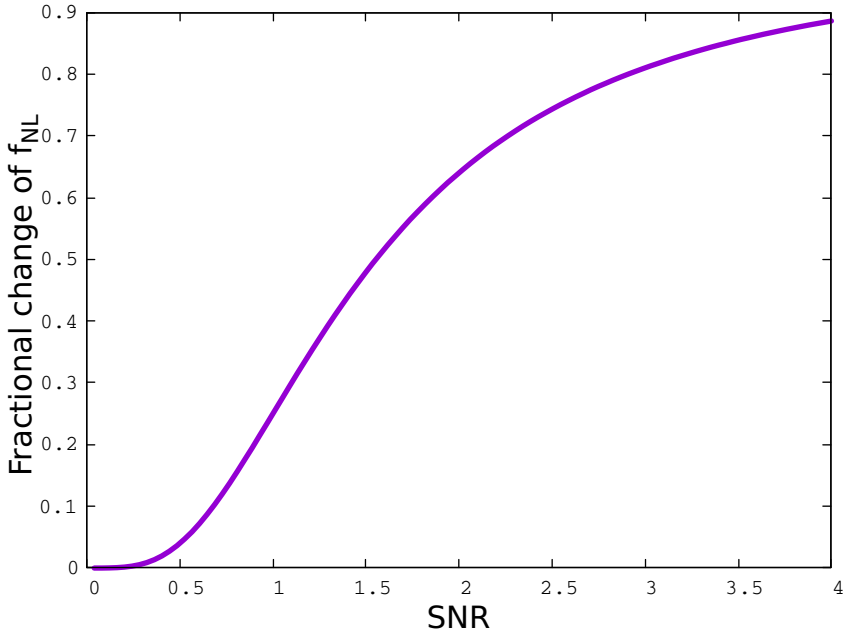

FIGURE 4.3: The fractional change of $f_{\rm NL}$, given by $(\sigma^u/\sigma^f)^4 = 1/(1+\epsilon^2)^2$, that is induced by the presence of Gaussian noise is shown as a function of the SNR ($=\epsilon^{-1}$).

The PDF of v is

$$P_v(x) = \frac{1}{\sqrt{2\pi(\sigma^v)^2}} \exp\left\{-\frac{x^2}{2(\sigma^v)^2}\right\}. \tag{4.34}$$

If u and v are uncorrelated, the PDF of f is given by the convolution of their PDFs, from which we get

$$\begin{aligned} P_f(x) &= \frac{1}{\sqrt{2\pi(\sigma^f)^2}} \exp\left\{-\frac{x^2}{2(\sigma^f)^2}\right\} \\ &\quad \times \left[1 + f_{\rm NL}\sigma^u \left\{\frac{(\sigma^u)^3 x^3}{(\sigma^f)^6} - 3x\frac{(\sigma^u)^3}{(\sigma^f)^4}\right\}\right]. \end{aligned} \tag{4.35}$$

In terms of $\nu = f/\sigma^f$, and redefining $f_{\rm NL}$ by absorbing the factor $\left(\sigma^u/\sigma^f\right)^4$, as

$$\widetilde{f}_{\rm NL} = \left(\frac{\sigma^u}{\sigma^f}\right)^4 f_{\rm NL}, \tag{4.36}$$

we get

$$P_f(\nu) = \frac{1}{\sqrt{2\pi(\sigma^f)^2}} e^{-\nu^2/2} \left[1 + \widetilde{f}_{\rm NL}\sigma^f \left\{\nu^3 - 3\nu\right\}\right]. \tag{4.37}$$

In terms of ϵ we have $(\sigma^u/\sigma^f)^4 = 1/(1+\epsilon^2)^2$, where we have used the condition that u, v are uncorrelated. Since $\sigma^u \leq \sigma^f$, we always have $\widetilde{f}_{\rm NL} \leq f_{\rm NL}$ and the fractional change is quantified by $\left(\sigma^u/\sigma^f\right)^4$. Comparing Eqs. 4.33 and 4.37, we see that the functional form of the PDF of f/σ^f is the same as that of u/σ^u, but with a decrease of the non-Gaussian level that is determined by the fractional change of $f_{\rm NL}$. In Fig. 4.3 we show a plot of the fractional change of $f_{\rm NL}$ versus the SNR $(= \epsilon^{-1})$. At low SNR, the composite field is 'Gaussianized' due to the presence of Gaussian noise, and the true non-Gaussianity of the signal can be recovered only for SNR $\gg 1$.

The area fraction V_0 is just the cumulative distribution function. Hence, we can anticipate that the fractional change of $f_{\rm NL}$ will directly translate into a decrease of ΔV_0 for f compared to u. However, the effect of the Gaussian noise on ΔV_1 and ΔV_2 cannot be inferred only from the PDF of f because they encode the effect of the variable p (first derivatives of the fields), and hence will not track the PDF directly.

We now focus on numerical computation of the non-Gaussian deviations of the MFs for u and f and comparison with the expected analytic expressions. For this, we define non-Gaussian deviation (ΔV_k) to quantify the non-Gaussian deviations of the numerically computed MFs as,

$$\Delta V_k = V_k - V_k^G, \tag{4.38}$$

where the superscript G refers to the Gaussian expectation. For a given field whose nature is apriori unknown, to get V_k^G we calculate σ_0 and σ_1 for the field and

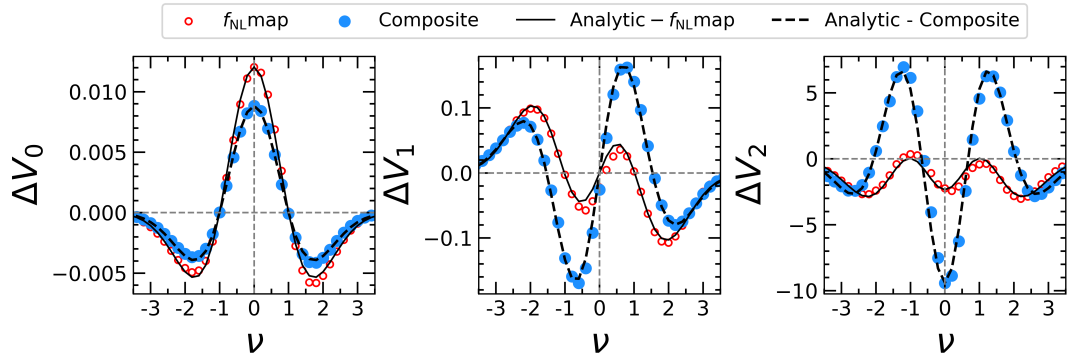

FIGURE 4.4: Plots of ΔV_k for the composite field f (blue dots) and the non-Gaussian signal field u (red dots). The corresponding ΔV_k^{ana} are also shown for f (black dashed line) and for u (black solid line). The amplitude of ΔV_0^f is lower than that of u, as anticipated. The amplitudes of both ΔV_1^f and ΔV_2^f are found to increase, and the shape is mildly different to that of u. This is due to the combined effect of A_k^f being larger than A_k^u and the relative strengths and signs between the generalized skewness cumulants.

use these values as inputs in the Gaussian analytic formulae given by eq. (4.38). From the simulated non-Gaussian CMB and noise maps, we get $\bar{\epsilon} \simeq 0.47$ and $\bar{p} \simeq 3.3$, where the overbars indicate that the values are averaged over the 1000 non-Gaussian CMB maps.

The presence of noise in the maps will alter the amplitudes A_k and the shapes of the MFs as a function of ν. As per the values of $\bar{\epsilon}$, $\bar{p}$ quoted above, we should get $A_k^f > A_k^u$ for $k = 1, 2$. Moreover, given that the input $f_{\rm NL}$ non-Gaussianity is of leading order, the generalized skewness moments are the only important higher-order cumulants. As a result, we can ignore σ_0^2 order (kurtosis) terms in the MFs.

In order to isolate the effect on the shapes of the MFs from the effect on the amplitudes, we study the normalized quantity $\Delta V_k/A_k$ for f and u. Due to the fact that $\Delta V_0/A_0$ for f depends only on $S(0)$, we expect that it will show a decrease with respect to that of u. $\Delta V_1/A_1$ depends on $S^{(0)}$ and $S^{(1)}$, for which, according to eqs. (4.19) and (4.20), has less values for f compared to u. Nevertheless, the shape of $\Delta V_1/A_1$ and whether its amplitude for f is increased or decreased with respect to u are determined by the relative sign of $S^{(0)}$ and $S^{(1)}$. Similarly, for V_2, whether

there is a decrease or increase of $\Delta V_2^f/A_2$ depends on the relative strengths and signs of all three generalized skewness cumulants. This is true regardless of the fact that all these cumulants have values for f that are lower than for u.

ΔV_k for the composite field f (blue dots) and the non-Gaussian signal field u (red dots) are shown in figure 4.4. Analytic ΔV_k for f and u is also shown by the dashed and solid black lines, respectively. We find that the numerical results have good agreement with the analytic formulae that we have derived. As anticipated above, we see that the amplitude of ΔV_0^f is lower than that of u. This is also consistent with our discussion on the PDF of the field. The amplitudes of both ΔV_1^f and ΔV_2^f are found to increase, and the shape is mildly different to that of u. As explained previously, this is because of the combined effect of A_k^f being larger than A_k^u and the relative strengths and signs between the generalized skewness cumulants.

Figure 4.5 shows $\Delta V_k/A_k$ for the composite field f (blue dots) and the non-Gaussian signal field u (red dots). Again, the solid lines are the analytic $\Delta V_k/A_k$ for f (dashed black) and u (solid black). As expected, there is a very good agreement between the numerical results and the analytic formulae. Additionally, the amplitudes of the MFs and their peak positions for f are found to be different compared to those of u.

4.4 Conclusion

In this chapter, we have extended the analytic formulae for MFs of $2d$ mildly non-Gaussian fields to composite fields, which are the sum of two fields. In the context of cosmology, these formulae gain significance when working with observed cosmological data, which is always a sum of the true signal and noise and also

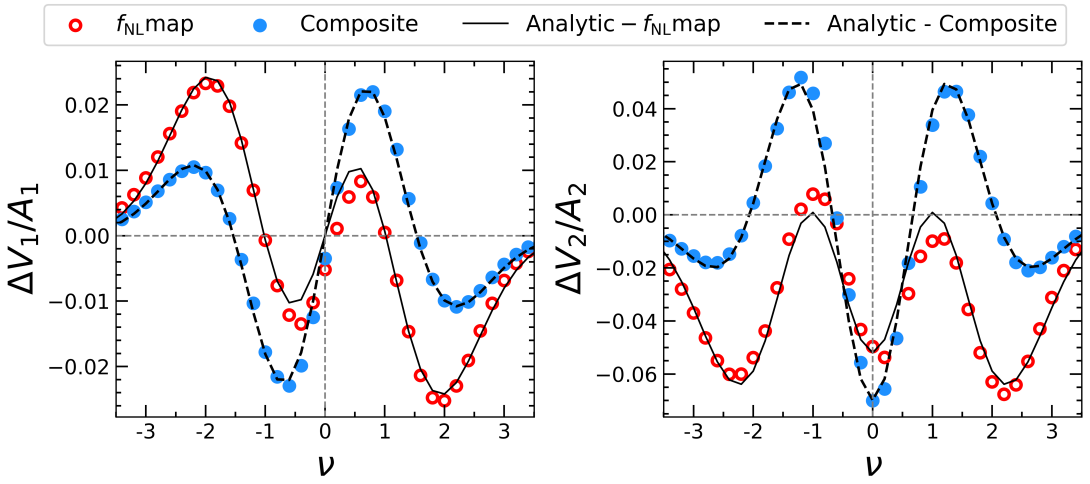

FIGURE 4.5: *Top*: Plots of $\Delta V_k/A_k$ for the composite field f (blue dots) and the non-Gaussian signal field u (red dots). The corresponding $\Delta V_k^{ana}/A_k$ are also shown for f and u by the black dashed and solid lines, respectively. As expected, there is a very good agreement between the numerical results and the analytic formulae. The amplitudes of the MFs and their peak positions for f are different from u due to the relative strength and signs of all three skewness cumulants.

possible contamination by other signals. The formulae presented in this work allow us the precise quantification of the effect of the secondary field on the morphology and statistical properties of the signal field. This, in turn, offers analytical control over the calculations.

Illustrating this with practical situations, we apply the formulae to two composite fields on the sphere; one field involves Gaussian CMB and Gaussian noise maps, while the other combines non-Gaussian CMB with Gaussian noise maps. In the case of two Gaussian fields, we use our formulae to quantify how the presence of noise introduces bias in the amplitudes of the MFs for the CMB map. We find that the amount of bias depends on the SNR value and the relative size of structures of the signal and noise fields. In the second case, apart from the amplitude bias, the presence of noise introduces modification in the nature of the non-Gaussianity of the composite field relative to that of the signal field. This modification can be quantified by estimating the change of the shapes of the non-Gaussian deviations of the MFs of the composite field relative to the signal.

The aforementioned explicit examples can easily be extended to non-Gaussian secondary fields. For instance, one can quantify the contamination of the CMB signal due to the presence of residual foregrounds as done in Chingangbam & Park (2013). It is also straightforward but tedious to extend to cases where the two component fields are correlated. Studying the properties of different foreground emissions in our Galaxy is one such scenario. We plan to carry out investigations along these lines in future. However, we reiterate that the results of this chapter are not limited to cosmology and can find applications to any practical examples of composite fields.

Chapter 5

Nature of Non-Gaussianity and Statistical Isotropy of Haslam 408 MHz Map*

5.1 Introduction

In modelling and simulating foregrounds at low frequencies, the small-scale fluctuations are generally assumed to be statistically isotropic Gaussian random fields (GRFs) (Tegmark et al. 2000; Delabrouille et al. 2013; Thorne et al. 2017). For example, in the commonly used `Hammurabi` code (Waelkens et al. 2009), the small-scale (turbulent) Galactic magnetic field (GMF) is approximated as statistically isotropic and Gaussian distributed. The assumptions of Gaussianity and SI of

*The work presented in this chapter is published as Rahman et al. (2021)

the foregrounds at small scales and away from the Galactic plane simplify their modelling. However, their validity based on physical grounds is not clear.

Since the interactions that govern the Galactic emissions are generally non-linear, we do not expect that the interaction may be expressed as a small perturbation term added to an interaction-free physical system. It is not clear that the statistical nature of each foreground component will approach Gaussianity at smaller scales. It is possible that if we remove the larger scale fluctuations, the fields do approach Gaussianity as a manifestation of the central limit theorem. However, it is important to test this as a function of resolution or scale. Further, the foreground fields are obviously anisotropic on the full sky since most of the emissions come from regions around the plane of the Galactic equator. It is important to test whether, after masking the Galactic regions, the fields approach SI probing towards small angular scales.

As we discussed earlier, the all-sky 408 MHz synchrotron map obtained by Haslam et al. (1981, 1982) has been an important input for modelling the synchrotron in the CMB component separation methods for WMAP and Planck (Bennett et al. 2013; Ade et al. 2016). Various statistical properties that focus on the two-point function of this map have been well studied (Cho & Lazarian 2010; Mertsch & Sarkar 2013). Ben-David et al. (2015) reported that this map is Gaussian at scales smaller than roughly 3°, using skewness and kurtosis statistics for the investigation. Rana et al. (2018) used the bispectrum and MFs to probe the non-Gaussianity of the Haslam map and reported findings that are in agreement with Ben-David et al. (2015).

In this chapter, we examine in detail the non-Gaussian nature and SI of the Haslam map using the Minkowski tensors as a unified statistical tool. Further, we calculate the generalized skewness and kurtosis cumulants that enter in the perturbative expansion of scalar MFs for weakly non-Gaussian fields about the zeroth-order

Gaussian expressions (Matsubara 2010; Matsubara & Kuriki 2020). We compare the non-Gaussian deviations of the MFs that are obtained using the analytic expressions with the exact numerical calculations. This comparison allows us to demonstrate that the perturbative expansions of the MFs about the zeroth-order forms expected for mildly non-Gaussian fields are valid in the cooler regions of the Haslam map. Moreover, the leading source of non-Gaussianity is the second-order perturbation terms, and hence, the kurtosis determines the nature of non-Gaussian deviations in the Haslam map.

The chapter is organized as follows. We begin our discussions with a brief description of the pipeline for our analysis and the details about the simulations of Gaussian maps obtained using the Haslam power spectrum in section 5.2. Section 5.3 contains the calculations and our main results. Finally, we summarise our results and discuss their implications in section 5.4. Appendix 5.A contains a discussion of the consistency checks between the Haslam map and the simulations. We show the PDF of the Haslam map in appendix 5.B.

5.2 Analysis pipeline and Gaussian isotropic simulations

We focus our analysis on cooler parts of the sky by applying different brightness temperature cuts to mask the regions above the chosen cutoff temperatures. We also analyse at different angular scales. For this purpose, we process the map following an appropriate pipeline. For comparison, we also generate 1000 Gaussian isotropic simulations using the Haslam power spectrum. The pre-processing pipeline and the Gaussian isotropic simulations are described below.

5.2.1 Masking

Since the main focus of our analysis is the high-latitude regions, we mask the Galactic plane and other pixels where the emission is very strong. The steps followed in the mask preparation are described below.

- First, we downgrade the Haslam map from $N_{\rm side}$= 512 to 128 as the effective beam size of the Haslam map is $56'$ (Remazeilles et al. 2015). This map has a mean value of 34.4 K. Then, to avoid the Galactic plane from our analysis, we mask the pixels with ($\mid b \mid < 10^{\circ}$).

- The Loop-I bright structure in the map is masked. This emission is due to a supernova remnant. The masked region has a $\pm 4^{\circ}$ width cut around a circle of radius 58° centered at $(l,b) = (329^{\circ}; 17.5^{\circ})$.

- Let us denote the brightness temperature cut by u_c. Five sky masks are constructed by applying different choices of u_c. Pixels having field values above u_c are set to zero. We carry out the analysis for the values $u_c = 22, 25, 30, 40, 60$ K. Our results will be presented for the cases $u_c = 25$ and 60 K. The effective sky fractions for these masks are 0.74 for $u_c = 60$ K, 0.69 for $u_c = 40$ K, 0.56 for $u_c = 30$ K, 0.41 for $u_c = 25$ K and 0.27 for $u_c = 22$ K .

To minimize the effect of sharp mask boundaries in our results, we apodize the masks by convolving with Gaussian function with 5° FWHM.

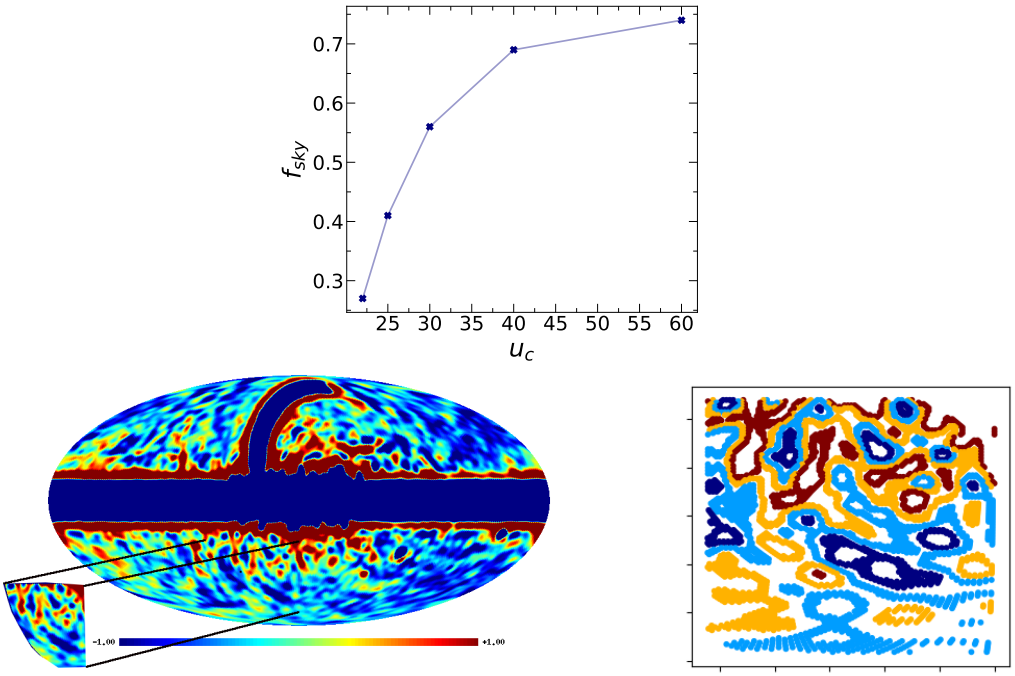

FIGURE 5.1: *Top*: The sky-fraction (f_{sky}) as a function of different temperature cuts (u_c) used in our analysis. *Bottom*: The left panel is the mean-free and normalized (u/σ_0) version of the same map after applying the brightness temperature cut $u_c = 60\,\mathrm{K}$ and band-passing with multipole cut $\ell_c = 30$. Excursion set boundaries are shown in the right panel for different field thresholds (different colours), corresponding to the cut-out patch on the lower left of the left panel. The boundaries are quite thick due to the choice of large field threshold bins.

5.2.2 Band-passing

In order to focus our analysis on specific angular scales that we are interested in, we use a band-pass filter defined as

$$f(\ell) = \frac{1}{4}\left\{1 + \tanh\left(\frac{\ell - \ell_c}{\Delta\ell}\right)\right\}\left\{1 - \tanh\left(\frac{\ell - \ell^*}{\Delta\ell}\right)\right\}. \tag{5.1}$$

This filter is multiplied with the Fourier amplitudes ($a_{\ell m}$s), thereby cutting off the $a_{\ell m}$s below a multipole scale ℓ_c, and above ℓ^*. The upper multipole cutoff (ℓ^*) is chosen as 180 in accordance with the $56'$ beam size of the Haslam map. $\Delta\ell$ sets the width of the cutoff region of the filter. We use $\Delta\ell = 10$ for the results presented in this paper. For a reasonable range of $\Delta\ell$, we find that the results are

robust. We vary ℓ_c to study the statistics of the map at different scales. We have also used other suitable filters, such as a cosine filter, and our results are found to be robust.

The final maps, which have undergone the aforementioned pre-processing steps, are then mean-subtracted and rescaled with the standard deviation. Computations of tensorial and scalar Minkowski functionals are done on this mean-free, unit standard deviation version of the Haslam map.

The top panel of figure 5.1 gives the sky-fraction (f_{sky}) left for the analysis after the application of various temperature cuts (u_c) on the map. The bottom left panel shows the mean-free and normalized (u/σ_0) version of the same map obtained after applying temperature cut $u_c = 60\,\mathrm{K}$, and band-passed with multipole cut $\ell_c = 30$. The bottom right panel shows the iso-field contours of a slice of the field shown in the lower left of the left panel. Different colours of the contours correspond to different field thresholds (ν). The lines are thick due to the choice of large field threshold bins.

5.2.3 Gaussian isotropic simulations

For the purpose of quantifying the level of non-Gaussianity and anisotropy of the Haslam map, we compare it with Gaussian isotropic simulations. We generate 1000 Gaussian isotropic simulations using the angular power spectrum of the Haslam map corrected for cut-sky, pixel and beam correction. This input spectrum is made the `PolSpice`[†] package (Chon et al. 2004). A detailed consistency check carried out for these simulations is discussed in appendix 5.A. The pre-processing pipeline discussed in sections 5.2.1 and 5.2.2 is applied to each simulation map so that both simulation and data maps are identically pre-processed. This is necessary to

[†] `http://www2.iap.fr/users/hivon/software/PolSpice/`

ensure that the comparison of the statistics that we compute from the data and simulation maps makes sense.

5.3 Analysis of Gaussianity and SI of Galactic synchrotron emission - results

This section presents the results obtained from analysing the Haslam map and its comparison with Gaussian isotropic simulations.

5.3.1 Spectra of the Haslam map

We first discuss the spectral parameters σ_0 and σ_1, and their ratio $r_c \equiv \sigma_0/\sigma_1$. Given the mean-free field u, $\sigma_0 \equiv \sqrt{\langle u^2 \rangle}$ and $\sigma_1 \equiv \sqrt{\langle |\nabla u|^2 \rangle}$. The top panels of figure 5.2, show σ_0 (left) and σ_1 (right) for varying ℓ_c, for the Haslam map for different values of u_c. The mean over 1000 Gaussian simulations is also shown along with the 1σ error bars. We can see that both σ_0 and σ_1 decrease with a decrease of u_c and towards higher ℓ_c, indicating a drop in the level of fluctuations of the field and its gradient, as we go to lower temperatures as well as smaller scales. Moreover, both these parameters for the Haslam map fall within 1σ error bars obtained from Gaussian simulations. This is expected as the simulations are generated from the power spectrum of the Haslam map and validate the correctness of these simulations.

The bottom panels show r_c. This quantity gives a measure of the typical size of structures in the field. The left panels show r_c for both $u_c = 60$ and 25 K, so as to enable their visual comparison. We see that higher u_c has slightly larger

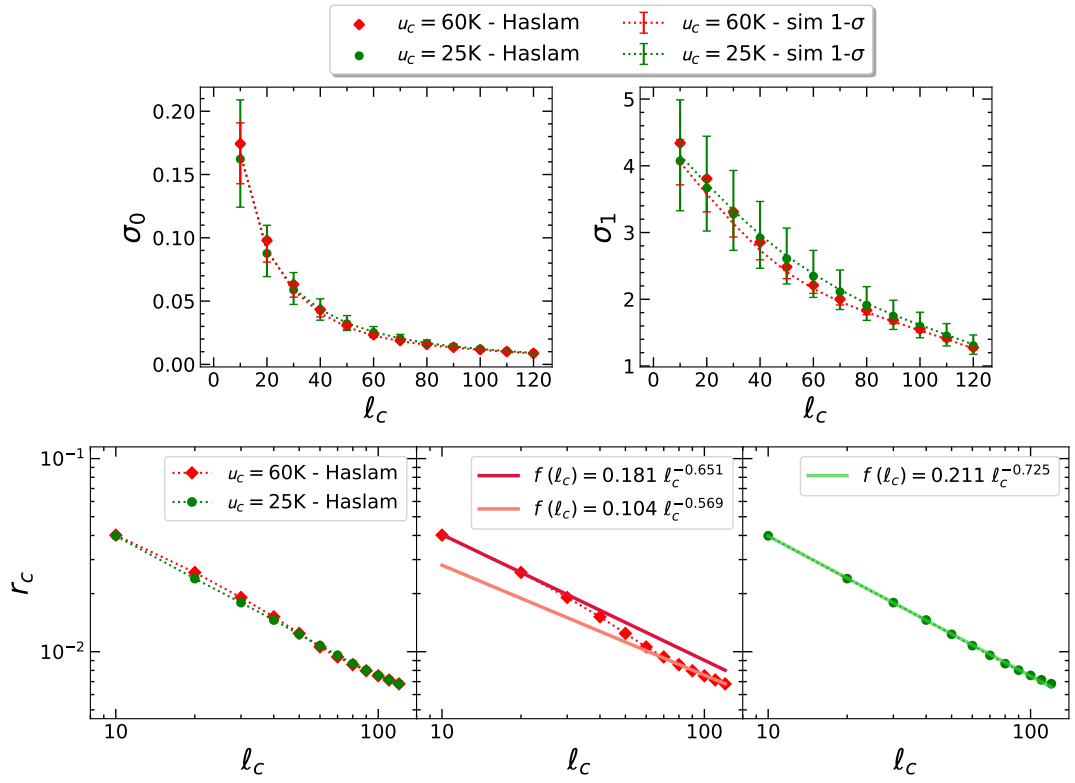

FIGURE 5.2: *Top*: σ_0 (left) and σ_1 (right) of the Haslam map for $u_c = 60$ K (red diamond) and 25 K (green circle) as a function of ℓ_c. Mean and 1σ error bars obtained from 1000 Gaussian isotropic simulations are also shown. Since the simulations are obtained using the power spectrum of the Haslam data, σ_0 and σ_1 for the observed data and simulations match within 1σ, as expected. *Bottom*: The left panel shows the correlation length, $r_c \equiv \sigma_0/\sigma_1$ versus ℓ_c for $u_c = 60$ K and 25 K. The middle panel shows r_c for $u_c = 60$ K fitted with two different power-law functions towards the low and high ℓ_c regimes, indicating a transition in the nature of the field at the intermediate ℓ_c scales. The right panel shows r_c for $u_c = 25$ K fitted by a single function.

structures towards lower ℓ_c. This indicates that if we include sky regions with higher temperatures, then there are larger regions having correlated temperature values. r_c also decreases with increasing ℓ_c, which is expected due to the subtraction of large-scale fluctuations and the fact that σ_0 decreases faster than σ_1. We have fitted the fall of r_c with respect to ℓ_c with power-law functions (shown in the middle and right bottom panels of figure 5.2). For $u_c = 60$ K, we could fit it with two functions at low ℓ_c region and high ℓ_c region. This indicates a transition in the nature of the field at the intermediate scales. For $u_c = 25$, we are able to fit r_c with a single function. This could be a hint to the difference in the nature of the

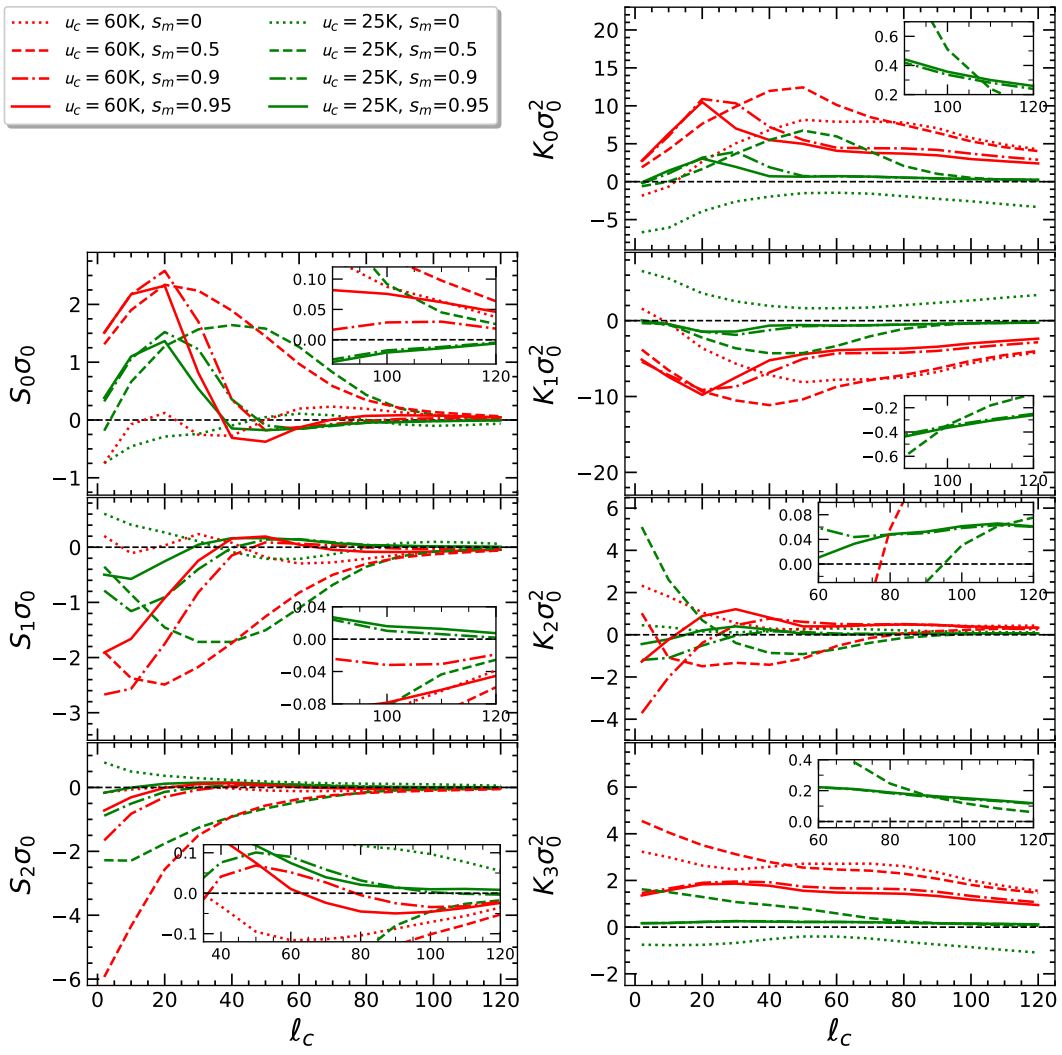

FIGURE 5.3: Skewness and kurtosis cumulants (defined in section 3.3.1) of the Haslam map for the case of temperature cut values $u_c = 60\,\mathrm{K}$ (red) and $u_c = 25\,\mathrm{K}$ (green), plotted as functions of the multipole cut ℓ_c. Different line types for each colour represent different values of s_m, and the associated sky fraction. All kurtosis cumulants have values larger than the skewness ones, indicating that the non-Gaussianity of the map is predominantly sourced by kurtosis terms.

field in the cooler regions (lower u_c) of the synchrotron sky, as seen in our further analysis.

5.3.2 Skewness and kurtosis of the Haslam map

In order to probe the non-Gaussian nature of the Haslam map, we next analyse the skewness, S_i, and kurtosis cumulants, K_i, defined in eqs. (3.17) and (3.18). Since σ_0 varies with ℓ_c, we interpret the cumulants with the appropriate power of σ_0 multiplied to them, i.e., $S_i\sigma_0$ and $K_i\sigma_0^2$. These quantities are the coefficients of the Hermite polynomials in the expressions for the first and second-order non-Gaussian deviations of the MFs, up to numerical factors. Hence, it is meaningful to compare them directly.

To minimize the errors arising from the mask boundary on the calculation of $S_i\sigma_0$ and $K_i\sigma_0^2$, and the scalar and tensorial MFs, we must stay sufficiently far away from the boundary. Upon smoothing the binary mask, pixels near the mask boundaries acquire values between zero and one. A rough estimate shows that for any smoothing scale, θ_s, a pixel value > 0.89 on a smoothed mask is approximately equivalent to $> 2\theta_s$ angular distance from the mask boundary. We introduce a parameter, s_m, to control how far away a smoothed mask pixel is from the boundary. s_m takes values in the range of zero to one. Pixels for which the smoothed mask has values $> s_m$ are included in the calculations. As s_m increases towards one, the sky fraction will decrease, thereby decreasing the statistical significance of the results. Hence, an optimum value of s_m has to be chosen so as to minimize the numerical error and maximize the statistical significance.

Figure 5.3 shows $S_i\sigma_0$ (left column) and $K_i\sigma_0^2$ (right column) as functions of the multipole cut ℓ_c, for $u_c = 60\,\mathrm{K}$ (red lines) and $25\,\mathrm{K}$ (green lines). The results are shown for different values of s_m. The inset boxes show the zoomed-in plots towards higher ℓ_c values. For lower ℓ_c, we see a large variation of the cumulants with s_m. Towards higher ℓ_c, they show approximately convergent behaviour for the larger s_m values, indicating that the effect of the mask boundary is minimized. Therefore, we will interpret the non-Gaussian behaviour of the Haslam map using

$s_m = 0.9$, for which the cumulants are shown by dot-dash lines in the plots.. The results for the cumulants are as follows:

- All four kurtosis cumulants have values whose magnitudes are considerably larger than those of the skewness ones, for both values of u_c and for all ℓ_c. This corroborates our inference from visual inspection of the probability distribution functions (PDFs) of the Haslam map shown in figure 5.B.1 in appendix 5.B.

- $S_i\sigma_0$ show clear decrease both with decreasing u_c and towards high ℓ_c. We see that $S_0\sigma_0$ and $S_1\sigma_0$ show rough oscillatory behaviour up to intermediate values of ℓ_c. Towards high ℓ_c, all three $S_i\sigma_0$ decrease monotonically.

- All the kurtosis cumulants also decrease from higher to lower values of u_c, and at all ℓ_c. Towards high ℓ_c, the magnitudes of all the $K_i\sigma_0^2$ show a mild monotonic decrease, except $K_2\sigma_0^2$ which appears to saturate at a small but finite value. $K_0\sigma_0^2$ and $K_1\sigma_0^2$ also exhibit rough oscillatory behavior similar to skewness parameters.

Based on the above points, we conclude that the nature of non-Gaussianity of the Haslam map at the range of scales probed here is predominantly sourced by kurtosis terms. Moreover, at smaller scales, the field shows convergence towards Gaussian behaviour. However, we note that it is important to probe down to even smaller scales, which is not feasible with the Haslam map. The next subsection will discuss the level of non-Gaussianity measured using the Minkowski functionals. Although beyond the scope of this paper, from the behaviour of the skewness and kurtosis parameters as functions of ℓ_c, it will be interesting to investigate further whether one can identify physically interesting scales associated with the distribution of cosmic rays and free electrons, and the properties of the GMF.

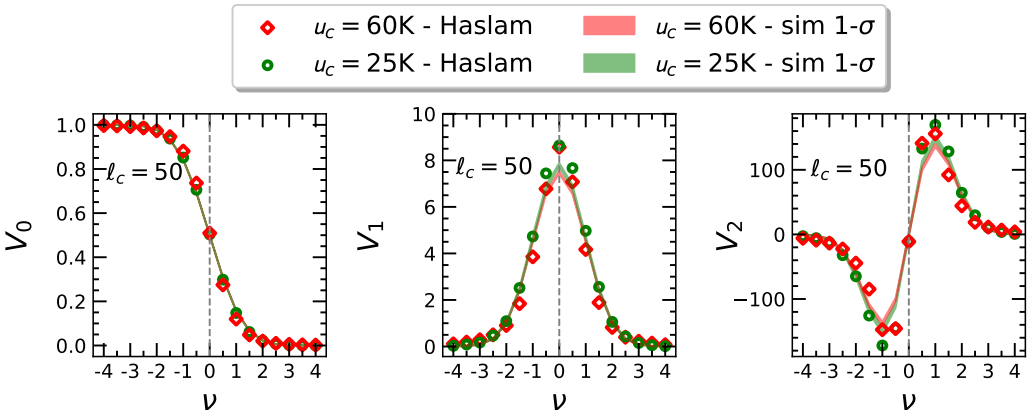

FIGURE 5.4: Scalar MFs of the Haslam map for $u_c = 60$ K (red diamonds) and $u_c = 25$ K (green circles), for $\ell_c = 50$. The ensemble mean and 1σ width obtained from 1000 simulated maps are also plotted to show the deviation.

5.3.3 Scalar Minkowski functionals for the Haslam map

We compute the scalar MFs using methods 1 and 2 described in sections 3.3.2.1 and 3.3.2.2, for the Haslam and the simulated Gaussian isotropic maps. We refer to the results of these calculations as 'exact numerical results'. We use the threshold range $-4 \leq \nu \leq 4$ with a bin size of $\Delta\nu = 0.5$. We show our results for the mask boundary threshold value $s_m = 0.9$, as discussed in section 5.3.2. The results for $u_c = 60$ K and 25 K for the intermediate scale $\ell_c = 50$ are shown in figure 5.4. The deviations of $V_k^{\rm Haslam}$ from the Gaussian mean values are easily discerned by eye.

In order to quantify the difference of the MFs between the Haslam map and the Gaussian simulations, we define

$$\Delta V_k \equiv V_k^{\rm Haslam} - V_k^{\rm G}, \tag{5.2}$$

where the superscript 'Haslam' refers to the Haslam map and 'G' stands for Gaussian simulation. For every k, we compute ΔV_k, normalized by the amplitude of $V_k^{\rm G}$ (indicated by superscript 'max'), for each Gaussian isotropic realization.

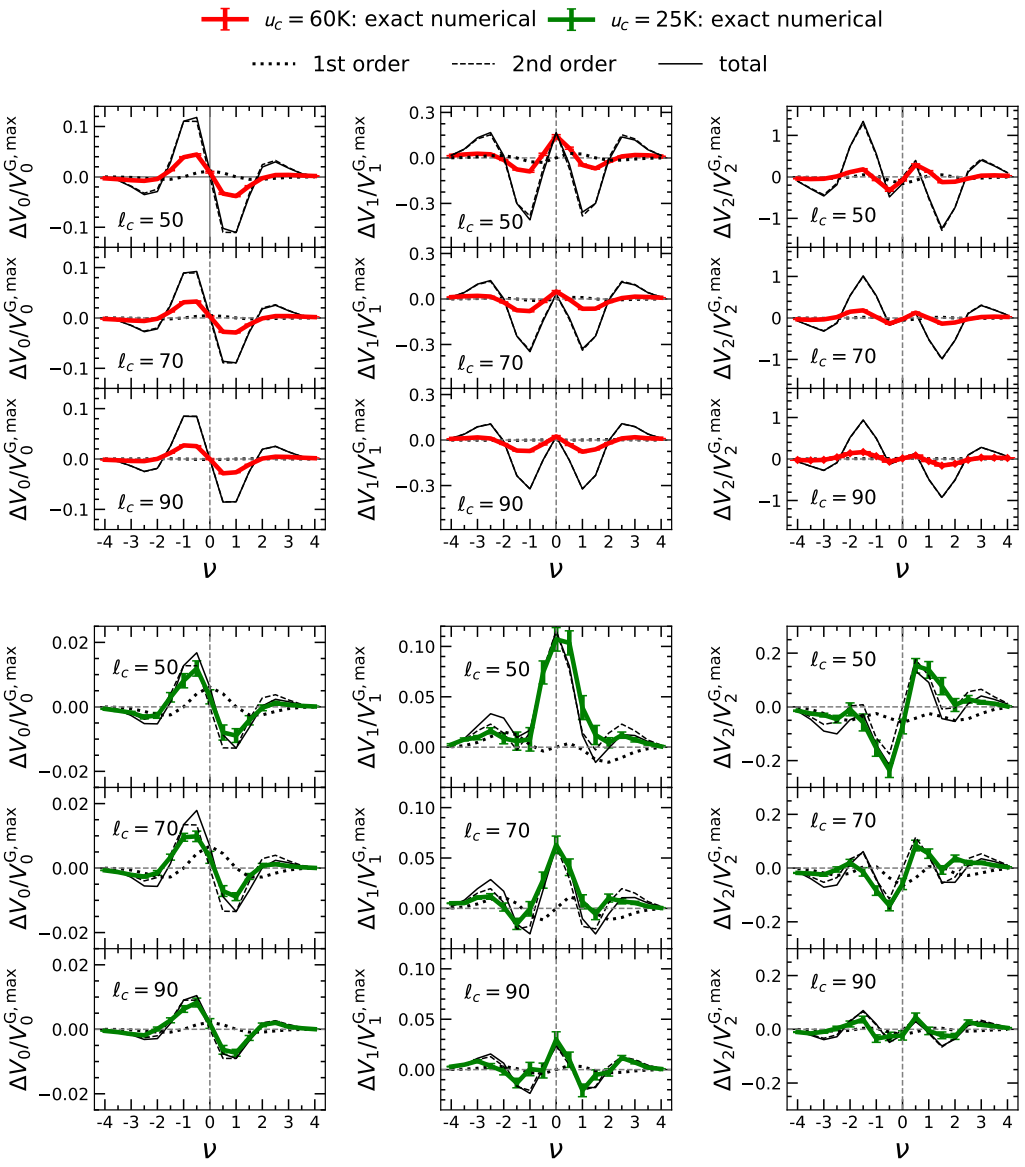

FIGURE 5.5: The deviations, $\Delta V_k/V_k^{\mathrm{G,max}}$, of the three MFs for Haslam data from Gaussian expectation for $u_c = 60\,\mathrm{K}$ (red solid lines) and $u_c = 25\,\mathrm{K}$ (green solid lines) are shown for $\ell_c = 50, 70, 90$. We use $s_m = 0.9$ for these results. The black lines correspond to the results obtained using perturbative expansion of MFs with only first-order terms (dotted lines), only second-order terms (dashed lines), and the sum of first- and second-order (solid lines). The dashed and solid black lines almost overlap since the contributions from the first-order terms are small.

Figure 5.5 shows the ensemble mean and 1σ error bars of the normalized ΔV_k for $u_c = 60$ K (red solid lines) and $u_c = 25$ K (green solid lines), and for $\ell_c = 50, 70, 90$ (top to bottom rows). For $u_c = 60$ K, the error bars are relatively smaller and, hence, hard to see by eye. All the plots shown in figure 5.5 are obtained using method 1. We obtain almost identical results from calculations using method 2. We summarize our findings from the exact numerical calculations as follows:

- The deviations have a characteristic shape as functions of the threshold. The overall amplitude of the deviations decreases as u_c is decreased while the shape is approximately maintained. This indicates that masking out very high-intensity regions, which correspond to values on the positive tail of the PDF of the field, makes it tend towards Gaussian nature. The nature of the non-Gaussian deviation of the field approximately remains the same even as we mask more high-temperature regions (decreasing u_c) and towards small angular scales (increasing ℓ_c).

- As we increase ℓ_c, the number of structures (equivalently, fluctuations of the field per unit area on the sphere) increases. As a consequence, the error bars on ΔV_k decrease with increasing ℓ_c. Therefore, even though the amplitude of the deviations decreases with increasing ℓ_c, the statistical significance of the deviations does not decrease proportionately and can remain high. This is particularly evident in the case of $u_c = 60$. At each ℓ_c and each ν, the error bar for $u_c = 25$ is generally higher than 60 because of the lower sky fraction.

- Lastly, we compare ΔV_k obtained from method 1 and 2. As mentioned earlier, method 1 contains small numerical inaccuracies due to the discretization of the δ function. However, when subtracting between the MFs obtained from the Haslam map and the Gaussian simulations, these numerical errors will mostly cancel out. A small part can still remain because the Haslam map is non-Gaussian, particularly for higher u_c and lower ℓ_c values. In comparison,

method 2 is free of these errors. We obtain very similar results for ΔV_k from method 2, indicating that the residual numerical errors for method 1 are insignificant and can be ignored. Another important point to mention is that we obtain marginally higher error bars from method 1, compared to method 2. The reason for this is the shot noise arising from the discrete harmonic transform associated with calculating field derivatives.

Next, we discuss the results obtained using the perturbative formulae of MFs given in section 3.3.1 and compare them with the exact numerical results. To do so, we define

$$\Delta V_k^{(1),\mathrm{pert}} = A_k v_k^{(1)}, \tag{5.3}$$

$$\Delta V_k^{(2),\mathrm{pert}} = A_k\, v_k^{(2)}, \tag{5.4}$$

$$\Delta V_k^{\mathrm{total,pert}} = A_k \left(v_k^{(1)} + v_k^{(2)}\right), \tag{5.5}$$

where $k = 0, 1, 2$, and A_k is the amplitude of the analytic expressions for MFs for the Gaussian case. The superscript 'pert' refers to the perturbative expansion described in section 3.3.1. For consistency with the exact numerical case, we normalize them by $V_k^{\mathrm{G,max}}$ (which is not always the same as A_k). In figure 5.5, the first-order results are shown by dotted black lines, the second-order by dashed black lines, and the total by solid black lines. First, for $u_c = 60\,\mathrm{K}$ (top panels accompanying the red plots), we can see that the first-order deviations for which skewness cumulants contribute are much smaller than the second-order deviations for which kurtosis cumulants contribute. As a consequence, the plots for the second-order and total deviations nearly overlap. Secondly, the total deviations up to second-order overestimate the amplitude of the deviations of all three MFs by over a factor of two, but the shape roughly agrees (as indicated by the location of zeros, peaks and troughs). This remains so even at high ℓ_c. Therefore, we conclude that for $u_c = 60\,\mathrm{K}$, the Haslam field is highly non-Gaussian even at the smallest

scales probed here. Hence, it is not meaningful to consider it as a Gaussian field plus a small non-Gaussian component.

In the lower panels of figure 5.5, we show the case of $u_c = 25$ K. We again find that the first-order deviations are smaller than the second-order for all MFs and all ℓ_c values considered here. So, the main contribution to the non-Gaussian behaviour of the relatively cooler signals of the Haslam map comes from the four kurtosis cumulants. Secondly, a good agreement is obtained between the non-Gaussian deviations of MFs obtained using analytical and numerical methods. The amplitude of the non-Gaussian deviations decreases as ℓ_c increases, indicating that the field approaches Gaussian behaviour at smaller scales. Therefore, we conclude that the cooler regions of the Haslam map can be well approximated as a mildly non-Gaussian field. The nature of the mild non-Gaussianity, however, does not significantly vary with angular scale, as implied by the shape of the deviations of the MFs. Our analysis with other temperature cuts for the cooler regions, such as $u_c = 22$ K and $u_c = 30$ K, shows trends similar to what is observed with $u_c = 25$ K. We are planning to do a detailed study on these regions in our future works, to understand more on the nature of synchrotron non-Gaussianity.

A visual comparison of figure 5.5 with the plots in figure 3.4 shows that the non-Gaussian nature of the Haslam map is similar to the local type $g_{\rm NL}$ non-Gaussianity of primordial inflationary fluctuations. This indicates the presence of an approximate parity symmetry in the fluctuations of synchrotron radiation.

5.3.3.1 Quantifying the level of non-Gaussianity

To quantify the statistical significance of the non-Gaussian deviations for V_k, we compute the difference between each statistic computed for Haslam data and its mean value obtained from Gaussian isotropic simulations in units of the standard

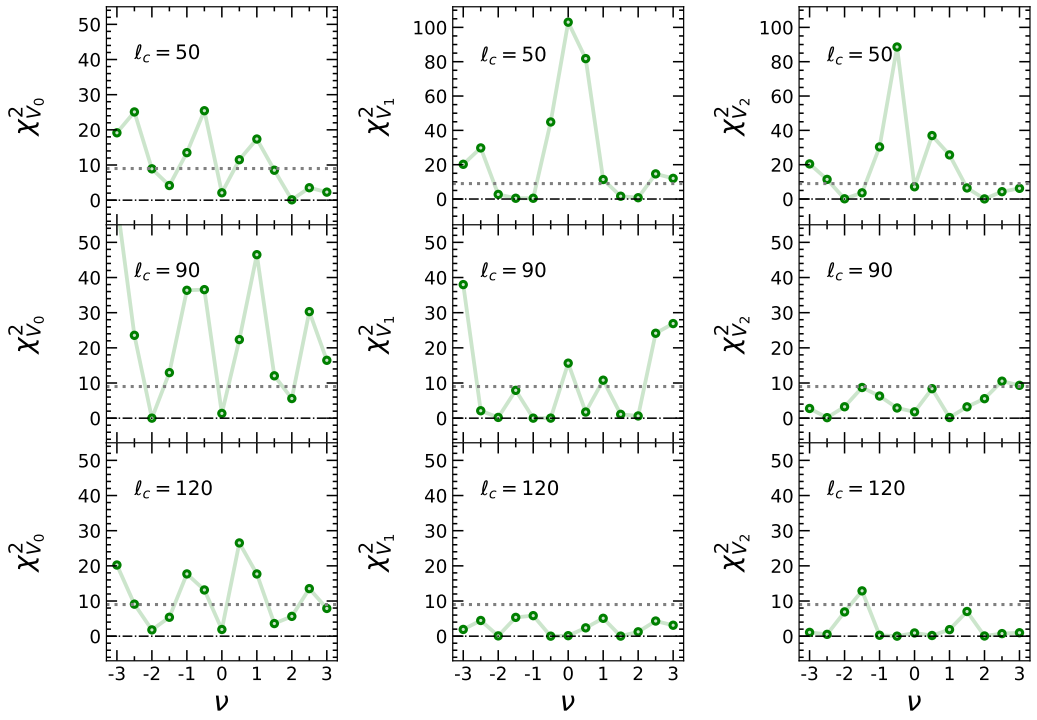

FIGURE 5.6: $\chi^2_{V_k}$ is shown as a function of threshold for each scalar MFs for $u_c = 25$ K, for different ℓ_c. It is seen that $\chi^2_{V_k}$ gets close to 3-σ for all thresholds as we increase ℓ_c. This indicates that the level of non-Gaussianity decreases as we remove more bright regions as well as large-scale structures in the Haslam map.

deviation. This is encapsulated by χ^2 which is defined, at each threshold ν, as follows,

$$\chi^2_{V_k}(\nu) = \frac{\left(V_k^{\rm Haslam}(\nu) - \overline{V}_k^{\rm G}(\nu)\right)^2}{\sigma^2_{V_k^{\rm G}}(\nu)} \tag{5.6}$$

We compute $\chi^2_{V_k}$ for all the values of u_c and ℓ_c that we consider here. We will not show χ^2 for $u_c = 60$ K since there is a high level of non-Gaussianity, and it is not meaningful to compute deviations from Gaussian expectation.

For each of the three scalar MFs, χ^2 for the case of $u_c = 25$ K are shown in figure 5.6. The line for $\chi^2 = 9$, which corresponds to 3σ is shown by the black dotted line for reference. Note that except for the case of V_0, the y-axis scales for the top panels showing $\ell_c = 50$ are different from the lower panels.

We observe that for all three MFs, χ^2 values decrease towards $\ell_c = 120$. The rate of decrease, however, varies. For V_0, the χ^2 values are higher than 9 for most threshold values, at all ℓ_c. For both V_1 and V_2, the values of χ^2 decrease as ℓ_c increases and for $\ell_c = 120$, are smaller than 3σ for all threshold values (except at $\nu = -1.5$ where it is higher than 9 for V_2).

We get the value of χ^2 for V_0 averaged over all threshold values for $\ell_c = 120$ is 11.08, corresponding to the statistical significance of 3.3σ. Therefore, from the behaviour of V_0, we conclude that the Haslam map for $u_c = 25$ K is mildly non-Gaussian with statistical significance 3.3σ. The nature of the non-Gaussianity is of the kurtosis type given by the cumulant K_0 since the non-Gaussian deviation of V_0 is determined by K_0.

5.3.4 Statistical isotropy of the Haslam map

Next, we discuss the results for $\mathcal{W}_1$. We again quantify the difference between the Haslam map and the Gaussian simulations as follows:

$$\Delta\mathcal{W}_1 \equiv \mathcal{W}_1^{\rm Haslam} - \mathcal{W}_1^{\rm G}, \tag{5.7}$$

$$\Delta\alpha \equiv \alpha^{\rm Haslam} - \alpha^{\rm G}, \tag{5.8}$$

where $\mathcal{W}_1^{\rm G}$ and $\alpha^{\rm G}$ are the values obtained from the Gaussian simulations, while the superscript 'Haslam' refers to the values for the Haslam map. As in the previous case, the deviations $\Delta\mathcal{W}_1$ and $\Delta\alpha$ are normalized with $\mathcal{W}_1^{\rm G,max}$ and $\alpha^{\rm G,max}$, respectively. We compute them for each Gaussian isotropic simulation.

We show the results in figure 5.7. The diagonal elements of $\mathcal{W}_1$ (left and middle) and α for $u_c = 60$ and 25 K, for $\ell_c = 50$ K are shown in the top row. The colour coding is the same as in figure 5.5. The mean values obtained from the 1000

Gaussian isotropic simulations corresponding to each u_c are shown by the solid lines, along with the 1σ regions. The ensemble mean of the diagonal elements of $\Delta\mathcal{W}_1$, along with 1σ error bars, are shown in columns one and two of the lower panels, for the same values of u_c and for $\ell_c = 50, 70, 90$. The physical information that can be deciphered from the elements of $\Delta\mathcal{W}_1$ is similar, up to statistical fluctuations, as ΔV_1, and we find that the behaviour is the same, as expected. Ensemble mean and 1σ error bars of $\Delta\alpha$ are shown in the third column of figure 5.7 for the same values of u_c and ℓ_c. We observe that $\Delta\alpha$ is smaller for smaller u_c, implying that the field becomes more isotropic when the warmer regions are excluded. This corroborates what we infer from visual inspection that high-intensity regions have large-scale correlations that appear to be direction-dependent.

Next, to proceed with the quantification of the statistical significance of any deviation from SI of the Haslam map, we take into consideration the fact that the probability distribution of α statistic is Beta distribution (Chingangbam et al. 2021) which has the following form,

$$P(\alpha) = \frac{\Gamma(a+b)}{\Gamma(a)\Gamma(b)}\alpha^{a-1}(1-\alpha)^{b-1}. \tag{5.9}$$

Here, the parameters a and b take positive values, which are determined by the physics of the emission. Due to this reason, for accurate quantification of the statistical significance of deviation from SI, we use the median value of α, denoted by $\widetilde{\alpha}^{\,\mathrm{G}}$ obtained from the 1000 simulations along with the 95% confidence interval. Our analysis shows that the values of mean and median differ by less than 1% at all threshold values. Let us denote the 95% confidence interval about the median by $[\delta_1, \delta_2]$. For each threshold, we determine δ_1 and δ_2 such that they satisfy

$$\int_{\widetilde{\alpha}^{\,\mathrm{G}}-\delta_1}^{\widetilde{\alpha}^{\,\mathrm{G}}} \mathrm{d}\alpha\, P(\alpha) = \int_{\widetilde{\alpha}^{\,\mathrm{G}}}^{\widetilde{\alpha}^{\,\mathrm{G}}+\delta_2} \mathrm{d}\alpha\, P(\alpha) = 0.475. \tag{5.10}$$

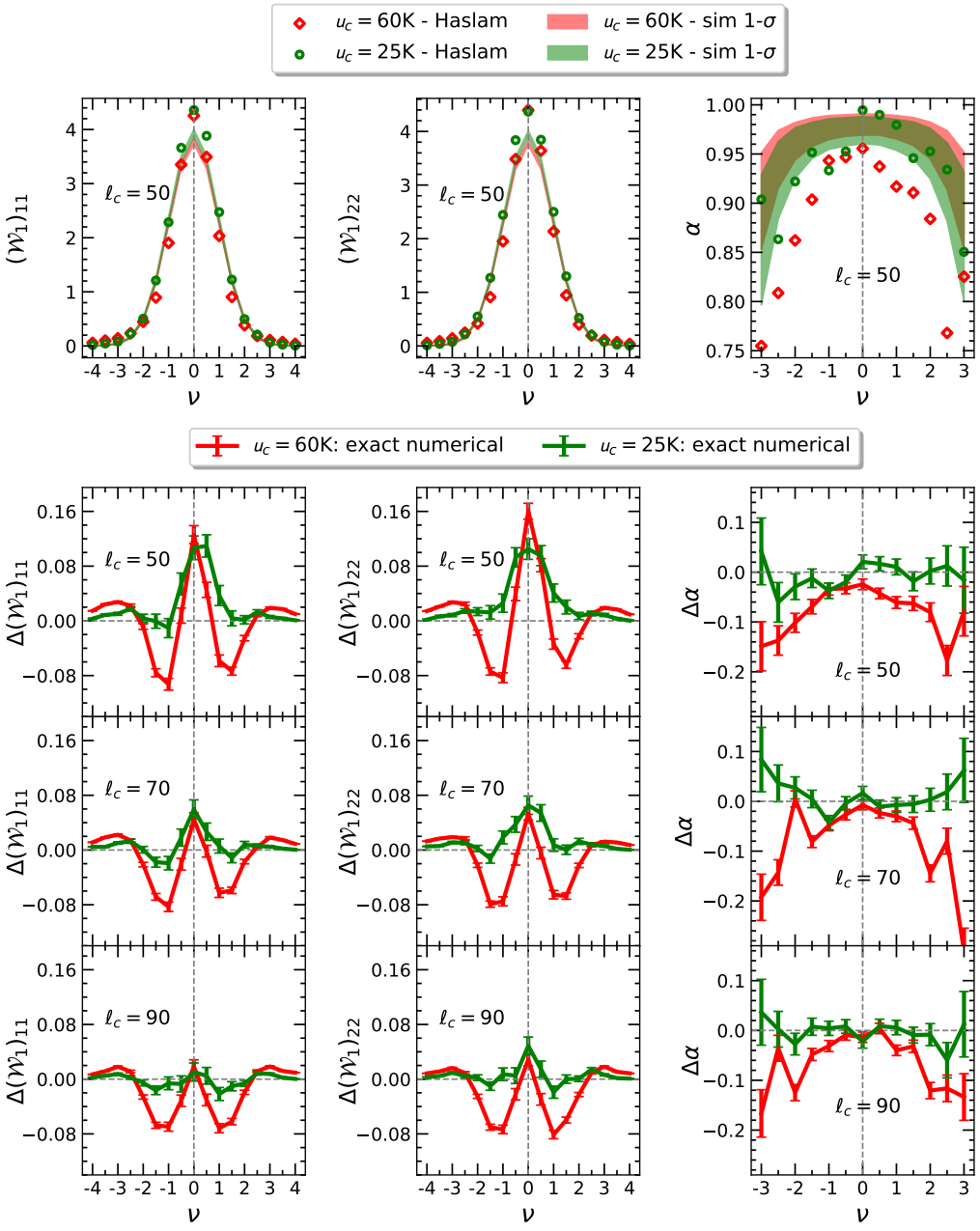

FIGURE 5.7: The first row shows the two diagonal components of tensor MF, $\mathcal{W}_1$ and the anisotropy parameter, α for two temperature thresholds $u_c = 60$ K and $u_c = 25$ K (red diamonds and green circles, respectively) for $\ell_c = 50$. The ensemble mean and 1σ width from 1000 simulated maps are also plotted to show the deviation. Note that, for α, the threshold range is (-3:3). The remaining rows represent the ensemble mean and 1σ width of the deviations, $\Delta\mathcal{W}_1$ and $\Delta\alpha$ with respective normalizations, for $u_c = 60\,\mathrm{K}$ (red solid lines) and $u_c = 60\,\mathrm{K}$ (green solid lines), for $\ell_c = 50, 70, 90$.

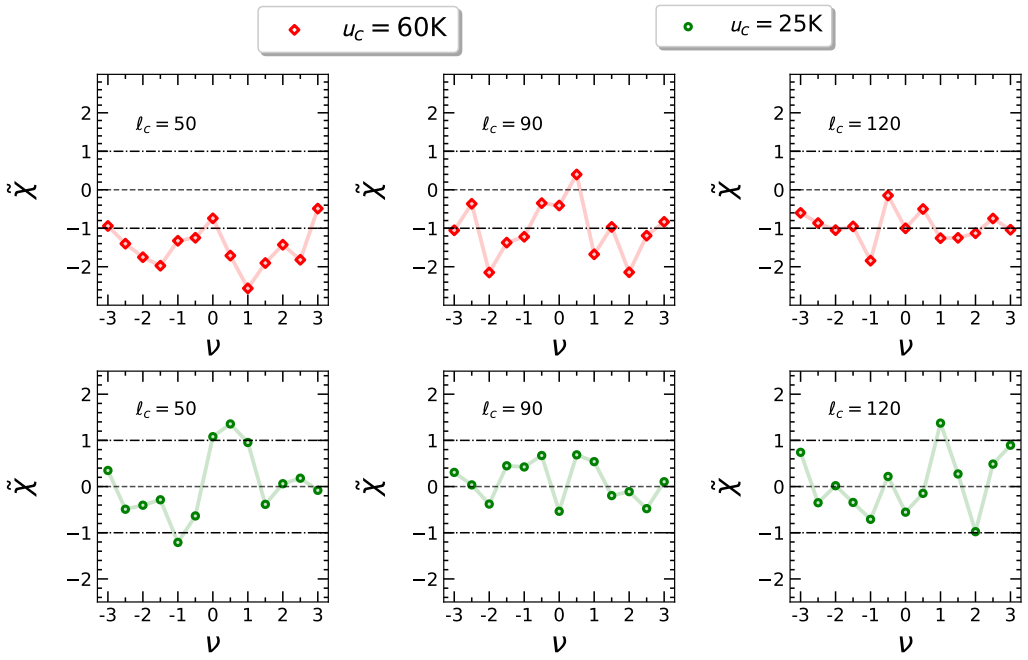

FIGURE 5.8: $\widetilde{\chi}$ values of $\Delta\widetilde{\alpha}$ at each threshold values for $u_c = 60\,\mathrm{K}$ (top panel) and $u_c = 25\,\mathrm{K}$ (bottom panel), and for $\ell_c = 50, 90, 120$. Lines corresponding to $|\widetilde{\chi}| = 1$ (95% confidence interval) are marked for reference.

Let $\Delta\widetilde{\alpha} \equiv \alpha^{\mathrm{Haslam}} - \widetilde{\alpha}^{\mathrm{G}}$. We define $\widetilde{\chi}$ at each threshold to quantify the statistical significance of $\Delta\widetilde{\alpha}$. $\widetilde{\chi}$ is given as,

$$\widetilde{\chi} = \begin{cases} \frac{\Delta\widetilde{\alpha}}{\delta_1}, & \text{if } \Delta\widetilde{\alpha} < 0, \\ \frac{\Delta\widetilde{\alpha}}{\delta_2}, & \text{if } \Delta\widetilde{\alpha} > 0. \end{cases} \tag{5.11}$$

For a Gaussian case, $\widetilde{\chi}$ is equivalent to the square root of the commonly used chi-squared statistic. $|\widetilde{\chi}| > 1$ implies α^{Haslam} is outside the 95% confidence interval and, hence, exhibits statistically significant deviation from the simulations. The sign of $\widetilde{\chi}$ contains useful information – if it is negative, it means more anisotropic, while positive values mean more isotropic than the median value. If the threshold bin size is sufficiently large, α at neighbouring thresholds are uncorrelated. The value $\Delta\nu = 0.5$ that we have chosen is sufficiently large and hence, we can neglect the correlations.

Figure 5.8 shows $\widetilde{\chi}$ versus threshold values, for different u_c and ℓ_c. Lines corresponding to $|\widetilde{\chi}| = 1$ are marked for reference. For $u_c = 60$ K, we find that $\widetilde{\chi}$ is negative for almost all threshold values for all ℓ_c, which is due to $\alpha^{\rm Haslam}$ being smaller than $\widetilde{\alpha}^{\rm G}$. This implies that the Haslam map is genuinely anisotropic in comparison to the isotropic simulations. Further, we observe that $\widetilde{\chi}$ becomes smaller as ℓ_c increases, indicating that the statistical significance of the anisotropy decreases at smaller angular scales. Hence, the small-scale fluctuations of the field tend to follow isotropic distribution. For the case of $u_c = 25$ K, we see that $|\widetilde{\chi}| \leq 1$ for most thresholds and the values fluctuate between positive and negative values for all ℓ_c. Therefore, after excluding the warmer regions of the field (decreasing u_c), we find that the Haslam map exhibits isotropic behaviour even at relatively large scales.

5.4 Summary of results and their implications

Using scalar Minkowski functionals and Minkowski tensors, we have carried out a careful investigation of the statistical properties of one of the major foreground components, namely the Galactic synchrotron given by the full sky 408 MHz Haslam map. The results are summarized as follows.

- Firstly, we find that the overall level of non-Gaussian deviations does decrease as more high-emission regions are masked and as we go down to smaller scales. This is not a new result and corroborates findings in earlier works.

- Our analysis reveals that the leading source of non-Gaussianity of the Haslam map, at all scales, arises from kurtosis terms, with skewness being subdominant. We demonstrate that in the cooler regions of the Haslam map, the non-Gaussian deviations of MFs agree very well with analytic perturbative

expressions, keeping up to kurtosis terms or second-order in the standard deviation of the field.

- The level of non-Gaussianity at the smallest angular scales of $\sim 1.5^\circ$ corresponding to $\ell_c = 120$ probed by the Haslam map has a statistical significance of 3.3σ. This is determined by the area fraction, V_0, which has dependence only on one kurtosis cumulant, K_0. Hence, we conclude that the assumption of Gaussian fluctuations in the synchrotron simulations is not appropriate at this scale. It is, therefore, important to analyse higher-resolution synchrotron maps to determine the validity of the Gaussian approximation at scales smaller than the Haslam scale.

- Lastly, we test the SI of the Haslam map and find that it becomes increasingly more isotropic in the cooler regions of the map as well as at smaller angular scales. This implies that the usual assumption of SI at small scales in component separation methods is supported by the properties of the Haslam map.

It is interesting to note that the shape of non-Gaussian deviations of the MFs for the Haslam map is reminiscent of curvaton models of inflation where the leading contribution for non-Gaussianity comes from terms containing cubic self-coupling of perturbations with coupling parameter $g_{\rm NL}$ (see for example, Enqvist & Takahashi (2008)). As a consequence, we can expect that any residual Galactic synchrotron contamination in the CMB will predominantly bias constraints on $g_{\rm NL}$. Our results indicate that it may be possible to model the Galactic synchrotron fluctuations at smaller scales, along the lines of inflationary perturbations, as an effective field that can be expanded as a Gaussian component plus a small perturbation of the type $\delta I(\vec{x}) \simeq \delta I^{(\rm G)}(\vec{x}) + g_{\rm NL}\left(\delta I^{(\rm G)}(\vec{x})\right)^3$. Here, 'G' stands for the Gaussian component. We expect that $g_{\rm NL}$ can be related to small-scale fluctuations of the GMF and the distribution of relativistic cosmic ray electrons and,

hence, will be useful in constraining them. We will address this issue in the near future.

Our results also imply that any residual synchrotron component that contaminates the CMB will most likely not be captured by estimators of non-Gaussianity, such as the bispectrum. Instead, it can be revealed by trispectrum or real space statistics such as MFs. Therefore, it is necessary to analyse foregrounds using a multitude of complementary statistics to uncover their true statistical nature. Further, it is important to probe non-Gaussianity and SI of foreground fields at scales smaller than the resolution of the Haslam map. It is also important to probe different Galactic components at frequencies ranging from radio to infrared, such as done by Coulton & Spergel (2019) using the bispectrum. We plan to carry out a detailed investigation of the non-Gaussian nature and SI of different foreground components at different frequencies relevant to the CMB, EoR and line intensity mappings using Minkowski tensors and trispectrum.

Appendix

5.A Consistency checks of the Gaussian simulations with Haslam data

Gaussian isotropic simulations of the Haslam map are obtained to quantify the statistics explored in this work. The power spectrum of the Haslam map is generated using `PolSpice` (Szapudi et al. 2001; Chon et al. 2004). It gives the full angular power spectrum of any given map corrected for masking, beam and pixel effects and the residuals via the incomplete sky coverage. This power spectrum acts as input for generating Gaussian isotropic simulations using `HEALPIX` subroutines. In essence, the Haslam data and simulations are expected to match at the power spectrum level, and it is crucial to check the consistency of these simulations with respect to the data.

Using `anafast` subroutine of `HEALPIX` package, the pseudo power spectrum (C_ℓ) is computed for Haslam data and 1000 simulations after following the pre-processing pipeline discussed in section 5.2. In figure 5.A.1, the binned power spectra of the data as well as the mean C_ℓ and 1σ error bars from the simulations are shown for two of the masks ($u_c = 60\,\mathrm{K}$ & $25\,\mathrm{K}$) used in our analysis. It is found that the power spectrum for Haslam data and Gaussian isotropic simulations match

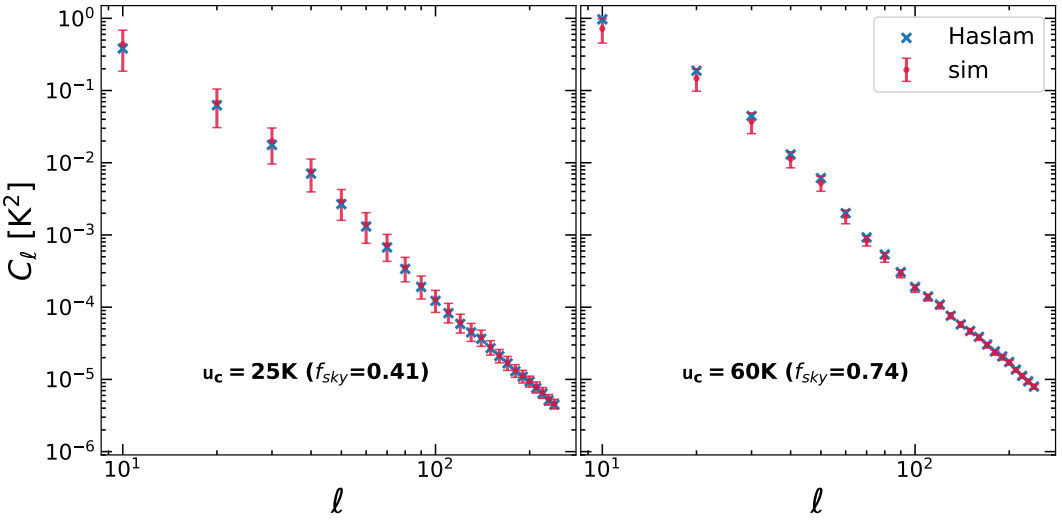

FIGURE 5.A.1: The binned angular power spectrum C_ℓ for the Haslam data and simulations obtained using `anafast` subroutine for two different sky fractions used in our analysis. The blue cross denotes the binned C_ℓ for Haslam data, while the red error bars indicate 1σ width of binned C_ℓ from 1000 Gaussian isotropic simulations. It is seen that 1σ matching is obtained for both the sky fractions. This confirms the accuracy of the power spectrum computed using `PolSpice` and, therefore, the credibility of our results compared with respect to the 1000 Gaussian isotropic simulations.

within 1σ in both cases. This confirms that the computation of the Haslam power spectrum using `PolSpice` is sufficiently accurate and, therefore, the credibility of our results compared with respect to the generated Gaussian isotropic simulations.

5.B Probability distribution function of the Haslam map

It is helpful to visualize the PDF of the Haslam map along with those of Gaussian simulations for different temperature and multipole cut values. To do so, we first define $\nu \equiv u/\sigma_0$ which is the field value normalized by the σ_0 value, for each ℓ_c. In figure 5.B.1, the PDFs of the Haslam map are shown as red diamonds for $u_c = 60$

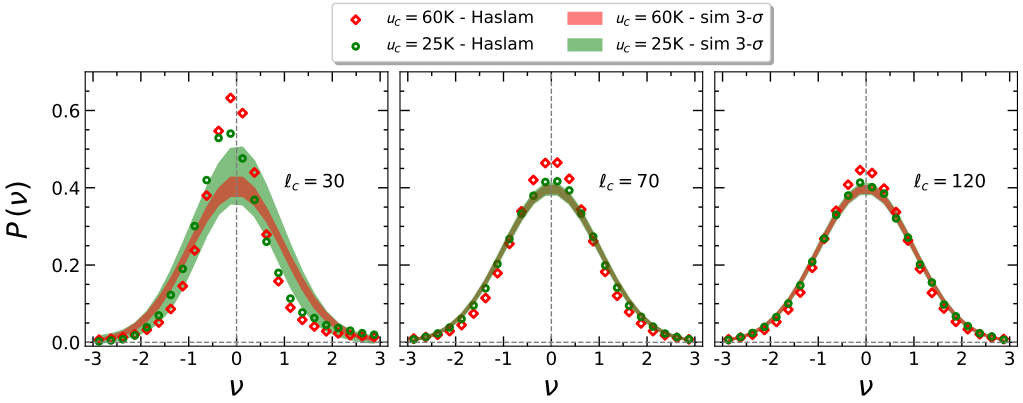

FIGURE 5.B.1: The PDFs for the Haslam map and 1000 Gaussian simulations for different values of u_c and ℓ_c. The PDFs visually indicate approximate symmetry about the field mean value zero and decreasing levels of deviation with respect to the Gaussian expectations, with decreasing u_c and towards higher ℓ_c. These results are obtained using the mask boundary threshold value, $s_m = 0.9$.

K and green circles for $u_c = 25$ K, using the mask boundary threshold value, $s_m = 0.9$. Visually, we find approximate symmetry about the field mean value zero and decreasing levels of deviation with respect to the Gaussian expectations, with decreasing u_c and increasing ℓ_c. From this figure, we can anticipate that the kurtosis cumulants will have larger values compared to the skewness ones, supporting our observation that the nature of Haslam non-Gaussianity is predominantly of kurtosis origin.

Chapter 6

Multi-frequency Statistics of Synchrotron Temperature and Polarization Maps*

6.1 Introduction

In the previous chapter, we carried out a detailed examination of the small-scale non-Gaussianity of the all-sky 408 MHz Haslam synchrotron map using scalar Minkowski functionals (MFs) and Minkowski tensors (MTs). Our analysis shows that within the limited resolution of the Haslam map, the level of synchrotron non-Gaussianity is not low enough to assume Gaussianity. However, there is a decreasing trend towards smaller scales. On the other hand, statistical isotropy (SI)

*The chapter is based on the work which has been accepted for publication in JCAP. The pre-print is available as Rahman et al. (2022)

was found to be valid at Haslam resolution. We also found that non-Gaussianity at small scales is kurtosis-type.

In this chapter, we extend this analysis and focus attention on the morphological properties of observed synchrotron temperature and polarization maps provided by WMAP (Bennett et al. 2013), Planck (Planck Collaboration et al. 2020a) and BeyondPlanck (BeyondPlanck Collaboration et al. 2020). For comparison, we also include the combined map of the 1.4 GHz radio continuum survey from Stockert and Villa-Elisa telescopes (Reich & Reich 1986; Testori et al. 2001). We analyse various all-sky maps observed at frequencies from 1.4 GHz to 33 GHz and make a comparison with the Haslam map. We also compare with simulated foreground maps given by the Python Sky Model (PySM) (Thorne et al. 2017). Then, we study the synchrotron maps given by different component separation pipelines of WMAP, Planck, and BeyondPlanck. The main objective of this work is to examine whether the statistical features of synchrotron radiation are frequency-dependent and to compare the non-Gaussian and SI nature of these observed synchrotron maps with previous results of the Haslam map. A similar analysis focusing on synchrotron polarization was carried out in a recent work by Martire et al. (2023).

The chapter is organized as follows. We begin with a short description of the data sets used in this work in section 6.2. In section 6.3, we explain the data analysis pipeline we adopt. Section 6.4 contains the results for the morphology of total foreground maps at different observing frequencies and comparison with simulated total foreground maps. Section 6.5 includes the results for the component-separated synchrotron temperature and polarization maps. In section 6.6, we conclude the chapter with a summary and discussion of our results. Appendix 6.A describes the estimation of instrumental noise for different experimental setups and maps. In appendix 6.B, we estimate the signal-to-noise ratio (SNR) of WMAP and Planck total foreground maps. In appendix 6.C, we discuss the possible contribution of

instrumental systematics in our results. Lastly, appendix 6.D discusses the morphology of two composite fields – synchrotron plus AME and synchrotron plus free-free.

6.2 Data sets used

In this section, we describe the data sets used in this work. We also describe Gaussian simulations and simulations of foreground emissions given by PySM.

There are various publicly available data sets for observations of diffuse emissions in the frequency range of the order of 100 MHz to 100 GHz. For our study here, we choose data sets that have full sky coverage. The particular data sets that are used in our analysis are given below[†].

6.2.1 All-sky temperature maps at different frequencies

The observed temperature data at specific frequencies (ν)[‡] in the range 0.408 to 33 GHz that we analyse (see section 6.4) are the following.

1. The Haslam 408 MHz map (Haslam et al. 1982) is used as the *fiducial* map which other data sets are compared with. We use the map provided by Remazeilles et al. (2015).

[†]Data sets are taken from
https://pla.esac.esa.int/
https://lambda.gsfc.nasa.gov/
https://beyondplanck.science/

[‡]In this chapter, the symbol ν denotes the frequency of the maps we are looking at, but in other chapters, it stands for the threshold values. Also, in this context, ν_t represents the threshold values.

2. The combined all-sky map at 1420 MHz from the northern sky survey using Stockert 25 m telescope (Reich & Reich 1986) and the southern sky survey with 30 m Villa Elisa telescope (Testori et al. 2001). We refer to this map as the Stockert-Villa map.

3. WMAP K band (23 GHz) and Ka band (33 GHz) maps (Bennett et al. 2013).

4. Planck 30 GHz map from PR3 data release (Planck Collaboration et al. 2020a).

We will refer to these as *frequency maps*. These maps contain all components of Galactic emissions, with the contribution of each component varying with the observing frequency.

6.2.2 Component separated temperature and polarization synchrotron maps

We use the synchrotron maps given by different component separation algorithms in WMAP and Planck experiments. The temperature maps are listed as follows:

1. *WMAP synchrotron map at K-band derived using Maximum Entropy Method (MEM)*: MEM is a pixel-based Bayesian model-fitting technique assuming a spectral model for different Galactic components and using external data sets as priors (Bennett et al. 2003). Here, the synchrotron spectrum is considered as a power law with spectral index $\beta_s = -3.0$, and the Haslam map is used as the external prior template for synchrotron emission.

2. *WMAP synchrotron map obtained using MCMC technique*: This is the standard MCMC approach of sampling the posterior distribution given the data

sets and a data model (Hinshaw et al. 2013b). The sky model is constructed based on the spectral features of different astrophysical components. Apart from the 5 WMAP frequency bands, the Haslam map is also included in the data analysis. Different MCMC maps are available based on slightly different assumptions in modelling foreground spectra, which are summarised below.

- MCMC-c — follows a power-law spectrum for synchrotron, free-free, and thermal dust emissions, with the synchrotron and dust spectral indices as free parameters.
- MCMC-e — includes spinning dust emission, but the synchrotron spectral index is fixed to -3.
- MCMC-f — similar to MCMC-e, except that the synchrotron spectral index is allowed to have spatial variation, with the spectrum taking a pure power law form.
- MCMC-g — similar to MCMC-f with the synchrotron spectral index varying as a function of frequency according to Strong et al. (2011), instead of a pure power-law.

3. *Planck synchrotron map derived using* `Commander` *pipeline*: `Commander` involves standard Bayesian formalism of fitting an explicit parametric sky model to the data and computing the joint posterior distribution. These parameters, corresponding to CMB as well as astrophysical components, are then estimated at each pixel by sampling the posterior via Gibbs sampling (Eriksen et al. 2008). In addition to Planck HFI and LFI data, the nine-year WMAP sky maps and the Haslam map are also used as external data sets to disentangle the degeneracy between different low-frequency Galactic components.

4. *BeyondPlanck synchrotron map*: BeyondPlanck is an end-to-end Bayesian technique that together takes care of instrument characterization, map-making, and component separation, using a single statistically consistent

data model (BeyondPlanck Collaboration et al. 2020). It is implemented as `Commander3`, an extended version of the `Commander` pipeline, applied to time-ordered data (TOD). In this analysis, Planck LFI data sets, along with Haslam and Planck dust maps, are used as input maps.

For polarization studies, we use the synchrotron maps given by WMAP MCMC-g and Planck `Commander` methods. Although other polarized foreground components like thermal dust are negligible in the low-frequency bands of WMAP and Planck, polarization maps are dominated by noise, and we use component-separated maps to minimize the bias due to it.

6.2.3 Simulated data

We use two kinds of simulated data for the analysis. Brief descriptions of the simulations are given below.

6.2.3.1 Gaussian Simulations

For quantifying the non-Gaussianity and anisotropy of a given map whose properties are a priori unknown, we need to compare with suitable Gaussian isotropic simulations. In this work, we generate these simulations by calculating the angular power spectrum of the given map and then using it as input for producing Gaussian isotropic maps. The angular power spectra are obtained using the `NaMaster`[§] package, which corrects for leakage due to masking, instrumental beam and pixelation effects (Alonso et al. 2019). Although the given map may contain non-Gaussian and anisotropy features, by using its power spectrum as input to

[§] https://github.com/LSSTDESC/NaMaster

produce Gaussian isotropic maps, we ignore the non-Gaussianity and anisotropy. We produce 1000 such maps with the `synfast` function of the `healpy`[¶] package. These simulations accurately replicate the given map at the power spectrum level and serve as Gaussian isotropic equivalents of the map being analysed.

6.2.3.2 PySM simulated temperature maps

The Python Sky Model (PySM) is a publicly available software package[‖] for simulating foreground emissions in intensity and polarization at microwave and sub-mm frequencies (Thorne et al. 2017). It provides simulations of the different foreground components. Though our analysis in this paper primarily focuses on synchrotron, other foreground emissions, like free-free and AME emissions, are also relevant when we study the observed data at different frequencies. For this reason, below we discuss the models of the synchrotron, free and AME incorporated in PySM that are relevant to our analysis here. PySM provides high-resolution maps of foreground emissions well above the resolution of the template maps used. This is prepared by injecting Gaussian isotropic fluctuations into these maps at small angular scales[**]. For further details, see Thorne et al. (2017). Note that we discuss simulations for temperature only. We do not make use of polarization simulations as we do not carry out an analysis of the frequency variation of polarization maps.

[¶] https://healpy.readthedocs.io/

[‖] https://pysm3.readthedocs.io/

[**] Different approaches are adopted to add small-scale information in foreground maps. For example, in Delabrouille et al. (2013); Remazeilles et al. (2015), for synchrotron, Gaussian random field G_{ss} is generated using a power-law model of power spectrum that fits well with the observational data. Thorne et al. (2017) adds a log-normal distributed map for synchrotron at small scales to ensure that the final map has positive values. The free-free power spectrum is flatter than the synchrotron, so a direct extrapolation using the angular power spectrum results in excess power at small scales. Instead, the gradient of the free-free power spectrum is fixed as $\gamma = -0.5$, and this power spectrum is used to generate the Gaussian realizations. The high-resolution thermal dust maps are used as a proxy for AME at small angular scales.

Synchrotron simulations: Synchrotron temperature spectrum is modelled as a power-law scaled to the 408 MHz all-sky `Haslam` map using the following relation,

$$I_\nu(\hat{n}) = I_{0.408}(\hat{n})\left(\frac{\nu}{0.408}\right)^{\beta_s(\hat{n})}, \tag{6.1}$$

where I_ν is the amplitude of the map at frequency ν (in GHz). β_s is the spatially varying synchrotron spectral index and $I_{0.408}$ is the amplitude of Haslam map. The above equation gives different models based on how β_s is modelled. We consider the three main PySM models of β_s in our analysis, which are explained below:

1. *Model* `s1`: A spatially varying β_s is assumed based on the all-sky spectral index map 'Model 4' of Miville-Deschênes et al. (2008), prepared using WMAP and Haslam synchrotron maps and a model of Galactic magnetic field. The variation of β_s with frequency is not considered here.

2. *Model* `s2`: This model takes into account only the spatial steepening of β_s away from the Galactic plane; β_s is a function of the Galactic latitude b, given by the relation $\beta_s = \beta_{b=0} + \delta_\beta \sin|b|$, in accordance with WMAP. Again, β does not vary with frequency.

3. *Model* `s3`: This model takes into account the curvature of β_s above a certain frequency ν_c, given as $\beta_s = \beta_0 + C\ln(\nu/\nu_c)$. The spatial variation is given by β_0, which follows the same model as in `s1`. The curvature parameter C is 0.052 with $\nu_c = 23$ GHz (Kogut 2012).

Figure 6.2.1 shows maps of β_s for models `s1` and `s2`. Model `s3` does not differ from model `s1` in morphology; hence, we have not shown it. Further, Gaussian isotropic realizations are directly injected into the Haslam map to enhance the small-scale information.

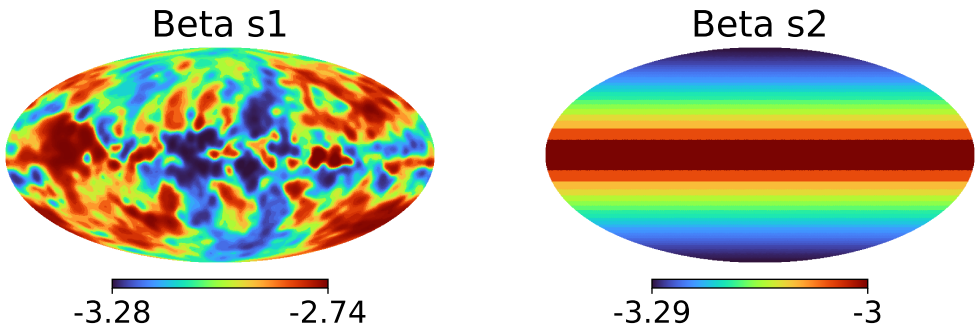

FIGURE 6.2.1: The synchrotron spectral index (β_s) maps for PySM models `s1` (left) and `s2` (right).

Free-free simulations: We follow the PySM free-free model called `f1`. This is the analytical model for free-free emission given in Draine (2011) and used in the `Commander` analysis (Planck Collaboration et al. 2016b), which gives a degree-scale map of free-free at 30 GHz. In addition, small-scale fluctuations are added to this map and then rescaled to the desired frequency following a spatially constant spectral index value of -2.14.

AME simulations: AME model considered is `a1`, which takes AME as the sum of two spinning dust populations based on the `Commander` pipeline (Planck Collaboration et al. 2016b). AME components are characterized by an emission template at a reference frequency and a peak frequency of the emission law. Both components follow a spatially varying emission template given by the `SpDust2` code. However, the first component has a spatially varying peak frequency, while the second one has a spatially constant peak frequency. Also, small-scale fluctuations are injected into the emission maps.

Dust simulations: For thermal dust emission, `d1` model is followed, which assumes the dust spectra to be a single-component modified black body (mbb). Planck 545 GHz map is used as dust templates in intensity, which is then scaled to different frequencies following the mbb spectrum using the (spatially varying) dust temperature and spectral index, derived from Planck data using `Commander`

algorithm (Planck Collaboration et al. 2016b).

6.3 Analysis pipeline

For meaningful comparison between different observed data sets and also a meaningful comparison of observed data with simulations, we first need to ensure that the observed and simulated data are produced at the same resolution, have the same physical units and all processing steps of masking and bandpass filtering must be identically applied. The observed data considered in this work are given at different resolutions. We downgrade all the maps (and upgrade WMAP MCMC maps) to $N_{\rm side} = 128$ as the Haslam data is given at this resolution. For consistency, we also convert the maps that are given in units of CMB temperature ($\rm K_{CMB}$) to the Rayleigh-Jeans unit ($\rm K_{RJ}$).

The main data analysis pipeline prior to the calculation of MFs and MTs consists of bandpass filtering to remove large-scale modes, followed by applying a mask. These steps are identically applied to all the observed and simulated data. Below we describe the bandpass filtering and masking processes.

Bandpass filtering: As done in chapter 5, to probe small-scale features of the field, a bandpass filter is applied in the harmonic space to suppress the large-scale fluctuations. The filter function we use is

$$f(\ell) = \frac{1}{4}\left\{1 + \tanh\left(\frac{\ell - \ell_c}{\Delta\ell}\right)\right\}\left\{1 - \tanh\left(\frac{\ell - \ell^*}{\Delta\ell}\right)\right\}. \tag{6.2}$$

This filter function contains two cutoff scales. The lower cutoff, ℓ_c, determines the scale beyond which larger size (smaller ℓ) fluctuations are filtered out. The higher cutoff, ℓ^*, is set by the beam size of the Haslam map (56 arcmins). We use $\ell^* = 180$. We also need to ensure that spurious ringing effects are not introduced

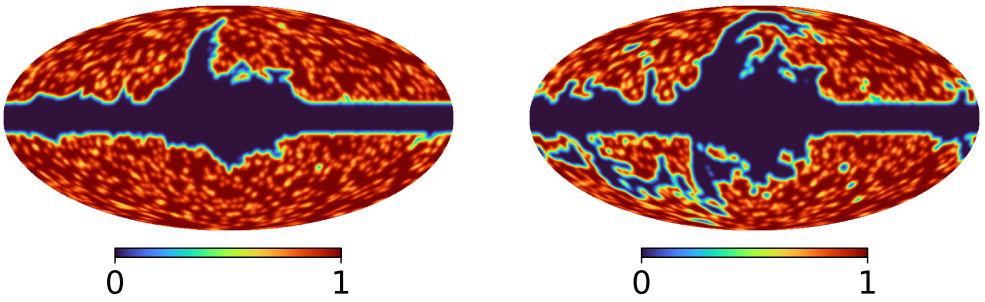

FIGURE 6.3.1: Maps of the *threshold* mask (left) and *filament* mask (right), after applying a Gaussian smoothing of FWHM = 180 arcmin.

after harmonic transform due to a sharp change of $a_{\ell m}$ values at ℓ_c. A too-small value of $\Delta\ell$ will introduce ringing, while too large will not provide a reasonable filter of modes. We choose $\Delta\ell = 10$ as a reasonable compromise between the above two factors. Directly applying the filter on foreground maps results in ringing structures due to the bright Galactic emission. To avoid this, we initially mask the Galactic region by identifying the pixels where the Haslam map has values greater than 80 K.

Masking: We mask some parts of the sky to exclude the brightest regions in the synchrotron sky while retaining the regions where synchrotron signals are significant and where CMB analysis is carried out.

We use the Haslam map as the reference for deciding high-emission regions. We also remove point sources identified by Planck. The steps involved in preparing the mask are as follows.

1. Apply a Galactic cut $\mid b \mid < 10°$, b being the Galactic latitude.
2. Sort all pixels in increasing order of the values of the Haslam map, and then mask 25% of the pixels counting down from the highest value. This corresponds to masking all the pixels in the reference map with values above 35 K.

3. Lastly, we multiply the above mask by the Planck LFI point sources mask to remove contamination from extra-galactic point sources.

We refer to this final mask as the *threshold mask*. It retains 65% of the sky. The left panel of figure 6.3.1 shows this mask.

For the purpose of testing the robustness of our findings, we use another mask in our analysis, the so-called *filament mask* (Vidal et al. 2015). This mask removes large filamentary structures seen in the Haslam map and WMAP polarization maps in addition to the masked regions of the threshold mask. It has a sky-fraction of 53%. Figure 6.3.1 (right panel) shows this mask.

To minimise the error due to the sharp mask boundary when performing harmonic transforms, we apodized the masks with a Gaussian smoothing of 3° FWHM. Also, we estimate the MFs only on pixels where the apodized mask has values greater than 0.9 so as to avoid any residual contamination from the boundary pixels.

6.4 Results – morphology of observed frequency maps and comparison with PySM simulated maps

In this section, we focus on the observed frequency maps outlined in section 6.2.1, studying their angular power spectra and morphology. We compare them with PySM simulated maps of the *total Galactic foregrounds* consisting of synchrotron, free-free, AME and thermal dust emissions. We then include a discussion of only synchrotron temperature simulations from PySM.

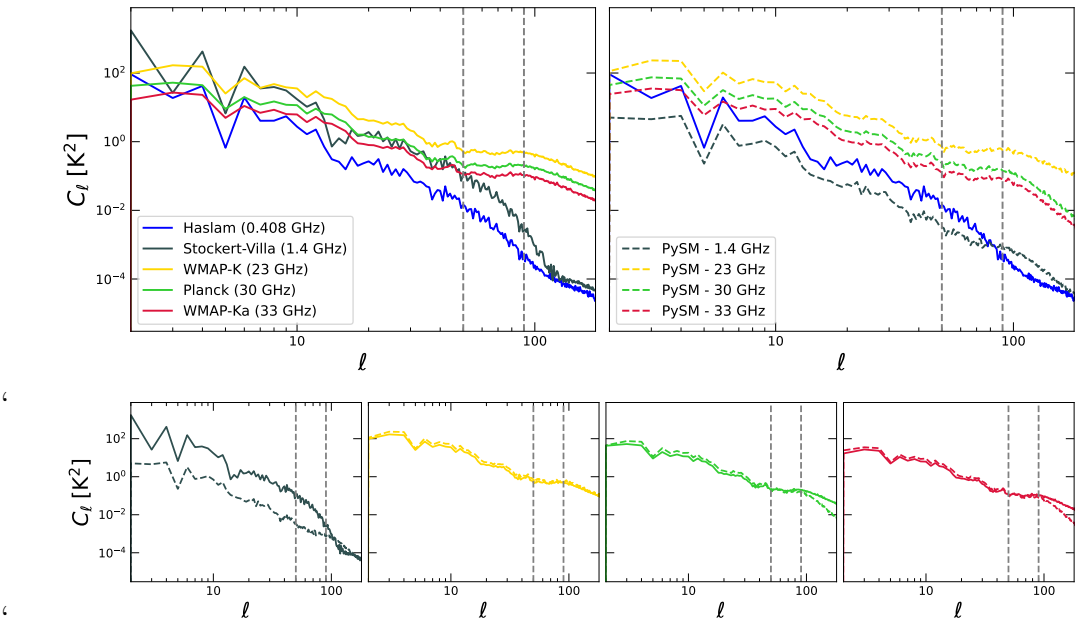

FIGURE 6.4.1: *Top left:* C_ℓs of the observed frequency maps. *Top right*: C_ℓs of the PySM simulated total foreground maps at the same frequencies as the left panel. *Bottom*: Comparison plots of observed frequency (solid lines) and corresponding PySm total foreground maps (dashed lines) at each frequency (increasing frequency from left to right). The vertical lines correspond to $\ell = 50, 90$.

Out of the observed frequency maps studied here, Haslam and Stockert-Villa maps are known to be predominantly synchrotron emission, while WMAP and Planck frequency maps contain CMB, AME, and free-free emissions apart from synchrotron (Davies et al. 2006; Ghosh et al. 2012). In order to focus only on the total foreground emission, best-fit CMB maps are subtracted from WMAP and Planck frequency maps. The CMB maps used are the ones provided by the respective experiment. We do not subtract the CMB component from the Stockert-Villa map, as the CMB contribution is expected to be negligible.

6.4.1 Angular power spectra of observed frequency maps and PySM simulated total foreground maps

For computing the power spectra, all maps are scaled to Haslam frequency (408 MHz) using the power-law synchrotron spectrum given by eq. (6.1), with a constant spectral index (β_s). For Stockert-Villa and the corresponding PySM map, we use $\beta_s = -2.5$, while for other maps at higher frequencies, we use $\beta_s = -3.0$, accounting for the spectral steepening at higher frequencies. We then calculate the angular power spectra of the maps after masking, using `Namaster`. This constant scaling makes the amplitudes of the power spectra comparable. But it will not affect the morphology, as discussed previously. The plots for the observed frequency maps are shown in figure 6.4.1 (top left). Also shown are the power spectra of simulations of the total foreground emissions obtained from PySM at the same frequencies (top right) as the observed frequency maps. The top left panel shows that the power spectra at 23, 30 and 33 GHz are distinctly flatter than those of Haslam and Stockert-Villa from roughly $\ell \sim 50$. Apart from a shift of the amplitudes, their shapes are similar. Stockert-Villa map shows a similar shape of the power spectrum as Haslam map till roughly $\ell \sim 90$. On the top right panels, we observe that the PySM simulated total foreground maps at the three higher frequencies also exhibit similar flattening behaviour. In contrast, the 1.4 GHz map is quite different from Stockert-Villa. We can observe that the shape of power spectrum for 1.4 GHz map is similar to the power spectra of PySM maps at higher frequencies.

In the bottom panels of figure 6.4.1, we compare C_ℓ of each observed frequency map with the corresponding simulated map so as to highlight their similarities or differences. We see that Stockert-Villa shows considerable differences across all scales from the simulation, as noted above. At 23 GHz, the power spectra of observed and simulated maps are overlapping, while at 30 and 33 GHz, the observed maps show higher power towards small scales. We will find this comparison of the

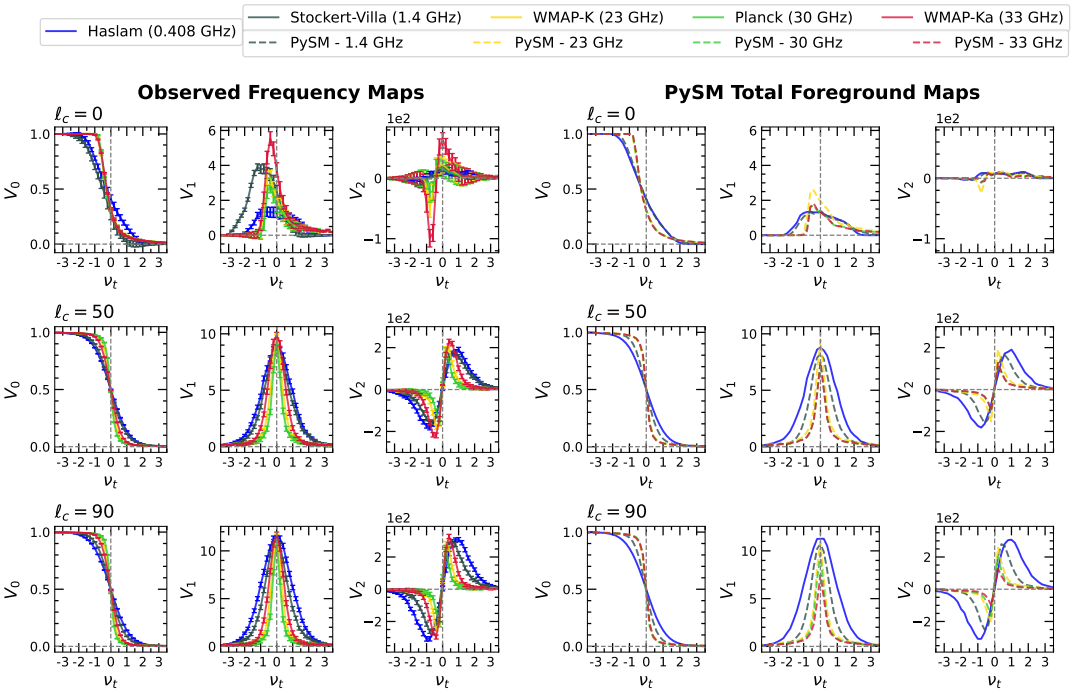

FIGURE 6.4.2: *Left, 'Observed Frequency Maps'*: MFs versus threshold values, ν_t, for each observed frequency map are shown, for different angular scales: $\ell_c = 0$, 50 and 90. *Right, 'PySM Total Foreground Maps'*: Same plots as the left panel, but for PySM total foreground maps simulated at the frequencies corresponding to the observed frequency maps.

power spectra between observed and simulated maps useful when we discuss the morphology of the maps below.

6.4.2 Morphology of observed frequency maps and comparison with PySM simulated total foreground maps

MFs are computed for all the maps after bandpass filtering for different values of ℓ_c and then masking. Our goal here is to understand how the morphology of the total foreground emissions transforms with frequency — from the frequency of the Haslam map where synchrotron dominates to higher frequencies where AME and free-free emissions become the dominant components. This exercise can shed

light on how morphological properties of synchrotron emission can be biased by contamination by residual AME or free-free emissions.

To estimate the uncertainties of the MFs arising from cosmic variance and instrumental noise for each observed frequency map we compute Gaussian simulations using its angular power spectrum as the input, as described in section 6.2.3.1. To each simulation, we add an instrumental noise map, prepared based on the steps outlined in appendix 6.A . We then compute MFs from the resulting maps and calculate their standard deviation σ at each threshold value. For the Planck map, we use 300 Full Focal Plane (FFP10) simulations, and thus only 300 Gaussian simulations are used (Planck Collaboration et al. 2020b). In all plots, we will show 2σ error bars.

MFs for the frequency maps for $\ell_c = 0$, 50 and 90 are shown on the left panels of figure 6.4.2 under the heading 'Observed Frequency Maps'. The case $\ell_c = 0$ corresponds to no bandpass filtering. We find considerable variation with frequency of all three MFs that can be easily discerned by eye for all ℓ_c values. For $\ell_c = 0$, there is a systematic increase of the amplitudes of V_1 and V_2 as the frequency increases. Since V_2 is a direct count[††] of the difference between the number of hot spots and cold spots (or structures) this amplitude increase indicates that the number of small scale fluctuations increases as the frequency increases. This increase of power for $\ell > 50$ for higher frequencies is observed in the power spectra shown in figure 6.4.1. In comparison, the Stockert-Villa map exhibits anomalous behaviour (or non-conformity with the trend followed by WMAP and Planck maps), which is most evident from the broad shape of V_1. This could be arising from the poorly understood instrumental effects and calibration uncertainties associated with this map. We intend to address these issues in the future.

[††]Strictly speaking, V_2 is equal to the Euler characteristic, which is the difference between the numbers of hot spots and cold spots on *flat space*. On the sphere, V_2 can be equated to the Euler characteristic to good approximation provided the number of hot/cold spots is high, as is the case for the fields under consideration here.

For $\ell_c = 50$ and 90, the amplitudes of both V_1 and V_2 are larger than those of $\ell_c = 0$. This is because filtering out large ℓ modes leaves behind only smaller-scale structures, which become more numerous as ℓ_c increases. We observe that the amplitudes become comparable for all the frequencies while the shapes still exhibit considerable differences. Visually, we can also see that the shapes V_1 and V_2 for higher frequencies are significantly more non-Gaussian than the Haslam map. This can be discerned by comparing with the expected shapes for Gaussian fields given in figure 3.3. This is due to AME and free-free becoming the dominant components at these frequencies. This is demonstrated in appendix 6.D where we compare the morphology of AME, synchrotron and AME+synchrotron, and free-free, synchrotron and free-free +synchrotron using simulations obtained from PySM.

We mention below two factors that can additionally contribute to the variation of the morphology of the total foreground with frequency and comment on their importance.

1. *Instrumental noise*: The error bars shown in figure 6.4.2 take into account instrumental noise as mentioned earlier. In appendix 6.B, we have determined the contribution of instrumental noise to the frequency maps of WMAP and Planck. SNR of the maps is found to be much higher than one at all pixels (see figure 6.B.1). This implies that noise has minimal effects on the variation of the morphology with frequency. We have also checked this expectation by repeating all calculations after applying an additional smoothing to all the maps since smoothing has the effect of decreasing noise, though at the cost of losing resolution. We find that our results are robust. Hence, we conclude that the frequency variation of the MFs is not due to white noise. Further, the contribution of instrumental systematics has been explored in appendix 6.C, using WMAP and Planck individual year maps. Our analysis shows that the error bars due to instrumental effects are smaller compared

to the morphological distinction in these maps. This implies that the systematics play a minimal role in the observed morphological differences. Note that we have not checked the instrumental effect for the Stockert-Villa map since the data that is available is not sufficient to estimate the SNR of the map and the instrumental uncertainties.

2. *Unresolved extra-Galactic point sources*: While the point sources mask provided by Planck is included in the threshold mask that we used in our calculations, it is possible that unresolved sources contribute to and contaminate the observed frequency maps. The effect of this on the angular power spectra will be to increase the power at higher multipoles (see also figure 14 and section 4.1 of Remazeilles et al. (2015)). This will lead to an increase in the number of structures at the corresponding scales, which positively contribute to V_1 and V_2. A proper quantification of the contribution and their distinction from true frequency variation of the total foreground field will require realistic modelling of the point sources, and we postpone it to a future investigation.

Next, we focus on simulations of the total Galactic foreground obtained from PySM at the same frequencies as the observed frequency maps. We then compare (visually) the morphology between the observed and simulated maps. This comparison serves the purpose of checking how well the foreground models of PySM reproduce the observed frequency maps beyond the power spectrum. We produce simulated maps containing synchrotron, free-free, AME and thermal dust emissions using PySM. The modelling of these components has been described in section 6.2.3.2.

MFs are computed for these maps after identically masking and bandpass filtering as done for the frequency maps. The results are shown in the right panels of figure 6.4.2. The values of ℓ_c and all the x and y axis ranges are the same as those for the observed frequency maps for easy comparison. For $\ell_c = 0$, visually, we see

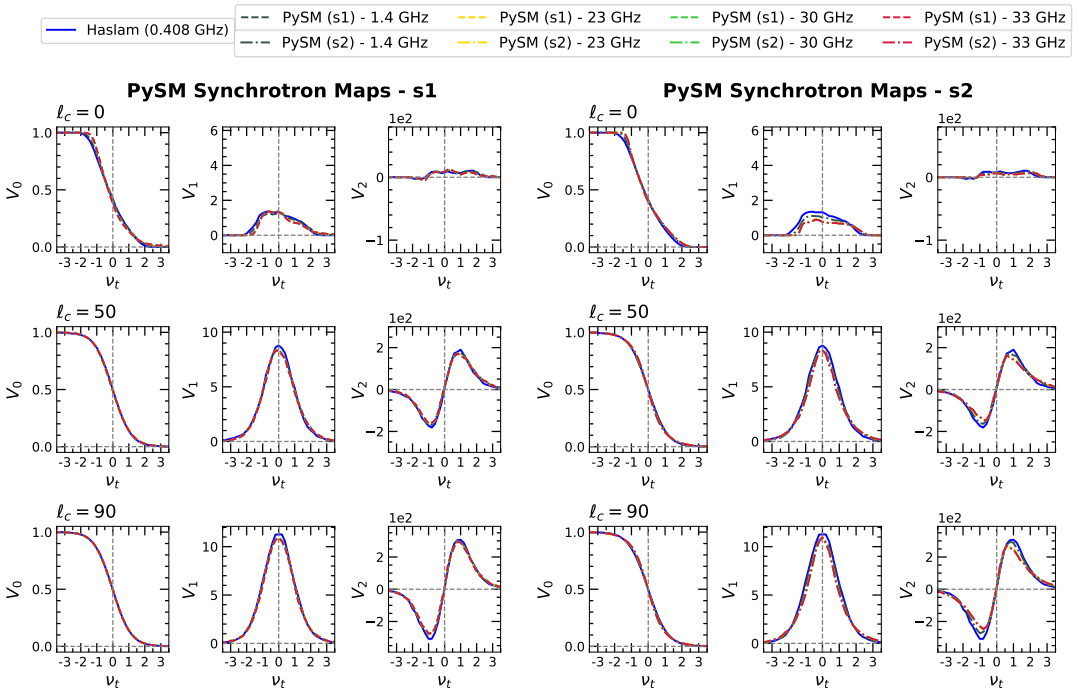

FIGURE 6.4.3: Plots of the MFs versus the threshold ν_t for PySM synchrotron maps for models `s1` (left panels), and `s2` (right panels), for $\ell_c = 0, 50$ and 90. The frequencies of the maps and the scales of all the panels are the same as in figure 6.4.2.

that the observed frequency maps and simulated PySM maps at each frequency, except 1.4 GHz corresponding to Stockert-Villa, show good agreement for V_0 both in amplitude and shape. The amplitudes of V_1 and V_2, however, are much lower for the simulations for all the frequencies. For smaller scales $\ell_c = 50$ and 90, we obtain better agreement of the shape and amplitudes of the three MFs with the corresponding MFs of the observed frequency maps. This indicates that PySM reproduces observed foreground maps better towards smaller scales compared to large scales.

6.4.3 Morphology of PySM simulated synchrotron temperature maps

We now discuss the morphology of PySM simulated synchrotron maps based on the two models `s1` and `s2`. We generate the maps at the same frequencies as the observed frequency maps. The morphology of these maps will be determined by the spatial variation of the synchrotron spectral index. For model `s1`, β_s fluctuates spatially only mildly. If we denote by σ_0^β and σ_1^β the rms of β and the rms of the gradient of β, respectively, we obtain the typical angular fluctuation size of β to be $\theta_c = \sigma_0^\beta/\sigma_1^\beta \sim 4^\circ$. Below this scale, MFs will only encode the morphology of the Gaussian small-scale fluctuations injected in PySM. Model `s2` has even less fluctuations since it varies only along the Galactic latitudes. Therefore, for both models, we expect only a small variation with frequency.

The results for V_k are shown in figure 6.4.3. All panels follow the same format as figure 6.4.2. The y-axis ranges for V_k are also the same. As anticipated in the paragraph above, for all three values of ℓ_c, we find that the variation with frequency of V_k for both the synchrotron models are smaller compared to what we found in figure 6.4.2. When we compare these results with the morphology of PySM total foreground maps, the large difference can clearly be attributed to the presence of the other foreground components, namely, free-free and AME, in the total foreground.

Further comparing models `s1` and `s2`, we find that both models do not differ much for $\ell_c = 0$. However, towards smaller scales, model `s2` demonstrates larger variation with respect to the Haslam map, and the difference increases as the frequency increases. This may not be immediately apparent when looking at figure 6.4.3, but it becomes noticeable in the overall trend of average morphology shown in figure 6.4.4 of the next subsection.

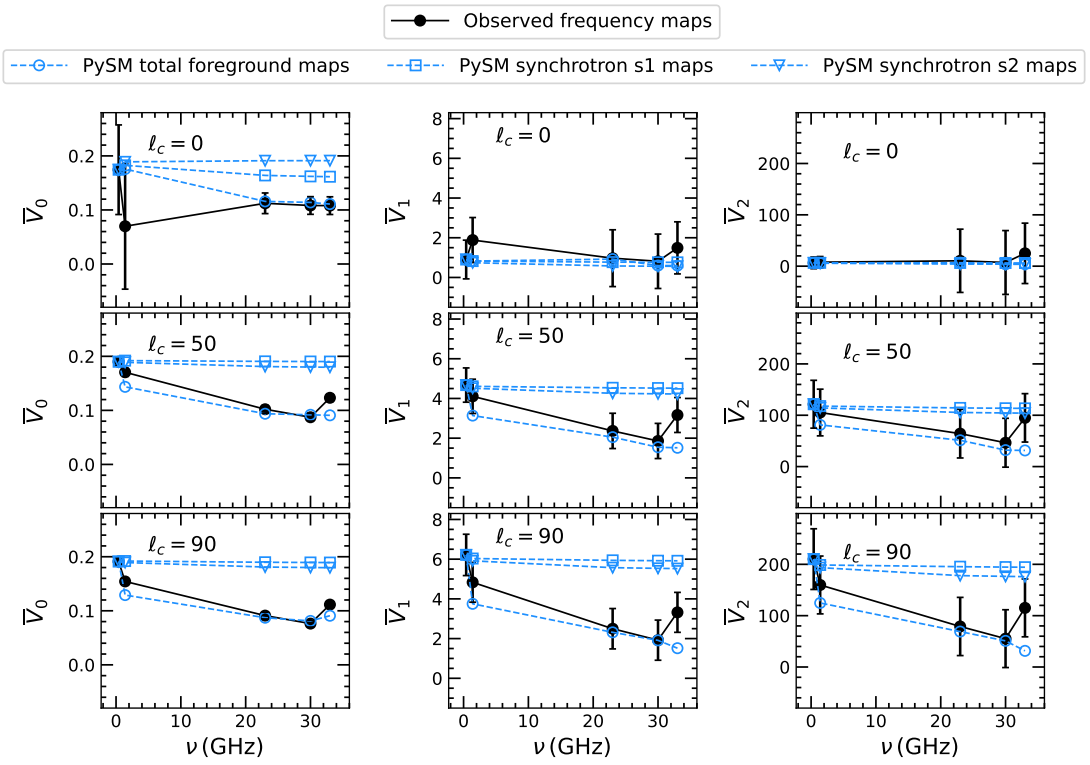

FIGURE 6.4.4: Average MFs, $\overline{V}_k$ defined by eq. (6.3), for observed frequency maps, PySM simulated total foreground maps, and PySM synchrotron model `s1` and `s2`, shown as functions of frequency ν.

6.4.4 Comparison of average morphology

To visualize how the *average* morphology changes as a function of the observing frequency, we define the average value of each MF, $\overline{V}_k$, for each map by integrating over the threshold in the range $\nu_{t,\min}$ to $\nu_{t,\max}$, as

$$\overline{V}_k(\nu) = \frac{\int_{\nu_{t,\min}}^{\nu_{t,\max}} \mathrm{d}\nu_t V_k(\nu_t, \nu)}{\nu_{t,\max} - \nu_{t,\min}}. \tag{6.3}$$

We choose $\nu_{t,\min} = -2$ and $\nu_{t,\max} = 2$ for V_1 and V_2. For V_0, $\nu_{t,\min} = 0$ and $\nu_{t,\max} = 2$. The average MFs are computed for observed frequency maps and the PySM maps discussed in the previous two subsections. The results are shown in figure 6.4.4. The error bars shown for the observed frequency maps are 2σ, where σ is the sum in quadrature of the standard deviations of the MFs at all the

threshold values considered[‡‡]. The values of $\overline{V}_k$ are higher for increasing ℓ_c, as expected. For all three MFs and for all three values of ℓ_c, we see good agreement between observed frequency maps and PySM total foreground maps at 23 and 30 GHz. At 33 GHz, all plots show large disagreement except $\overline{V}_0$ at $\ell_c = 0$. The PySM synchrotron maps for both models exhibit almost no variation in frequency.

Lastly, we stress that the analysis here is focused mainly on synchrotron emission. A full discussion on the morphology of other foreground signals, their contributions to the total morphology and the effect of point sources is beyond the scope of this work and is postponed to future study.

6.5 Results - morphology of component separated synchrotron temperature and polarization maps

Having probed the morphology of observed frequency maps containing synchrotron, free-free, AME and thermal dust emissions at different observing frequencies, we next focus attention on component-separated synchrotron temperature and polarization maps.

6.5.1 Synchrotron temperature maps

Different component separation pipelines used in various CMB experiments utilize distinct methodologies as outlined in section 6.2.2. In an ideal situation where all pipelines give the same true synchrotron map, all the maps should exhibit the same morphology. In reality, the efficiency of separating out the different astrophysical

[‡‡]We have ignored the correlations of the MFs at different threshold values.

components differs, and there can be residual contamination from other components in the component maps. Comparison of the different component-separated maps is usually made at the map level by examining the scatter between pixel values or at the C_ℓ level (Planck Collaboration et al. 2016d). Here, we compare using MFs, going beyond the power spectra to compare the integrated effect of all orders of N-point correlations.

6.5.1.1 Power Spectra of synchrotron temperature maps

We begin our analysis by discussing the angular power spectra (C_ℓ) of the various component-separated synchrotron maps estimated using `NaMaster`. C_ℓs for Haslam and Stockert-Villa maps are also included for comparison. Among the different synchrotron maps, Planck and BeyondPlanck maps are given at a reference frequency of 408 MHz, while WMAP maps are at 23 GHz. For a meaningful comparison of different maps at the power spectrum level, we have re-scaled all the maps to the Haslam frequency, using a constant spectral index value, $\beta_s = -3.0$ for WMAP and $\beta_s = -2.5$ for Stockert-Villa maps. As discussed in section 3.3, this frequency scaling does not alter the overall morphology of the maps under study.

The power spectra are shown in figure 6.5.1. The top panel shows the full multipole range of interest, $0 \leq \ell \leq 180$. We observe that at low ℓ (large angular scales), the power spectra of all the synchrotron maps roughly follow a power-law form with different spectral indices. BeyondPlanck map shows the closest agreement with the Haslam map across all scales. WMAP MCMC-e and Planck also track the behaviour of the Haslam map down to relatively smaller scales ($\ell \sim 80$) compared to the other WMAP maps. From this behaviour, we can anticipate that these three maps will show morphological properties that are relatively closer to the Haslam map. Note that C_ℓ of WMAP MCMC-g (and possibly `f`) exhibit

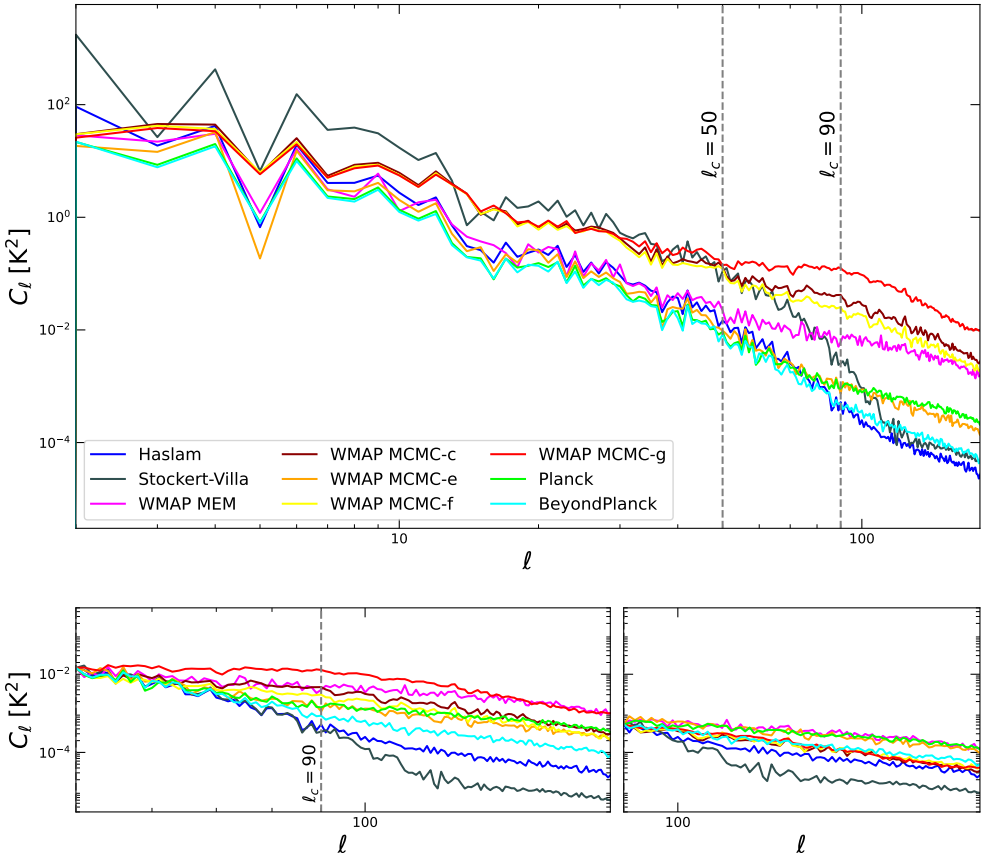

FIGURE 6.5.1: *Top*: Angular power spectrum, C_ℓ, for the full multipole range $0 \leq \ell \leq 180$, of different component separated synchrotron temperature maps given by WMAP and Planck. C_ℓ for Haslam and Stockert-Villa maps are also given for comparison. *Bottom left*: Same plot as the top but for multipole range $\ell = 50$ to 180. The amplitudes of all maps have been rescaled to match that of the Haslam map at $\ell = 50$ so as to highlight the slope differences. *Bottom right*: Same plot for multipole range $90 \leq \ell \leq 180$, and amplitudes rescaled to match that of Haslam map at $\ell = 90$.

discernible similarity with C_ℓs of WMAP K and Ka with a flattening of power at $\ell \gtrsim 50$ (compare with figure 6.4.1). The power spectrum of the Stockert-Villa map is quite different from the others. It exhibits a 'knee' with a change of slope and becomes relatively flat above $\ell \sim 100$.

Figure 6.5.1 (bottom left panel) shows the multipole ranges $50 \leq \ell \leq 180$ (left), where we have rescaled the amplitudes for all maps to match that of Haslam map at $\ell = 50$. This rescaling is done so as to highlight the differences in the shape

of the power spectra. The y-axis range is the same as the top panel. Towards larger ℓ (small scales), relative to the Haslam map, we observe varying degrees of flattening of the power spectra of the different maps (except Stockert-Villa). As mentioned in section 6.4.2 there can be some contribution of residual point source contamination to this flattening of power. Next, in the same figure, the bottom right panel shows the multipole ranges $90 \leq \ell \leq 180$ (left), with the amplitudes for all maps rescaled to match that of the Haslam map at $\ell = 90$. Relative to the Haslam map, we still observe some flattening, though of a lesser degree, for the power spectra of different maps.

6.5.2 Minkowski functionals for synchrotron temperature maps

Figure 6.5.2 shows the MFs for all the component-separated maps under consideration. The error bars shown are 2σ, computed from Gaussian simulations to which instrument noise maps are added (see appendix 6.A). The top row corresponds to $\ell_c = 0$ and, hence, is a comparison of the morphology of the full maps containing information on the entire range of scales. It is evident that BeyondPlanck, Planck, and WMAP MCMC-e maps exhibit good agreement with the Haslam map for all MFs within 2σ. This correlates with the agreement of their power spectra at most scales. Since the Haslam map is used as a template for Planck and BeyondPlanck maps, the agreement is not surprising. The other maps are significantly different from the Haslam map at different threshold ranges for all three MFs. WMAP MCMC-c, f, g show good agreement with each other, while WMAP MEM shows significant differences from them. Stockert-Villa is also significantly different.

Next, we examine the MFs for intermediate to small scales set by $\ell_c = 50$, shown in the second row of figure 6.5.2. From all three MFs, we find that BeyondPlanck and WMAP MCMC-e agree with the Haslam map within 2σ. The MFs of these

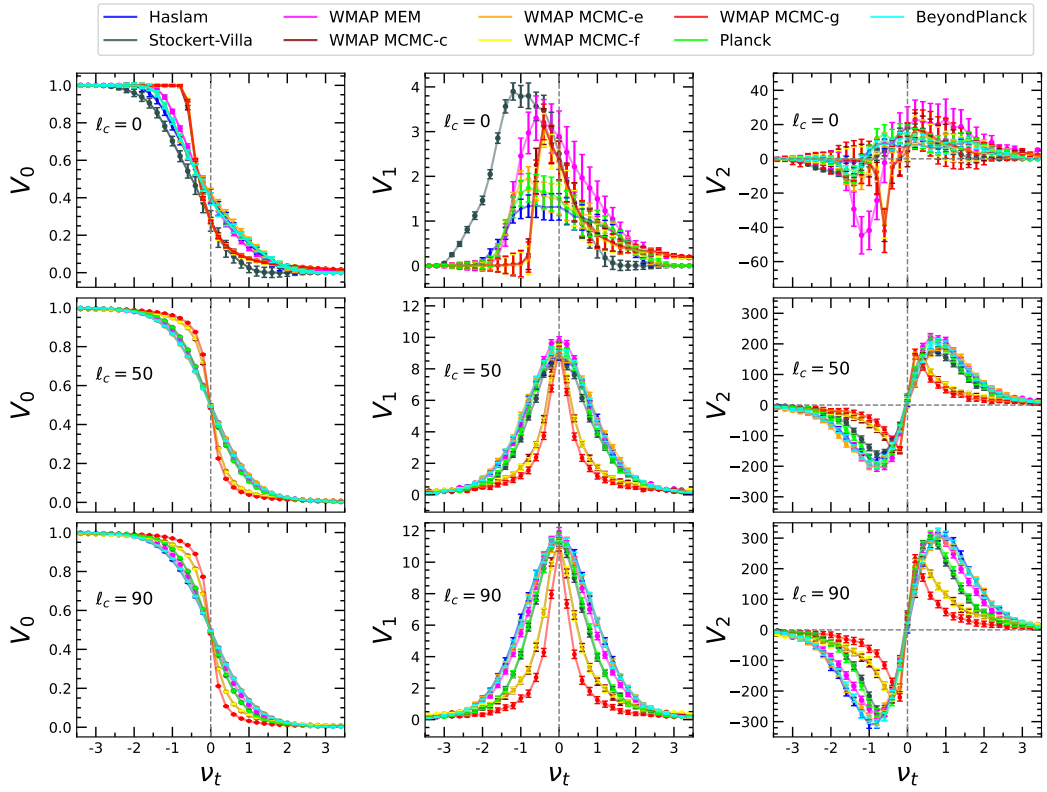

FIGURE 6.5.2: Scalar MFs for various component separated synchrotron maps for $\ell_c = 0$ (top row), $\ell_c = 50$ (middle row), and $\ell_c = 90$ (bottom row). The error bars denotes 2σ deviation. For $\ell_c = 0$, we find that BeyondPlanck, Planck, and WMAP MCMC-e maps exhibit good agreement with the Haslam map for all MFs within 2σ. For smaller scales, BeyondPlanck and WMAP MCMC-e has good agreement with Haslam map, unlike Planck and other WMAP maps. This disagreement could be due to residual point sources or residual foregrounds contained in these maps.

maps are also closest to Gaussian behaviour, as can be inferred from a comparison of their shapes with figure 3.3. From V_1 we see that the Planck map differs from Haslam at roughly 2σ, with a marginal increase of non-Gaussianity, while the other MFs show good agreement. Stockert-Villa also shows similar behaviour as Planck for V_0 and V_2. WMAP MCMC-c, f, g again show significant differences from the Haslam map and exhibit a much higher level of non-Gaussianity. They show good agreement amongst themselves, though with g differing from c,f at 2σ. The similarity of the shapes of the MFs for these three maps with those of the composite fields AME+synchrotron and free-free+synchrotron, shown in appendix 6.D is noteworthy. Combined with the similarity of the power spectra of these fields with

those of the total foreground mentioned in the previous subsection, this suggests that there is contamination by residual AME and/or free-free emissions in these maps. Interestingly, filtering large-scale modes $\ell < 50$ renders the WMAP MEM map closer to the Haslam map.

The MFs for small scales set by $\ell_c = 90$ are shown in the last row of figure 6.5.2. From all MFs, we find that BeyondPlanck and WMAP MCMC-e still show good agreement with the Haslam map. The difference between Planck and Stockert-Villa is now much more significant compared to when large-scale modes are included. WMAP MCMC-c, f, g again show significant differences from the Haslam map with a high level of non-Gaussianity. The difference between g from c, and f is much more pronounced. As discussed above for $\ell_c = 50$, this indicates that these component-separated maps contain residual free-free and/or AME foreground components. WMAP MEM still shows good agreement with the Haslam map at roughly 2σ.

To summarize, we find significant morphological differences between Haslam, WMAP, Planck and BeyondPlanck maps. Our analysis suggests that there are two possible physical causes for these differences. We discuss them below.

1. *Unresolved point sources*: It has been shown in Andersen et al. (2022) that BeyondPlanck is contaminated by fewer unresolved point sources compared to Planck. (See figure 22 of Andersen et al. (2022) which displays difference maps between the Planck and BeyondPlanck foreground component maps where the presence of unresolved point sources in Planck maps at high latitudes are clearly visible). From this, combined with the flattening of the power spectrum of the Planck map towards small scales relative to the Haslam map, we deduce that the presence of point sources is responsible (at least partly) for the difference in the MFs between Planck and Haslam at small scales. Since we use the same point sources mask for the WMAP

maps, there must also be some contribution of residual point sources to their morphology. The similarity of MCMC-e to Haslam is interesting because it is the one that assumes a spatially constant power-law form for the intensity in the synchrotron modelling. Other MCMC methods keep the spectral index as a free parameter. Given that the point sources also follow a power-law spectra (albeit with a steeper index), MCMC maps, except e, are more susceptible to erroneously identifying point sources as synchrotron signals.

2. *Contamination by residual AME and/or free-free emissions*: A major improvement in the Planck component separation methods over WMAP is the better estimation of AME through the improved model for AME spectra Planck Collaboration et al. (2016d). So, the morphological similarity amongst the MCMC-c, f, and g maps and the difference from Haslam, Planck, and BeyondPlanck indicate that the residual AME component contributes to the overall morphology of these MCMC maps. However, our analysis does not distinguish contamination by residual AME from free-free; there can also be contributions from free-free (see the shapes of the MFs in appendix 6.D).

6.5.2.1 Nature of non-Gaussianity of component separated synchrotron maps

MFs are powerful tools for detecting the presence of non-Gaussianity whose nature is a priori unknown. In our previous chapter, we showed that towards smaller scales, the Haslam map is kurtosis-dominated, and skewness is relatively small. This cannot be efficiently detected by the bispectrum but will show up in the trispectrum. Here, we carry out the same analysis to quantify the level and type of non-Gaussianity for the component-separated synchrotron maps. In order to distinguish different kinds of non-Gaussianity, it is useful to probe the individual

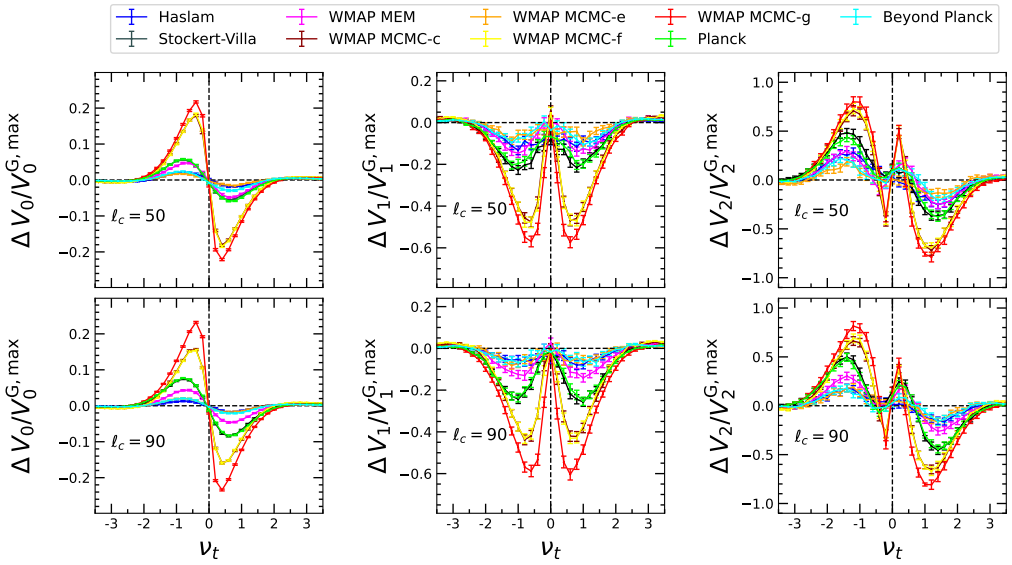

FIGURE 6.5.3: Non-Gaussian deviations $\Delta V_k/V_k^{\mathrm{G,max}}$ for component separated synchrotron temperature maps. Error bars denote 2-σ deviation from the mean values. The shapes are characteristic of kurtosis-type non-Gaussianity, indicating that the nature of the non-Gaussianity of the fluctuations in the Planck, Stockert-Villa and WMAP synchrotron maps are also of kurtosis-type.

generalized skewness and kurtosis moments (see section 5.3.2). Here, we will not show the individual moments but will focus on their consolidated effect.

To quantify the non-Gaussian deviation of a given field, we use:

$$\Delta V_k = V_k - V_k^G, \tag{6.4}$$

where the superscript G refers to the Gaussian expectation. For each component-separated map that we study, we need to calculate V_k^G. This is obtained from Gaussian simulations (section 6.2.3.1) to which instrument noise maps are added. Then, we subtract V_k^G from V_k to obtain the non-Gaussian deviation ΔV_k. For $\ell_c = 0$, the fields have $\Delta V_k/V_k^G > 1$, and hence, it is not meaningful to discuss mild deviations from Gaussian nature in terms of perturbative expansions. Therefore, we focus on smaller scales. Figure 6.5.3 shows $\Delta V_k/V_k^G$ versus ν_t for all the component separated maps, for $\ell_c = 50$ and 90. The error bars are 2σ. We make the following observations.

Shape of deviations and nature of non-Gaussianity: The non-Gaussian deviation shapes for all the maps are roughly similar to that of the Haslam map. The shapes are characteristic of kurtosis-type non-Gaussianity (Rahman et al. 2021; Matsubara 2010), with the relative differences depending on which of the generalized kurtosis variables are dominant. Thus, we conclude that the nature of the non-Gaussianity of the fluctuations in the Planck, Stockert-Villa and WMAP synchrotron maps are also of kurtosis-type.

Level of non-Gaussian deviations: For both values of ℓ_c, we find that Beyond-Planck and WMAP MCMC-e have comparable levels of non-Gaussianity with Haslam, while the other maps show higher levels. The level of non-Gaussianity for Planck, WMAP, MCMC-c, f, g and MEM, and Stockert-Villa maps do not show a decrease towards smaller scales (an increase of ℓ_c). This can be explained by point source contamination for Planck as well as WMAP maps, as discussed in the previous subsection. In addition, the WMAP maps contain the effect of residual contamination by other foregrounds, particularly AME (Planck Collaboration et al. 2016d). A summary of the significance of the non-Gaussian deviations is given along with the results for polarization in table 6.5.1 in section 6.5.4.

6.5.2.2 Statistical isotropy

To probe the SI of the component-separated synchrotron temperature maps, we use the α statistic defined in eq. (3.27). We compute α for all the maps for different bandpass filter scales. We also compute α for the 1000 Gaussian simulations plus noise corresponding to each map. The results for α are shown in figure 6.5.4 for $\ell_c = 50$ and $\ell_c = 90$. Each panel corresponds to one map for each ℓ_c. The coloured diamonds show α versus ν_t for each map. Since α follows Beta probability distribution, we compare α of each map with the median α for the corresponding

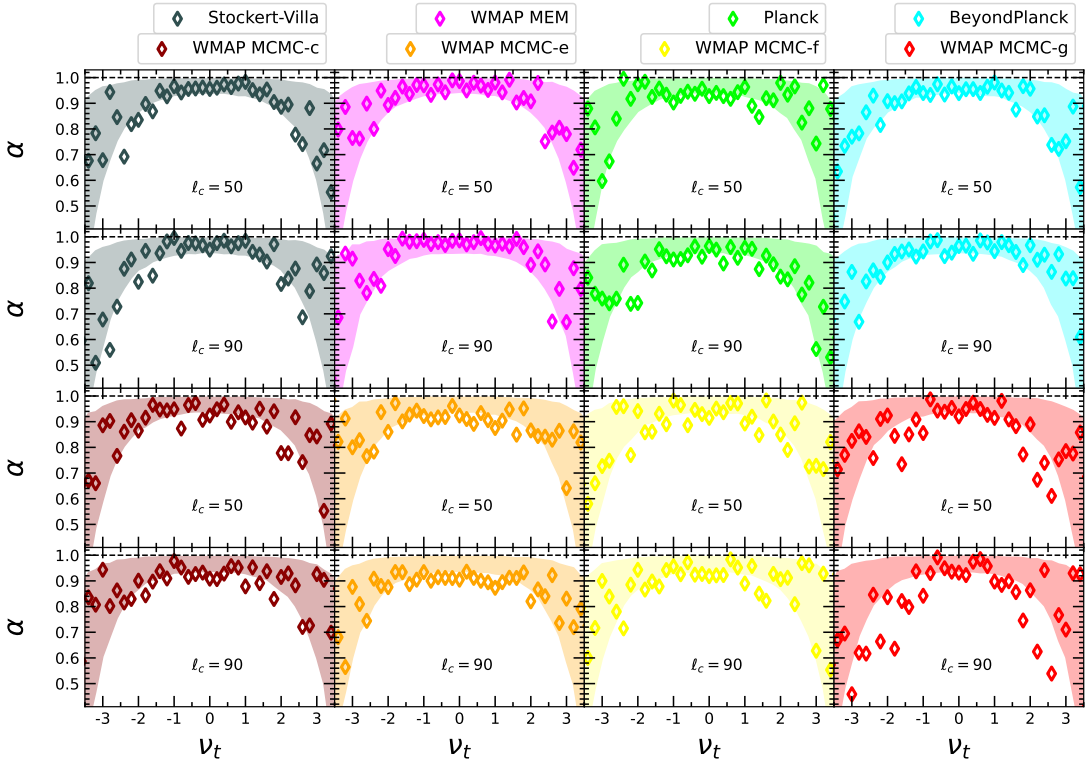

FIGURE 6.5.4: SI parameter α versus ν_t, for component separated synchrotron maps. The shaded regions show the 95% confidence interval about the median values at each threshold obtained from 1000 Gaussian simulations. BeyondPlanck and WMAP MEM maps are relatively more isotropic compared to other synchrotron maps.

1000 Gaussian maps. The shaded regions correspond to the 95% confidence levels (CL) about the median values.

Note that values of α less than the 95% CL lower limit are the ones with significant anisotropy. We find that BeyondPlanck and WMAP MEM are comparatively the most isotropic for both ℓ_c values, with almost all α lying within 95% CL. Planck map shows anisotropy at a few thresholds, and there are more anisotropic threshold values for $\ell_c = 90$ compared to 50. This correlates with the higher level of non-Gaussianity towards smaller scales seen earlier and is likely due to residual point sources in the map. WMAP MCMC c, f, g maps also exhibit anisotropy at several threshold values, and it is visually clear that WMAP MCMC-g shows the highest level of anisotropy at both scales. Again, this correlates with what we found for

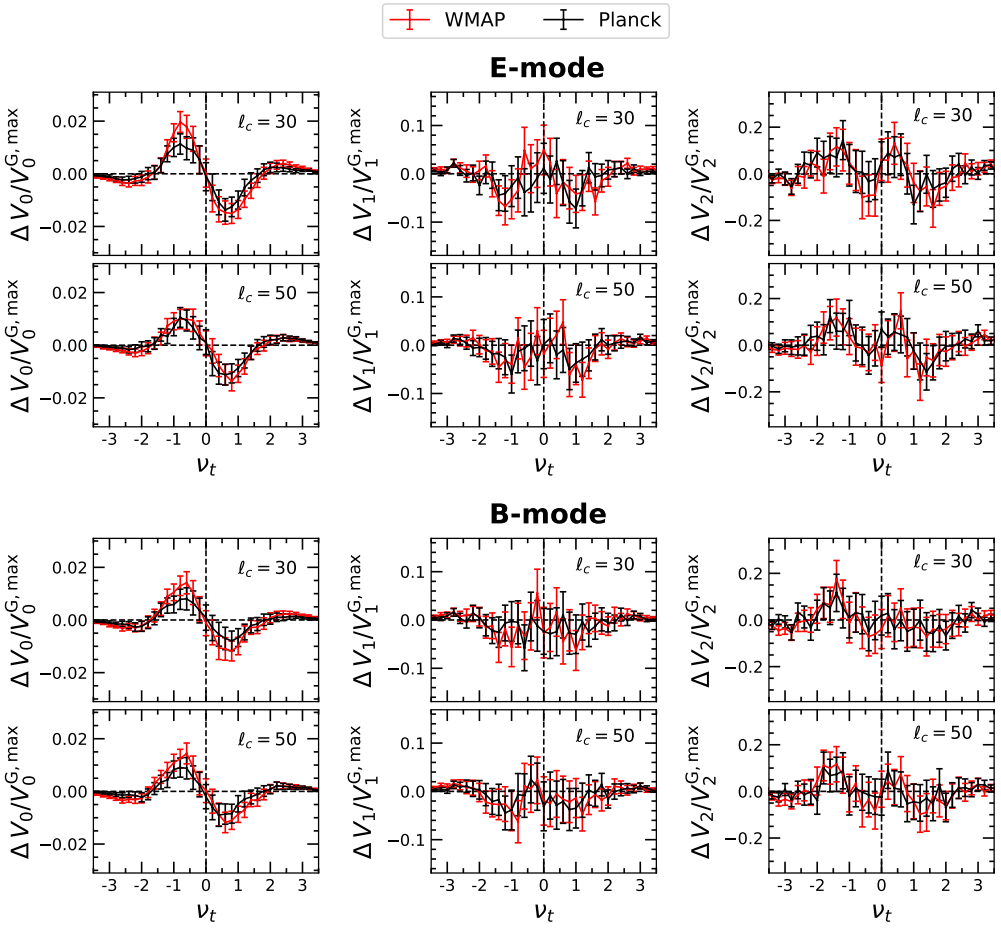

FIGURE 6.5.5: Non-Gaussian deviations ($\Delta V_k/V_k^{\mathrm{G,max}}$) for component separated E and B mode synchrotron polarization maps from WMAP and Planck. Error bars are 2-σ around the mean values. The shape of ΔV_k indicates that the non-Gaussianity of synchrotron polarization maps are also of kurtosis origin.

the level of non-Gaussianity in the previous subsection. We find that WMAP MCMC-e also shows significant anisotropy at several threshold values for both bandpass filter scales. Since this map shows a low level of non-Gaussianity, the significant anisotropy is not in alignment with the other maps for which we find higher anisotropy for higher non-Gaussianity.

6.5.3 Morphology of synchrotron polarization

Next, we discuss the morphology of component-separated synchrotron polarization maps provided by WMAP and Planck. We focus on bandpass filter scales $\ell_c = 30$ and $\ell_c = 50$ since instrumental noise dominates in the maps towards smaller scales. We use the Planck polarization maps derived using the `Commander` component separation method. For WMAP, we use the polarization maps derived using the MCMC technique (MCMC-g). MFs are calculated for E and B mode maps, which are obtained using `NaMaster`. We also compute MFs for 1000 Gaussian simulations generated using the power spectrum of each map after adding instrumental noise realizations (see appendix 6.A).

Figure 6.5.5 shows the non-Gaussian deviations of the MFs for E and B mode maps of WMAP and Planck. The shape of the deviations for both E and B mode maps shows excellent agreement with what was obtained for the Haslam (temperature) map (compare with figure 6.5.3). This finding confirms that the Galactic synchrotron exhibits kurtosis non-Gaussianity both in temperature and polarization, with the skewness contribution being sub-dominant. As was found for the Haslam map, we find that ΔV_0 provides more stringent confirmation of the nature of non-Gaussianity than ΔV_1 and ΔV_2.

6.5.4 Statistical significance of non-Gaussian deviations

To estimate the significance of non-Gaussian deviations, we calculate χ^2 defined as,

$$\chi^2_{\rm uc} = \frac{1}{N_{\rm tot}} \sum_{k=0}^{2} \sum_{\nu_t=-3}^{3} \frac{\left(V_k^{\rm data}(\nu_t) - \overline{V}_k^{\rm G}(\nu_t)\right)^2}{\sigma^2_{V_k^{\rm G}}(\nu_t)} \tag{6.5}$$

$V_k^{\rm data}$ is the MF estimated for different synchrotron maps, $\overline{V}_k^{\rm G}(\nu_t)$ is the mean of the respective Gaussian simulations, and $\sigma^2_{V_k^{\rm G}}(\nu_t)$ the standard deviation. The threshold bin width is 0.4. The total number of statistics is $N_{\rm tot} = 16 \times 3 = 48$. The subscript *uc* (uncorrelated) indicates that the correlations between the threshold values and among different MFs are not taken into account here. Note that we choose a larger bin size to minimize the bias resulting from neglecting these correlations.

Table 6.5.1 shows the square root of $\chi^2_{\rm uc}$ values for different component-separated synchrotron temperature and polarization maps. For temperature maps, we find that the values are quite large, indicating that the maps are highly non-Gaussian, even at the relatively smaller scales considered here. Compared to the Haslam map, all maps except WMAP MCMC-e and BeyondPlanck have higher levels of non-Gaussianity that increase as ℓ_c increases. WMAP MCMC-e also shows a slight increment as we go to small scales, unlike BeyondPlanck. This again signifies the better treatment of point sources in the BeyondPlanck analysis. As discussed in section 6.5.2 and also in appendix 6.D, our analysis strongly suggests that this is due to residual contamination by other Galactic components, with some contribution from unresolved point sources. It should be noted that the $\chi^2_{\rm uc}$ values given in the previous chapter were estimated for a sky fraction of 40%. The current analysis, however, is carried out on 65% of the sky to retain the sky regions with a high SNR. Hence, they cannot be compared directly.

For polarization, the $\chi^2_{\rm uc}$ values are smaller than the values for temperature. All the maps show a decrease of $\chi^2_{\rm uc}$ towards smaller angular scales. We find that the main contribution to the $\chi^2_{\rm uc}$ is coming from V_0 for all the temperature and polarization maps. This is evident from figures 6.5.3 and 6.5.5, where V_0 has error bars smaller than that of V_1 and V_2. This was also observed in our previous analysis of the Haslam map. In the case of polarization, the $\chi^2_{\rm uc}$ values are lower due to the increased level of noise present in these maps.

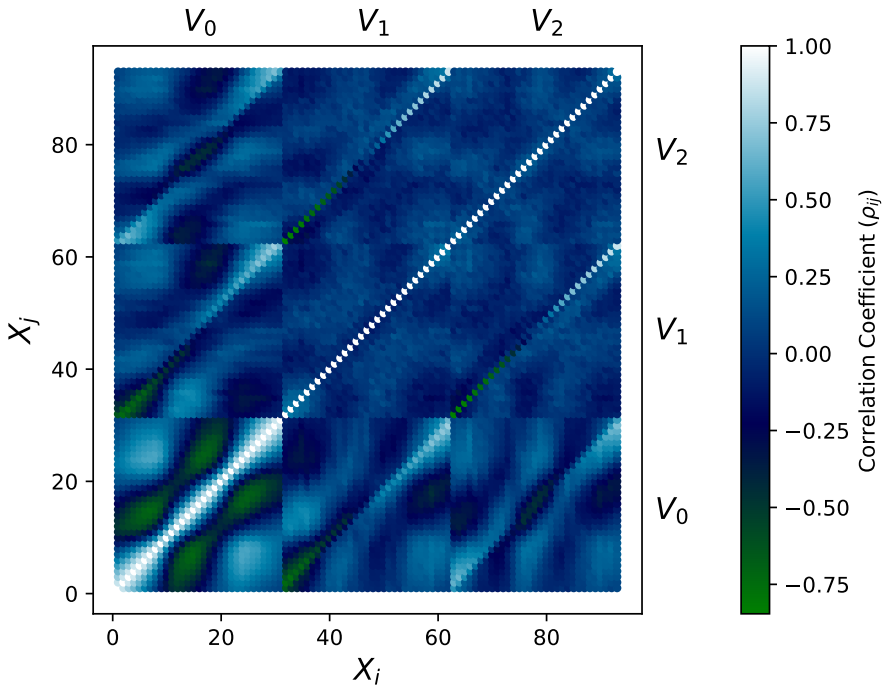

FIGURE 6.5.6: Correlation coefficient, $\rho_{ij} = C_{ij}/\sqrt{C_{ii}C_{jj}}$ estimated using 1000 simulations corresponding to Haslam map.

In Table 6.5.2, the square root of the χ^2 values, considering correlations (also, after dividing with the number of statistics; reduced χ^2) is shown. Here, χ^2 is defined as,

$$\chi^2 = \sum_{i=1}^{n}\sum_{j=1}^{n}[X_i^{\rm data} - \overline{X}_i^{\rm G}]C_{ij}^{-1}[X_j^{\rm data} - \overline{X}_j^{\rm G}], \tag{6.6}$$

where X is the vector, $X \equiv \{V_0(\nu_t), V_1(\nu_t), V_2(\nu_t)\}$ for the threshold values $\nu_t \in [-3, 3]$ with bin size $\Delta\nu_t = 0.2$. C_{ij} is the correlation matrix given by,

$$C_{ij} = \langle [X_i^{\rm sim} - \overline{X}_i^{\rm G}][X_j^{\rm sim} - \overline{X}_j^{\rm G}]\rangle. \tag{6.7}$$

$\langle\rangle$ denotes the average over 1000 Gaussian simulations with noise maps, specific to each data set, added to them. The vector X contains $31 \times 3 = 93$ statistics. It is seen that except for Haslam, WMAP MCMC-e and BeyondPlanck, incorporating correlations leads to larger χ^2 values. For polarization, including the effect of correlations lowers the χ^2 values. Nevertheless, our results and the inferences drawn from them remain consistent even after accounting for correlations. Figure 6.5.6

Temperature									
ℓ_c	Haslam	Stockert - Villa	WMAP MEM	WMAP MCMC-c	WMAP MCMC-e	WMAP MCMC-f	WMAP MCMC-g	Planck	Beyond Planck
50	9.54	19.49	16.18	42.19	7.15	42.20	50.60	19.83	9.75
90	7.33	29.25	17.93	46.01	8.66	46.25	63.23	29.95	9.19
Polarization									
ℓ_c	—	WMAP E-mode		WMAP B-mode		Planck E-mode		Planck B-mode	
30	—	3.65		3.10		2.48		1.94	
50	—	2.81		3.26		2.71		2.18	

TABLE 6.5.1: The square root of $\chi^2_{\rm uc}$, quantifying the non-Gaussian deviations of different component-separated synchrotron temperature and polarization maps. Here, the correlations between different thresholds and among different MFs are not considered.

shows the correlation coefficient for X, defined as $\rho_{ij} = C_{ij}/\sqrt{C_{ii}C_{jj}}$ obtained for the simulations corresponding to Haslam map.

We have repeated the analysis with the filament mask (right panel of figure 6.3.1) for both temperature and polarization maps and found no significant difference from the results discussed above. This suggests that large-scale filamentary structures in the synchrotron sky do not affect our results.

6.6 Summary and discussion

In this chapter, our primary goal is to understand the nature of non-Gaussian deviations of Galactic synchrotron emissions on different length scales. For this

Temperature									
ℓ_c	Haslam	Stockert - Villa	WMAP MEM	WMAP MCMC-c	WMAP MCMC-e	WMAP MCMC-f	WMAP MCMC-g	Planck	Beyond Planck
50	6.28	28.28	19.12	72.51	4.85	69.79	98.70	33.56	8.22
90	5.39	52.13	22.00	70.87	7.01	65.16	121.85	58.94	8.27
Polarization									
ℓ_c	—	WMAP E-mode		WMAP B-mode		Planck E-mode		Planck B-mode	
30	—	2.14		1.85		1.76		1.42	
50	—	1.73		1.95		1.73		1.42	

TABLE 6.5.2: The square root of χ^2, by taking into account the correlations among different threshold values and between three MFs. We find that for temperature maps, except for Haslam, WMAP MEM and BeyondPlanck, the χ^2 values are quite large. For polarization maps, the values are lower due to the increased level of noise present in those maps.

purpose, we analysed the morphological properties of two sets of Galactic foreground maps.

The first set of maps we analyse is comprised of observed Galactic total emissions at different frequencies ranging from 408 MHz to 33 GHz. This analysis reveals how the morphology of the total Galactic foreground transforms as synchrotron emission, which is the main component towards lower frequencies, becomes the sub-dominant component at 23 GHz and higher frequencies. From the results of this study, we can anticipate the impact of residual contamination by other foreground components on the morphology of component-separated synchrotron maps. Since the observed frequency maps have high SNR, it is unlikely that our results are biased by instrumental noise. Furthermore, we have demonstrated that the results we have obtained remain unaffected by the instrumental systematics

inherent in these maps. We then compare them with the morphology of simulated total foreground emission maps obtained from PySM. This comparison reveals significant amplitude and shape differences of the MFs between the observed maps and the simulations on large scales and relatively better agreement towards smaller scales.

The second set of maps we analyse are component-separated synchrotron temperature maps from WMAP, Planck and BeyondPlanck, and polarization maps from WMAP and Planck. From all the maps studied, both temperature and polarization, we conclude that the nature of non-Gaussian deviation of small-scale fluctuations of synchrotron emission is of kurtosis type. This is in agreement with our earlier finding from the Haslam map in the previous chapter. We have included instrumental noise in estimating the uncertainties. Also, we have taken into account the role of instrumental systematics in our results, and it has been found to be minimal. This result is important from two perspectives. First, it provides a concrete direction for modelling small-scale fluctuations of synchrotron emission as mildly non-Gaussian fields of kurtosis nature rather than Gaussian. The isotropic nature of the BeyondPlanck map, in agreement with the Haslam map, also implies that the modelling of small-scale fluctuations of synchrotron as a statistically isotropic field is in the right direction. These findings can, therefore, improve component separation pipelines, which is particularly important for B-mode experiments. In fact, Martire et al. (2023) have recently developed a methodology for including the kurtosis nature in generating non-Gaussian synchrotron models. Secondly, this result implies that contamination of the true CMB by residual synchrotron component will most likely result in kurtosis-type non-Gaussianity. Hence, it will not be detectable by 3-point statistics such as the bispectrum. Preliminary work to determine the type of non-Gaussianity induced by residual foregrounds in WMAP data using MFs was carried out in Chingangbam & Park (2013). It is timely to revisit such analysis in light of our current results.

Lastly, we comment on the comparison of the morphology of different component-separated synchrotron temperature maps. This comparison serves to analyse the performance of various pipelines that are adopted for WMAP and Planck data, beyond the usual zeroth order comparison at the map and power spectrum level. Accurate component separation by each independent method must lead to the same morphology, that is, a similar level of non-Gaussianity and SI. Using the Haslam map as the benchmark, we find that BeyondPlanck and WMAP MCMC-e are the best-performing pipelines. The other maps show differences that are significant. In particular, the Planck map shows a significant difference towards small scales, which is likely to be due to the presence of unresolved point sources. The other WMAP maps show even larger differences at different scales. This is likely to be due to unresolved point sources and contamination by residual AME and/or free-free emissions. It is important to acknowledge that the contribution of WMAP and Planck systematics in the observed morphological distinctions is not ruled out; however, quantifying their impact is beyond the scope of this study. A systematic investigation of the various contributions from residual contamination and point sources in the future will be very valuable.

Our results underscore the need for further improvement of the component separation techniques. It will be interesting to extend our analysis to other low-frequency surveys like S-PASS (at 2.3 GHz) (Carretti et al. 2019), C-BASS (at 5 GHz) (Harper et al. 2022), and the QUIJOTE-MFI (from 11 to 19 GHz) (Rubino-Martin et al. 2023). We would like to explore the morphological properties of other Galactic components and plan to carry out these extensions in the near future. It is also important to provide a physical explanation for the kurtosis nature of Galactic synchrotron emissions.

Appendix

6.A Estimation of instrumental noise

The uncertainties of the MFs for the observed frequency maps and the component-separated synchrotron maps shown in the paper include instrumental noise. For estimating the uncertainties, we need noise maps for each experimental setup. For the Planck LFI 30 GHz frequency map, we do not produce noise simulations ourselves. We use 300 FFP10 noise simulations provided by Planck (Planck Collaboration et al. 2020b). For the other observed frequency and component-separated maps, the instrumental noise properties differ from map to map. We generate them using noise characteristics provided by the experiment. We describe them case by case below.

- For Haslam and Stockert-Villa maps, we are provided with the noise rms values of the instruments. These are 800 mK (Remazeilles et al. 2015) and 17 mK (Testori et al. 2001), respectively. For each observed map, we generate 1000 noise maps, each of which is Gaussian random numbers at each pixel with the respective rms values as the standard deviation.

- To generate the noise maps for WMAP K and Ka frequency maps, we use the following equation

$$\sigma^2(\hat{n}) = \sigma_0^2 / N_{\rm obs}(\hat{n}), \tag{6.8}$$

  where $\hat{n}$ is the sky direction, σ_0 and $N_{\rm obs}$ are, respectively, the noise rms and the number of observations taken at every pixel for each frequency band. For K band, $\sigma_0 = 1.429\,\mathrm{mK}$, and for Ka band it is $1.466\,\mathrm{mK}$ (Bennett et al. 2013). We use $N_{\rm obs}$ for K and Ka bands provided by WMAP. Then, we generate Gaussian random numbers at each pixel with $\sigma(\hat{n})$ as the standard deviation. We generate 1000 such noise maps.

- The component-separated WMAP MCMC, Planck, and BeyondPlanck data sets include the synchrotron posterior rms maps. We use these map values as the standard deviation for generating 1000 Gaussian random numbers at every pixel.

- For WMAP MEM synchrotron map, noise rms maps are not provided. So, we identify the most noisy frequency channel, which is W2, to generate the noise maps. This makes our error estimates conservative. We use $\sigma_0 = 6.94\,\mathrm{mK}$ (Bennett et al. 2013) and $N_{\rm obs}$ map provided by WMAP. We then generate the noise map using eq. (6.8).

  We use this map as the rms map for generating 1000 Gaussian random numbers at each pixel.

- For WMAP MCMC polarization maps, the Q, U posterior rms maps are provided. These map values serve as the standard deviation for generating noise realizations, similar to what is followed for temperature maps.

- For Planck `Commander` polarization maps, we consider the difference between two half-mission maps as the noise realization.

6.B SNR of WMAP and Planck frequency maps

In this section, we estimate the SNR of the Planck LFI 30 GHz map, WMAP K band and Ka band maps. The left panel of figure 6.B.1 shows WMAP K and Ka and Planck LFI 30 frequency maps after subtracting the best fit CMB maps from WMAP and Planck, respectively. The middle panel shows the maps containing instrumental noise from the respective maps in the left panel. These noise maps are obtained as explained below:

- For Planck, the noise map is generated by subtracting the two half-ring maps. Half-ring maps are the maps prepared using only the first or second halves of each ring (pointing period) of the telescope, so the sky signal is expected to be the same, but the noise will differ. By subtracting these maps, we can isolate the noise content.
- For WMAP K and Ka bands, we average the observed maps of the first four individual years and similarly average for the next four years. Then, we subtract the two resulting maps to estimate the noise.

We then obtain the SNR map, which is the signal map (shown in the left panel) divided by the standard deviation of the respective noise map (shown in the middle panel). This map is shown in the third column of figure 6.B.1. We find that the SNR maps of both WMAP and Planck have high values across all the pixels.

6.C Effect of instrumental systematics

Instrumental effects can introduce alterations to the morphology of the maps we have been studying, potentially affecting our overall analysis and interpretation.

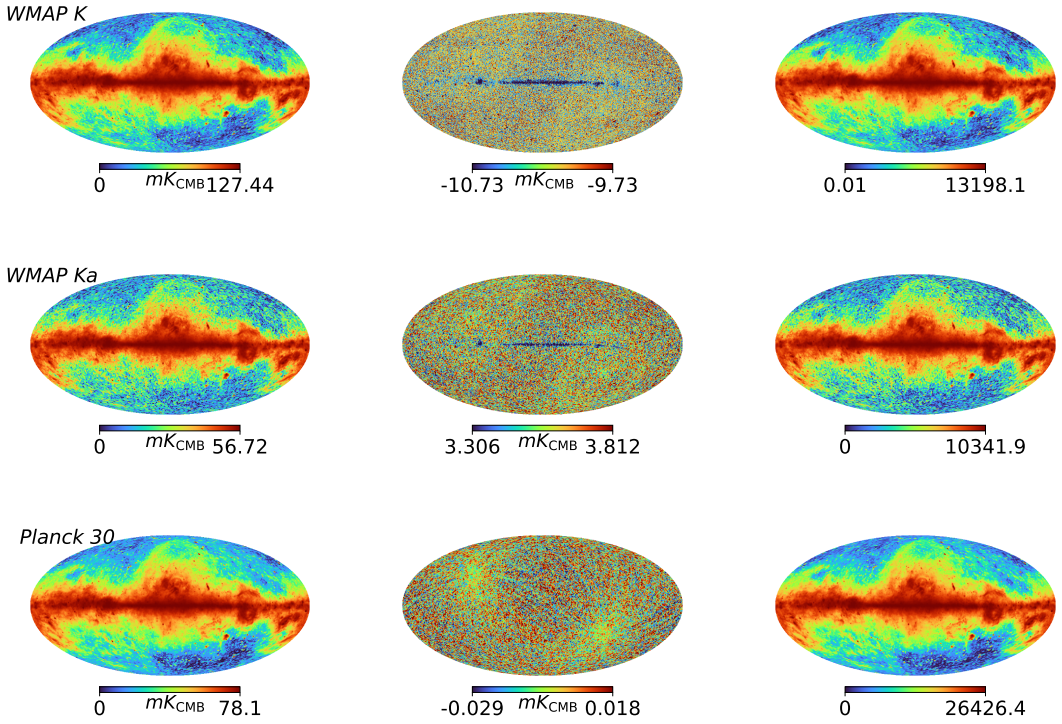

FIGURE 6.B.1: *Left column:* Maps of WMAP K band (top), Ka band (middle) and Planck LFI 30 GHz (bottom), after subtracting the best-fit CMB map given by the respective experiments. *Middle column:* Maps showing the instrumental noise in the corresponding map on the left. *Right column*: Maps of the SNR for the same.

This section explores the possible role of instrumental systematics in the morphological distinctions we have observed in the maps we studied. Our focus lies on WMAP and Planck products, as examining the instrumental effects of Stockert-Villa requires a comprehensive understanding of the instrument and calibration techniques. We reserve this topic for a future study.

To quantify this, we focus on the observed frequency maps of WMAP (K and Ka) and Planck (30 GHz), which largely contribute to the derived synchrotron products of the respective missions. We use the individual year maps at each frequency (9 years for WMAP and 4 years for Planck) and study how the morphology varies at each year. Under the assumption that the signal remains consistent across each year, while the noise and instrumental effects vary with time, we obtain an

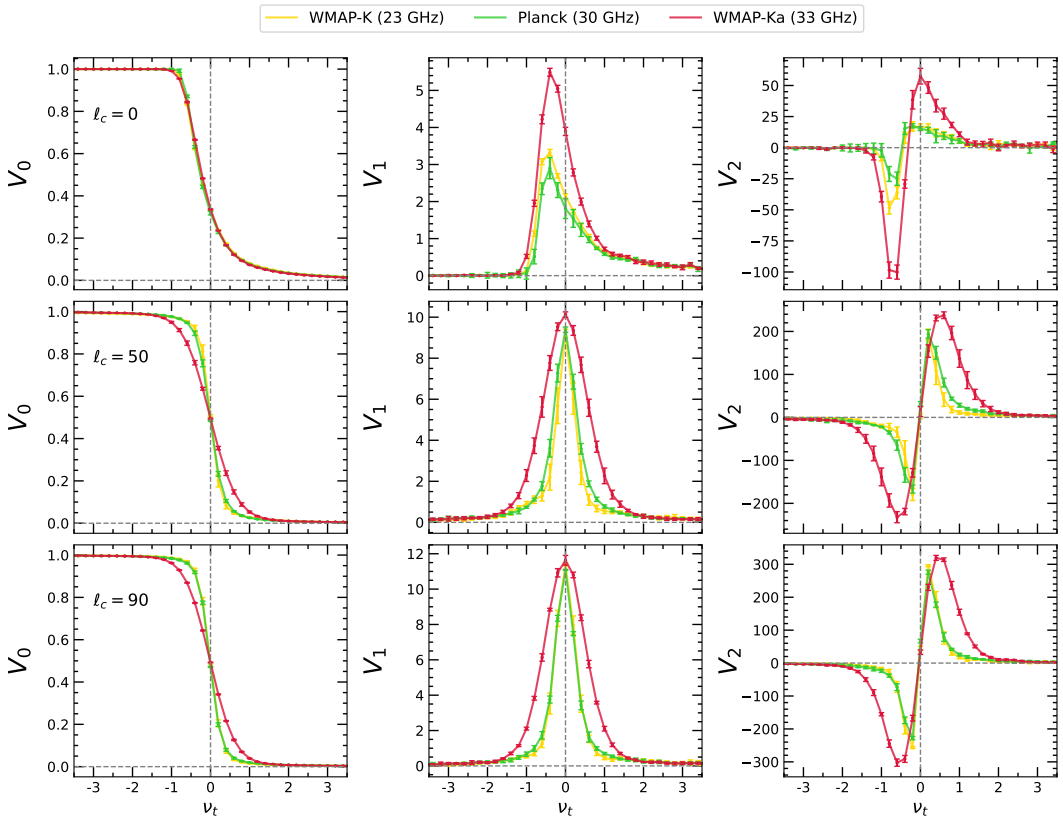

FIGURE 6.C.1: *Top*: Mean and 2σ error bars of MFs for WMAP and Planck individual year frequency maps at small angular scales. We find that the mean MFs for each frequency map fall beyond the 2σ error bars of other maps. This indicates that the systematics has a negligible effect on the observed morphological distinctions of the frequency maps.

estimate of how significant the noise and systematics are, in each frequency band. We calculate the three scalar MFs for these maps at different angular scales ($\ell_c = 0$, $\ell_c = 50$ and $\ell_c = 90$). The results of the mean MFs and 2σ error bars are shown in Figure 6.C.1. The error bars represent the preliminary assessment of both the systematics and noise present in each map.

We find that the mean MFs for each frequency map fall beyond the 2σ error bars of other maps. This indicates that the systematics has a negligible effect on the observed morphological distinctions of the frequency maps. To put it differently, the morphological differences we are observing are significantly larger than the

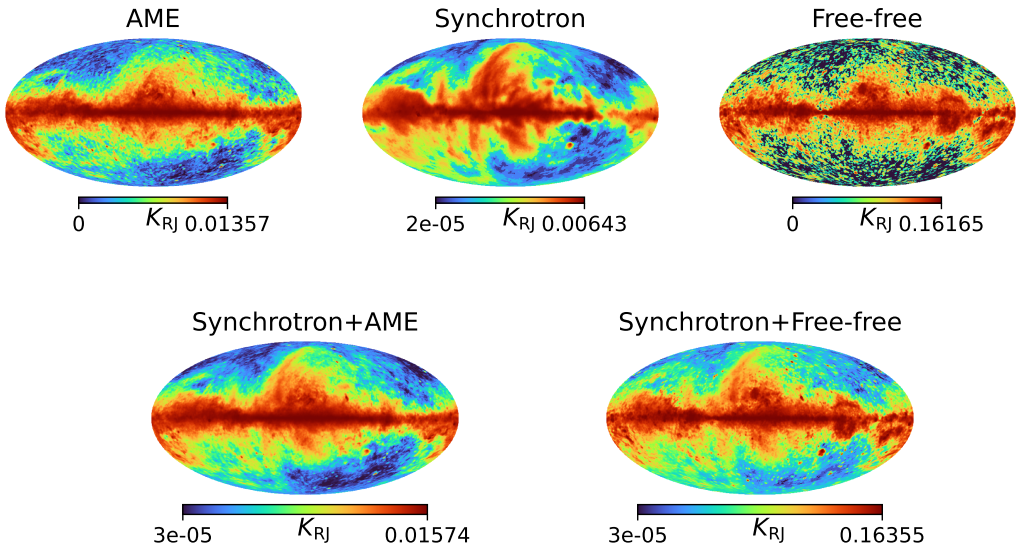

FIGURE 6.D.1: *Top*: Maps of AME (left), synchrotron (middle) and free-free (right) emissions at 23 GHz generated using PySM. *Bottom*: Maps of the sums of synchrotron and AME (left), and synchrotron and free-free (right).

systematic uncertainties. This trend is seen for all the three MFs at all the scales we studied. Consequently, the synchrotron products derived using these maps remain unaffected by the instrumental effects. Therefore, our analysis implies that the morphological distinctions we observe for different synchrotron maps at both small and large scales are not biased by the instrumental systematics.

6.D Morphology of composite foreground fields

Here, we want to probe how the MFs of the sum of two foreground components differ from the MFs of the individual components. For this purpose, we generate maps of synchrotron, AME and free-free emissions at 23 GHz using PySM. The maps and their sums are shown in figure 6.D.1. Note that the ranges of the field values shown differ from map to map. At 23 GHz, free-free is the most dominant, followed by AME and synchrotron. Visually, we can also see that

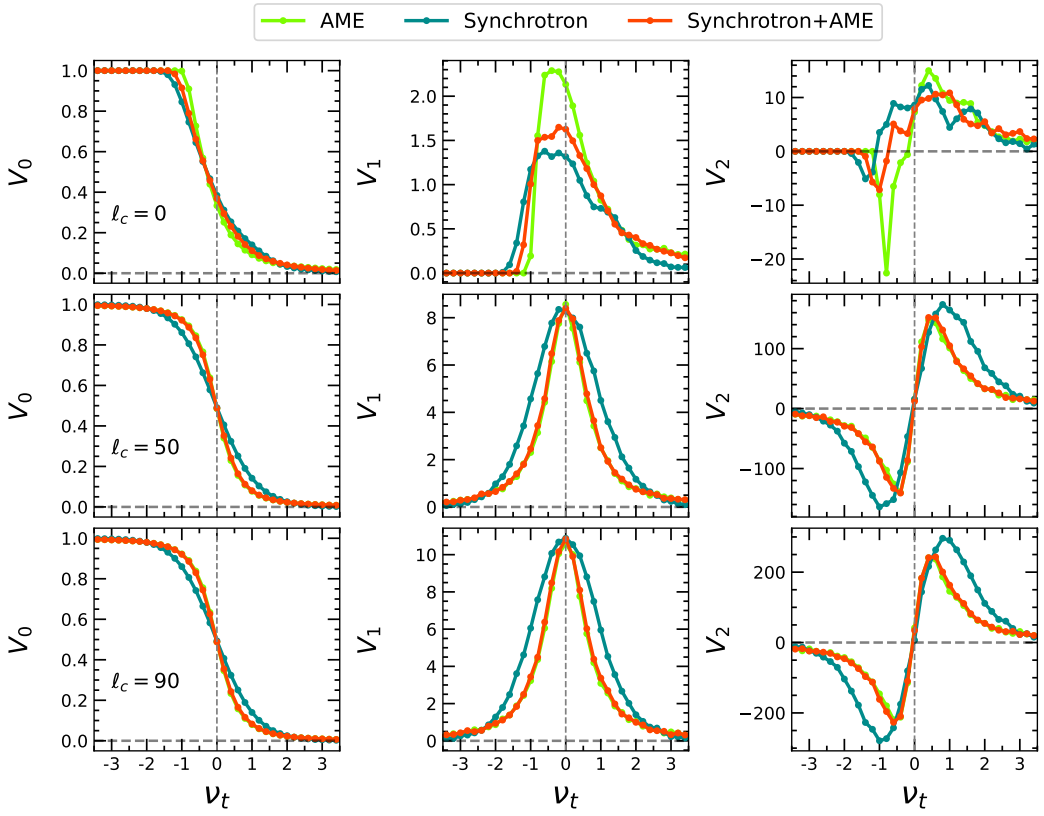

FIGURE 6.D.2: MFs for the synchrotron, AME and their sum for different angular scales. We find that V_1 and V_2 for AME have higher amplitudes than synchrotron due to the smooth nature of synchrotron fluctuations. In the sum field, the behaviour is primarily determined by AME as it is the dominant field at 23 GHz relative to synchrotron.

synchrotron fluctuations are considerably smoother (implies less power on smaller scales) compared to AME and free-free.

For each of the five maps, we compute MFs after bandpass filtering and masking identically. The results are shown in figure 6.D.2 and 6.D.3. Figure 6.D.2 compares the MFs of AME, synchrotron and their sum in each panel, with the rows from top to bottom corresponding to $\ell_c = 0, 50$ and 90. For $\ell_c = 0$, we can clearly see that V_1 and V_2 for AME have higher amplitudes compared to synchrotron. This can be understood by comparing their typical size of structures quantified by $\theta_c = \sigma_0/\sigma_1$. The amplitudes of V_1 and V_2 are set by θ_c^{-1} and θ_c^{-2}, respectively, at the zeroth order Gaussian approximation of any given field. Synchrotron has larger

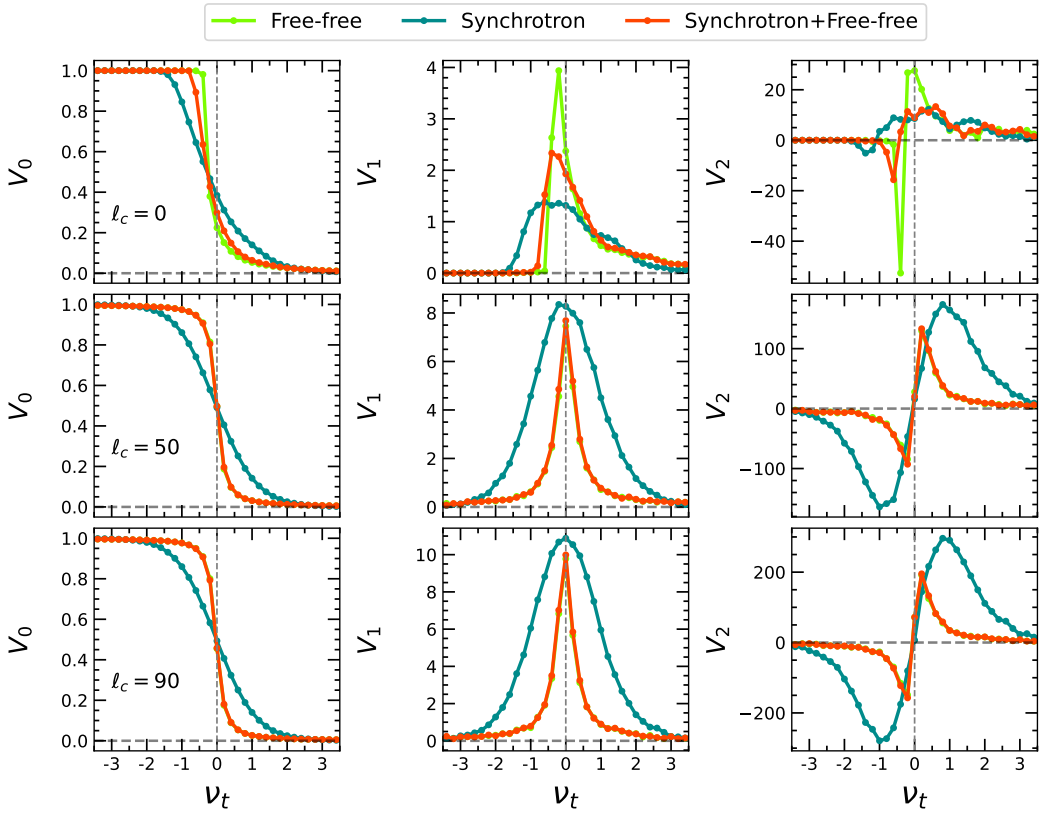

FIGURE 6.D.3: MFs for the synchrotron, free-free and their sum for different angular scales. Free-free has more amplitude owing to their size of structures smaller than synchrotron. Moreover, the sum field features are mostly determined by free-free as synchrotron is subdominant at 23 GHz.

θ_c compared to AME due to its relatively smoother nature, and as a consequence, we can expect, and we find, lower amplitudes for V_1 and V_2. For $\ell_c = 50$ and 90, we find that the MFs of the sum of the two fields are determined primarily by that of AME (overlapping red and green plots). This is due to AME being the dominant field at 23 GHz as well as the relative smoothness of the synchrotron.

Figure 6.D.3 compares the MFs of free-free, synchrotron and their sum, similar to the comparison with AME. Again, synchrotron is much smoother than free-free. We again obtain the MFs of the sum of the two fields to be roughly average of the MFs of the individual fields for $\ell_c = 0$, while for $\ell_c = 50$ and 90, the morphology of the sum is primarily determined by free-free.

It is straightforward to extend the above comparison to the sum of the three fields. For the frequency used here, 23 GHz, the morphology of the sum will be determined mainly by free-free since it is the dominant component. We stress that the results will vary with observing frequency as different component fields dominate at different frequencies. We have not considered thermal dust emission here since it remains sub-dominant at the frequencies considered in our paper. A point that is interesting to note is that AME and free-free emissions are relatively more non-Gaussian than synchrotron at $\ell_c = 90$, as can be discerned from the shapes of V_1 and V_2 and comparison with figure 3.3. This shows that in constructing models for these fields, the 'small' scale beyond which they can be assumed to be Gaussian, if they approach Gaussian behaviour at all, will be smaller than that of synchrotron. We also note that the use of these findings to interpret the results in section 6.4.2 is based on the assumption that the models of the emissions input in PySM are accurate. If PySM is inaccurate, there will be some variation in the morphology. However, the inferences for composite fields will broadly remain valid.

Chapter 7

Statistical Properties of Foreground Components – Free-free, AME and Thermal Dust Emissions*

7.1 Introduction

In the previous chapters, we have studied the statistical properties of Galactic synchrotron radiation. This study is valuable for CMB and Epoch of Reionization (EoR) experiments. Now, we focus our attention on the other Galactic foregrounds like AME, free-free and thermal dust emissions. The physical origin of these emissions is discussed in detail in Chapter 2. These three are the major components in the frequency ranges that are targeted for CMB. However, AME and thermal dust emission are not important for EoR observations.

*This chapter is based on the papers that are under preparation.

As CMB experiments become increasingly sensitive at arcminute and arcsecond angular scales, the availability of high-resolution foreground models becomes important in enhancing the accuracy of component separation pipelines. Although the common practice in small-scale foreground modelling is to inject Gaussian realizations (Delabrouille et al. 2013; Remazeilles et al. 2015; Thorne et al. 2017), there are several recent endeavours to acquire high-resolution estimates of thermal dust and synchrotron maps (Krachmalnicoff & Puglisi 2021; Hervias-Caimapo & Huffenberger 2022; Irfan 2023). In this pursuit, unravelling the nature and level of non-Gaussianity at small angular scales of all the Galactic components plays a crucial role in preparing accurate foreground models. Morphological tools are instrumental in achieving this goal.

The kurtosis nature of synchrotron non-Gaussianity at small angular scales is an intriguing feature that can provide important insights into the astrophysics of synchrotron emission as well as foreground modelling for CMB experiments. This observation naturally leads to the question of investigating the non-Gaussian features exhibited by other major Galactic emissions at small scales. This chapter looks deeper into this aspect, exploring the properties of free-free, AME and thermal dust emissions.

Kurtosis non-Gaussianity can potentially originate from the underlying log-normal probability distribution of the synchrotron field. If this holds true, then all fields that exhibit the log-normal distribution can be expected to display kurtosis non-Gaussianity. Taking a more generalized perspective, it is possible that all random fields following positively skewed distributions showcase kurtosis behaviour at small scales. Note that Galactic emissions are interstellar radiation fields with positively skewed distributions (see the histograms of different Galactic foreground maps shown in figure 7.3.1). If this is indeed the case, kurtosis nature becomes a universal behaviour for positively skewed distributions. We begin this chapter by investigating this point. We apply the Minkowski functional (MF) formalism on

three toy models of random fields characterized by positively skewed distributions, namely chi-squared, log-normal, and Rayleigh fields. We examine their statistics at different angular scales. Then, we investigate the statistical properties of AME, free-free and dust maps given by Planck and quantify the level and nature of non-Gaussianity present in these fields.

This chapter is structured as follows. Section 7.2 examines the non-Gaussian characteristics of toy models, studying random fields with different probability distributions. In section 7.3, we analyse non-Gaussian deviations of major Galactic foregrounds, such as AME, free-free, and thermal dust emissions. By studying temperature maps at various angular scales, we observe the behaviour of non-Gaussian features with scale. Section 7.4 presents a summary of our key findings and discussions.

7.2 Non-Gaussianity of positively skewed random fields - toy examples

We start our analysis by exploring the small-scale statistics of a few toy examples — random fields following different probability distributions, namely chi-squared, log-normal and Rayleigh distributions. We briefly discuss these distributions below and recommend Johnson et al. (1994) for more details.

Chi-squared distributed field: In statistics and probability theory, the sum of squares of k-independent normal random variables follows the chi-squared distribution. This distribution is parameterized by k, which specifies the number of degrees of freedom. The probability density function (PDF) is given as,

$$\mathcal{P}(x) = \frac{1}{2^{k/2}\Gamma(k/2)} x^{k/2-1} e^{-x/2}. \tag{7.1}$$

The chi-squared distribution is a positively skewed distribution, with the extent of skewness determined by the value of k. It is extensively utilized in statistics for hypothesis testing, goodness-of-fit analysis, and constructing confidence intervals. Its wide-ranging applications make it a fundamental tool for drawing inferences and making statistical inferences in various fields of study. Figure 7.2.1 (top-left panel) shows the density function $\mathcal{P}(x)$ for different values of k.

For our calculations, we have generated a chi-squared distributed random field by summing the square of six independent Gaussian random fields ($k = 6$), which are mean-free and have standard deviation unity. Figure 7.2.1 (middle-left panel) shows the chi-square distributed map along with the histogram of the map (bottom-left panel).

Log-normal distributed field: A random variable whose logarithm is Gaussian distributed has a log-normal probability distribution. In other words, if the variable x is log-normal distributed, then $z = \ln(x)$ follows a Gaussian distribution. The PDF for a log-normal variable x is,

$$\mathcal{P}(x) = \frac{1}{x\sigma_0\sqrt{2\pi}} \exp\left(- \frac{(\ln x - \mu)^2}{2\sigma_0^2} \right). \tag{7.2}$$

For any Gaussian random variable z, $x = e^{\mu+\sigma_0 z}$ is a positive variable which is log-normal distributed, with two parameters μ and σ_0. For the purpose of our analysis, we have obtained a log-normal random field by taking the logarithm of a Gaussian field, with $\mu = 0$ and $\sigma_0 = 0.3$. In figure 7.2.1, the top panel of the second column illustrates the PDF of the log-normal distribution corresponding to different σ_0 values. The second column also includes the log-normal map prepared (middle panel) along with the histogram of the map (bottom panel).

Rayleigh distributed field: When two independent Gaussian random variables, u and v, with mean zero and variance σ_0^2, are combined as the square root of

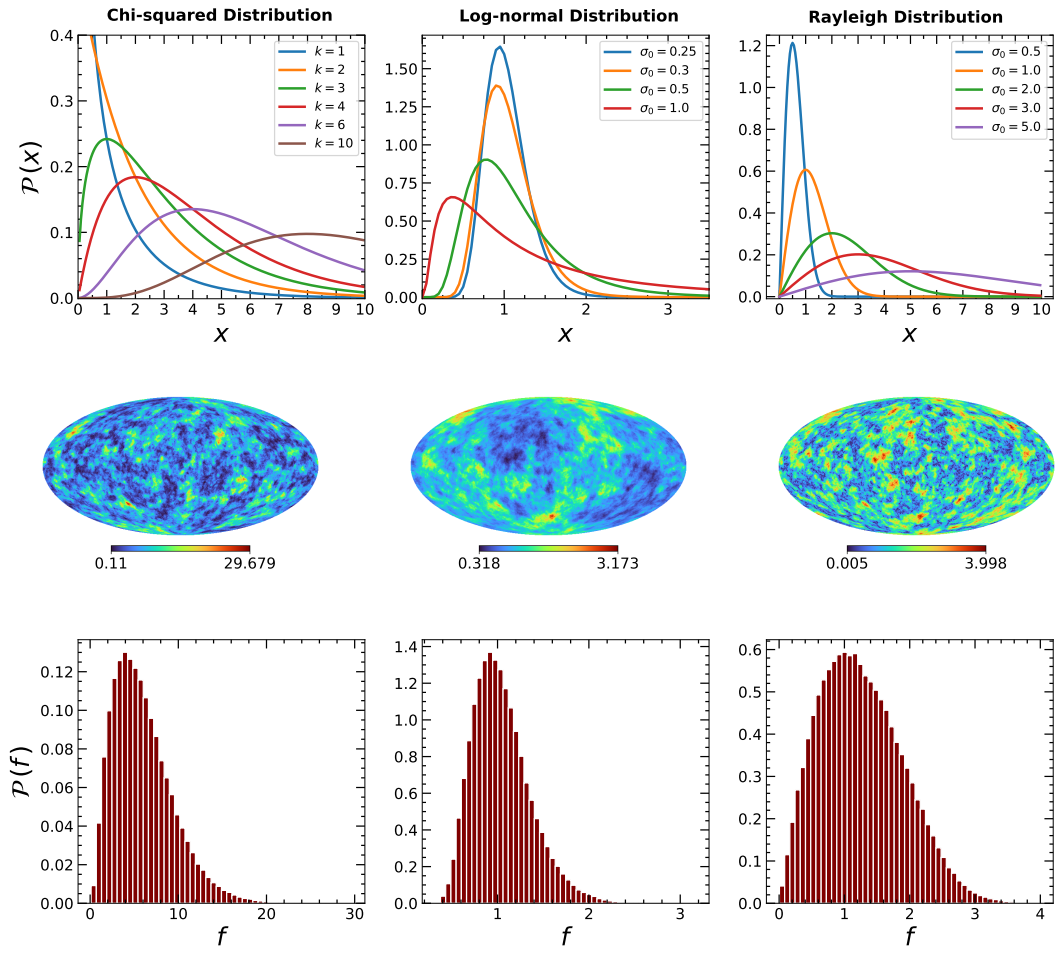

FIGURE 7.2.1: *Top*: PDF of the chi-squared (left), log-normal (middle) and Rayleigh (right) distributions for different values of their respective parameters. The value of μ is kept as zero for log-normal distribution. *Middle*: Maps following chi-squared, log-normal and Rayleigh distribution. *Bottom*: The normalized histogram of the field values of the maps shown in the middle panel.

their sum of squares ($x = \sqrt{u^2 + v^2}$), the resulting x variable follows a Rayleigh distribution. PDF for a Rayleigh distribution is given by,

$$\mathcal{P}(x) = \frac{x}{\sigma_0^2} e^{-x^2/2\sigma_0^2}. \tag{7.3}$$

Rayleigh-distributed random field is prepared by taking the square root of the sum of squares of two Gaussian fields with mean zero and unit variance. Figure 7.2.1 (top-right panel) shows the shape of Rayleigh distribution for different σ_0 values. Also, the middle- and bottom-right panels show the Rayleigh map generated (with

$\sigma_0 = 1$) and the histogram of the map, respectively.

Next, we examine how the non-Gaussian features of these random fields, with varying PDFs, behave at small angular scales. The three maps are prepared at a resolution of $N_{\rm side} = 128$ after applying a Gaussian beam of FWHM = 60 arcmin. To isolate small-scale fluctuations and remove large-scale modes, we apply the same tanh bandpass filter used in the chapters 5 and 6, as defined in eq. (6.2). For the uppercut, ℓ^*, we select a value of 180, corresponding to the scale of the applied Gaussian beam. Also, $\Delta\ell$ is taken as 10. For the three toy maps, scalar MFs are calculated for four different values of ℓ_c: 20, 50, 90, and 140.

Since our main interest is to quantify non-Gaussianity, we calculate the deviation of MFs for these maps from their corresponding Gaussian maps. For this purpose, we generate Gaussian isotropic simulations using the angular power spectrum[†] of these maps. Also, we define non-Gaussian deviation as,

$$\Delta V_k = V_k - V_k^G, \tag{7.4}$$

where the superscript G refers to the Gaussian maps. Figure 7.2.2 shows ΔV_k normalized with the amplitude of V_k^G for all three maps at different angular scales. These results are obtained by averaging over 1000 Gaussian isotropic maps.

We find that as we go to smaller angular scales, irrespective of the probability distribution, all the maps exhibit decreasing levels of non-Gaussianity. This is evident from all the three ΔV_ks. ΔV_k of chi-squared and log-normal maps exhibit characteristic shape similar to that of kurtosis type $g_{\rm NL}$ non-Gaussianity, which was seen for Haslam and other synchrotron maps before. However, for Rayleigh maps, the shape of ΔV_k is different, resembling the shape of non-Gaussianity where skewness dominates (see figure 3.4 for comparison).

[†]Power spectrum is computed using the `anafast` subroutine of `healpy` package.

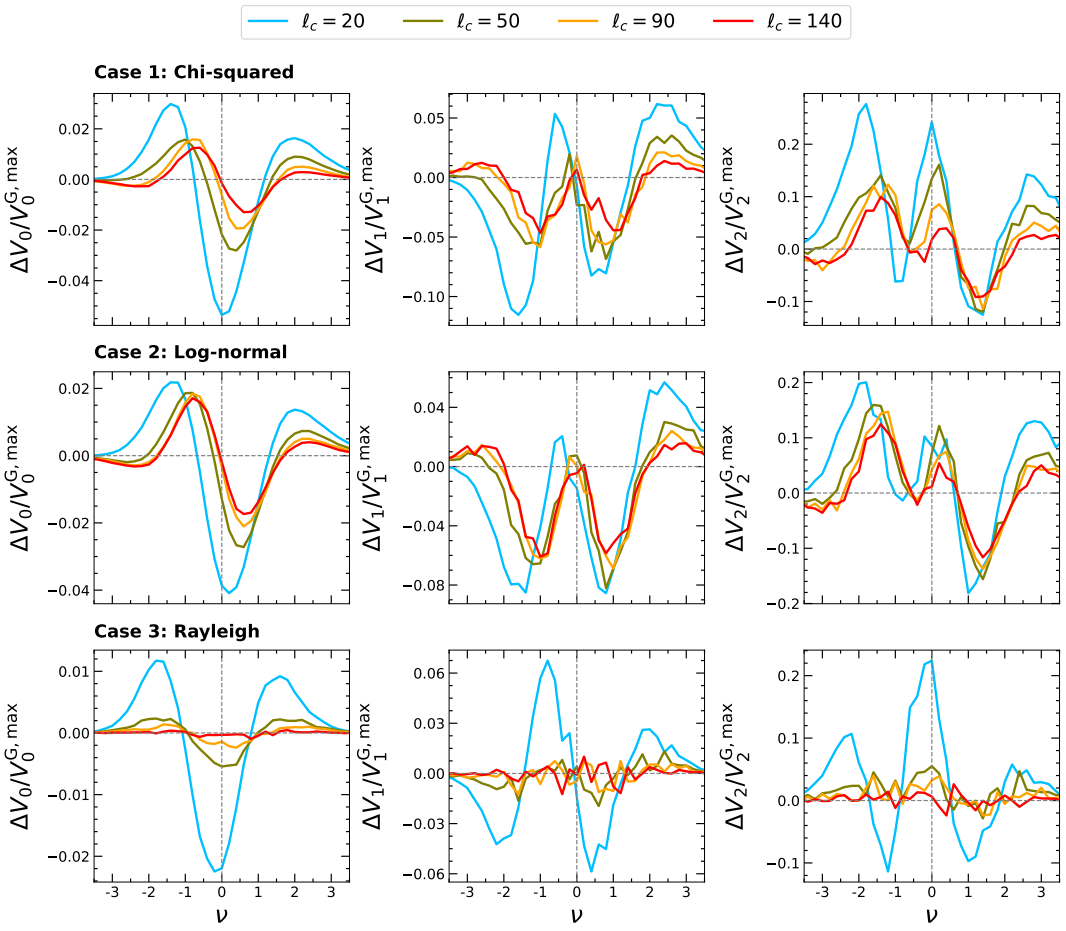

FIGURE 7.2.2: Non-Gaussian deviation (ΔV_k) for random fields with arbitrary PDFs at different angular scales. We find that as we go to smaller angular scales, irrespective of the probability distribution, all the maps exhibit decreasing levels of non-Gaussianity. However, the shape of non-Gaussian deviations are specific to the underlying distribution, with chi-squared and log-normal maps exhibiting shapes corresponding to kurtosis non-Gaussianity while Rayleigh distribution has skewness-dominated non-Gaussianity.

This demonstrates that kurtosis non-Gaussianity is not a universal feature of positively skewed random fields. The nature of non-Gaussianity at small scales depends on the nature of the field under consideration. However, irrespective of the PDF, the fields become more Gaussian as the large-scale fluctuations are discarded.

7.3 Small-scale statistics of foreground components

Next, we analyse the non-Gaussian nature of free-free, AME and thermal dust emissions at small angular scales. The following Galactic emission temperature maps from Planck[‡] are used for this study.

- **Free-free:** We use the Planck free-free emission measure map derived using the Commander component separation method. This map has a resolution set by $N_{\rm side} = 256$, with FWHM = 60 arcmin.
- **AME:** Commander AME temperature map is used for AME. This map is also at $N_{\rm side} = 256$, with FWHM = 60 arcmin.
- **Thermal dust:** The Planck 545 GHz frequency map is used for thermal dust emission. At these frequencies, thermal dust is known to be the dominant emission. This map is provided at $N_{\rm side} = 2048$. For our calculations, we downgrade the map to $N_{\rm side} = 1024$.

Figure 7.3.1 shows the foreground maps studied along with their histograms. Planck CMB Common Intensity Mask is used to mask the high-intensity pixels in the Galactic region. It has a sky fraction of 77.9%. To minimise the errors associated with sharp mask boundaries, the mask is apodized with 120 arcmin Gaussian beam for $N_{\rm side} = 256$ and 30 arcmin Gaussian beam for $N_{\rm side} = 1024$ analyses. The smoothened mask is shown in figure 7.3.2. Note that all the maps are presented in different units, as provided by Planck. Since rescaling the field with a unit conversion factor does not alter the morphology, we do not standardize all the maps to the same units.

To quantify the non-Gaussian deviations, Gaussian isotropic simulations corresponding to each of the foreground maps are generated. We create 1000 Gaussian

[‡]The maps are obtained from https://pla.esac.esa.int/

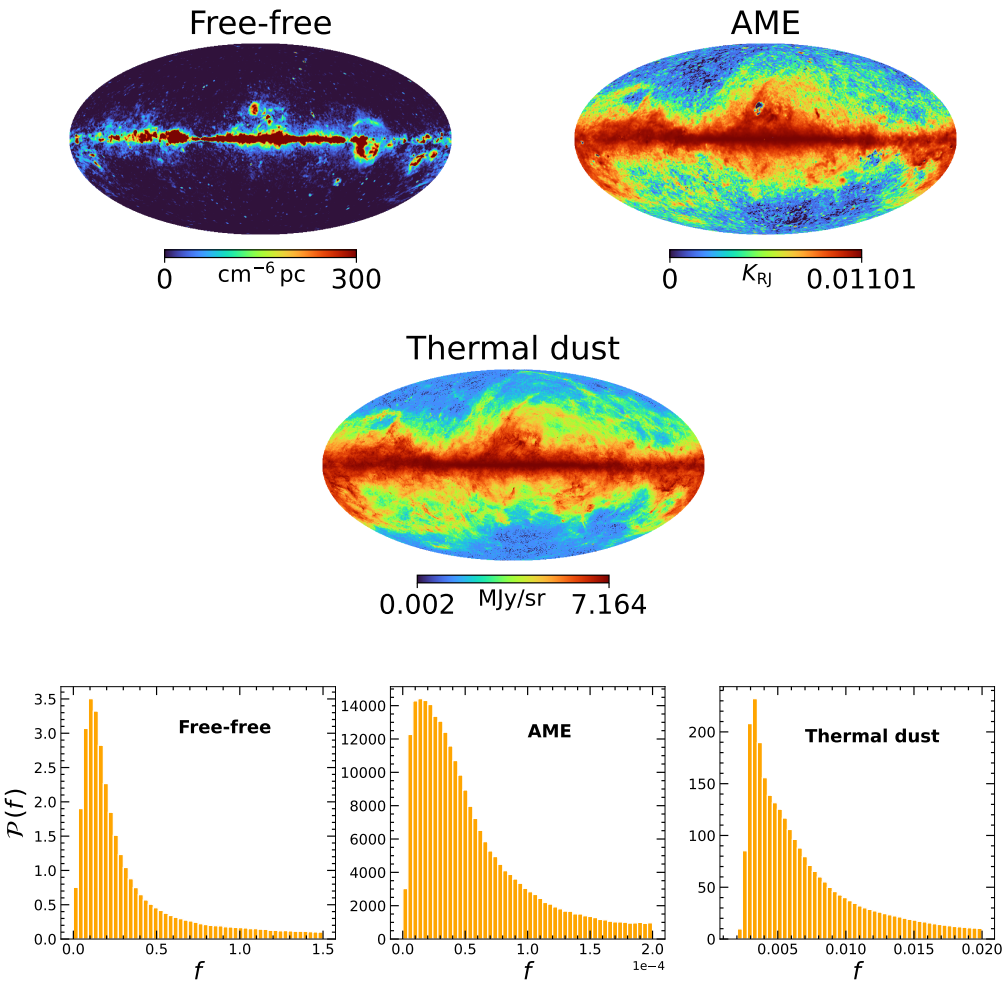

FIGURE 7.3.1: Maps of different Galactic components considered in this study — free-free (top left), AME (top right) and thermal dust (middle). These maps are obtained from Planck. Note that the units are as given by Planck, and we have not standardized them. The color scale for free-free map follows a linear scale, while the scale is histogram equalised for AME and thermal dust maps. *Bottom:* The histogram of the maps given above.

simulations using the power spectrum of the respective maps. Similar to the previous chapter, the power spectrum is computed using the `NaMaster`[§] package, which takes care of the biases associated with incomplete sky coverage.

Figure 7.3.3 shows the non-Gaussian deviations (ΔV_k) of free-free and AME maps. They are computed for different ℓ_c values ($\ell_c = 20, 50, 90$, and 140). We find that similar to synchrotron maps, the level of non-Gaussianity decreases for higher ℓ_c

[§] https://namaster.readthedocs.io/

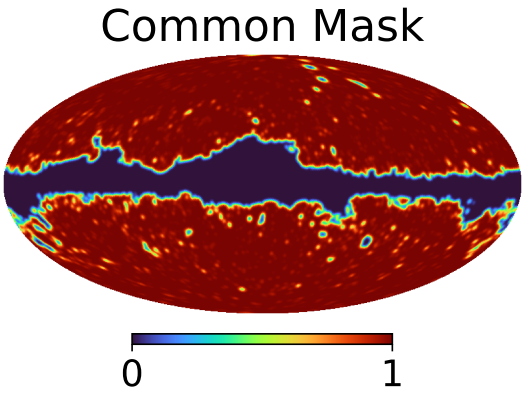

FIGURE 7.3.2: Planck CMB common intensity mask used in the analysis. A Gaussian smoothing with FWHM = 120 arcmin is applied. This mask has a sky-fraction of 77.9%.

values, implying that the fields tend to become Gaussian at small scales. This is true for both AME and free-free maps. More importantly, ΔV_k exhibits the shape of that of kurtosis non-Gaussianity for both AME and free-free maps, despite the differences in the astrophysical mechanism responsible for these emissions.

Next, we discuss thermal dust emission. Using the high-resolution Planck dust maps, we can explore further small scales. Here, we choose the uppercut to be $\ell^* = 1200$. ΔV_k for the thermal dust map are shown in figure 7.3.4. As observed for synchrotron, free-free, and AME, the nature of non-Gaussianity in the dust maps is also of kurtosis type. Also, the level of non-Gaussianity decreases towards small angular scales. However, the rate at which non-Gaussianity amplitude falls with the scale is slower than that of other signals.

To estimate the scale dependence of non-Gaussianity for various Galactic components, we examine how the non-Gaussian deviations vary as a function of ℓ_c. We define the average of ΔV_k[¶],

$$\Delta\overline{V}_k = \frac{1}{N_{\rm tot}} \sum_{\nu=-2}^{2} |\Delta V_k(\nu)|, \tag{7.5}$$

[¶]We ignore the correlations between the thresholds (ν), as done in the previous chapter.

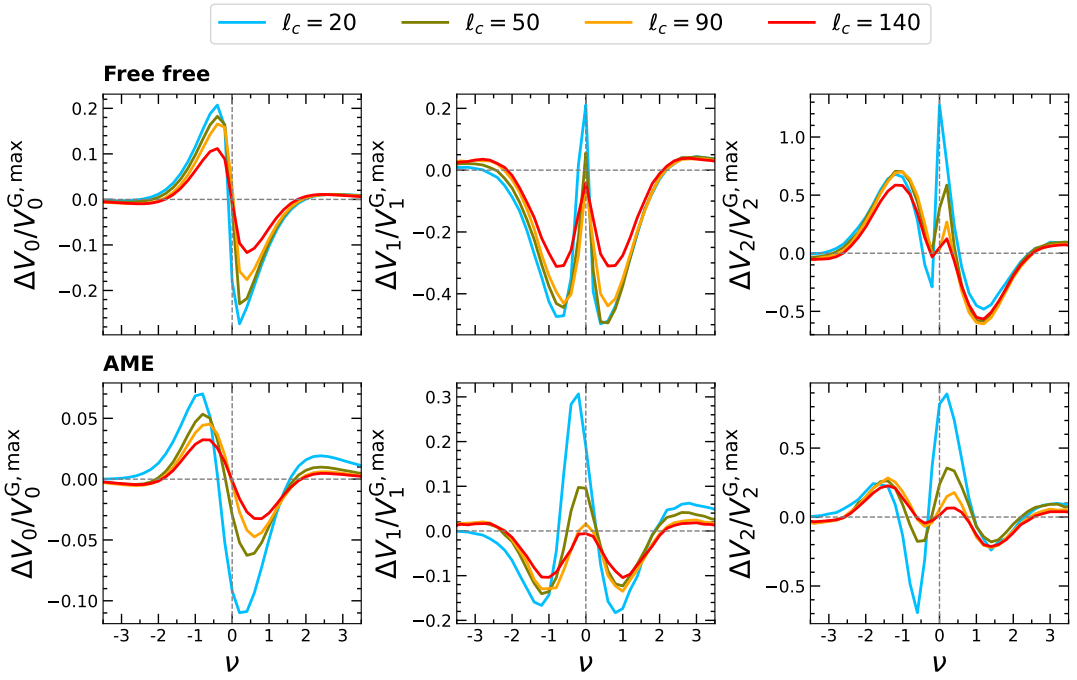

FIGURE 7.3.3: Non-Gaussian deviation (ΔV_k) for Planck free-free and AME foreground maps. The plots show that the level of non-Gaussianity decreases for higher ℓ_c values, implying that the fields tend to become Gaussian at small scales. This is similar to the results we got for synchrotron maps in the previous chapters. More importantly, ΔV_k exhibits the shape of that of kurtosis non-Gaussianity for both AME and free-free maps, despite the differences in the astrophysical mechanism responsible for these emissions.

where $N_{\rm tot} = 21$, as the bin size we choose is $\Delta\nu = 0.2$.

Figure 7.3.5 shows the variation of this quantity with respect to angular scales ℓ_c for different foreground components, including synchrotron. In the top panel, we show the results for all the components, extending up to $\ell_c = 140$. Synchrotron results are obtained using the Haslam map. The lower panel exclusively presents results for the dust map, covering scales down to $\ell_c = 900$.

We find that foreground signals exhibit distinct levels of non-Gaussianity. At all angular scales, the amplitudes of ΔV_k are notably higher for free-free and thermal dust compared to synchrotron and AME. As a function of ℓ_c, the level of non-Gaussianity falls for all the emissions. However, the rate of decrease is

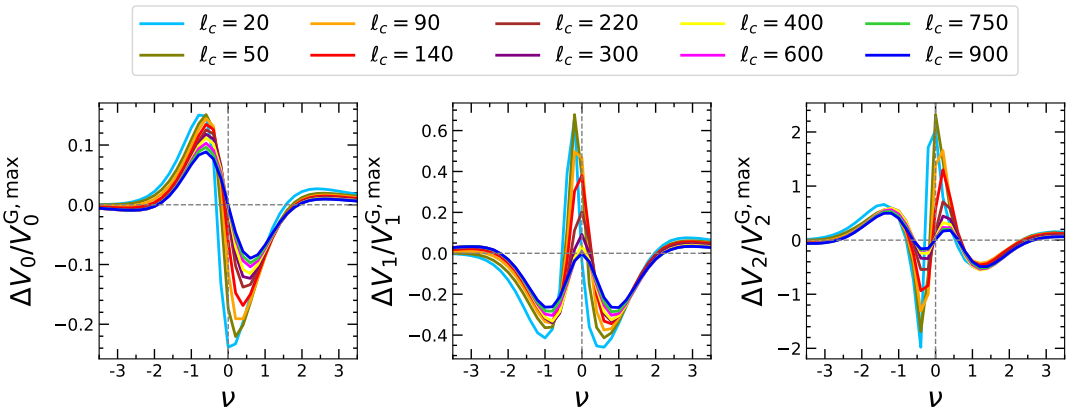

FIGURE 7.3.4: Non-Gaussian deviation (ΔV_k) for thermal dust emission. Like other Galactic emissions, the level of non-Gaussianity decreases towards small angular scales, with the nature of non-Gaussianity being of kurtosis origin. It should be noted that the rate at which non-Gaussianity amplitude falls with the scale is slower than those for other emissions.

different for different emissions. As an example, non-Gaussianity exhibits only a modest reduction in dust maps, even at angular scales as fine as arcminutes. This indicates that both the level of non-Gaussianity and the rate at which it declines with angular scales rely on the astrophysics of these emissions. Despite this, all these emissions exhibit a kurtosis-type non-Gaussianity. Table 7.3.1 provides a summary of the nature and amplitudes of non-Gaussianity for different foreground fields considered in this study.

All of these findings carry significant implications in the context of non-Gaussian modelling for foreground signals. Irrespective of the signal, kurtosis non-Gaussianity can be considered in modelling foregrounds at small angular scales. However, the extent of non-Gaussianity and the scale over which non-Gaussian modelling becomes necessary are distinct for each foreground, necessitating a better understanding of the underlying emission mechanism. A comprehensive examination of how the level of non-Gaussianity relates to the astrophysical properties of specific emissions is not within the scope of this current work but is planned for investigation in the near future.

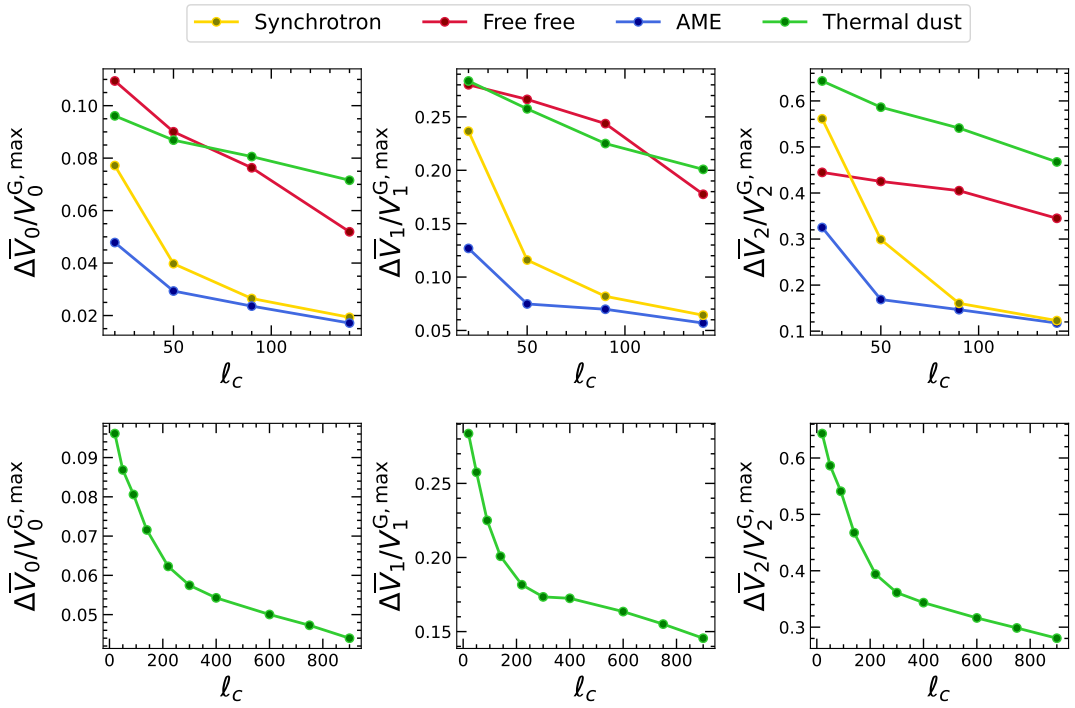

FIGURE 7.3.5: *Top*: Average non-Gaussian deviation ($\Delta\overline{V}_k$) with respect to the parameter ℓ_c for free-free, AME and thermal dust maps. Additionally, the results for the synchrotron map (Haslam) are provided for comparison. *Bottom*: The same plot as the above, focusing on thermal dust emission up to $\ell_c = 900$. It shows that the level of non-Gaussianity and the rate at which it falls with angular scales are different for different emissions. Nevertheless, the kurtosis nature of non-Gaussianity remains consistent across all emissions.

7.4 Summary and discussions

In this chapter, we have explored the characteristics of non-Gaussianity observed in free-free, AME and thermal dust emission and compared them with synchrotron. We first analyse a set of toy models consisting of random fields that follow positively skewed PDFs. Our objective is to investigate whether the kurtosis nature of non-Gaussianity is a universal feature of positively skewed random fields at small angular scales. In our analysis of positively skewed fields, we found that both chi-squared and log-normal distributed maps exhibit kurtosis non-Gaussianity. However, the shape of non-Gaussian deviations of MFs for the Rayleigh map is dominated by skewness. Based on this test, we conclude that kurtosis non-Gaussianity

Foreground Map	Non-Gaussianity			
	Nature	$\Delta\overline{V}_k^{50}$	$\Delta\overline{V}_k^{90}$	$\Delta\overline{V}_k^{140}$
Synchrotron	kurtosis	0.15	0.08	0.06
Free-free	kurtosis	0.26	0.24	0.19
AME	kurtosis	0.09	0.08	0.06
Thermal dust	kurtosis	0.31	0.28	0.27

TABLE 7.3.1: The table summarises the nature and amplitudes of non-Gaussianity observed in various foreground fields considered in this study. The amplitude is expressed in terms of $\Delta\overline{V}_k$ averaged over all the three scalar MFs. The superscript denotes the angular scale (ℓ_c) probed for each map. Our analysis indicates that the nature of non-Gaussianity of all the foreground maps is of kurtosis origin, with skewness being subdominant. Also, our findings reveal that, as we explore smaller angular scales, the amplitude of non-Gaussianity for all the maps decreases, with the rate of decrease being specific to the Galactic emission.

is not a universal property of random fields at small angular scales but depends on the PDF of the field. However, it is important to mention that for all the fields, the degree of non-Gaussianity reduces as we progressively remove large-scale modes and focus on smaller scales. This observation is in agreement with the findings we obtained previously for synchrotron maps.

We then explore the behaviour of different foreground components regarding non-Gaussian features. This study involves examining Galactic emission maps, specifically free-free emission, AME, and thermal dust emission, obtained from Planck data. From our analysis using MFs, we observe that the nature of non-Gaussianity in all these Galactic components is kurtosis-type, with skewness being sub-dominant. By combining our findings with the previous synchrotron results, we can confidently conclude that kurtosis non-Gaussianity is a common characteristic observed in all the foreground maps at small scales, irrespective of the different astrophysical sources of these signals. This finding holds significance for the small-scale modelling of Galactic foregrounds, especially in the context of CMB experiments. We

propose that, instead of assuming the small-scale foreground fields to be Gaussian distributed, it is more realistic to model them as mildly non-Gaussian kurtosis fluctuations. The approach developed by Martire et al. (2023) based on kurtosis non-Gaussianity for small-scale synchrotron modelling is a relevant step in this direction.

Nevertheless, in order to introduce non-Gaussianity at small scales, it is of utmost importance to quantify the scale dependence of non-Gaussian deviations. This involves identifying the scales where kurtosis non-Gaussianity can be appropriately approximated and the scales where Gaussian approximations hold true. Such knowledge is vital for accurately modelling foreground fields and minimising the bias associated with the models. *Our findings demonstrate that the scale-dependence of non-Gaussian deviations varies across different Galactic components and is contingent on their specific emission mechanisms.* For instance, in the case of thermal dust emission, which we have analysed up to arcminute scales, there is less reduction in non-Gaussianity, even at the smallest scale probed ($\ell_c = 900$). In summary, our morphological analysis opens new direction in modelling Galactic components at small angular scales.

Chapter 8

Beyond Minkowski Functionals and Tensors — Total Absolute Curvature*

8.1 Introduction

Minkowski functionals (MFs) serve as prevalent statistical estimators for exploring the morphological characteristics of various cosmological and astrophysical fields. These quantities are based on integral geometry and measure the geometric and topological properties of the connected regions and holes in the excursion set of a random field. In the preceding chapters, we have harnessed the potential of these tools in extracting the statistical features of foreground emissions. The vector and tensor generalizations of MFs provide additional degrees of freedom (Schröder-Turk

*This chapter is based on the papers that are under preparation.

et al. 2010; Chingangbam et al. 2017b), thereby expanding their applicability in the study of random fields. For example, the tensor generalization of contour length, Contour Minkowski Tensor (CMT), contains information on how anisotropic the structures are on an excursion set and tracks the presence of global alignment in the data (Ganesan & Chingangbam 2017; Appleby et al. 2018a). Betti numbers are related topological quantities, which count the connected regions and holes in the excursion set and contain independent information (Chingangbam et al. 2012; Park et al. 2013). While these quantities provide valuable insights into the morphological attributes of different fields in nature, there is scope for further enhancement in this direction to fully understand the properties of these fields.

Among the three scalar MFs, the area fraction is directly tied to the field values and does not involve the field derivatives. Conversely, contour length and genus are defined as the integral along the boundary of the excursion set and contain the information of the first and second derivatives of the field. In other words, the information comprising the two first derivatives and three second derivatives is condensed in the form of these two scalar MFs. With the aim of maximizing the understanding of random field properties, one can explore new geometrical and topological quantities by constructing other combinations of field derivatives. In this chapter[†], we introduce *total absolute curvature (K)*, which contains information not captured by the MFs. This quantity was studied for the first time by Chern & Lashof (1957). Here, we introduce it for excursion sets of smooth random fields in $2d$.

Similar to MFs, K has a distinct functional form as a function of threshold, which depends on the nature of the field. This property makes it useful in quantifying the non-Gaussianity of a random field. Here, we provide the analytical ensemble

[†]This chapter slightly diverges from the main theme of the thesis, which is the characterization of the statistical properties of foreground emissions. However, the tool presented here promises to be useful in studying foreground fields.

expectation formulae of K for a Gaussian isotropic field. We then present the numerical computation of K for different mildly non-Gaussian fields, such as $f_{\rm NL}$ and $g_{\rm NL}$ local-type non-Gaussianity. The results of these calculations offer additional insights into identifying the level and nature of non-Gaussianity in random fields.

This chapter is structured in the following way. In Section 8.2, we start by defining total absolute curvature for a single structure and then generalized to excursion set boundaries of the smooth random field. Then, we describe how to calculate K for random fields on a sphere and provide its analytical ensemble expectation for a Gaussian isotropic field. A discussion on K for fields that are mildly non-Gaussian is given in section 8.3. We conclude this chapter by summarizing our key findings and their potential applications in section 8.4.

8.2 Total absolute curvature for random fields on a sphere

For any closed curve C parametrized by it's arc length ℓ, the total absolute curvature is defined as (Chern & Lashof 1957),

$$K = \frac{1}{2\pi} \int_C |\kappa| \, d\ell, \tag{8.1}$$

where κ is the geodesic curvature of the curve.

Let us begin with a few simple examples. For a circle with radius r, $\kappa = 1/r$ and thus, K is unity. For any other convex region (closed curves for which κ is positive at every point), K is the same as the genus and is unity. This is according to the

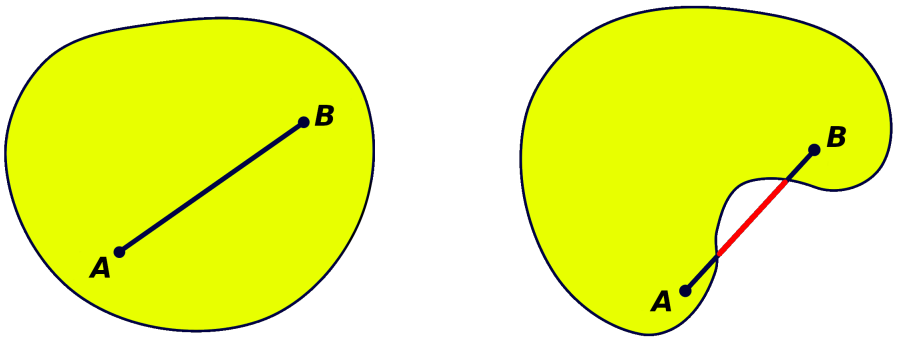

FIGURE 8.2.1: A convex region (left) and a non-convex region (right). K is unity for a convex region, while it is greater than 1 for a non-convex region.

Gauss-Bonnet theorem, which says that for a closed curve C,

$$\int_C \kappa \, d\ell = 2\pi. \tag{8.2}$$

If the closed curve contains negative κ values (non-convex regions), the value of K is greater than 1. In geometry, a set or a region is said to be convex if the line segment connecting any two points inside the region lies completely inside the region. Otherwise, it is referred to as a non-convex region. Figure 8.2.1 shows a convex region (left) and a non-convex region (right).

Now, let us extend K for the closed curves on the excursion set for random fields. Consider a field u, defined on a $2d$ manifold. We assume u to be mean-free and has standard deviation σ_0. For each threshold value ν, we obtain the excursion sets whose boundaries (given by the condition, $u = \nu\sigma_0$) form closed curves. We can generalize the definition of K as,

$$K(\nu) = \frac{1}{2\pi A} \int_{\partial Q_\nu} |\kappa| \, d\ell, \tag{8.3}$$

where A is the area of the manifold under consideration. It is important to note that eq. (8.3) defines the total absolute curvature per unit area (using the same symbol as in eq. (8.1)).

In terms of the field u and it's derivatives, K is given as,

$$K(\nu) = \frac{1}{8\pi^2} \int_M |\nabla u| \, \delta(u - \nu\sigma_0) \, |\kappa| \, da. \tag{8.4}$$

This equation is similar to the expression for genus given in eq. (3.44). κ is expressed in terms of u and it's derivatives as given in eq. (3.46). As in section 3.3.2.1, δ-function is approximated as $\delta(u - \nu\sigma_0) = 1/\Delta\nu$, if $u \in [\nu\sigma_0 - \Delta\nu/2, \nu\sigma_0 + \Delta\nu/2]$ and zero elsewhere. $\Delta\nu$ is the bin size.

For a Gaussian isotropic field u, one can obtain the analytic ensemble expectation value for K in terms of the vector $X \equiv (u, u_{;1}, u_{;2}, u_{;11}, u_{;12}, u_{;22})$,

$$\langle K(\nu) \rangle = \frac{1}{2\pi} \int dX P(X) \, |\nabla u| \, \delta(u - \nu\sigma_0) \, |\kappa|, \tag{8.5}$$

where $P(X)$ is the joint PDF of X. As the field is Gaussian distributed,

$$P(X) = \frac{1}{\sqrt{(2\pi)^6 \det \Sigma}} \exp\left(-\frac{1}{2} X^T \Sigma^{-1} X \right). \tag{8.6}$$

Σ is the covariance matrix (Tomita 1986) expressed in terms of σ_0, $\sigma_1 \equiv \langle |\nabla u|^2 \rangle$ and $\sigma_2 \equiv \langle (\nabla^2 u)^2 \rangle$, as

$$\Sigma = \begin{pmatrix} \sigma_0 & 0 & 0 & -\sigma_1/2 & -\sigma_1/2 & 0 \\ 0 & \sigma_1/2 & 0 & 0 & 0 & 0 \\ 0 & 0 & \sigma_1/2 & 0 & 0 & 0 \\ -\sigma_1/2 & 0 & 0 & \sigma_2/2 & \sigma_2/6 & 0 \\ -\sigma_1/2 & 0 & 0 & \sigma_2/6 & \sigma_2/2 & 0 \\ 0 & 0 & 0 & 0 & 0 & \sigma_2/6 \end{pmatrix}. \tag{8.7}$$

The final expression[‡] for the ensemble expectation of K at each ν is,

$$\begin{aligned}\langle K(\nu)\rangle &= A_\gamma \int_0^\infty \mathrm{d}J \Bigg[2\pi\Bigg\{\int_0^{\alpha_0} \mathrm{d}\alpha\, G\ \cos\alpha - \int_{\pi-\alpha_0}^{\pi} \mathrm{d}\alpha\, G\ \cos\alpha \\ &\quad - \int_{\alpha_0}^{\pi-\alpha_0} \mathrm{d}\alpha\, G\ \cos\alpha\Bigg\} \\ &\quad + \int_{\alpha_0}^{\pi-\alpha_0} \mathrm{d}\alpha\, G\{4\theta_m \cos\alpha + 2\sqrt{2}\sin\alpha\sqrt{1-2\cot^2\alpha}\}\Bigg], \end{aligned} \tag{8.8}$$

where,

$$A_\gamma = \frac{1}{16\pi^3}\left(\frac{\sigma_1}{\sigma_0}\right)^2 \frac{1}{\gamma\sqrt{1-\gamma^2}} \tag{8.9}$$

$$G(\nu, J, \alpha) = J^3 e^{-\frac{J^2}{2}} \sin\alpha \exp\left\{-\frac{1}{2}\left(\frac{\nu+\gamma J\cos\alpha}{\sqrt{1-\gamma^2}}\right)^2\right\}. \tag{8.10}$$

$$\alpha_0 = \cot^{-1}\left(\frac{1}{\sqrt{2}}\right), \quad \theta_m = \cos^{-1}\left(-\sqrt{2}\cot\alpha\right), \quad \gamma = \sigma_1^2/\sigma_0\sigma_2. \tag{8.11}$$

Here, J and α are the polar coordinates obtained from J_1 and J_2 which are defined in terms of the eigenvalues of the Hessian of the field u as,

$$J_1 = \lambda_1 + \lambda_2, \qquad J_2^2 = 2(\lambda_1 - \lambda_2)^2. \tag{8.12}$$

We now demonstrate the agreement between the numerical calculations and the analytic formula. We compute K numerically for 200 Gaussian isotropic CMB maps. The analytic K is computed by carrying out the numerical integration given in eq. (8.8). The results are shown in Figure 8.2.2. We see that the results are in good agreement.

The shape of K is symmetric and depends on γ values. γ is a factor which involves σ_2, the variance of the second derivatives of the field. Because of this, K provides extra information compared to MFs.

[‡]The derivation of the analytical expectation is not included in the thesis and will be published as Chingangbam et al. (2024).

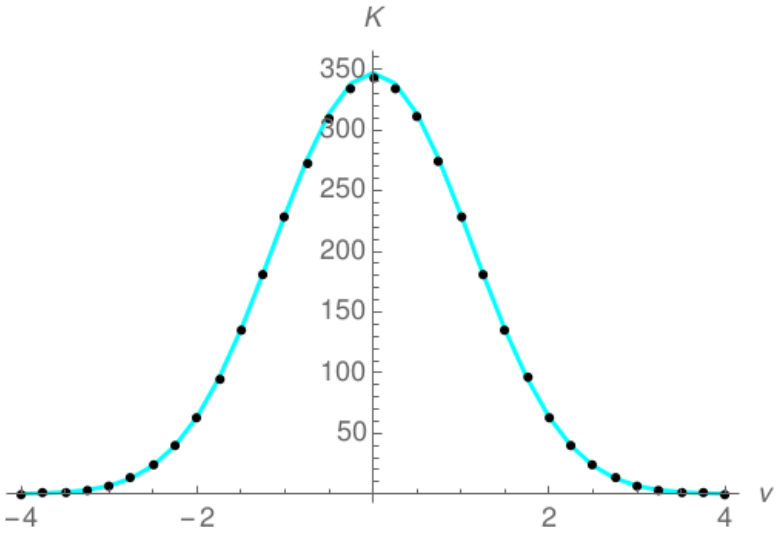

FIGURE 8.2.2: Absolute curvature K computed for 200 Gaussian isotropic CMB maps (denoted by brown dots) compared with the analytical formula given in eq (8.8) (cyan line). We see that numerical results are in good agreement with the analytical formula.

8.3 *K* for mildly non-Gaussian fields

Next, we study the behaviour of K for mildly non-Gaussian fields on $\mathcal{S}^2$. We analyse the non-Gaussian CMB maps with local-type non-Gaussianity obtained using eq. (3.41) in the Sachs-Wolfe (SW) limit. Our focus is to illustrate the power of K in providing additional information for non-Gaussianity. Here, we work in the SW limit, which is sufficient to obtain the non-Gaussian information. A complete analysis of non-Gaussian CMB maps using a full radiative transfer function will be carried out in the near future.

We generate 1000 non-Gaussian CMB maps in the SW limit using eq. (3.41), with `healpix` resolution $N_{\rm side} = 512$ for three cases: only $f_{\rm NL}$, only $g_{\rm NL}$ and $f_{\rm NL}$ plus $g_{\rm NL}$. We take $f_{\rm NL} = 100$ and $g_{\rm NL} = 10^6$, for which the non-Gaussian terms are of comparable amplitudes. We also generate 1000 Gaussian CMB maps.

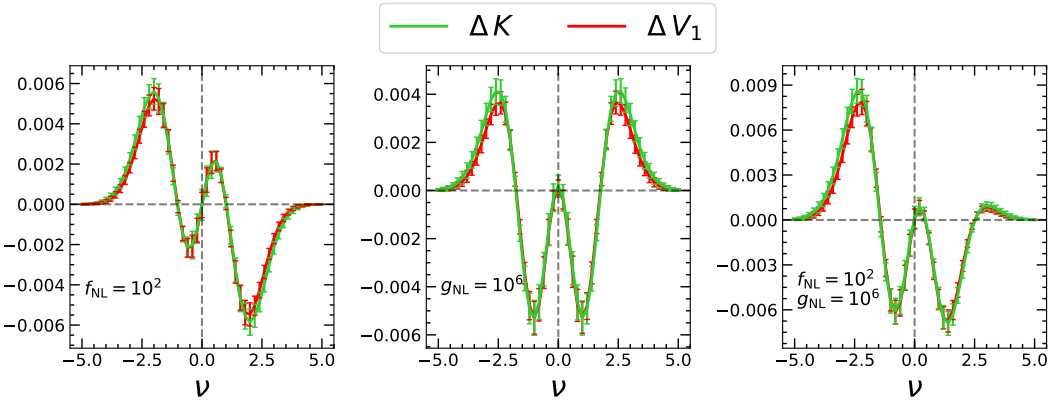

FIGURE 8.3.1: Non-Gaussian deviations for K for local-type non-Gaussian CMB maps: only $f_{\rm NL}$ (left), only $g_{\rm NL}$ (middle) and $f_{\rm NL}$ plus $g_{\rm NL}$ (right). ΔV_k for contour length is also shown for comparison. The results are obtained using 1000 non-Gaussian and Gaussian CMB maps. The error bars represent 1σ region. Although the shape of ΔK is similar to ΔV_1, they contain independent information and complement each other.

As done previously for MFs, we define the non-Gaussian deviation for K as,

$$\Delta K = K - K^G, \tag{8.13}$$

where K^G is the K computed for corresponding Gaussian maps. ΔK measures the level and nature of non-Gaussianity.

Figure 8.3.1 shows the average non-Gaussian deviations, ΔK, normalised using the amplitude of K^G for different non-Gaussian cases. For comparison, ΔV_k for contour length is also given. It is seen that ΔK shows the characteristic shapes for different non-Gaussian cases. We observe that there is some similarity of the shape of ΔK with the shape of ΔV_1. However, they are not identical, and they differ at high thresholds. They contain independent information.

Our analysis demonstrates the potential of K as a statistical tool in quantifying the non-Gaussian nature of any random field. Together with MFs, MTs and Betti numbers, K can be used to extract the non-Gaussian features of CMB and any other random fields. We plan to use it for studying foreground maps in the future.

8.4 Summary and discussions

Expanding the suite of morphological tools is crucial to maximising our knowledge about the properties of random fields. In this chapter, we have introduced the total absolute curvature (K), a new morphological tool to probe the geometric and topological properties of smooth random fields.

K measures the absolute values of geodesic curvature integrated along the boundaries of the connected regions in an excursion set. We have presented the estimator for K applicable to discretized 2D random fields and estimated the analytical expectation value of K for a Gaussian isotropic field. Further, we have studied the non-Gaussian deviation of K for mildly non-Gaussian fields, the local-type $f_{\rm NL}$ and $g_{\rm NL}$ CMB maps in the SW limit. Non-Gaussian deviation for K has a characteristic shape similar to contour length but contains supplementary information. Our analysis underscores the capability of this novel statistical quantity to capture the non-Gaussian features of random fields.

Chapter 9

Conclusions

The eternal mystery of the world is its comprehensibility.

Albert Einstein

The primary objective of this thesis is to understand the statistical features of Galactic emissions in the context of ongoing and upcoming CMB experiments. Through rigorous analysis employing various statistical and morphological tools, we explore various properties of these emissions to improve the efficiency of the component separation methods used in the experiments. This facilitates a more accurate recovery of the CMB signal from the raw data, thereby minimising the potential biases in the cosmological inferences. While our primary focus during the analysis was on CMB, the results presented in this thesis hold relevance for both EoR 21 cm experiments and Line Intensity Mapping experiments. Below, we provide a concise overview of the key findings we have obtained. We also outline potential future directions that will extend the analysis carried out in this thesis.

Analytic formula for MFs for composite fields: We begin our analysis by studying

the morphology of composite fields in terms of their constituent fields. This is done by extending the analytical formulae for MFs of mildly non-Gaussian fields in d dimensions. In real-life applications, there exist various situations where the data is a sum of true signal and noise and/or contaminated by other signals. Using the formulae of MFs, we are able to quantify the extent to which the presence of secondary fields can introduce bias to properties of the signal of interest. As a practical illustration, we apply our formalism to two examples: the first involves a composite field consisting of a Gaussian CMB map and a Gaussian noise map, while the second involves a composite field made up of a non-Gaussian CMB and Gaussian noise. Our analysis shows that in the first case, the presence of noise alters the amplitude of the MFs for CMB. The degree of bias depends on the SNR value and the relative size of the structures of the signal and noise fields. In the case of non-Gaussian CMB maps, the presence of noise can lead to a change in the nature of non-Gaussianity apart from the amplitude shift. This modification is quantified by examining how the generalized skewness-kurtosis parameters get altered due to noise, thereby affecting the shape of non-Gaussian deviations.

Statistical properties of Haslam 408 MHz synchrotron map: We start characterizing the statistical features of Galactic emissions by studying the non-Gaussianity and SI of the all-sky Haslam 408 MHz synchrotron map. Haslam map is widely used as the template for Galactic synchrotron in CMB experiments. They are also used in EoR experiments to mitigate synchrotron contamination in detecting 21-cm emission. In synchrotron modelling, small-scale fluctuations are approximated as Gaussian distributed and statistically isotropic. One of the main goals of this work is to check the validity of this assumption. We use morphological tools, MFs and MTs, to quantify the level and nature of non-Gaussianity in the synchrotron field at different sky regions and angular scales. Additionally, our analysis is supported by statistical tools such as angular power spectrum, one-point PDFs and skewness-kurtosis parameters. Our results show that the overall level of non-Gaussianity in the Haslam map decreases as we go to smaller angular scales, in agreement with the

previous studies. The level of non-Gaussianity also falls down as brighter regions in the sky are masked. Nevertheless, further quantification reveals that at the Haslam resolution ($\sim 1.5^\circ$), the non-Gaussianity is not insignificant enough to assume the synchrotron fluctuations as Gaussian distributed at small angular scales. An important finding of the Haslam analysis is that the Galactic synchrotron exhibits kurtosis-type non-Gaussianity, with skewness being subdominant. Moreover, in the cooler regions of the Haslam map, the non-Gaussian deviations of MFs fit very well with the analytic perturbative expressions, keeping up to second-order terms. These results have important implications in the small-scale modelling of synchrotron signals. The SI tests using MTs show that the Haslam map is statistically isotropic as the bright regions are masked as well as at smaller angular scales, consistent with the assumptions taken in synchrotron modelling.

Multi-frequency analysis of synchrotron temperature and polarization maps: A natural extension of the Haslam analysis is to probe the statistical properties of synchrotron maps given by other experiments. In the next work, we study the morphological features of observed frequency maps as well as the component-separated synchrotron maps given by WMAP and Planck telescopes. Our main goals are twofold. First, we determine the variation of morphological properties of the total foreground with observing frequency and compare it with simulations. For this, we have used the maps containing total Galactic emissions with frequencies from 408 MHz to 33 GHz. This study elucidates how the morphology varies with frequency due to the relative dominance of different foreground components at different frequencies. We then compare these maps with the foreground simulations obtained using PySM, offering insights into how well the simulations are able to reproduce the observed multi-frequency data sets. Secondly, we determine the nature of non-Gaussianity and SI of synchrotron fluctuations towards smaller scales using various component-separated synchrotron temperature and polarization maps. We find that all maps exhibit kurtosis-type non-Gaussianity, in agreement with the Haslam map. This finding strongly motivates us to model small-scale fluctuations

of synchrotron emission as a mildly non-Gaussian field (of kurtosis nature) rather than a Gaussian field. All the maps are statistically isotropic at small scales. However, we find that there exist significant morphological differences between Haslam, WMAP, Planck and BeyondPlanck synchrotron maps. This could be because of the presence of residual contamination due to AME and/or free-free or unresolved point sources in the WMAP and Planck synchrotron products. Our results, therefore, throw light on the need for further improvement in the component separation methodologies in CMB experiments. Finally, the kurtosis nature of synchrotron non-Gaussianity indicates that the residual contamination of synchrotron in the cleaned CMB maps results in kurtosis-type non-Gaussianity. In such scenarios, 3-point statistics like bispectrum would be ineffective in identifying these residuals.

Morphological Properties of free-free, AME and thermal dust emissions: We investigate the non-Gaussian properties of other major Galactic emissions such as AME, free-free and thermal dust emissions. The main goal of this work is to see if the kurtosis-origin of non-Gaussianity observed in synchrotron maps is a universal property of astrophysical fields. Before delving into foreground maps, we analyse a set of toy models, random fields that follow positively skewed PDFs such as chi-squared, log-normal and Rayleigh distributions. Our analysis using MFs reveals that out of the three, only chi-squared and log-normal exhibit kurtosis-type non-Gaussianity at small scales. The non-Gaussian deviations of MFs for the Rayleigh field have a shape consistent with skewness-dominated non-Gaussianity. This demonstrates that the kurtosis nature of non-Gaussianity is not a universal trait of all random fields; rather, it varies based on the specific PDF associated with each field. Next, we examine the free-free, AME and thermal dust maps provided by Planck. Our results indicate that regardless of the distinct astrophysical mechanism of emission, all these foreground maps contain non-Gaussianity of kurtosis origin. However, the level of non-Gaussianity and the rate at which it declines with angular scales differs among different foregrounds, with these variations being

dictated by the underlying physics of the emission processes. Instead of assuming the small-scale foreground fields to be Gaussian distributed, we propose that it is more realistic to model them as mildly non-Gaussian kurtosis fluctuations. It should be noted that when injecting kurtosis non-Gaussianity at small scales, it becomes essential to know the scale dependence of non-Gaussianity and estimate the threshold scale beyond which Gaussian approximation holds true. These properties are different for different foreground components. We plan to carry out this analysis in the near future.

Total Absolute Curvature: We introduce a new statistical tool, known as total absolute curvature (K), to probe the geometric and topological properties of random fields in nature. Defined as the absolute curvature parameter integrated over the boundaries of the excursion sets, this quantity provides independent information and complements MFs in extracting the properties of random fields. We have obtained the estimator for K for a discretized random field on the sphere and presented the analytical expectation value of K for Gaussian isotropic fields. By studying the non-Gaussian deviations of K for non-Gaussian CMB maps, we have established the potential of this new morphological descriptor in constraining the non-Gaussian features in cosmological and foreground fields of different kinds.

Below, we mention some possible future directions of the analysis that was carried out in this thesis.

- We plan to develop pipelines for component separation that incorporate kurtosis non-Gaussianity for foreground components at small scales that we have observed.
- Our derivation of the MFs for a composite field can be further extended to include terms that are second-order in σ_0 (kurtosis terms). The applications of these formulas, both in CMB and large-scale structure data, will be

valuable. For example, we can quantify how residual foregrounds can bias primordial non-Gaussianity. We plan to carry out this work in the future.

- The analysis done for Haslam and other synchrotron maps can be extended to data sets such as SPASS, QUIJOTE, CBASS, etc. These data sets have higher signal-to-noise for polarization compared to Planck and WMAP. Hence, they hold much promise for a deeper understanding of the statistical properties of both temperature and polarization foregrounds. This work will be undertaken in the near future.

- Using the whole suite of statistical tools, such as MFs, MTs, Betti numbers and total absolute curvature, we intend to conduct a detailed quantification of the primordial non-Gaussianity using the CMB data.

Bibliography

Abazajian K. N., et al., 2016, arXiv e-prints, p. arXiv:1610.02743

Abazajian K., et al., 2019, arXiv e-prints, p. arXiv:1907.04473

Ade P. A. R., et al., 2015, Phys. Rev. Lett., 114, 101301

Ade P. A. R., et al., 2016, A&A, 594, A25

Ade P., et al., 2019, JCAP, 2019, 056

Adler R. J., 2010, The Geometry of Random Fields. Society for Industrial and Applied Mathematics, doi:10.1137/1.9780898718980, https://epubs.siam.org/doi/abs/10.1137/1.9780898718980

Alam S., et al., 2021, PRD, 103, 083533

Ali-Haimoud Y., Hirata C. M., Dickinson C., 2009, MNRAS, 395, 1055

Allys E., Levrier F., Zhang S., Colling C., Regaldo-Saint Blancard B., Boulanger F., Hennebelle P., Mallat S., 2019, A&A, 629, A115

Allys E., et al., 2023, PTEP, 2023, 042F01

Alonso D., Sanchez J., Slosar A., LSST Dark Energy Science Collaboration 2019, MNRAS, 484, 4127

Alpher R. A., Herman R., 1948, Nature, 162, 774

Alpher R. A., Herman R. C., 1949, Phys. Rev., 75, 1089

Andersen K. J., et al., 2022, arXiv e-prints, p. arXiv:2201.08188

Andrade U., Goncalves R. S., Carvalho G. C., Bengaly C. A. P., Carvalho J. C., Alcaniz J., 2022, JCAP, 2022, 088

Appleby S., Chingangbam P., Park C., Hong S. E., Kim J., Ganesan V., 2018a, ApJ, 858, 87

Appleby S., Chingangbam P., Park C., Yogendran K. P., Joby P. K., 2018b, ApJ, 863, 200

Appleby S., Kochappan J. P., Chingangbam P., Park C., 2022,] 10.3847/1538-4357/aca530

Aylor K., Haq M., Knox L., Hezaveh Y., Perreault-Levasseur L., 2020, MNRAS, 500, 3889

BICEP2 Collaboration et al., 2014, *Physical Review L*, 112, 241101

Baccigalupi C., Burigana C., Perrotta F., De Zotti G., La Porta L., Maino D., Maris M., Paladini R., 2001, A&A, 372, 8

Balkenhol L., et al., 2023, PRD, 108, 023510

Bardeen J. M., 1980, PRD, 22, 1882

Bardeen J. M., Bond J. R., Kaiser N., Szalay A. S., 1986, ApJ, 304, 15

Bartolo N., Komatsu E., Matarrese S., Riotto A., 2004, PhR, 402, 103

Basak S., Delabrouille J., 2013, MNRAS, 435, 18

Baumann D., 2022, Cosmology. Cambridge University Press, doi:10.1017/9781108937092, https://doi.org/10.1017/9781108937092

Baumann D., et al., 2009, in Dodelson S., et al., eds, American Institute of Physics Conference Series Vol. 1141, CMB Polarization Workshop: Theory and Foregrounds: CMBPol Mission Concept Study. pp 10–120 (arXiv:0811.3919), doi:10.1063/1.3160885

Ben-David A., von Hausegger S., Jackson A. D., 2015, JCAP, 2015, 019

Bennett C. L., et al., 2003, ApJS, 148, 97

Bennett C. L., et al., 2013, The Astrophysical Journal Supplement Series, 208, 20

BeyondPlanck Collaboration et al., 2020, arXiv e-prints, p. arXiv:2011.05609

Bharadwaj S., Sahni V., Sathyaprakash B. S., Shandarin S. F., Yess C., 2000, ApJ, 528, 21

Boughn S. P., Crittenden R. G., 2005, *New Astronomy Reviews*, 49, 75

Buchert T., France M. J., Steiner F., 2017, Class. Quantum Gravity, 34, 094002

Burigana C., La Porta L., Reich W., Reich P., Gonzalez-Nuevo J., Massardi M., De Zotti G., 2006, PoS, CMB2006, 016

Cardoso J.-F., Martin M., Delabrouille J., Betoule M., Patanchon G., 2008, arXiv e-prints, p. arXiv:0803.1814

Carretti E., et al., 2019, MNRAS, 489, 2330

Chang C. L., et al., 2022, arXiv e-prints, p. arXiv:2203.07638

Chern S.-S., Lashof R. K., 1957, Am. J. Math., 79, 306

Chingangbam P., Park C., 2009, JCAP, 2009, 019

Chingangbam P., Park C., 2013, JCAP, 2013, 031

Chingangbam P., Rahman F., 2023, arXiv e-prints, p. arXiv:2311.12571

Chingangbam P., Park C., Yogendran K. P., van de Weygaert R., 2012, ApJ, 755, 122

Chingangbam P., Ganesan V., Yogendran K. P., Park C., 2017a, Physics Letters B, 771, 67

Chingangbam P., Yogendran K. P., Joby P. K., Ganesan V., Appleby S., Park C., 2017b, JCAP, 2017, 023

Chingangbam P., Goyal P., Yogendran K. P., Appleby S., 2021, PRD, 104, 123516

Chingangbam P., Yogendran K. P., Appleby S., Rahman F., Park C., 2024, Total absolute curvature for random fields in two dimensions, In prep.

Chluba J., Hill J. C., Abitbol M. H., 2017, MNRAS, 472, 1195

Cho J., Lazarian A., 2010, ApJ, 720, 1181

Chon G., Challinor A., Prunet S., Hivon E., Szapudi I., 2004, MNRAS, 350, 914

Codis S., Pichon C., Pogosyan D., Bernardeau F., Matsubara T., 2013, Monthly Notices of the Royal Astronomical Society, 435, 531

Coulson D., Crittenden R. G., Turok N. G., 1994, *Physical Review L*, 73, 2390

Coulton W. R., Spergel D. N., 2019, JCAP, 10, 056

Coulton W., Miranthis A., Challinor A., 2023, MNRAS, 523, 825

Davies R. D., Dickinson C., Banday A. J., Jaffe T. R., Gorski K. M., Davis R. J., 2006, MNRAS, 370, 1125

Delabrouille J., Cardoso J.-F., 2009, Diffuse Source Separation in CMB Observations. Springer Berlin Heidelberg, Berlin, Heidelberg, pp 159–205, doi:10.1007/978-3-540-44767-2_6

Delabrouille J., et al., 2013, A&A, 553, A96

Dickinson C., 2016, in 51st Rencontres de Moriond on Cosmology. pp 53–62 (arXiv:1606.03606)

Dickinson C., Davies R. D., Davis R. J., 2003, MNRAS, 341, 369

Dickinson C., et al., 2018, New Astronomy Reviews, 80, 1

Dickinson C., et al., 2019, MNRAS, 485, 2844

Dodelson S., 2021, Modern Cosmology. Elsevier, doi:10.1016/c2017-0-01943-2

Draine B. T., 2003, ARA&A, 41, 241

Draine B. T., 2011, Physics of the Interstellar and Intergalactic Medium. Princeton University Press, Princeton, doi:10.1515/9781400839087

Draine B. T., Hensley B., 2013, ApJ, 765, 159

Draine B. T., Hensley B. S., 2016, ApJ, 831, 59

Draine B. T., Lazarian A., 1998a, ApJL, 494, L19

Draine B. T., Lazarian A., 1998b, ApJ, 508, 157

Draine B. T., Lazarian A., 1999, ApJ, 512, 740

Ducout A., Bouchet F. R., Colombi S., Pogosyan D., Prunet S., 2013, MNRAS, 429, 2104

Dunkley J., et al., 2009, in Dodelson S., et al., eds, American Institute of Physics Conference Series Vol. 1141, CMB Polarization Workshop: Theory and Foregrounds: CMBPol Mission Concept Study. pp 222–264 (arXiv:0811.3915), doi:10.1063/1.3160888

Durrer R., 2015, Classical and Quantum Gravity, 32, 124007

Enqvist K., Takahashi T., 2008, JCAP, 2008, 012

Eriksen H. K., et al., 2004a, The Astrophysical Journal Supplement Series, 155, 227

Eriksen H. K., Banday A. J., Górski K. M., Lilje P. B., 2004b, ApJ, 612, 633

Eriksen H. K., Jewell J. B., Dickinson C., Banday A. J., Górski K. M., Lawrence C. R., 2008, ApJ, 676, 10

Fernández-Cobos R., Vielva P., Barreiro R. B., Martínez-González E., 2012, MNRAS, 420, 2162

Fields B. D., Olive K. A., Yeh T.-H., Young C., 2020, JCAP, 2020, 010

Finkbeiner D. P., 2003, ApJS, 146, 407

Finkbeiner D. P., Davis M., Schlegel D. J., 1999, ApJ, 524, 867

Fixsen D. J., 2009, ApJ, 707, 916

Friedmann A., 1924, Zeitschrift für Physik, 21, 326

Fuskeland U., et al., 2021, A&A, 646, A69

Galloway M., et al., 2022, arXiv e-prints, p. arXiv:2201.03509

Gamow G., 1948, Phys. Rev., 74, 505

Ganesan V., Chingangbam P., 2017, JCAP, 2017, 023

Ganesan V., Chingangbam P., Yogendran K. P., Park C., 2015, JCAP, 2015, 028

Gay C., Pichon C., Pogosyan D., 2012, PRD, 85, 023011

Ghosh T., Banday A. J., Jaffe T., Dickinson C., Davies R., Davis R., Gorski K., 2012, MNRAS, 422, 3617

Górski K. M., Hivon E., Banday A. J., Wandelt B. D., Hansen F. K., Reinecke M., Bartelmann M., 2005, ApJ, 622, 759

Goyal P., Chingangbam P., 2021, JCAP, 08, 006

Goyal P., Chingangbam P., Appleby S., 2020, JCAP, 2020, 020

Guth A. H., 1981, PRD, 23, 347

Guth A. H., Pi S. Y., 1982, Phys. Rev. Lett., 49, 1110

Génova-Santos R., et al., 2016, MNRAS, 464, 4107

Hadwiger H., 1959, Mathematische Zeitschrift, 71, 1432

Hanany S., et al., 2000, ApJL, 545, L5

Harper S. E., et al., 2022, MNRAS, 513, 5900

Harrison E. R., 1967, MNRAS, 137, 69

Haslam C. G. T., Klein U., Salter C. J., Stoffel H., Wilson W. E., Cleary M. N., Cooke D. J., Thomasson P., 1981, A&A, 100, 209

Haslam C. G. T., Salter C. J., Stoffel H., Wilson W. E., 1982, Astron. astrophys., Suppl. ser. (Print), 47, 1

Henderson R., Makarenko I., Bushby P., Fletcher A., Shukurov A., 2017, arXiv e-prints, p. arXiv:1703.07256

Hensley B. S., Bull P., 2018, ApJ, 853, 127

Hervias-Caimapo C., Huffenberger K. M., 2022, ApJ, 928, 65

Hikage C., Matsubara T., 2012, MNRAS, 425, 2187

Hill J. C., 2018, PRD, 98, 083542

Hinshaw G., et al., 2013a, ApJS, 208, 19

Hinshaw G., et al., 2013b, ApJS, 208, 19

Hivon E., Górski K. M., Netterfield C. B., Crill B. P., Prunet S., Hansen F., 2002, ApJ, 567, 2

Hu W., 2001, PRD, 64, 083005

Hu W., White M., 1997, New A, 2, 323

Hubble E., 1929, Proceedings of the National Academy of Sciences, 15, 168

Hunter J. D., 2007, Computing in Science & Engineering, 9, 90

Irfan M. O., 2023, MNRAS, 520, 6070

Joby P. K., Chingangbam P., Ghosh T., Ganesan V., Ravikumar C. D., 2019, JCAP, 2019, 009

Johnson N. L., Kotz S., Balakrishnan N., 1994, Continuous Univariate Distributions Volume 1. Wiley, NewYork, https://ideas.repec.org/a/eee/csdana/v21y1996i1p119-119.html

Jung G., Racine B., van Tent B., 2018, JCAP, 2018, 047

Kamionkowski M., Kosowsky A., Stebbins A., 1997, PRD, 55, 7368

Kapahtia A., Chingangbam P., Appleby S., Park C., 2018, JCAP, 2018, 011

Kapahtia A., Chingangbam P., Appleby S., 2019, JCAP, 2019, 053

Kapahtia A., Chingangbam P., Ghara R., Appleby S., Choudhury T. R., 2021, JCAP, 05, 026

Keating B. G., Ade P. A. R., Bock J. J., Hivon E., Holzapfel W. L., Lange A. E., Nguyen H., Yoon K. W., 2003, in Fineschi S., ed., Society of Photo-Optical Instrumentation Engineers (SPIE) Conference Series Vol. 4843, Polarimetry in Astronomy. pp 284–295, doi:10.1117/12.459274

Kim J., Naselsky P., Christensen P. R., 2008, PRD, 77, 103002

Kitayama T., et al., 2023, PASJ, 75, 311

Kochappan J. P., Sen A., Ghosh T., Chingangbam P., Basak S., 2021,] 10.1103/PhysRevD.103.123523

Kofman L., Linde A., Starobinsky A. A., 1997, PRD, 56, 3258

Kogut A., 2012, ApJ, 753, 110

Kogut A., et al., 1993, ApJ, 419, 1

Kogut A., Banday A. J., Bennett C. L., Gorski K. M., Hinshaw G., Smoot G. F., Wright E. I., 1996, ApJL, 464, L5

Komatsu E., Spergel D. N., 2001, PRD, 63, 063002

Kovac J. M., Leitch E. M., Pryke C., Carlstrom J. E., Halverson N. W., Holzapfel W. L., 2002, Nature, 420, 772

Krachmalnicoff N., Puglisi G., 2021, ApJ, 911, 42

Krachmalnicoff N., et al., 2018, A&A, 618, A166

La Porta L., Burigana C., Reich W., Reich P., 2008, A&A, 479, 641

Lange A. E., et al., 2001, Phys. Rev. D, 63, 042001

Lazarian A., Pogosyan D., 2012, ApJ, 747, 5

Leach S. M., et al., 2008, A&A, 491, 597

Leitch E. M., Readhead A. C. S., Pearson T. J., Myers S. T., 1997, ApJL, 486, L23

Lemaître A. G., 1931, MNRAS, 91, 483

Lewis A., Challinor A., 2006, PhR, 429, 1

Lewis A., Challinor A., Lasenby A., 2000, ApJ, 538, 473

Lim E. A., Simon D., 2012, JCAP, 2012, 048

Linde A. D., 1982, Phys. Lett. B, 108, 389

Macellari N., Pierpaoli E., Dickinson C., Vaillancourt J. E., 2011, MNRAS, 418, 888

Makarenko I., Shukurov A., Henderson R., Rodrigues L. F. S., Bushby P., Fletcher A., 2018, MNRAS, 475, 1843

Maldacena J. M., 2003, JHEP, 05, 013

Martin J., Ringeval C., Vennin V., 2014, Physics of the Dark Universe, 5, 75

Martire F. A., Barreiro R. B., Martínez-González E., 2022, JCAP, 2022, 003

Martire F. A., Banday A. J., Martínez-González E., Barreiro R. B., 2023, JCAP, 04, 049

Martínez-González E., Diego J. M., Vielva P., Silk J., 2003, MNRAS, 345, 1101

Mather J. C., et al., 1990, ApJL, 354, L37

Matsubara T., 2003, ApJ, 584, 1

Matsubara T., 2010, PRD, 81, 083505

Matsubara T., Kuriki S., 2020, arXiv e-prints, p. arXiv:2011.04954

Matsumura T., et al., 2014, Journal of Low Temperature Physics, 176, 733

Mauskopf P. D., et al., 2000, Astrophys. J. Lett., 536, L59

Mecke K. R., Buchert T., Wagner H., 1994, A&A, 288, 697

Meerburg P. D., et al., 2019, Primordial Non-Gaussianity (`arXiv:1903.04409`)

Meisner A. M., Finkbeiner D. P., 2015, ApJ, 798, 88

Mertsch P., Sarkar S., 2013, JCAP, 06, 041

Minkowski H., 1903, Mathematische Annalen, 57, 447

Miville-Deschênes M.-A., Ysard N., Lavabre A., Ponthieu N., Macías-Pérez J. F., Aumont J., Bernard J. P., 2008, A&A, 490, 1093

Mukhanov V., 1992, Physics Reports, 215, 203

Mukhanov V. F., Chibisov G. V., 1981, ZhETF Pisma Redaktsiiu, 33, 549

Munshi D., Smidt J., Cooray A., Renzi A., Heavens A., Coles P., 2013, MNRAS, 434, 2830

Novikov D., Schmalzing J., Mukhanov V. F., 2000, A&A, 364, 17

Novikov D., Colombi S., Doré O., 2006, MNRAS, 366, 1201

Orlando E., Strong A., 2013, MNRAS, 436, 2127

Park C., et al., 2013, J. Korean Astron. Soc., 46, 125

Peebles P. J. E., 1980, The large-scale structure of the universe

Pelgrims V., Clark S. E., Hensley B. S., Panopoulou G. V., Pavlidou V., Tassis K., Eriksen H. K., Wehus I. K., 2021, A&A, 647, A16

Penzias A. A., Wilson R. W., 1965, ApJ, 142, 419

Perlmutter S., et al., 1999, ApJ, 517, 565

Philcox O. H. E., 2023a, arXiv e-prints, p. arXiv:2306.03915

Philcox O. H. E., 2023b, PRD, 107, 123516

Planck Collaboration et al., 2014, A&A, 571, A16

Planck Collaboration et al., 2016a, A&A, 594, A1

Planck Collaboration et al., 2016b, A&A, 594, A10

Planck Collaboration et al., 2016c, A&A, 594, A17

Planck Collaboration et al., 2016d, A&A, 594, A25

Planck Collaboration et al., 2017, A&A, 599, A51

Planck Collaboration et al., 2020a, A&A, 641, A1

Planck Collaboration et al., 2020b, A&A, 641, A3

Planck Collaboration et al., 2020c, A&A, 641, A4

Planck Collaboration et al., 2020d, A&A, 641, A6

Planck Collaboration et al., 2020e, A&A, 641, A9

Planck Collaboration et al., 2020f, A&A, 641, A11

Platania P., Burigana C., Maino D., Caserini E., Bersanelli M., Cappellini B., Mennella A., 2003, A&A, 410, 847

Pogosyan D., Pichon C., Gay C., 2011, PRD, 84, 083510

Polarbear Collaboration et al., 2014, ApJ, 794, 171

Pranav P., 2021, arXiv e-prints, p. arXiv:2109.08721

Qu F. J., et al., 2023, arXiv e-prints, p. arXiv:2304.05202

Rahman F., Chingangbam P., Ghosh T., 2021, JCAP, 07, 026

Rahman F., Chingangbam P., Ghosh T., 2022, arXiv e-prints, p. arXiv:2212.06076

Rana S., Ghosh T., Bagla J. S., Chingangbam P., 2018, MNRAS, 481, 970

Regaldo-Saint Blancard B., Levrier F., Allys E., Bellomi E., Boulanger F., 2020, A&A, 642, A217

Regaldo-Saint Blancard B., Allys E., Boulanger F., Levrier F., Jeffrey N., 2021, A&A, 649, L18

Regaldo-Saint Blancard B., Allys E., Auclair C., Boulanger F., Eickenberg M., Levrier F., Vacher L., Zhang S., 2023, ApJ, 943, 9

Reich P., Reich W., 1986, A&A, 63, 205

Remazeilles M., Delabrouille J., Cardoso J.-F., 2011, MNRAS, 418, 467

Remazeilles M., Dickinson C., Banday A. J., Bigot-Sazy M. A., Ghosh T., 2015, MNRAS, 451, 4311

Remazeilles M., Dickinson C., Eriksen H. K. K., Wehus I. K., 2016, MNRAS, 458, 2032

Remazeilles M., Rotti A., Chluba J., 2021, MNRAS, 503, 2478

Rezaie M., et al., 2023, arXiv e-prints, p. arXiv:2307.01753

Riess A. G., et al., 1998, AJ, 116, 1009

Riess A. G., et al., 2022, ApJL, 934, L7

Robertson H. P., 1935, ApJ, 82, 284

Rubino-Martin J. A., et al., 2023, MNRAS, 519, 3383

Rybicki G. B., Lightman A. P., 1985, Radiative Processes in Astrophysics. Wiley-VCH Verlag GmbH & Co. KGaA, doi:10.1002/9783527618170, https://doi.org/10.1002/9783527618170

Sahni V., Sathyaprakash B. S., Shandarin S. F., 1998, ApJL, 495, L5

Sakharov A. D., 1967, Pisma Zh. Eksp. Teor. Fiz., 5, 32

Salopek D. S., Bond J. R., 1990, PRD, 42, 3936

Sartoris B., et al., 2016, MNRAS, 459, 1764

Schlegel D. J., Finkbeiner D. P., Davis M., 1998, ApJ, 500, 525

Schmalzing J., Buchert T., 1997, ApJL, 482, L1

Schneider R., 2013, Convex Bodies The Brunn-MinkowskiTheory. Cambridge University Press, doi:10.1017/cbo9781139003858, https://doi.org/10.1017/cbo9781139003858

Schröder-Turk G., Kapfer S., Breidenbach B., Beisbart C., Mecke K., 2010, Journal of Microscopy, 238, 57

Seljak U., Zaldarriaga M., 1997, *Physical Review L*, 78, 2054

Seljebotn D. S., Bærland T., Eriksen H. K., Mardal K. A., Wehus I. K., 2019, A&A, 627, A98

Silsbee K., Ali-Haïmoud Y., Hirata C. M., 2011, MNRAS, 411, 2750

Smoot G. F., et al., 1992, ApJL, 396, L1

Starobinskii A. A., 1979, ZhETF Pisma Redaktsiiu, 30, 719

Strong A. W., Orlando E., Jaffe T. R., 2011, A&A, 534, A54

Sunyaev R. A., Zeldovich Y. B., 1970, Ap&SS, 7, 3

Szapudi I., Prunet S., Pogosyan D., Szalay A. S., Bond J. R., 2001, ApJL, 548, L115

Tegmark M., Efstathiou G., 1996, MNRAS, 281, 1297

Tegmark M., Eisenstein D. J., Hu W., de Oliveira-Costa A., 2000, ApJ, 530, 133

Tellarini M., Ross A. J., Tasinato G., Wands D., 2016, JCAP, 2016, 014

Testori J. C., Reich P., Bava J. A., Colomb F. R., Hurrel E. E., Larrarte J. J., Reich W., Sanz A. J., 2001, A&A, 368, 1123

Thorne B., Dunkley J., Alonso D., Næss S., 2017, MNRAS, 469, 2821

Thorne B., Knox L., Prabhu K., 2021, MNRAS, 504, 2603

Thornton R. J., et al., 2016, ApJS, 227, 21

Tomita H., 1986, Progress of Theoretical Physics, 76, 952

Tristram M., Macías-Pérez J. F., Renault C., Santos D., 2005, MNRAS, 358, 833

Tristram M., et al., 2022, PRD, 105, 083524

Uhlemann C., Pajer E., Pichon C., Nishimichi T., Codis S., Bernardeau F., 2018, MNRAS, 474, 2853

Vazquez Gonzalez J. A., Padilla L. E., Matos T., 2020, Revista Mexicana de Física E, 17, 73–91

Vidal M., Dickinson C., Davies R. D., Leahy J. P., 2015, MNRAS, 452, 656

Virtanen P., et al., 2020, Nature Methods, 17, 261

Waelkens A., Jaffe T., Reinecke M., Kitaura F. S., Enßlin T. A., 2009, A&A, 495, 697

Walker A. G., 1937, Proceedings of the London Mathematical Society, s2-42, 90

Westfold K. C., 1959, ApJ, 130, 241

Wise J. H., 2019, arXiv e-prints, p. arXiv:1907.06653

Yadav J. K., Bagla J. S., Khandai N., 2010, MNRAS, 405, 2009

Zaldarriaga M., 2001, PRD, 64, 103001

Zonca A., Singer L., Lenz D., Reinecke M., Rosset C., Hivon E., Gorski K., 2019, The Journal of Open Source Software, 4, 1298

de Bernardis P., et al., 2000, Nature, 404, 955

van de Weygaert R., et al., 2013, arXiv e-prints, p. arXiv:1306.3640

van der Walt S., Colbert S. C., Varoquaux G., 2011, Computing in Science and Engineering, 13, 22

von Hausegger S., Gammelgaard Ravnebjerg A., Liu H., 2019, MNRAS, 487, 5814